
UNIVERSITY OF
BIRMINGHAM

# DEVELOPMENT OF A LORENTZ FORCE DRIVE SYSTEM FOR A TORSIONAL PADDLE MICRORESONATOR USING FOCUSED ION BEAM MACHINING

By

Sahand Chitsaz Charandabi

A thesis submitted to
The University of Birmingham
For the degree of
**Doctor of Philosophy**

SCHOOL OF MECHANICAL ENGINEERING
THE UNIVERSITY OF BIRMINGHAM
FEBRUARY 2014

# Abstract

This thesis focuses on the concept, design, fabrication and characterisation of a torsional micro paddle resonator. The ultimate intention is to use the device for rapid detection of anthrax bacteria. A comprehensive research was carried out to review the state of the art in MEMS based mass sensing. Various driving and detection strategies were investigated and discussed. Based on evidence from literature, a novel approach was adopted to realise a device with improved functionality and overcome currently existing drawbacks. The working principle of the proposed device is based on electromagnetic actuation and monitoring of the shift in resonance frequency of a micro paddle. The design of the paddle was optimised using theoretical and finite element methods. Dual beam Focused Ion Beam (FIB) machining techniques were used to fabricate the prototype devices. The chosen substrate is a LPCVD 200 nm thick silicon nitride membrane. Prior to milling the substrate, the sputtering rate of silicon nitride was validated experimentally to ensure machining stability. Different actuating pattern designs were fabricated to generate torque including micro spiral coil, micro dual loop, and single conductive track on the micro paddle. The geometry was finalised for a defined working condition of 1 MHz resonance frequency. Important fabrication parameters were discussed and damage prevention issues were investigated. The sensitivity to the added mass was experimentally characterised and found to be 2.35 fg/Hz. To characterise the asymmetrical paddle resonator, piezoelectric excitation was applied to the device and a laser Doppler vibrometer was used to record the resonant frequency. Resonant frequencies of 0.841 and 0.818 MHz were detected by testing the device in an air medium and a quality factor of about 300 was calculated by applying a Lorentzian curve fit to collected data.

*I dedicate this thesis to my parents.*

# Acknowledgments

First I would like to thank my supervisors Prof. Philip Prewett and Dr. Carl Anthony for their help, guidance and supervision throughout the period of my research course. I wish to thank Dr. Xianghong Ma and Zhao Ding for their fruitful collaboration and their kind help to provide vibration testing facilities. I would also like to thank Prof. John Preece regarding bio chemical aspect of this project.

I wish to thank Dr. Andy Murray for his assistance in micro fabrication of the stencil masks.

I would like to thank my colleagues Haseena, Aydin, Nasim, Sean, Hossein, Nor, Ali Mohammadkhani, Ali Kubba, Jay, Rob, Ali M. Sadeghioon and Hany at the centre for micro and nano technology of Birmingham University.

I also wish to thank Prof. Farhang Bakhtar, and Dr. Mozafar Saadat for their helpful personal advice.

I would like to particularly thank Haseena B. Muhammad for her kind help with Latex and thesis correction, and also her assistance throughout my write up period.

I would specially like to thank my father, Sirous, for his financial support and endless encouragement and my mother and sisters, Solmaz, Sonia and Sama, for their love and care throughout my academic life.

Sahand Chitsaz Charandabi

Birmingham

February 7, 2014

# Publications

During the course of this project, the following Journal Papers and Conference Proceedings have been published:

### Journal Papers

1. S. Chitsaz Charandabi, P. D. Prewett, C. A. Hamlett, C. J. Anthony, and J. A. Preece, "Nano planar coil actuated micro paddle resonator for mass detection", Microelectronic Engineering, 88 (8), 2229-2232 (2011)

### Conference Proceedings

1. S. Chitsaz Charandabi, P. D. Prewett, C. J. Anthony, X. Ma, and C. A. Hamlett, "Torsional micro paddle resonator for rapid detection of BWAs", Poster Presentation, International Conference on Micro and Nano Engineering (MNE), 19th - 22nd September, Italy (2010)

2. S. Chitsaz Charandabi, M. Malboubi, C. J. Anthony, and P. D. Prewett, "Design, fabrication and surface treatment of a micropaddle resonator for ultra low mass detection", Oral Presentation, International Conference on Micro and Nano Engineering (MNE), 19th - 23rd September, Germany (2011)

3. S. Chitsaz Charandabi, Aydin Sabouri, H. Ostadi, P. D. Prewett, C. J. Anthony and K. Jiang, "FIB milling characterisation of nanoporous materials", Oral Presentation, International Conference on Micro and Nano Engineering (MNE), 19th - 23rd September, Germany (2011)

4. S. Chitsaz Charandabi, C. J. Anthony, and P. D. Prewett, "Development of a torsional

paddle microresonator for mass detection", International Conference on Nanotechnology (IEEE-Nano), poster presentation, 20th - 23rd August, United Kingdom (2012)

5. S. Chitsaz Charandabi, Aydin Sabouri, H. Ostadi, P. D. Prewett, C. J. Anthony and K. Jiang, "Characterisation of nanoporous materials using focused ion beam milling method", International Conference on Nanotechnology (IEEE-Nano), poster presentation, 20th - 23rd August, United Kingdom (2012)

*"**Success** usually comes to those who are too busy to be looking for it"*

- Henry David Thoreau

# Contents

# List of Figures

# List of Tables

# 1

# Introduction

## Contents




**Summary** This chapter provides a background and motivation for the development of mass detection systems. An introduction to MEMs systems is given with an overview of some of their major applications particularly in the field of in mass detection. The motivation for the work is given, followed by the aims and objectives of this study. Finally, an overview of the thesis structure is given.

## 1.1 Background

Biosensors have attracted considerable interest over the recent years as detection of specific substances is key to many applications ranging from clinical analysis to environmental control, security and monitoring of industrial processes [1–4]. One particular present day concern is the threat of bioterrorism. The use of biological agents such as anthrax, glanders and cholera in shape of bio warfare weapons has been employed since World War I and still continues, as highlighted by a number of high profile anthrax attacks on US soil, and ricin[1] attacks in the United Kingdom following the September 11, 2001 terrorist attacks. There has thus emerged a need for the critical detection of hazardous pathogens and toxic molecules in the environment to minimize health hazards and prevent the spread of microbe-related diseases [5–9]. The requirements for rapid detection, high sensitivity and accurate measurement of such threats has led to a high volume of research on the innovation of chemical and biological sensors[10–13].

The application of Microelectromechanical systems (MEMS) technology has played a key role in the realisation of state of the art chemical/ mass sensor based detection devices[14, 15]. MEMS are miniaturised devices, consisting of a combination of electrical and mechanical components. They are capable of sensing, controlling and actuating on the micro scale and can function individually or in arrays to generate effects on the macro scale [16]. Their characteristic dimensions are in the range of several microns to a millimetre. Figure 1.1 shows the micro to nano scale range and gives an overview of the natural entities for didactic comparison.

MEMS based devices have numerous applications in industrial, security, environmental

[1] A potent poison from castor beans

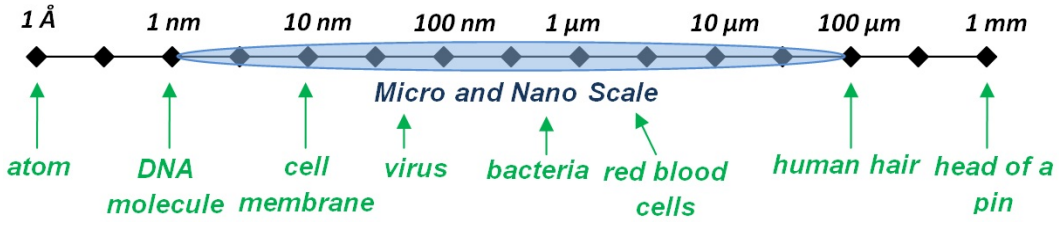


FIGURE 1.1: Schematic illustrating the scale-range where nano science applies, starting from single atom and molecule to virus, bacteria and supermolecular entities (Adapted from [17]).

control and biomedical sectors [18].

The adoption of a MEMS based approach for biosensing applications can be attributed to the merging of silicon microfabrication techniques with surface functionalisation biochemistry [2]. The application of MEMS technologies allows the development of devices that could easily be integrated into portable "lab-on-chip" platforms to perform "point-of-care" analysis because, for many applications, portability is a major issue [19]. Additional advantages of this approach over conventional detection sensors include [20]:

- Lower detection limits and sample volumes
- Rapid and high sensitivity detection
- Reduced material requirements to fabricate devices
- Reduced power consumption
- Reliability, portability and stability
- Potential low cost due to batch fabrication
- Possibility for incorporating sensing transducer and control system on the same substrate

The basis of these devices is the chemical adsorption of target molecules onto the surface of the sensing element. MEMS chemical sensors transduce physical quantities into measurable output signal by utilising a chemically selective coating that has a specific affinity to

the target substance [21]. A schematic of the working principle of chemical sensors is depicted in Figure 1.2. A receptor specific to a single chemical or biological target is utilised for immobilising the species of interest and then a wide variety of physical and chemical mechanisms are implemented for detection and transduction, leading to a measurable signal response [22].

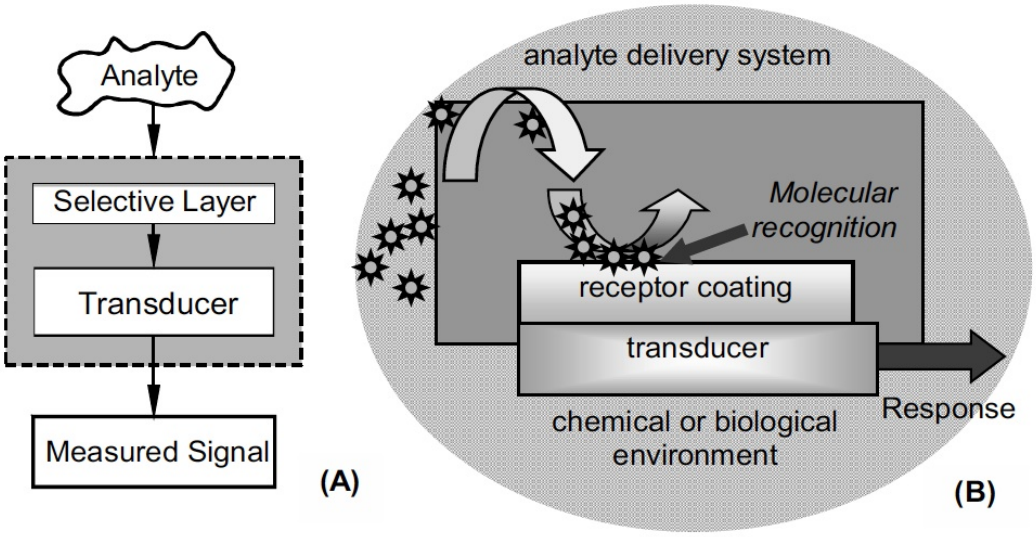


FIGURE 1.2: Operating principle of a chemical sensor. (A) General schematic of the chemical sensor, which produces an output signal in response to the existance of target molecule. (B) Chemically modified surface as a receptor layer applied to a chemical sensor allows a highly selective response [21].

The operation of MEMS biosensors relies on the mechanical movement of micro machined components such as cantilevers, bridges and paddles. In these systems, as a result of adsorption of a targeted substance, two mechanisms can be applied. One is deflection of the sensing part, which is due to a difference in mechanical properties of receptor layer and substrate material. As target molecules land on the surface, they change surface properties of the receptor layer which in turn, results in bending of the sensing component. A second approach is based on a dynamic mode of operation, where absorption of target molecules

creates an alteration in the frequency of the vibrational component which can be recorded [21, 23, 24].

State of the art devices adopt a mass sensing principle which is based on the detection of a change in resonance frequency of an oscillating microresonator based on the added mass due to adsorption of a target substance. With the advantages of ultra-high sensitivity (detection in the range of few femtograms), fluorescence labeling free, insitu detection and low cost fabrication, such bio sensors based on micro machined resonators have been gaining significant interest in recent years [25]. Additionally, the employment of resonators with ultra-high mass sensitivity are particularly desirable because of their inherent high frequency operation in their fundamental mechanical mode which is beneficial for realising high speed sensors with ultimate sensitivity [26]. Ultra-high sensitivity mass detection capability gives information about the existence of a specific gas or bio-agent at levels down to femto and picograms. This allows the detection for much lower amounts of the agent allowing detection in faster times as less agent needs to reach detector or for situations where a very low trace amount of contaminant agent is present. This could help to detect a hazardous species in a short time and prevent terrorist attack and accidental poisoning.

## 1.2 Motivation

Chemically functionalised MEMS resonant sensors offer a higher sensitivity for detection due to their small size and frequency stability. They have shown potential for applications in detection of biowarfare agents, relevant to both national and international security [27]. To this end, the goal of the work carried out in this thesis is to develop a device which utilises chemically modified microresonators to detect bio-warfare agents using a mass detection

approach. The intended device would be small enough to probe areas which are difficult to access with current, more bulky detection systems. The potential low cost of such a device, coupled with its small size, would allow numerous such devices to be placed in a network of sensors, thus allowing simultaneous detection for the presence of biowarfare agents over a large area. The device uses electromagnetic actuation system due to contact-less drive method. It also benefits from simple electronic circuit design and manufacturing since there is no bilayer of metal or PZT required. Also with electromagnetic actuation there are no small gaps required that result in excessive film damping as in capacitive drives. In addition, the bending static mode of operation devices have bilayers in order to transmit the deflection. This causes the system to be under stress at all times. This would cause to produce cracks and reduces the life span of the device.

One of the applications for the use of such a device that is targeted in this work is the detection of Bacillus anthracis. The named bacteria is an infamous pathogen known to cause anthrax, a noncontagious but potentially fatal disease that can be aquired through inhalation or injection of the spores (via eating or through cuts in skin). Bacillus anthracis, shown in Figure 1.3 is a Gram positive bacterial that is 3 - 10 $\mu$m in length and 1 - 1.5 $\mu$m in width [28]. The Bacillus anthracis bacteria can exist in two different forms: rod-shaped organisms and spores. The rod shaped organisms grow and proliferate in favorable nutrient rich environments. In adverse conditions, the organisms morph into spores which consist of a central cell surrounded by various protective layers. Dipicolinic acid (DPA) exists in these protective layers making up 5 - 14 $\%$ of the spores dry weight and thus being a useful biomarker for anthrax spores which the sensors in this work can be designed to detect [29].

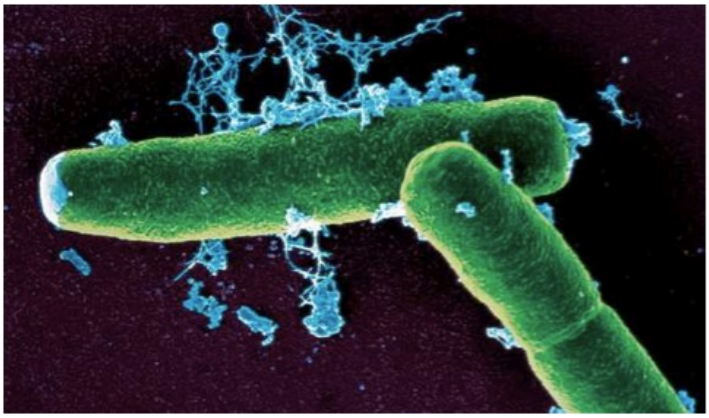

FIGURE 1.3: Scanning Electron Micrograph (SEM) of anthrax bacteria (Bacillus anthracis), which causes the disease anthrax in humans and livestock[2].

In addition to the detection of Basillus anthracis, the developed sensors will also be suitable for detection of the volatile compounds (VCs) given off by explosives. Commercially available detectors currently on the market are typically hand held and weigh approximately 1.5 kg with the cheapest system costing approximately $ 70 per unit [30, 31]. The detection sensitivity of these commercial devices is well below 8000 - 10000 anthrax spores, which is considered to be the LD50[3] value of aerolised anthrax spores [32]. Research on the development of anthrax detection sensors attempt to address the above mentioned limitations of commercially available systems.

Thus, the work in this thesis aims to realise a sensing device with ultra-low mass detection capability in the range of femtograms, which is advantageous over current commercial systems.

[2]http://scienceforums.com/gallery/image/2185-anthrax-bacteria/ (Cited 20/10/2011)
[3]Lethal Dose 50%

## 1.3 Aims and Objectives

This project aims to develop a novel vibrational ultra sensitive mass detection resonator operable using electromagnetic actuation principles, for detection in an air environment. The main areas that will be addressed in this thesis are the following:

- Design of a sensitive resonator element
- Fabrication of the designed resonator
- Characterisation of the fabricated device

## 1.4 Novelty of the Research

The research presented in this thesis shows the development of a platinum nanocoil on a silicon nitride micropaddle resonator where the coil is designed to form the key part of a Lorentz force drive system for the micropaddle, that will allow it to be driven into resonance by an alternating electric current flowing through the coil. The paddle sensor concept has several advantages over conventional cantilever systems (refer to sections 3.1 and 3.3). The Lorentz drive method has particular advantages over other methods, which are discussed in detail in chapter 2. These include the much lower power requirement of the integrated coil that has benefits for remote wireless sensing applications. The research specifically presents the development of the fabrication process of the coil on the micropaddle using focused ion beam technology. To the author's knowledge this is the first such coil fabricated on a resonator of this sort and is the first time that one has been fabricated on both sides of the paddle to give a dual coil. To be able to design the coil the limitations of the chosen focused ion beam micro fabrication technology had to be investigated and understood. This

knowledge is reported in the thesis and acts as a source for researchers intending to fabricate similar sized features in the future. Detailed fabrication process flows are also developed for the fabrication of the coil and the micropaddle and are reported in chapter 4, these will enable other researchers to fabricate similar coils for this and other applications in the future.

## 1.5 Thesis Overview

In the following chapters, the development of the mass detection device is described. Chapter 2 provides a literature review covering the state of the art in MEMS based chemical/ mass sensing. A review of mass sensitive cantilevers, transduction mechanisms, operation modes and driving and monitoring mechanisms is presented. An overview of recent developments in the field is given with a discussion on potential applications.

Chapter 3 describes the theory and design of a micro paddle resonator. A system-level-model is developed and presented in this chapter along with advantages of the micro paddle design and Lorentz force actuation system. General equations of motion for vibrational systems are described followed by derivations for the proposed design. The operating principle of the micro paddle is presented and frequency variation parameters discussed. Analytical calculations of force and torque are given followed by the results of computer simulation for predicting the heat, magnetic flux, self-inductance generated in the coil and the natural frequency of the micro paddle. Furthermore, heat generation simulations were added for three different designs, where the results are compared and considerations have been taken into account in order to prevent temperature to reach the melting point.

Chapter 4 provides a description of the fabrication process used to realise the device. A description of substrate preparation and machining parameters are provided. The motivation

for the use of focused ion beam methods in the fabrication of the proposed micro paddle is given. The principle of operation of focused ion beam milling is presented followed by details of the fabrication steps employed in the realisation of the micro paddle resonator. Fabrication constraints were discussed and the final produced prototype device is presented.

The focus of Chapter 5 is on the testing and characterisation of the prototype devices. In this chapter results from different tests are presented, discussed and compared. The response of the sensor to a known added mass is tested and thus sensitivity of the device is estimated.

Chapter 6 provides a conclusion to work conducted in this thesis. The possibilities for the future work and suggestions for potential improvements for enhanced device performance are then given.

# 2

# Literature Review

## Contents




**Summary** This chapter provides a literature review on biosensors, chemical sensors and sensors based on mass loading effect and gives a comprehensive description of different

working mechanisms and operating modes. The advantages of MEMS devices over conventional systems are given. A review of the state of the art in the field is presented along with the strengths and weaknesses. The use of chemically functionalised surfaces is introduced followed by a summary on Self Assembled Monolayers (SAM).

## 2.1 An Introduction to Biosensors

Leland C. Clark, a scientist in biochemistry, first developed enzyme electrodes in 1962. Since then, there has been an explosive growth of research conducted in this area with research communities from different disciplines including physics, chemistry and material science joining to collaborate and develop more sophisticated and reliable biosensing devices [33]. Two commonly used definitions of biosensors cited by S. P. J. Higson and D. M. Frazer, are "a biosensor is a chemical sensing device in which a biologically derived recognition entity is coupled to a transducer, to allow the quantitative development of some complex biochemical parameter" and "a biosensor is an analytical device incorporating a deliberate and intimate combination of a specific biological element (that creates a recognition event) and a physical element (that transduces the recognition event)" [34].

Biosensors can have a variety of biomedical, industry, and military applications, as shown in Figure 2.1. A major application is in blood glucose sensing because of its abundant market potential. However, in the non-clinical sector, it has been widely used for environment control, in the food industry and in detection of bioagents [35].

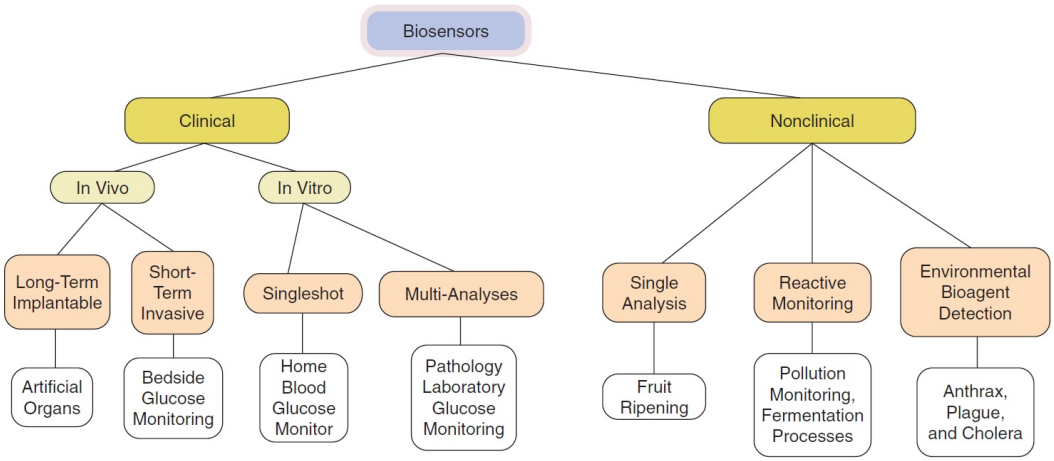


FIGURE 2.1: Potential applications of biosensors [33].

There are two main elements of a biosensor; the biological sensing element (bioelement) and the transducer. A bioelement is a biological molecular species (e.g. an antibody, enzyme, nucleic acid) or a living biological system (such as cells, tissue) that uses a biochemical mechanism for recognition [36]. They can bind or interact with specific analytes and serves as the recognition element thus defining the specificity of the sensor. The physical transducer detects the interaction between the bioelement and the target molecule and translates the change into a measurable effect such as an electrical signal, an optical emission or a mechanical motion. Examples of physical signals which can report the presence of target analyte molecules are fluorescence signals from dyes, electric fields from molecular charges, mass changes or refractive index changes from the adsorption of dimolecules onto sensor surfaces [37]. Figure 2.2 shows the basic components of a biosensor.

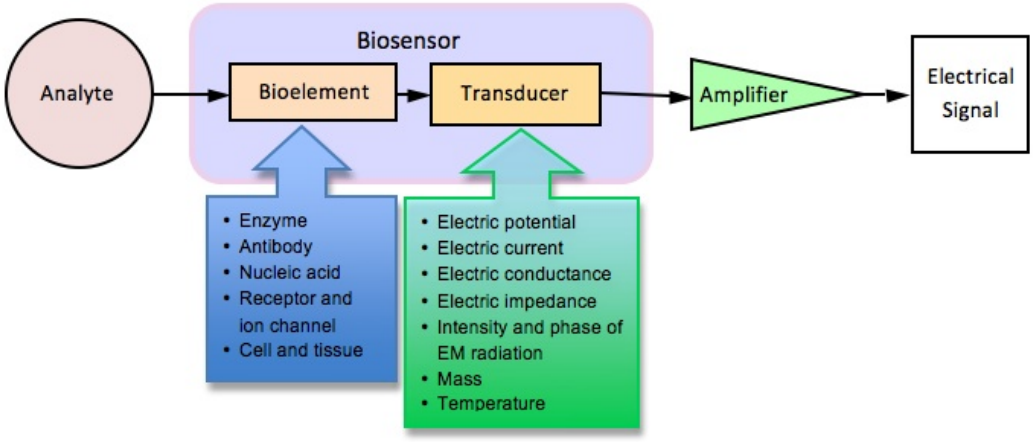


FIGURE 2.2: Schematic diagram of a biosensor showing the various components (Adapted from [38]).

Biosensors can be classified in a number of different ways. One such classification is based on the biological element used; giving rise to enzyme, immonosensor (antigen/antibody) or cell-based sensors [36].

Depending on the detection protocol employed, one can also differentiate between label-free (direct) and labelled (indirect) sensors. Label-free sensors detect the original and unmodified molecules and can be used for on-line monitoring or fast and direct detection (Figure 2.3 (A)). In labelled sensors, the target analyte molecules are first tagged with a label such as fluorescent tags or dyes. The presence of this label then acts as an indicator for the presence of the target molecule (Figure 2.3 (B)). Although labelling can improve sensitivity of the sensor, it tends to be time and cost consuming.

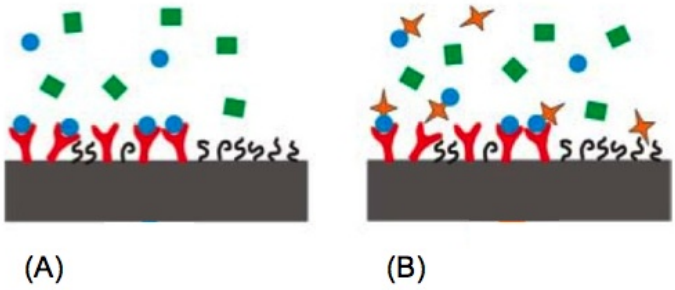


FIGURE 2.3: Biosensing principle. A bioelement layer of receptor molecules (red) attached to the sensor recognises and binds to target analyte molecules (blue circles) but does not bind background molecules (green squares). A molecular layer (black lines) protect the sensor against unspecific adsorption. (A) Label-free detection. (B) A label is attached to the target analyte and the sensor detects the presence of the label [37].

Yet another method of biosensor classification deals with the transduction mechanism employed. As previously mentioned, the transducer measures the change that occurs as a result of interaction between the bioelement and analyte and converts this change into a measurable signal [38]. Thus biosensors can be categorised into optical, mass, electrochemical and thermal biosensors.

The detection limit of biosensors can be lowered in one of three ways: Firstly, by using

biorecognition molecules or modifying surface chemistry to enhance the binding characteristics, secondly by limiting non-specific binding and finally by using more sensitive transducers [39]. In this thesis, the focus is on implementing a highly sensitive transducer element in order to develop a high sensitivity device.

## 2.2 Classification of Biosensors Based on Transduction

### 2.2.1 Thermal Biosensors

Thermal biosensors function by exploiting a fundamental property of biological processes, which is the generation or absorption of heat. These sensors are fabricated by combining immobilized analyte specific enzyme molecules with temperature sensors [33]. They measure the thermal energy absorbed or released during the biochemical reaction that occurs between the enzyme molecule and targeted analyte [40]. MEMS thermal biosensors have previously been demonstrated that detect changes in temperature using either thermistors or thermopiles [41]. Thermistors exhibit a change in electric resistance with temperature, which allows measurement of absolute temperatures. Thermopiles use a set of thermocouple junctions connected in series. This allows the measurement of differences in temperature between two regions where the thermocouple junctions are located [41].

Common applications of this type of biosensor include the detection of pesticides and pathogenic bacteria [33].

### 2.2.2 Optical Biosensors

Optical biosensors work based on detecting changes in properties such as absorption, refractive indices, fluorescence, phosphorescence, chemiluminescence, etc. that can occur when cells bind to receptors immobilized on the transducer surface.

The implemented detection protocols can be either fluorescence-based detection or label-free detection. In fluorescence-based detection, either target molecules or biorecognition molecules are labeled with fluorescent tags, such as dyes. The intensity of the fluorescence indicates the presence of the target molecules and the interaction strength between target and biorecognition molecules. Although fluorescence-based detection is extremely sensitive laborious labelling processes are required, which can also potentially interfere with the function of a biomolecule.

In label-free detection, target molecules are not altered, and are detected in their natural forms. For example, measurement of a change in refractive index induced by molecular interactions can be related to the sample concentration or surface density.

In 2007, Acharya et al. reported a label free optical biosensor for detection of anthrax spores. A schematic of the device is shown in Figure 2.4.

The device comprised laser light transmission measurement integrated with immobilized short peptide ligands. The sensor array was microfabricated on a glass wafer and consisted of two columns of gold coated rings (4.8 mm outer diameter and 200 $\mu$m inner diameter). The gold coated ring completely blocks transmission of the laser light, however the light is able to pass through the inner transparent region which is coupled to short peptide ligands and functions as a sensor well. Upon spore binding, the laser beam is blocked by the captured spores subsequently decreasing the overall transmission intensity. The device was

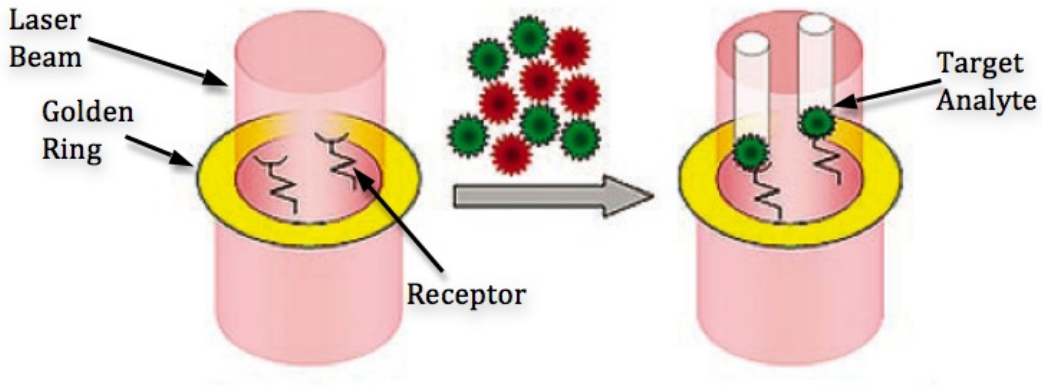


FIGURE 2.4: Schematic diagram of optical biosensor developed by Acharya et al. (2007) [42].

demonstrated to be able to detect as few as 34 anthrax spores.

In a different work by Yilmaz et al. in 2010, another example of optical detection mechanism based on fluorescent emission was presented [43]. Here, molecular printboards act as monolayers of $\beta$-cyclodextrin ($\beta$-CD) on a surface to which building blocks are attached in a noncovalent fashion that allow ratiometric Dipicolinic Acid (DPA) sensing. They developed luminescent patterns for the detection of DPA on a receptor surface. The schematic presented in the Figure 2.5 shows the working principle.

The process begins with printing of equimolar mixture of 1 and 2 onto $\beta$-CD monolayer by utilising microcontact printing technique ($\mu$CP) to generate surface patterns of the ligand pairs. After thorough rinsing with water and drying, the patterned surface was imaged by fluorescence microscopy using filter B and R. As such, filter B collects the naphthalene emission of 2, while filter R only collects the $Eu^{3+}$ emission of 1-$Eu^{3+}$. Next, the glass slides were immersed in a $EuCl_3$ solution for 30 min to convert 1 into 1-$Eu^{3+}$, monitored by fluorescence imaging. Subsequently, substrates were incubated into aqueous solutions of DPA with different concentrations (pH 6.5) for 10 min with continuous stirring. After rinsing

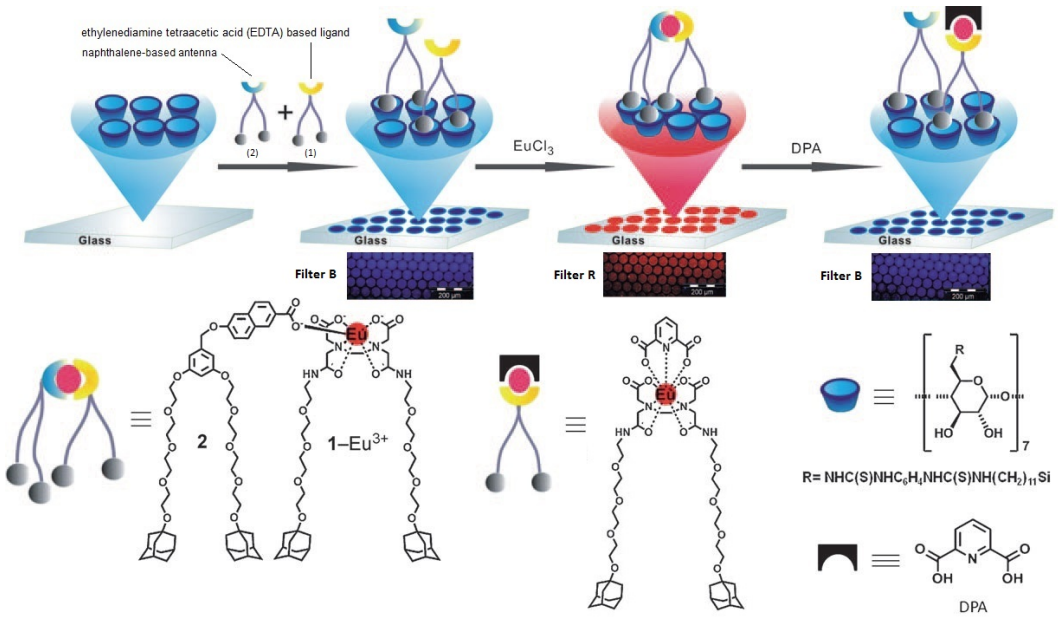


FIGURE 2.5: The construction of the supramolecular sensing-surface system and the detection of the anthrax biomarker DPA (top) and compounds used in this study (bottom) [43].

and drying, the substrates were again imaged [43]. This method is rather time consuming and requires manual handling.

However, more advanced technology was developed by Universal Detection Technology recently, where detection of 16 spores per litre in 15 minutes was achieved in an automation system. The device known as BSM-2000 is shown in Figure 2.6.

FIGURE 2.6: Illustration of BSM-2000 unit, a system for airborne bacterial spore monitoring [1].

The working mechanism of the BSM-2000, is based on optical detection. Here, detection of the target material is signalled by emission of a green light and concentration of the spores can be calculated with fluorescence spectroscopy. The luminescence is directly correlated to the number of spores captured thus giving a "Positive" result if the captured spore count surpasses the threshold set on the device. The device was designed for constant and unattended monitoring of public spaces. It samples air at a rate of 100L per minute, and then uses heat to "pop" spores, thus releasing a chemical from inside called dipicolinic acid (which is unique to bacterial spores). The acid reacts with a sensor (macrocyclic ligand bonded to terbium) triggering luminescence under UV light. As reported, the device has a capability to detect 16 spores per litre in 15 minutes with full automation and inexpensive operation costs.

### 2.2.3 Electrochemical Biosensors

Electrochemical biosensors measure the change in electrical properties of a solution that occurs as a result of oxidation and reduction reactions. The earliest reported biosensor was based on electrochemical transduction principle using current measuring or amperometric techniques [33].

Electrochemical biosensors are mainly used for the detection of hybridised DNA, DNA binding drugs and glucose concentration [33]. An electrochemical impedance spectroscopic biosensor for bacterial detection was first reported in 2002 by Ruan et al [44].

[1]Universal Detection Technology, https://www.rkb.us/(Cited 14/11/2011)

### 2.2.4 Mass detection biosensors

Mass detection biosensors function by detecting minute changes in mass due to binding of a target analyte to the sensor. One of the most accurate methods involves the measurement of the frequency of a vibrating structure that is functionalised against an analyte of interest. Binding of the target analyte to the sensor causes a shift in the frequency of the sensor due to the added mass. Frequency can be measured very accurately, and so even small mass change can be monitored. This detection method has become popular because of its capability of label-free on-line analysis for antigen-antibody interactions. In addition, high frequency moves away from low frequency noise found in electronic readout systems. Resonators can be made in smaller sizes, which increases their operational frequency and sensitivity [21]. Small resonant systems allow to have arrays and different chemicals can be used in order to provide high specificity [45]. Also in compare to an static mode which is introduced later, a certain number of molecules have to be accumulated on the sensor surface in order to produce enough stress and eventually bend the sensing part whereas in a dynamic resonating system, even small number of target molecules increase the mass of the vibrating plate and influences the resonant frequency of the vibration. In addition, from meteorology aspect, in dynamic mode, a precise resonant shift event is spotted whereas in static mode it is a detection of continues deflection. Therefore, the dynamic system has a higher sensitivity and responds in shorter time scale. Various transducer techniques have been used for detecting the change including, piezoelectric, piezoresistive, capacitive, optical and electromagnetic [46–49]. In this work, the transducer element will be a frequency based mass detector. MEMS based cantilevers are most commonly used as the resonating structures of the sensor [50]. The minimum detectable added mass is proportional to the total mass of

the device. Therefore, the use of MEMS technology in implementing mass sensors allows considerable mass resolution [1].

A more detailed discussion on such systems are given in the following section.

## 2.3 MEMS Based Mass Detection Biosensors

The sensitivity of a mass detection sensor to added mass relies largely on the mass of the sensor itself. In other words the smaller the sensor, the smaller the detectable mass. The dimensions of biological analytes being exceedingly small, brings about the need for micro scale vibrating structures to detect them. MEMS as miniaturized technology contribute with many advantages over conventional analytical techniques, which are as follows:

- Simple procedure and quick response
- High sensitivity and low cost
- Low analyte requirement and non-hazardous procedure
- Exceptionally high sensitivity due to their high surface to volume ratio
- Excellent reproducibility through well established silicon microfabrication techniques
- Resolution many orders of magnitude greater than conventional sensors
- Compatibility with array arrangement for multi chemical selectivity (Figure 2.7)

In general, MEMS based sensors can have variety of shapes [51, 52] such as V shape suspended structures, circular, square or rectangular membranes that are fixed by single, dual or multiple supports and so on (Figure 2.8).

MEMS based structures have been most commonly employed as transducer elements in mass detection biosensors. [2, 27, 57]:

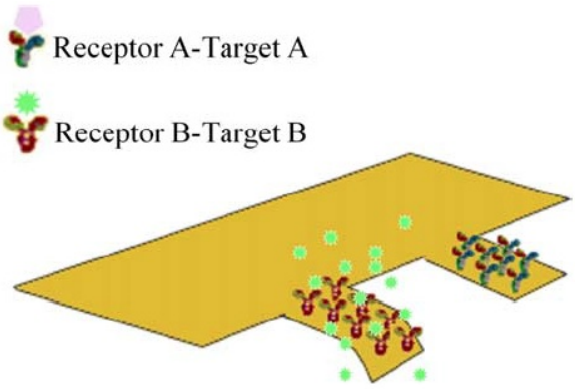


FIGURE 2.7: Schematic diagram of a multiarray sensor.

FIGURE 2.8: Top view of some basic MEMS based sensor structures [22, 23, 53–56].

Microcantilevers transducers either use the change in characteristic resonant frequency due to changes in mass (dynamic mode) or the deflection of the cantilever due to changes in surface stress (static mode) to detect adsorption of a target molecules [39]. Thus, physical contact of a stimulant on the cantilever is converted into an output signal. Because of their high surface to volume ratio, the surface effects are extremely large which makes it feasible for microcantilever sensors to work in a liquid or air medium. To make the sensors specific to a target a chemically selective coating can be applied to the surface of the sensing element. Many chemically selective coatings for chemical specification have been implemented for this purpose along with molecular recognition methods. For example, Iqbal et al. discussed the use of nucleic acid-based detection and immunological-based detection methods. The use of Self Assembled Monolayers (SAM) (described in Section 2.7) has been explored in works by Pinnaduwage et. al., because of their simple coating procedure and their covalent binding

to the sensor surface. SAMs are well known due to their stability and direct transmission [58–60].

The range of transduction mechanisms employed in MEMS based sensors are depicted in Figure 2.9. Here, the two main modes of operation for cantilever based devices are static and dynamic.

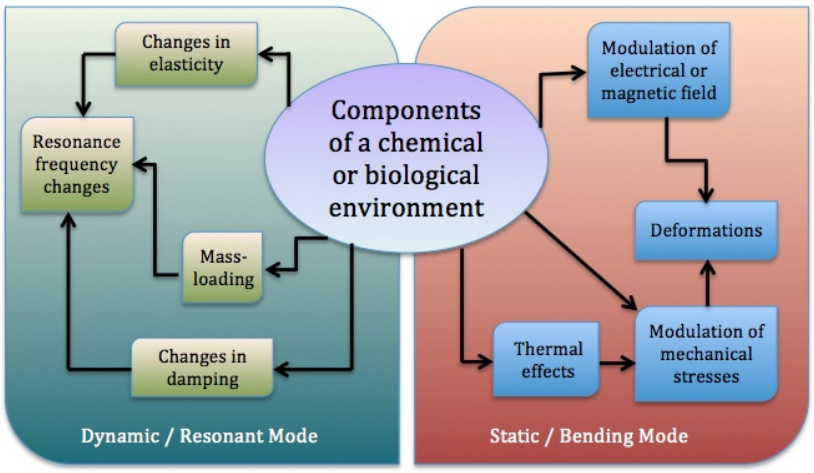


FIGURE 2.9: Operational modes of MEMS based sensors and methods of transduction systems (Adopted from [21]).

### 2.3.1 Static/ Bending Mode

In static or bending mode, the substrate material is usually coated with a stress sensitive layer [61]. On binding of target molecules to functional groups on the sensor surface, surface stress is generated which induces deflection of the mechanical element. Stoney's equation can be used to express thin film stress effect. Stoney (1909) had observed that deposition of a thin metal film on a thick substrate causes tension or compression when there is no external force applied on the system. Therefore, he developed a relation between the stress in the film and

the amount of bending in the substrate [62]. The Stoney's equation is as follows [63]:

$$\sigma^{(t)} = \frac{E_s h_s^2 k}{6h_t(1-\nu_s)} \tag{2.1}$$

where $t$ and $s$ subscripts represent the thin film and substrate, respectively. $E$ is the Young's modulus and $\nu$ is the Poisson's ratio. $h_t$ and $h_s$ are the thin film thickness and substrate thickness. Here $k$ is the curvature. In this equation when stress is known curvature can be obtained and also works the other way around. This formula can be applied by considering the following assumptions [63]:

- Both film and substrate thickness are uniform and have the same radius $R$, and also $h_t \leqslant h_s \leqslant R$.
- There is infinitesimal strains and rotations of the plate system.
- The film and substrate are homogeneous, isotropic, and have linear elastic properties.
- The states of the film stress are in-plane isotropic or equi-biaxial[1] while the out-of-plane direct stress and all shear stresses vanish.
- The curvature components of the system are equi-biaxial while the twist curvature vanishes in all directions.
- The entire surviving stress and curvature components are spatially constant over the surface of the plate system.

After considering the stress and curvature effect on coated substrate, the force applied on the system has to be calculated. The relationship between the resulting applied force and deflection of the element can be described by Hooke's Law as folows:

[1]Two equal stress components in any two, mutually orthogonal in-plane directions.

$$F = -k_{spring}\Delta z \tag{2.2}$$

Where *F* is the applied force, spring $k_{spring}$ is spring constant and $\Delta$ *z* is the deflection of the bending component.

The spring constant determines the flexibility and sensitivity of a cantilever and is defined by its dimension and material constants as given in Equation 2.3 [37]

$$k_{spring} = \frac{Ewt^3}{4L^3} \tag{2.3}$$

Where *E* is the Young's modulus, *w* is the cantilever width and *L* is the cantilever length, and *t* is the thickness.

The flexibility of the membrane is important in these mechanisms and silicon/ silicon nitride substrates provide very good mechanical properties. Stiffness of silicon and silicon nitride is one of the major factors in this regard and their modulus of elasticity is in the range of 200 to 300 GPa as reported in many references [37, 64–66]. For this reason that most of the MEMS microcantilevers are silicon or silicon nitride based. A schematic of the working mechanism for static/ bending mode of operation is shown in Figure 2.10.

Basically, the change in resistance of the cantilever is measured with respect to a reference cantilever, which is made next to the sensor cantilever. The reference cantilever is not chemically modified and therefore is inert. This is to reduce system noise (including temperature variation). Here, the sensor cantilever is coated on one side with a layer specifically to bind with target molecules. Usually polyethylene glycol is used to make the lower side (opposite to the functionalised layer) biologically inert. When the target molecules bind onto

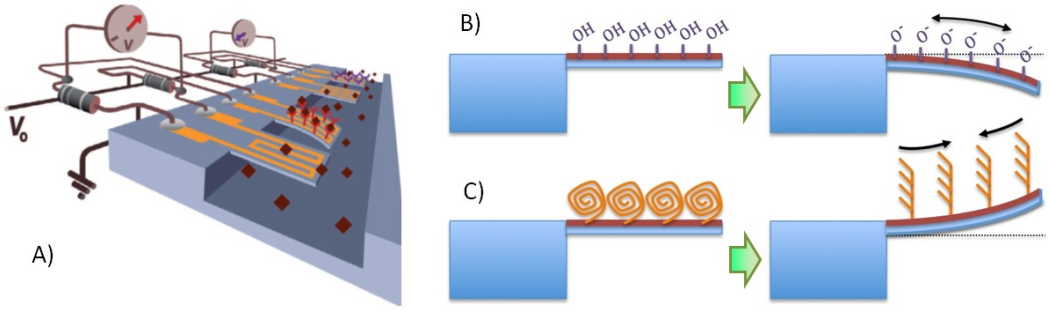


FIGURE 2.10: (A) Schematic drawing of micro cantilever measuring principle in bending mode of operation. Practical examples: (B) Surface stress causes tension of the membrane by removal of ($H^+$) from the molecule group. (C) Surface stress causes compression in the membrane during the hybridization phenomena [37, 67].

the sensitive surface, the cantilever bends based on the surface stress between the upper and lower surfaces. To control this, the sensor cantilever is connected to the reference cantilever by two resistors to make a Wheatstone bridge. This results in accurate measurement, where an output signal is monitored due to a change in the deflection of the two cantilevers and hence noise signal is reduced significantly [67]. An example of such a system is illustrated in Figure 2.10. Here, removal of proton ($H^+$) from the molecule group on the membrane surface creates negative surface charges and electrostatic repulsion. This phenomena imposes bending in the membrane in a tensile direction. In Figure 2.10. (C), when molecules are immobilized on the receptor, $_{ss}$DNA[1], with its coil structure undergoes hybridization to a stiff $_{ds}$DNA[2] which relaxes the repulsive steric interactions causing the membrane to bend in a compressive direction [37, 68].

This system is usually designed to be applied in liquid (aqueous) environment. This is because in some biosensing applications the complexity of biochemical processes is much more than physical or chemical sensing and this is due to the nature of the working environment [2, 69].

[1]Single-stranded random coil DNA (flexible structure)
[2]Hybridized double-stranded DNA (stiff structure)

One of the limitations of the static mode of operation is that it cannot provide high sensitivity in comparison with dynamic systems. This is because sufficient adsorption of target molecules on the surface of the sensing component is required. Furthermore, factors at the solid surface-molecule-liquid interface including ion distribution, hydrophobic or entropic interactions can influence sensor functionality. The binding of molecules to the sensor surface can lead to conformational changes, changes in surface charge or molecular density in the sensing layer. In addition, conformational changes can occur by binding of molecules to the sensor surface which leads to amendments in surface charge or molecular density in the receptor layer [37]. Since, surface stress takes place in the presence of many atoms and molecules, it is important to take into account the following considerations:

- the interactions of molecules with the surface.
- the lateral interactions in the molecular layers parallel to the surface.

Moreover, in practice a precision readout system is also required and all this in return, demands expensive instruments. However, a key advantage of this operating mode is its simplicity, since no actuator is required to drive it. Nevertheless, the reported minimum detection of this system can be down to one tenth of a nanometre in beam deflection [37].

### 2.3.2 Dynamic/ Resonance Mode

In dynamic mode of operation, the change in resonant frequency due to added mass is measured. Resonant frequency happens where there is a maximum in vibration spectrum. This frequency mainly depends on the mass of the body, geometry, and its spring constant. The idea was first introduced by Cleveland et al. where the spring constant of a cantilever was determined by measuring its natural frequency prior to and after adding small masses onto

the vibrating component [70]. In comparison, static mode, where bending is related to the stress in surface and this is determined by the number of interactions of the molecules with the surface would be difficult to quantify without a calibration. An outstanding advantage of dynamic modes of operation is the absolute information that can be obtained by just knowing the mass of the original sensor and the resonant frequency of the sensor as indicated by Equation 2.7. This is because it just involves counting of the frequency. In general, the measurand or target mass modifies a characteristic of the oscillating body such as:

- frequency of resonance
- amplitude of resonance
- phase at resonance

In this approach, an actuating system is required to excite the vibrating component at its resonant frequency. In general, biosensors based on dynamic mode of operation employ a vibrating cantilever fixed at one end and coated with a receptor layer at its other, free-moving end. The chemical compound of the receptor layer is specific to the material being detected, such as E. coli, anthrax or proteins that are biomarkers for disease. When the target analyte is present in the sample flowing through the biosensor, it binds to the cantilever and shifts the frequency of vibration in a way that can be detected electronically. The cost in the higher complexity of the dynamic mode as opposed to the static mode is compensated by sensitivity levels down to attograms. The schematic of the dynamic operating system is shown in Figure 2.11.

In dynamic/ resonance mode, cantilevers are excited close to their resonance frequency. The natural frequency of a vibrating body can be obtained by the following formula,

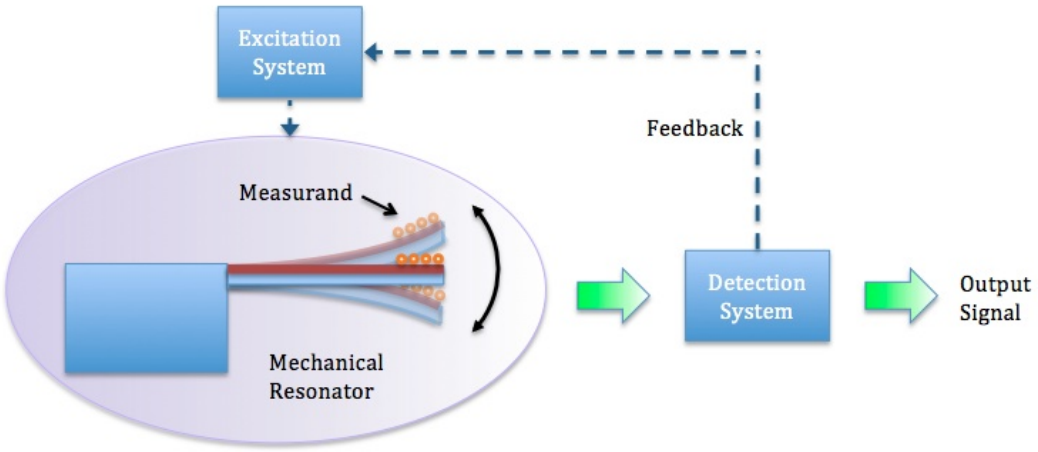


FIGURE 2.11: Schematic representation of the dynamic mode of operation [71].

$$f = \frac{1}{2\pi}\sqrt{\frac{k_{spring}}{m^*}} \tag{2.4}$$

where $k_{spring}$ is the spring constant and $m^*$ is an effective mass.

An added mass, for instance due to adsorption of a target analyte, causes a shift in resonance frequency of the oscillating cantilever. The effective mass change due to the frequency change is given in the equation 2.5

$$\Delta m = \frac{k_{spring}}{4n\pi^2}\left(\frac{1}{f_1^2} - \frac{1}{f_0^2}\right) \tag{2.5}$$

where $f_0$ and $f_1$ are the resonance frequencies before and after mass adsorption, respectively and $n$ is equal to 1 in case the landed mass is located precisely at the free end and n is about 0.24 when the detected mass is unformly distributed over a rectangular section of the cantilever [46, 72].

The relationships described above highlight the influence of the dimensions of the structure on the operation of a resonant sensing device. The change in intensity of a particular

physical phenomenon as a result of change in the dimensional scale of a body can be described in terms of scaling. As previously shown in Equation 2.3, the spring constant of a cantilever, $k_{spring}$ is proportional to its dimensional scale. Considering a generic linear dimension, $l$, the spring constant $k_{spring}$ scales as $l$. A ten fold increase in linear dimensions would lead to a ten fold increase in stiffness. The effective mass of the body however, is proportional to the cubic power of the dimensional scale; ie. $m^*$ scales as $l^3$. A ten fold increase in linear dimensions would cause the mass to increase by a factor of thousand. Thus, from Equation 2.4, it is clear that the resonant frequency is inversely proportional to the dimensional scale ($f$ scales as $l^{-1}$); a decrease in linear dimensions leads to an increase in the resonant frequency by an equivalent factor.

The sensitivity is defined by the ratio of change in resonant frequency to change in mass as given in Equation 2.6.

$$S = \frac{\Delta f}{\Delta m} \tag{2.6}$$

Thus, given the previously defined relationships of frequency and mass to the dimensional scale, the sensitivity $S$ scales as $l^{-4}$. In other words, a tenfold decrease in the dimensions of the vibrating body would lead to a ten thousand fold improvement in sensitivity of the device to mass change. The limiting factor in the mass resolution of a device is the minimum frequency that can be detected by measurement system. Previous works have reported detection capabilities in the ranges of femto, atto and zeptograms [27, 57, 73–78].

Microfabricated cantilevers are often made of silicon or silicon nitride based on their mechanical properties, specially their modulus of elasticity. This mode of operation is

usually applied in low viscous medium since viscosity reduces mass resolution and consequently lowering of the Q-factor. Dynamic mode of operation has capability to measure mass changes down to the single molecule level in ultra-high vacuum which provides an extremely high sensitivity in miniature sensors. Additionally, as described earlier, decreasing dimensions of the vibrating component results in better sensitivity in frequency shift [79]. Furthermore, external driving system will result in an increase in the vibration amplitude and the quality factor, which minimises the minimum detectable frequency shift and enhances mass detection sensitivity [72]. The geometry of the resonator and location of the absorbed particle play an important role in relationship between shifts in resonant frequency and changes in mass. For a cantilever beam, the relation is described by a responsivity function, *R(x)*, which is defined as the ratio of the resonant shift , $\Delta f$, to the increase in mass, $\Delta m$, as a function of position, $x$, of the absorbed mass along the beam. For simplicity, an assumption of evenly distributed mass along the resonator can be made. By averaging over the responsivity function this relation can be expressed in Equation 2.7.

$$\Delta f = R(x)\Delta m = -\frac{f_0}{2m_0}\Delta m \tag{2.7}$$

where $m_0$ is the initial mass of the vibrating component. In order to maximize the magnitude of the responsivity it is critical to reduce the mass of the resonator, while maintaining high resonance frequencies [75]. In all of dynamic mode of operations, the vibratory mass of the resonator, its resonance frequency, and quality factor (Q) are core in establishing its mass sensitivity [80].

## 2.4 Resonator Characteristics

### 2.4.1 Q-factor

One of the fundamental factors to characterise a resonator device is its energy efficiency. In resonators the term Q-factor is used to describe a ratio of the total energy stored in the system ($E_M$) to the energy lost per cycle ($E_C$).

$$Q = 2\pi\left(\frac{E_M}{E_C}\right) \tag{2.8}$$

As a structure approaches resonance frequency, the amplitude of its vibration will maximise. The magnitude of this amplitude is limited by the damping effects presented in the operating medium and internal anchoring. The level of damping acting on the system can be expressed by Q-factor (also known as quality factor). In the frequency-amplitude diagram, sharpness of the resonance enables the resonant frequency to be easily defined. Figure 2.12 (a), presents the parameters involved in calculation of Q-factor. A comparison between high and low quality factor resonance modes is depicted in Figure 2.12 (b). High Q-factor leads to higher performance MEMS resonator devices in most cases. However, it also implies the oscillating structure is well isolated from its surroundings. Therefore, the influence of external force is very small [81].

The Q-factor can also be obtained from the Figure 2.12 using the following equation,

$$Q = \left(\frac{f_0}{\Delta f}\right) \tag{2.9}$$

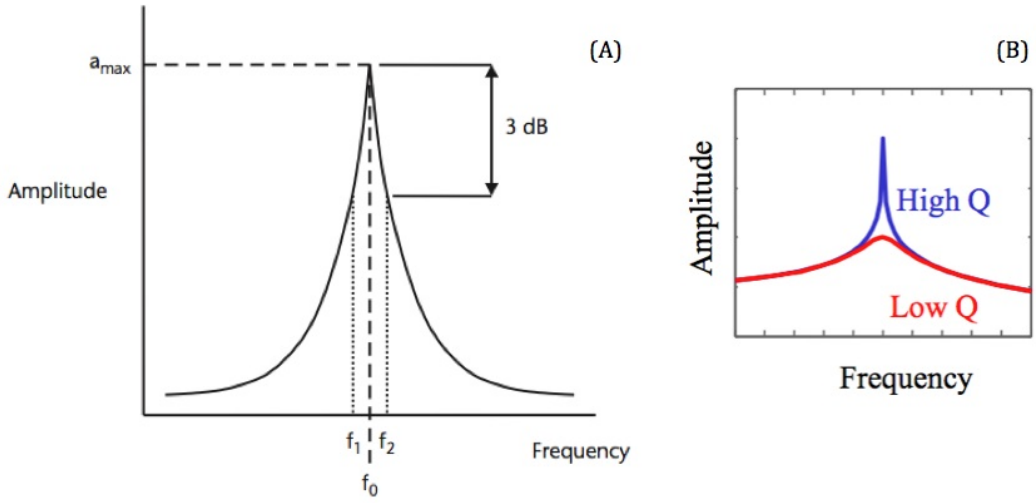


FIGURE 2.12: A typical characteristic of a resonant system. (a) Schematic of a resonance curve showing important parameters. (b) An illustration of high and low quality factor resonance curves [81].

where resonant frequency $f_0$ corresponds with $a_{max}$, the maximum amplitude of displacement, and $\Delta f$ is the difference between $f_1$ and $f_2$ where amplitudes of vibration 3 dB lower than $a_{max}$. From this equation it is clear that Q-factor is inversely proportional to $\Delta$f. Thus, as the difference is smaller, the Q-factor is higher and the resonance peak is sharper. However, this approach relies merely on the steps in frequency measurement, which are collected by experimental testing of the device. In spite of this, a more accurate method for determining the resonator Q-factor is data curve fitting method. One of the most common fits applied to resonators is Lorentzian fit. The equation 2.10, describes the Lorentzian curve.

$$A = \frac{A_0}{\sqrt{1 + 4Q^2[\frac{f}{f_0} - 1]^2}} \tag{2.10}$$

where $f_0$ is the frequency value that corresponds to $A_0$. This is the most accurate fit for resonant curve of miceromechanical resonators by employing nonlinear least-squares fit. Accordingly, Q and $f_0$ can be obtained by passing the Lorentzian fit through the data from

which the resonant peak is plotted.

The Q-factor is limited by many mechanisms which depends on energy dissipation of the resonator. There are three damping mechanisms causing this:

- (1/$Q_a$): The energy lost to a surrounding fluid.
- (1/$Q_s$): The energy coupled through the resonator's supports to a surrounding solid
- (1/$Q_i$): The energy dissipated internally within the resonator's material.

The relation between Q-factor and all above parameters is expressed in the equation 2.11:

$$\frac{1}{Q} = \frac{1}{Q_a} + \frac{1}{Q_s} + \frac{1}{Q_i} \tag{2.11}$$

This shows by minimization of the energy loss mechanisms, Q-factor will be maximised. Majority of the largest energy losses are associated with (1/$Q_a$). This is very influenced by operational medium. These effects can be itemised as follows:

- Surrounding gas pressure
- Size and shape of the resonator
- Direction of resonator vibrations
- Resonator proximity to adjacent surfaces

However, gas damping can be ignored in vacuum operating medium and is used in most MEMS resonator applications. Molecular damping occurs between 1 and 100 Pa, when surrounding molecules are independent of each other. The collision between the molecules and resonator surface causes damping while resonator vibrates. Structural damping, 1/$Q_s$, is based on energy coupled from the resonator though its supports to the fixed structure and needs to be minimised by optimised design of the resonator structure [81]. In sensor applications, if a resonator is exposed to a target analyte to a change in its mass, a shift in

its resonant frequency could be used to detect the target molecule. The shift in resonant frequency needed for detection or sensing of a mass change is determined more precisely if the resonator has a high Q. Since high Q factor indicates a sharper frequency response at resonance, it helps to have an accurate measurement. Even a small shift can be detected in this system, whereas in a system that Q factor is low the width of the frequency response at peak or resonance is wider and it is difficult to accurately spot where exactly the resonant frequency is located within the frequency axis. It is necessary to monitor different addition of noise into the system in order to have accurate analysis of mass sensing limit. Other researches have shown the main source of noise is thermomechanical fluctuations. In this regard, the minimum detectable change in mass can be presented as Equation 2.12 [82]:

$$\delta M \approx 2M_{eff}\sqrt{\frac{E_{th}}{E_c}}\sqrt{\frac{\Delta f}{Q\omega_0}} \tag{2.12}$$

where $M_{eff}$ is the effective mass of the resonator, $E_{th}$ is the thermal energy, $E_c$ is the maximum drive energy at resonant vibration amplitude, $\Delta F$ is the measured bandwidth, $Q$ is the resonator quality factor, and $\omega_0$ is the angular resonance frequency. Therefore, high Q is desirable as it leads to better frequency stability and results in lower mass detection. Additionally, a high Q value is desirable for oscillators and filter applications, where the frequency of operation needs to be carefully monitored.

### 2.4.2 Nonlinear effects

Nonlinear behaviour begins to appear at higher vibration amplitudes, this effect shows a nonlinear function of resonator displacement and its restoring force and is present in all resonant structures. When a fixed-fixed beam deflects horizontally, it results in a stretching

of its neutral axis. This stretching results in a stiffer spring in a similar manner to a wire being tensioned. This tensile force applies to the beam whilst it is vibrating, results in an increase in resonant frequency. This effect is known as spring hardening. If clamped ends are not firm the effect is called soft spring whereby the resonant frequency lowers with increasing amplitude. However, the geometry of the resonator plays an important role in the magnitude and effect of nonlinearity. The equation of motion for an oscillating force applied to an undamped structure is given by Equation 2.13 [81], where *m* is the mass of the system, *F* is the driving force, $\omega$ is the frequency, *y* is the displacement, and *s(y)* is the nonlinear function.

$$m\ddot{y} + s(y) = F_0 cos(\omega t) \tag{2.13}$$

In most of the real case situations *s(y)* can be expressed by Equation 2.14 [81], which has a cubic term.

$$s(y) = s_1 y + s_3 y^3 \tag{2.14}$$

By substitution of 2.14 in 2.13, dividing through by *m*, and simplification, the following equation can be obtained.

$$m\ddot{y} + s_1/m(y + s_3/s_1 y^3) = F_0 cos(\omega t) \tag{2.15}$$

where $s_1/m$ is $\omega_{os}^2$ ($\omega_{os}$ presents the resonant frequency for small amplitudes of vibration) and $s_3/s_1$ is denoted by $\beta$. The restoring force (R) acting on the system is therefore given by Equation 2.16 [81].

$$R = -\omega_{os}^2(y + \beta y^3) \tag{2.16}$$

In the case of zero $\beta$, the restoring force is a linear function of displacement, if $\beta$ is positive, the system experiences the hard spring nonlinearity, a negative $\beta$ associates with the soft spring effect. Hard and soft nonlinear effects are presented in Figure 2.13

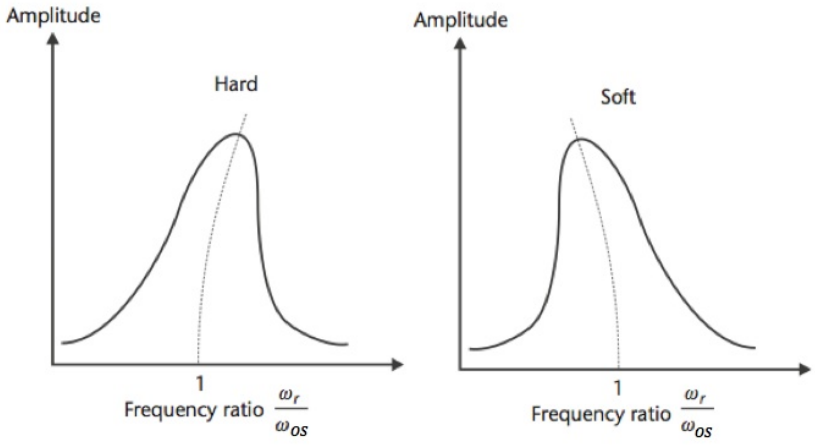


FIGURE 2.13: The hard and soft nonlinear effects [81].

As the amplitude of vibration increases and the nonlinear effect begins to start, the resonant frequency exhibits a quadratic dependence upon the amplitude, as shown in Equation 2.17.

$$\omega_r = \omega_{os}\left(1 + \frac{3}{8}\beta y_0^2\right) \tag{2.17}$$

to work out the variable $\beta$, the Equation 2.17 needs to be applied to an experimental analysis of the resonant frequency and maximum amplitude for a range of drive levels. The maximum amplitude of vibration is dependent upon the energy supplied by the resonator's drive mechanism and the Q-factor of the resonator. The cause of nonlinear behaviour is

according to a high Q-factor or excessive driving input. Nonlinear behaviour is undesirable since they can degrade the accuracy of a resonant sensor.

### 2.4.3 Hysteresis

In a resonating structure, if amplitude of vibration exceeds a critical value, a nonlinear system can exhibit hysteresis. This occurs when the amplitude has three possible values at given frequency. This critical value can be determined by applying Equation 2.18

$$y_0^2 > \left( \frac{8h}{3\omega_{os} \mid \beta \mid} \right) \tag{2.18}$$

where *h* is the damping coefficient and can be found by measuring the Q-factor of resonator at small amplitudes and applying the equation 2.19 [81].

$$h = \frac{\omega_{os}}{2Q} \tag{2.19}$$

### 2.4.4 Driving Systems

Driving systems are required to excite the resonator. In the following sections, key concepts of the major excitation techniques used to drive micro cantilevers to their resonance mode are explored.

### 2.4.5 Electrostatic

Electrostatic driving systems function by applying an AC voltage between two conductive plates (a fixed electrode and movable plate or resonator). This potential difference produces an attractive electrostatic force that bends the resonator towards the other electrode [81].

The actuation force is defined by the applied voltage (V), gap separation between the two plates (g), and area of overlap between the two plates (A) and is given by:

$$F = \frac{\varepsilon_0 \varepsilon_r A V^2}{2g^2} \tag{2.20}$$

One of the difficulties in implementing electrostatic actuation mechanisms is damping due to squeezed film effect in the very small air gaps needed to produce big excitation forces. Furthermore, this method of excitation usually requires operating voltages in the tens of volts [47].

### 2.4.6 Piezoelectric

Piezoelectric driving systems are based on change in geometrical parameters by applying a voltage to the piezoelectric material and can be applied in two ways:

1. By placing the device onto the piezoelectric stage which is driven electronically sweeping through the frequency range
2. By integrating piezoresistive material on the microcantilever providing on chip mechanical movement

AC-voltage induces a mechanical stress to the piezoelectric material and then causes the resonator to bend [47].

### 2.4.7 Electrothermal

Electrothermal driving systems use thermal expansion of materials to actuate the resonator. This is achieved by providing a heating cycle with a frequency matching the resonators fundamental frequency. The mechanical strain on a solid material ($\epsilon$) is proportional to the

temperature change ($\delta$T) and is given by the following equation:

$$\epsilon = \alpha_T \delta T \tag{2.21}$$

Where $\alpha_T$ is the materials coefficient of thermal expansion.

The resonator is heated by means of an alternating current (AC) through an integrated resistance on the resonator. This driving mechanism has been demonstrated up to frequencies in the MHz range [48]. The downside of the thermal excitation is the heat generation and the related low efficiency of the driving mechanism [47].

### 2.4.8 Electromagnetic

Electromagnetic driving implements the use of the Lorentz force. The lorentz force is a force on a moving charge in the presence of a magnetic and electric field. In all the above sections, by tuning the frequency of the driving voltage the frequency of the driving force can be controlled to match the cantilevers fundamental frequency and usually velocity and displacement are the point of interest. The force is generated since an AC-current is forced to flow through the resonator perpendicularly to the static magnetic field. An example of such a driving system can be seen in the work of Lee et al. [46]. A 4 $\times$ 4 array set up was used where in each array two resonators have been used, a small resonator utilises the sensing mechanism and a larger resonator is for driving element. The larger structure with integrated coil is placed in the middle of two permanent magnets for the in plane magnetic field. An AC-current then applied through the metal track on the surface of the resonating element, which vibrates the structure by means of Lorentz force. The resulting motion of the smaller

resonator in presence of the magnetic field, induces an electromotive force to a metal loop. By monitoring the change in electromotive force; the small resonator can be used as a sensor for bio applications. The schematic in the Figure 2.14 presents the working principle.

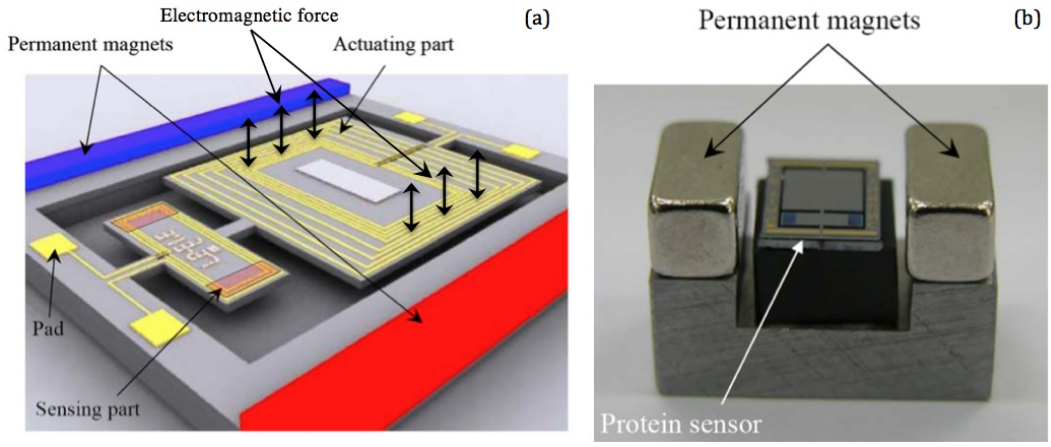


FIGURE 2.14: Electromagnetic bio sensor developed by Lee et al. A schematic of an electromagnetic bio sensor showing driving and detection elements (a), optical image of manually assembled bio sensor [46].

In the reported work, a magnetic field of 0.5 T is provided in the plane of sensor by two permanent magnets which are placed in either sides of sensor structure. 1st resonance mode at 2.7 KHz is detected by a scanning laser vibrometer and inputs were feed by a network analyser. This excitation method provides relatively large driving forces at low operating voltages, but requires relatively large driving currents. As shown in Figure 2.14 the magnetic excitation can be achieved by combining low-resistance excitation coils or current lines with a magnetic material [49, 83, 84]. This driving technique is used in this thesis and described in depth in chapter 3.

## 2.5 Readout Systems

In this section, a brief description of the common readout techniques is presented.

### 2.5.1 Optical Method

Various optical based approaches have been implemented for characterisation of MEMS resonators. One such technique is based on measurement of the emission of fluorescence light due to interaction of the target with a receptor. Here, emission intensity represents the target density in the medium. Such an approach has been demonstrated by Yilmaz et al. (2010) as described in section 2.2.2.

Another approach involves the measurement of the reflection of a single laser beam to a detector. The laser vibrometer has been successfully used as a measurement tool for this purpose in the characterisation of MEMS resonators because of its advantages in terms of being contactless and demonstrating high positional resolution [85]. Here, a laser beam is directed to the vibrating surface and the doppler shift in frequency in the reflected beam and velocity of the surface is measured. Displacement of the target is then computed by integrating the velocity measurement [86].

The optical lever or beam deflection method is a commonly employed technique for measuring the displacement of a cantilever [2, 37, 87]. Here, a laser beam is focused on the flexible end of the cantilever and is reflected off onto a position-sensitive detector (PSD). The shift in the position of the reflection spot on the light-sensitive detector is porportional to the magnitude of cantilever beam deflection. The schematic in Figure 2.15 describes the detection mechanism.

Inferometry is another optical based deflection measurement technique whereby interference of a reference laser beam with the reflected beam from the cantilever is measured [2]. The cleaved end of an optical fibre is brought in close proximity to the cantilever surface. One part of the light is reflected at the interface between the fibre and surrounding media,

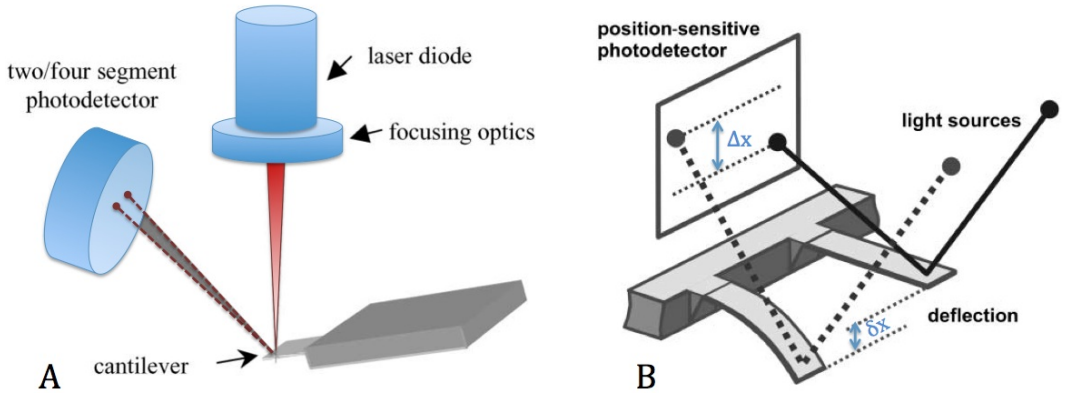


FIGURE 2.15: Optical lever deflection detection method. (A) Configuration of laser beam and detector and positioning of membrane [2] (B) Nanometer deflection of membrane ($\delta$x) translated into a change of position of the reflected laser spot on a position-sensitive detector by several micrometers ($\Delta$x) (Adapted from [37]).

and the other part is reflected at the cantilever back into the fibre. These two beams interfere inside the fibre, and the interference signal can be measured with a photodiode [53].

The main disadvantage in using optical methods is the need for lasers, photo-detectors or more advanced optics which result in a bulky and non integrated measurement systems. Hence they tend to be unsuitable for system-on-chip applications.

### 2.5.2 Piezoresistive Method

In this method resistance of a piezoresistive layer which is coupled to the cantilever, is measured when the membrane undergoes stress due to bending. CMOS[3]-MEMS are mainly use this readout method due to good piezoresistive properties delivered by silicon and polysilicon. This method is capable of being integrated on a single chip but limits the miniaturization of the cantilever since piezoresistor wiring is required to be fitted onto the sensing membrane. Another shortcoming is that, it requires current to flow through the cantilever, which in turn results in additional dissipation of heat and relevant thermal drifts. Despite these difficulties,

[3]Complementary Metal Oxide Semiconductor

many researchers reported successful mass resolution less than an attogram [76, 88, 89].

### 2.5.3 Piezoelectric Method

Monitoring of the changes based on this method requires deposition of piezoelectric material, such as ZnO and PZT, on the moving membrane. In accordance with the piezoelectric effect, transient charges are induced in the piezoelectric layer when deformation occurs. The major disadvantages of this technique is as follows:

- In order to obtain sufficient output signals it requires the thickness of the piezoelectric film to be well above the value that correspond to optimal mechanical characteristics.
- It require electrical connections to the resonating body.
- It is inefficient when slowly changing cantilever deflections need to be measured.

The above mentioned shortcomings have led to the limited adoption of piezoelectric readout mechanisms in MEMS sensors [90–92].

### 2.5.4 Capacitive Method

The capacitance readout is based on a measurement of the capacitance between a conductor on the cantilever and an electrode on a fixed substrate separated from the cantilever by a small gap [93]. Deflection of the cantilever due to adsorption of a target analyte causes a change in the capacitance which is measured. Capacitance readout systems are highly sensitive and can provide absolute displacement however, they are unsuitable for measurements of large displacements and susceptible to interferences with variations in the dielectric constant of the medium [2, 93, 94].

### 2.5.5 Electron Tunnelling Method

This method is utilised mainly in AFM tip deflection. The tunnelling occurs between a conducting tip and the cantilever separated by a subnanometer gap. This phenomena can be described as:

$$I \propto Ve^{-a\sqrt{\phi s}} \tag{2.22}$$

where, $V$ is the bias voltage, $\phi$ is the height of the tunneling barrier, $s$ is the tunnelling gap distance, and $a$ is a conversion factor with a value of 1.025 $\text{Å}^{-1}\text{eV}^{-1/2}$. Extremely high sensitivity of the tunnelling readout is associated with its non-linear response and a limited dynamic range [18, 95, 96].

## 2.6 Review of State of Art in Mass Detection Biosensors

MEMS mass sensors have shown to be a successful approach in obtaining greater mass resolution, simple working mechanism, low cost and low power requirements. A number of these approaches are based on reducing the number of absorbates required for detection, substrate used and effective driving and detection mechanisms. Furthermore, the use of vibrating cantilevers in resonant mode provides detection in the attogram mass range and even lower [97–99]. Attributes, such as high fundamental frequencies, diminished active masses, tolerable force constants, significantly high quality (Q) factors, even higher than those of electrical resonant circuits make the MEMS approach highly suitable for developing mass sensors [100]. The concept of employing MEMS resonant cantilevers as mass sensing devices was first introduced in the 1990's. In 1994, Binh et al. proposed a novel cantilever

design for study of catalysis with MHz resonance frequency range and a mass resolution of $10^{-18}$g. Thundat et al. demonstrated detection of mercury vapor in air using an oscillating silicon nitride microcantilevers in 1995 [101–103]. More recently, Lavrik's and Datskos's group have been one of the pioneers in development of ultra sensitive biodetection sensors. This group reported the development of micro cantilever resonators for femtogram mass detection, infrared MEMS detectors and microcalorimetric[4] spectroscopy detection method of detection for Bacillus subtilis and Bacillus cereus [18, 21, 27, 28, 93]. Some of their work is presented in Figure 2.16.

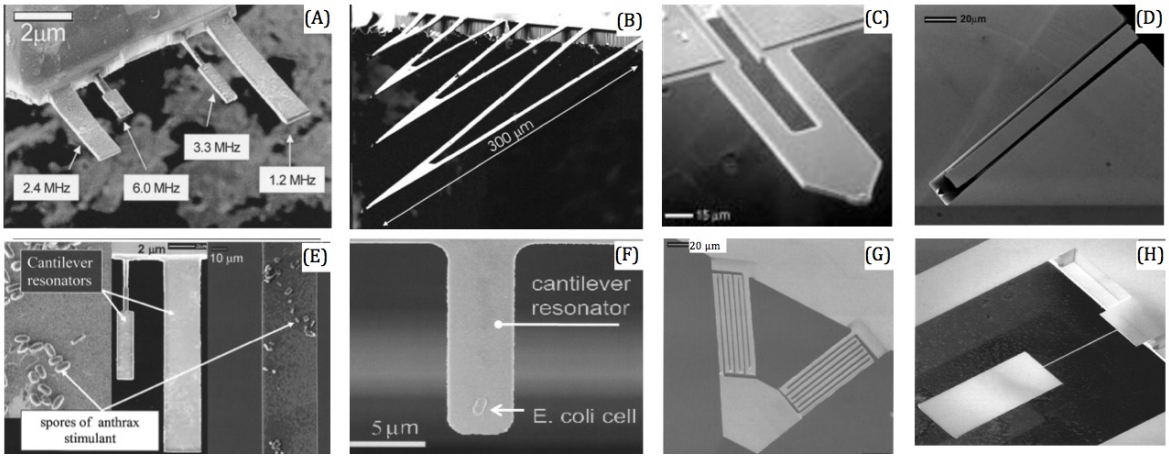


FIGURE 2.16: Some of the presented works developed by Lavrik et al. for mass detection purposes. (A) Ion scanning micrograph obtained using a FIB instrument. This picture demonstrates some fabricated Si based microcantilever resonators with frequency range of 1 to 6 MHz. (B) Commercially available triangular microcantilevers used in AFM. (C) Piezoresistive single crystal Si microcantilever. (D) Cantilever with improved thermal isolation optimized for calorimetry. (E) and (F) Resonating cantilever devices that provide mass sensitivity sufficient for a single cell detection. (G) and (H) FIB produced microcantilevers. The increased path-length or the narrowed region connecting the suspended rectangular structure to the base provides substantially smaller thermal conductance as compared to the unmodified cantilever [18, 21, 27, 28, 93].

Roukes's group at Caltech, USA have published many pieces of work in ultra sensitive mass detection. Their research focuses on the use of high frequency nanoelectromechanical systems (NEMS) based resonator sensor elements for mass detection.

[4]science of measuring the heat of chemical reactions or physical changes

NEMS are electromechanical systems with dimensions in the deep submicron level that are mainly operated in their resonant modes [80]. Their miniscule mass and high mechanical quality factors make them attractive candidate structures for mass sensing applications. However for such devices, challenges lie in attaining reproducible nanofabrication and implementing suitable transduction mechanisms for displacement detection. This is because, vibration amplitudes of mechanical elements decreases in proportion with their size, thereby bringing about the need for ultra-high sensitivity transducers. Electronic and optical coupling transduction techniques that commonly employed in mems resonant mass detectors become unsuitable at this scale as the readout signals are dominated by noise.

Roukes group have presented mass detection devices that utilise nanomechanical double clamped beam resonators as their core sensing element and a magnetomotive or electromotive actuation mechanism. These beams were fabricated from SiC and by varying the geometrical dimensions of the beam, devices of varying mass sensitivity were demonstrated. A scanning electron micrograph (SEM) of the first generation of their fabricated NEMS beams with fundamental flexural resonant frequencies from 2 to 134 MHz are shown in Figure 2.17.

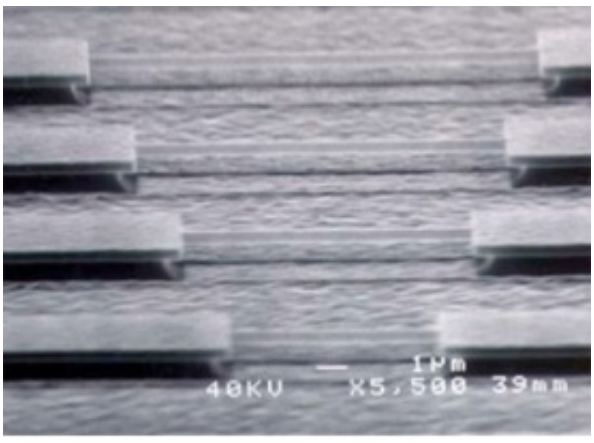


FIGURE 2.17: Mass sensitive NEMS doubly clamped beams developed by Roukes et al.

They conducted mass sensing experiments by directing a weak flux of gold atoms on

the resonator. The experiments were conducted within a cryogenic ultra-high vacuum environments. Results are shown in Figure 2.18. They show the shift in frequency, $\Delta\omega/2\pi$ (bottom) induced by sequential 40 ag (1 ag = $10^{-18}$ g) gold atom adsorption upon a 14.2$\mu$m $\times$ 670nm $\times$ 259nm silicon carbide doubly clamped beam resonator. The (initial) fundamental frequency $f_0$ of the structure $\omega_0/2\pi \approx 32.8$ MHz [80]. The accreted mass of gold atoms, $\Delta$m, in the upper plot was measured by a separate quartz crystal detector. The frequency fluctuations of the system correspond to a mass sensitivity of 2.5 ag for the 2 ms averaging time employed [80].

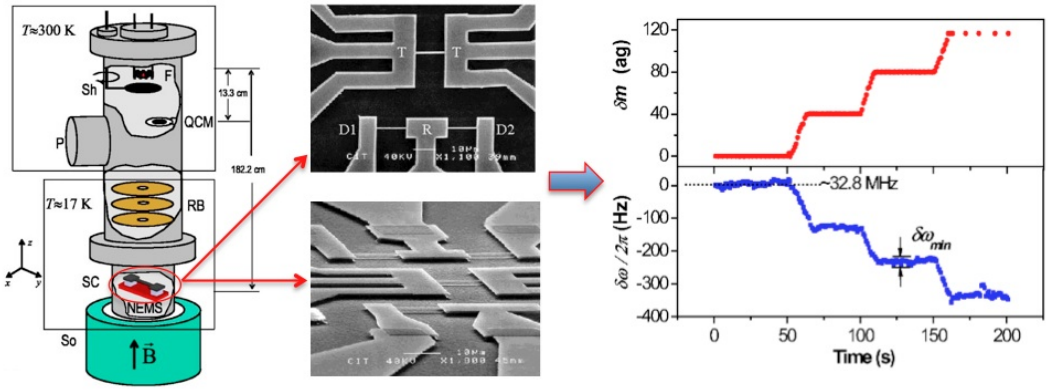


FIGURE 2.18: Mass sensing experiments on NEMS doubly clamped beam based resonator using Au atoms showing attogram scale resolution [80].

In other works, they used gaseous species such as $N_2$ molecules and Xe atoms as target masses to test a resonator with beam dimensions of 2.3$\mu$m $\times$ 150nm $\times$ 100nm and fundamental resonant frequency, $f_0$, of 190 MHz [74]. The experimental configuration employed is shown in Figure 2.19. Here, A gas nozzle with a 100 $\mu$m aperture was used to provide a controlled flux of $N_2$ or Xe atoms or molecules. The flux was gated by a mechanical shutter to provide calibrated, pulsed mass accretions upon the NEMS device. The mass flux was determined by direct measurements of the gas flow rate, in conjunction with effusive-source formulas for the molecular beam emanating from the nozzle. Sequential mass depositions

were thus executed in situ upon the tested device within a cryogenic ultra-high vacuum environment. The resulting frequency shift of the NEMS device was tracked in real time by a very high frequency (VHF) phase-locked loop as shown in Figure 2.19. Here, each step in the data corresponds to a ∼100 zg mass accretion (∼2000 $N_2$ molecules) resulting from opening the mechanical shutter for 5 s [74].

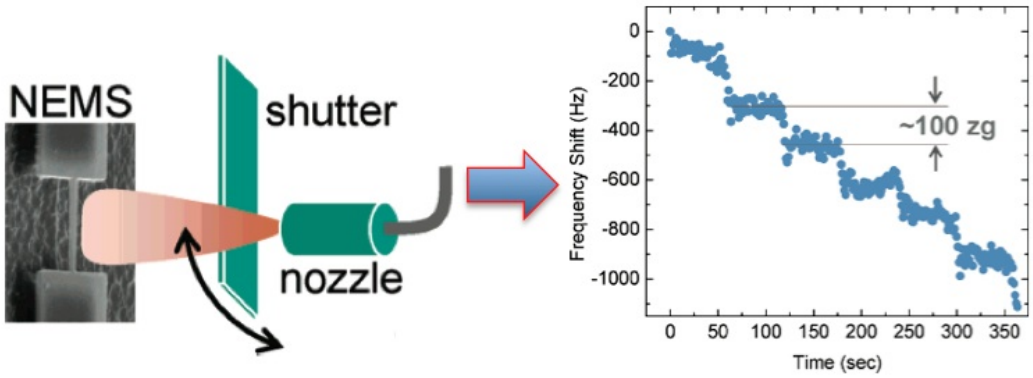


FIGURE 2.19: Mass sensing experiments on NEMS doubly clamped beam based resonator using $N_2$ molecules, showing zeptogram scale resolution [74].

Besides clamped beam resonator structures, Rouke's group have also explored the use of thin metal film integrated transducers on high frequency nanoscale cantilevers. They fabricated nanocantilevers from 70 nm thick silicon carbide and coated them with a 30 nm thick gold film as the piezoresistive transducer layer. In contrast to the earlier experiments where gas molecules were pre-absorbed onto the uncoated, cooled surfaces, the nano cantilever devices were tested under ambient conditions by promoting adsorption of specific target species. This was enabled by coating the device surface with a thin polymer film having a high partition coefficient[5] for the species of interest. The results for testing of two cantilevers having resonant fequencies of 8 MHz (dimensions of $2.7\mu m \times 0.8\mu m \times 0.1\mu m$) and 127 MHz (dimensions of $0.6\mu m \times 0.4\mu m \times 0.1\mu m$) are shown in Figure 2.20. Here, the

[5]The partition coefficient is a ratio of concentrations of un-ionized compound between the two solutions.

devices were exposed to a series of 1,1-difluoroethane gas pulses at room temperature and atmospheric pressure. As seen in the figure, the resonance frequencies of the cantilevers first decreased rapidly in response to injection of the gas and then recovered as the adsorbed gas species desorb from the coating. The 8 MHz cantilever was able to resolve masses of 10 ag, while the 127 MHz cantilever demonstrated a resolution of 1 ag.

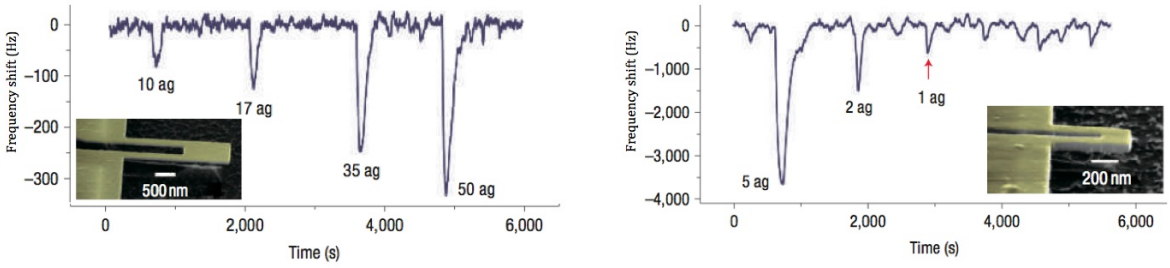


FIGURE 2.20: Real-time NEMS chemisorption measurements, 1,1-difluoroethane gas molecules are chemisorbed onto the polymer-coated surfaces of two separate nanocantilever devices. The measurements are carried out in air, at atmospheric pressure and room temperature. The left and right traces are measured with 8 MHz and 127 MHz nanocantilevers respectively. The minimum resolvable mass is below 1 ag (red arrow).

Zhang's group at the National Institute of Advanced Industrial Science and Technology in Japan have carried out research to realise high Q factor resonant devices. In 2008, they proposed the use of single crystal silicon cantilevers with on-chip piezoelectric lead zirconate titanate (PZT) actuators. The use of silicon cantilevers was suggested over commonly used peizoelectric thin film based sensors in order to limit Q factor degrading energy dissipation. These energy losses arise from the multilayer device structures in PZT integrated cantilevers (structural layer, electrode layer, piezoelectric film and electric passivation layer) and their higher density ($\rho$ = 7500 kg/m$^3$) and mass in comparison with silicon ($\rho$ = 2330 kg/m$^3$), which on the contrary also has a greater Young's modulus (179 GPa for single crystal silicon) compared to PZT (63 GPa).

A schematic of the design proposed by Zhang's group (2008) is shown in Figure 2.21 (A).

Here, two PZT actuators were arranged on both sides of a silicon cantilever and connected to it using thin beams. The piezoelectric actuator was separated from the resonant cantilever to reduce energy losses. Four cantilevers were fabricated with a constant width of 30 $\mu$m and lengths of 100, 150, 200 and 300 $\mu$m. The Q factor of the devices was experimentally measured using a laser Doppler vibrometer and network analyser. The measured and calculated Q factor values for each cantilever is shown in Figure 2.21 (B). As shown, they were able to demonstrate an impressive Q factor of 1113 for the 100 $\mu$m length device [14].

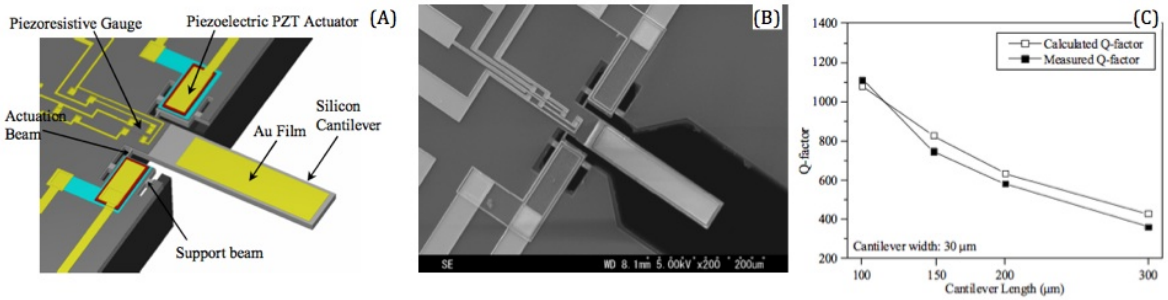


FIGURE 2.21: (A) Schematic of mass detection sensor developed by Zhang et al., (B) SEM image of a fabricated cantilever, (C) Calculated and measured Q factor values at fundamental resonant modes for cantilevers fabricated by Zhang et al. [14] .

Recently this group presented high sensitive micro disk resonators that integrated on-disk piezoelectric PZT thin films as transducers. The silicon based disks had diameters of 160$\mu$m and incorporated PZT films for better impedance matching to CMOS, for disk self-actuation self-sensing at low actuation voltages and low power consumption [54]. To minimise the energy dissipation, the size of the PZT disks were limited and three different design layouts (Type A, B and C) were investigated as shown in Figure 2.22. Q-factor values of the disks were measured using a laser Doppler vibrometer and a network analyzer. The results, depicted in Figure 2.22 demonstrated a high Q factor of 1319 at resonant frequency of 1.34 MHz in air for the microdisk with Type A configuration.

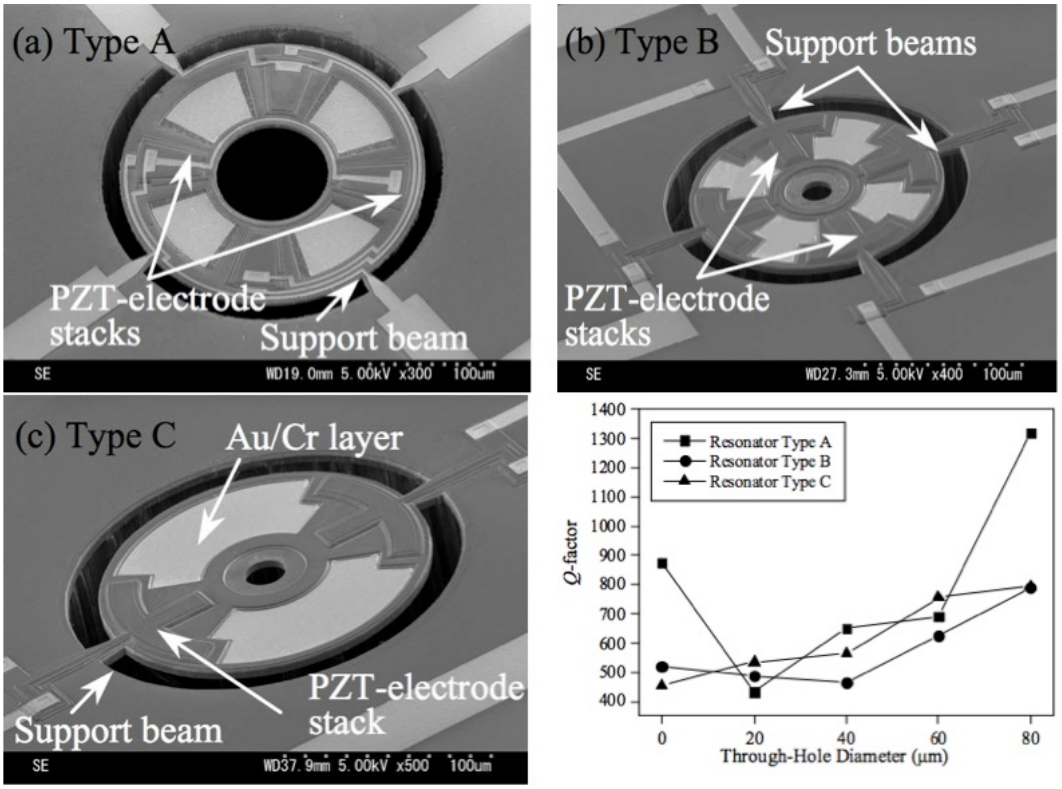


FIGURE 2.22: SEM images of Type A, B and C microdisk resonators developed by Zhang et al. and Q factor measurements in air.

In the presented circular disk designs, as the size of through-hole diameter increases the Q factor increases. This could be based on the amount of material used where vibration happens, since combination of multiple layers increases energy dissipation of the structure.

Llics group have demonstrated the use of nanomechanical resonator arrays in the detection of virus and individual DNA binding [3, 99, 104]. They used polycrystalline silicon or silicon nitride nanomechanical oscillators as sensitive mass detectors. Figure 2.23(A) shows a scanning electron micrograph of the resonator developed by Llic et al. It incorporates a 6 $\mu$m $\times$ 0.5 $\mu$m $\times$ 0.15 $\mu$m cantilever with a 1 $\mu$m $\times$ 1 $\mu$m paddle. In order to characterise the deivce, a piezoelectric actuator was used to excite the device (under vacuum) and optical inferometric techniques were used to measure the frequency spectrum. The measured frequency spectra of the unloaded cantilever, antibody loaded and bacullovirus loaded

cantilevers are shown in Figure 2.23(B).

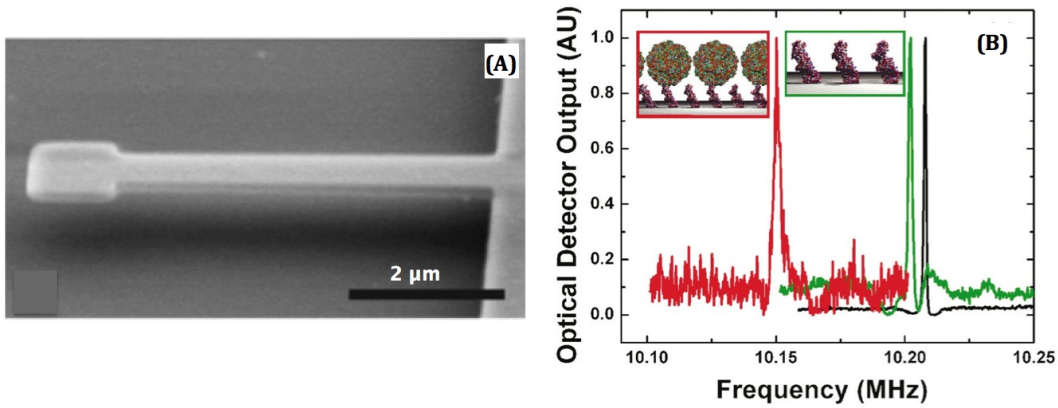


FIGURE 2.23: SEM image of cantilever oscillator developed by Llic et al. (A), Measured frequency spectra of the unloaded cantilever (black), antibody loaded (green) and bacullovirus loaded (red) cantilevers (B) [10].

A summary of the state of art in MEMS mass sensing resonators is shown in Table 2.1.

TABLE 2.1: Detailed list of the state of the art of MEMS mass sensing resonators

| **Author** | $f_0$ (MHz) | $S_m$ | $\Delta m$ | $\delta M$ **(ag)** | ***Q factor*** | **Actuation/ Readout** | **Resonatore type** | **Target analyte** | **Medium** | **Approximate dimension** |
|---|---|---|---|---|---|---|---|---|---|---|
| Feng et al. [78] (2007) | 199.68 | 0.714 zg/Hz | 70.1 fg | - | 2000 | Electromagnetic/ Piezoresistive | SiNW nanowire | - | Vacuum T $\approx$ 25K | 2.25$\mu$m 142nm (dia.) |
| Yang et al. [74] (2006) | 190 | 1.16 zg/Hz | 0.1 ag | 0.02[1] | 5000 | Magnetomotive/ Electromotive | SiC bridge | $N_2$ | UH vacuum T = 37K | 2.3$\mu$m $\times$ 150nm $\times$ 100nm |
| Li et al. [76] (2007) | 127 | 1.43 zg/Hz | 1 ag | 0.1[2] | 400 | None/ Piezoresistive | SiC cantilever | $C_2H_4F_2$[3] | Air | 0.6$\mu$m $\times$ 0.4$\mu$m $\times$ 0.1$\mu$m |
| Ekinci et al. [80] (2004) | 32.8 | 0.39 ag/Hz | 40 ag | 2.5[4] | 3000 | Magnetomotive/ Electromotive | SiC bridge | Au atoms | UH vacuum T = 17K | 14.5$\mu$m $\times$ 670nm $\times$ 259nm |
| Llic et al. [3] (2004) | 13.4 | - | 6.3 ag | 0.4 | 4500 | Piezoelectric/ Optical cantilever | Silicon nitride | Thiolate SAM | Vacuum | 4-10$\mu$m $\times$ 1-3$\mu$m $\times$ 160-260nm |
| Llic et al. [104] (2005) | 11 | 5.1 zg/Hz | 1.6 ag | 0.05 | 3000-5000 | Piezoelectric/ Optical | Silicon nitride cantilever (with Au dots) | dsDNA | Vacuum | 3.5-5$\mu$m $\times$ 1$\mu$ $\times$ 90nm |

| **Author** | $f_0$ (MHz) | $S_m$ | $\Delta m$ | $\delta M$ **(ag)** | ***Q factor*** | **Actuation/ Readout** | **Resonatore type** | **Target analyte** | **Medium** | **Approximate dimension** |
|---|---|---|---|---|---|---|---|---|---|---|
| Llic et al. [10] (2004) | 10 | 0.41 ag/Hz | 2.3 fg | 50 | $10^4$ | Piezoelectric/ | PolySi Optical (antibody coated) | Baculo cantilever | Vacuum virus | $6\mu$m $\times$ 500nm $\times$ 150nm |
| Lavrik et al. [27] (2003) | 2.2 | 2.8 ag/Hz | 5.5 fg | 570 | 25 | Photothermal/ Optical | Silicon cantilever (gold coated) | Acid[5] | Air | $6\mu$m $\times$ $2\mu$m $\times$ 100nm |
| Gupta et al. [98] (2004) | 1.27 | 0.16 ag/Hz | 9.5 fg | - | 5 | - / - | Silicon cantilever | Vaccinia virus | Air | 3.6$\mu$m $\times$ 1.7$\mu$m $\times$ 30nm |
| Davila et al. [97] (2007) | - | 0.1 fg/Hz | 740 fg | - | - | Thermal/ LDV[6] | SOI[7] cantilever | B. anthracis spore | Air | $20\mu$m $\times$ $9\mu$m $\times$ 200nm |
| Jin et al. [61] (2006) | 0.298 | - | 29 fg | - | 857 | Electromagnetic/ Piezoresistive | Silicon cantilever | - - | Air | $300\mu$m $\times$ $100\mu$m $\times$ $3\mu$m |

[1] sensitivity for a 1 s averaging time
[2] sensitivity for a 1 Hz readout bandwidth
[3] difluorethane
[4] sensitivity for 2 ms averaging time
[5] 11-mercaptoundecanoic acid
[6] laser Doppler vibrometer
[7] silicon-on-insulator

As it can be extracted from the Table 2.1 most of the works have been taken place in a laboratories with off sensor optical position sensing detection system. For real applications in security sensing of biological agents, low power standalone sensors are required with all components of the sensing system integrated in one package, allowing them to be small, robust and capable of remote operation. MEMS allow the sensing and actuating elements to be integrated into the device for on-chip dynamic detection [61, 103, 105, 106]. Integrated system helps to save space and simplifies the fabrication. In addition, when there is a need to make arrays of devices it helps to have organised systems in locations next to each other and use the space in an optimised way. Since the ultimate goal of this project is to develop anthrax detection sensor, current state-of-the-art in detection of anthrax is explained in the next section.

### 2.6.1 Current State-of-the-Art Detection for Anthrax Detection

As it was mentioned in the introduction chapter, anthrax is a type of Bacillus bacterium which is Gram-positive and rod-shape[107]. This bacteria excretes dipicolinic acid (DPA), the adjunct that is planned to be detected as a marker to indicate the presence of the bacteria. Variety of approaches have been used in order to detect anthrax bacteria based on detection of the presence of DPA. Researchers used different methods for detecting DPA including:

- Exploitation of the luminescence of lanthanide/DPA complexes ($Tb^{3+}$ and $Eu^{3+}$) in solution [8, 108–110].
- Liquid and transition metal chromatographic techniques [111, 112].
- Molecular imprinting method [112, 113].
- Potentiometric methods [114].

- Approaches using surface enhanced Raman scattering (SERS) [115, 116].
- Sensing anthrax using Polymerase Chain Reaction (PCR) [117].

Therefore, variety of methods were used to develop commercial anthrax detector devices, which utilise either lanthanide luminescence DPA sensing (AdvntTM, [118] Life Safety SystemsTM, [119]and Universal Detection Systems [120]), or PCR gene sensing method (Smiths DetectionTM [121]). The most improved detection capability is 16 spores per litre of air in these commercial devices. However, with a sampling rate of 100 L/min and a response time of about 15 minutes this equates to a large number of spores to enable detection. MEMS systems have also limitations in order to detect anthrax spores and this can be expressed as follows:

- Differential mobility spectroscopy [122] which has a limit of detection several orders of magnitude higher than required for bioweapons detection.
- Photo-thermal sensor technique incorporating IR spectroscopy on a deflected AFM cantilever demonstrating nanogram resolution (about 1000 spores) [123].
- Resonant mass detection [123] that has been limited to validating the previous photo-thermal technique.

The LD50 value of aerolised anthrax is only 8000 anthrax spores [32]. The main concern with applying the solution method for DPA detection as the indicator of anthrax is that Bacillus Bacteria are widely spread in water, soil and air [107] and all excrete DPA, and this would always increase the chance of false detection due to non-toxic naturally occurring species in the detection operating medium. In addition, there are many difficulties in PCR method for biowarfare agent detection. This method is slow (requires 30 to 60 minutes), sample preparation can negatively affect results and careful temperature control is necessary for the DNA amplification. It is not well suited for in field autonomous operation. Finding a

solution to these obstacles is the challenge to current researches.

## 2.7 Biofunctionalisation of the Sensor Surface

As mentioned earlier, biosensors consist of biological recognition ligand and physical or chemical signalling component. To enable recognition of the target analyte, it is necessary that the surface of the sensor is modified by a chemical compound or bio-layer [5]. This reactive layer provides the selectivity and specificity to the biosensor, due to its high capacity to recognize a specific analyte. In many biosensors, in response to biological species such as bacteria or contaminants antibodies are produced, which in turn can be measured. Variety of sensor formats have been employed for pathogen analysis using antibodies as covered in section 2.2. The sensitivity of these techniques depend on the properties of transducer and the quality of the antibody.

Figure 2.24 represents how a surface of the microstructure plays a significant role in detection of a free target analyte and transfers biomolecular interactions into a digital signal which are interpreted by a data acquisition readout system.

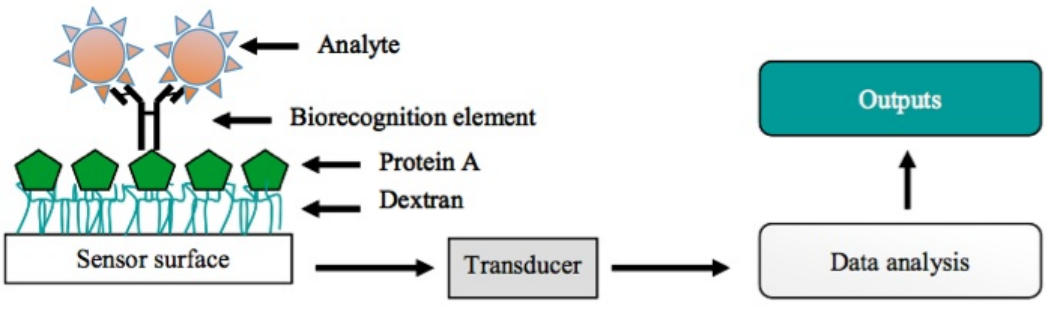


FIGURE 2.24: A Schematic of a simple biosensor with chemically functionalised surface [5].

A key requirement for the detection of biological species is the ability to modify the surface microstructure to allow biospecific recognition [60]. As demonstrated in Figure 2.24, a full-length antibody is absorbed on protein A immobilised on a carboxymethylated dextran-coated sensor surface and is used for the capture of a target analyte. Based on this physiochemical interaction, changes in mass, temperature, electrical potential can be generated. This is then converted via a microstructural transducer to a signal which can be analysed by an user. The selectivity, reproducibility and resolution of the sensor is very much dependant on the receptor layer [2]. In order to have a high quality receptor layer, it is important to take into account the following considerations:

- Low thickness (the thinner the layer, lesser the degradation in mechanical properties of the sensor)
- Uniformity (produces uniform stress over the surface of the sensor)
- Compactness (to avoid interactions with the solid substrate beneath)
- Robust structure (to enable covalent binding)
- Allow accessibility by the target molecule
- Long active life

Typical reactive layers widely used for biosensors are self assembled monolayers and numerous classes of polymers [124]. Self-assembled monolayer (SAM) formation induced by the strong chemisorption between the substrate and head group of selected organic molecule provides one of the most elegant approaches towards making ultra-thin organic films of controlled thickness [125]. It allows the assembly individual molecules into highly ordered architectures for obtaining a desired function. One of the common methods to create ordered monolayers is to use the self-assembling properties of alkane chain molecules with thiol (-SH) groups on gold substrate or silanes (-SiOX) on silicon substrates.

An advantage of SAMs is the relative simplicity with which they can be prepared in a laboratory. The substrate is simply dipped in the required dilute solution for a specific time period, then washed with the same solvent and dried, often using a gun of dry argon. Alternatively, gas phase evaporation of the adsorbent can also form good monolayers, although structural control sometimes is difficult [125]. Several factors affect the formation and packing density of monolayers like the nature and roughness of substrate, solvent, nature of the adsorbate, temperature and the concentration of the adsorbate [125].

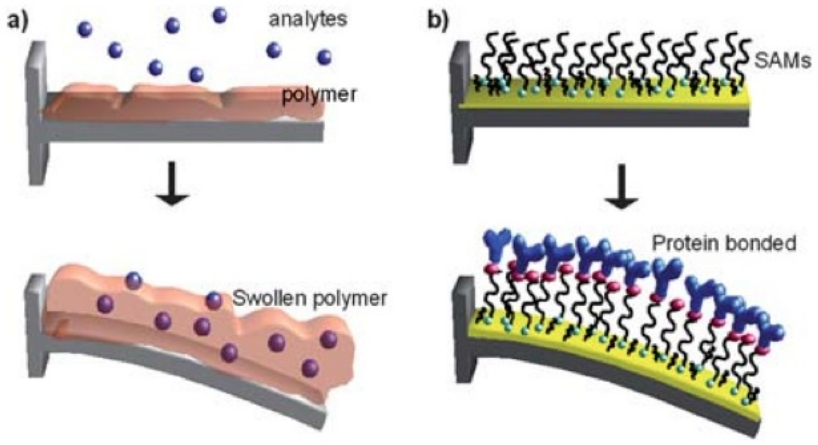


FIGURE 2.25: Scheme of the response of microcantilevers when using a) a polymer or b) SAMs sensing layers [124].

In a different approach, addition of specific functional groups to a solid surface can also be achieved by application of polymers. As shown in Figure 2.25, during analyte absorption, the polymer layer covering the cantilever swells, thus magnifying the cantilever bending. Betts et. al used spin coating techniques to deposit thin films (150 nm) of different polymers and then used Focused Ion milling (Discussed in Chapter 4) to remove the coatings in areas it was not required.

## 2.8 Summary

In this chapter the operating principles of biosensors was introduced and an overview of their main components was given. Biosensors were described as having two core elements: the bioelement and the transducer element. Different biosensor classifications were presented based on their transduction mechanisms and each of their advantages and limitations explored. The MEMS based mass detection approach was then described in detail because of its potential for high sensitivity, low power consumption robust devices. An overview of the state of the art in MEMS based mass sensors was presented and gaps in the research identified. The most commonly implemented MEMS transducer elements were cantilever based resonators and the emphasis of recent research was seen to be on the optimisation of the geometrical parameters of the device in order to achieve a higher quality factor. Finally a brief summary of the concept of bio/ chemical functionalisation of the sensor surface was given. The application processes such as self assembled monolayers that are used in order to enhance the specificity of the mass sensor to a target analyte was described. The literature review showed that chemically functionalised resonant sensors offered higher sensitivity due to their small size and frequency stability. In the following chapters, the focus turns to the development of a highly sensitive mass sensor through implementation of a highly sensitive transducer element. The use of a torsional micro paddle resonator as the core element is explored because of its promising output characteristics that have been demonstrated in recent works. Based on the strengths offered by implementing an electromagnetic driving mechanism, this approach is further investigated in this thesis.

# 3

# Theory and Design

## Contents




**Summary** In this chapter, background theory of the microresonators is given. Then, system-level model of the device is presented and explained. Design concept of MEMS vibrational systems is described. Following an overview of the operating principles of microresonators, the design of a micro torsional paddle resonator is undertaken. Analysis of the designed system is carried out using both analytical and numerical techniques. Finite Element (FE)

Analysis was used to evaluate various proposed designs and enable comparisons of functional performance.

## 3.1 Background theory of microresonators

A resonator can be defined as a frequency selective amplifier which on appropriate excitation goes into vibration. The resonant frequency of a device is determined by physical properties of the resonator material, its layout, dimensions, mechanical assembly and excitation signal [25]. Resonant sensors which have high sensitivity and resolution, low power consumption and digital output characteristics play an important role in MEMS based mass detection.

As depicted in Chapter 2, many micro cantilever based mass detection sensors, which build on the measurement of shift in resonant frequency have been employed for high resolution mass detection. The resolution of a resonant cantilever depends on its effective mass and quality factor. Accordingly, an ultra high mass resolution can be achieved by decreasing the cantilever dimensions, thus decreasing its effective mass [80]. However, reducing the dimensions of the cantilever limits the target analyte sensing/adsorption area.

In the next sections, the design of a torsional paddle microresonator (TPM) is described. A sensing device incorporating such a structure relies upon an increase in the moment of inertia of the paddle about the torsional spring axis and a consequential reduction in the resonant frequency, upon mass adsorption. The use of a TPM has several advantages over commonly used mico cantilevers. These include, a larger detection region with the similar size structure, higher stability due to dual supporting anchors, a near linear response to the added mass and utilization of the bending moment to drive, therefore requiring less power for significant displacement [57, 126].

In every system design it is necessary to go through theory, modeling, simulation and produce prototypes for the proof of performance test. Figure 3.1 illustrates the steps involved in the development stages of the torsional micropaddle resonator.

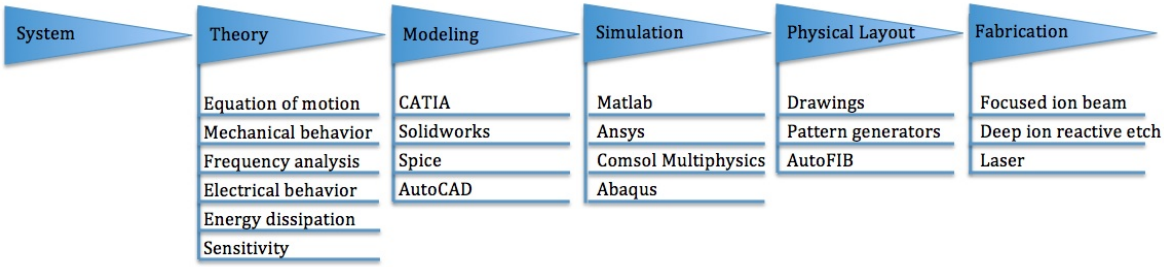


FIGURE 3.1: Modeling hierarchy for micro and nanoresonator design (Adapted from [25]).

Generally, a system model comprises of a MEMS resonator and an amplifier integrated circuit for read out of the MEMS current. An example of typical plots of the frequency response of the read out circuit of a MEMS resonator are shown in Figure 3.2.

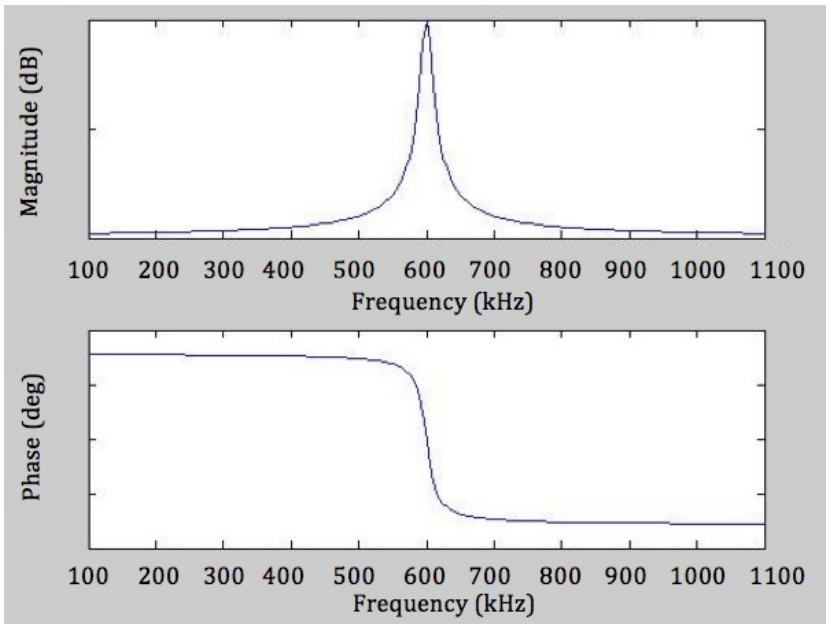


FIGURE 3.2: Bode plot (frequency response) of the read-out circuit from a vibrating resonator.

### 3.1.1 Equation of Motion

To understand functionality of resonators it is important to establish the associated equations of motion. In this section, the bending and torsional resonant responses of micro paddles

are given and a general formula of the motion is described, which is then modified for the proposed torsional micro paddle.

A paddle is a supported plate which enables translation, rotation or displacement in a translational-rotary manner. On adsorption of mass on the paddle, its moment of inertia increases about the torsional axis and reduces the resonant frequency.

The structure of MEMS resonators have an infinite number of eigenfrequencies, also known as eigenvalues. Under specific conditions the structure can be driven into its resonance. As previously described, various transduction mechanisms can be used to excite the MEMS device causing the resonator to mechanically vibrate at the fundamental modes. This causes the resonator to deflect, expand or twist [25]. The resonant behaviour of a MEMS resonator can be expressed by the model of a mechanical damped harmonic oscillator. The governing equation of motion for the dynamics of such a system is given by:

$$m_{eff}\ddot{x} + D\dot{x} + kx = F_{ext}(x,t) = F_0 Sin(\omega t) \tag{3.1}$$

Where $x$ is the time varying harmonic oscillation, $m_{eff}$ is the equivalent mass, $D$ is the damping constant, $k$ is the spring constant, $F_{ext}$ is the external force applied to the resonator and $F_0$ is the amplitude of the harmonic force signal with frequency $f$. Since the resonating mode in this project is rotational, an equivalent form of the equation 3.1 based on torque is presented later. The solution to equation 3.1 is a complementary function, which shows the initial vibration and disappears quickly. The particular solution for this equation associates with a sustained motion. For a simple harmonic motion excited by an external force to a

certain frequency, below solution can be assumed [127].

$$x = Xsin(\omega t - \phi) \tag{3.2}$$

This equation represents the displacement vector lags the force vector by $\phi$, which validates the motion occurs after the application of the force. Therefore, equation 3.1 can be presented as follows:

$$m_{eff}X\omega^2 Sin(\omega t - \phi + \pi) + DX\omega Sin(\omega t - \phi + \frac{\pi}{2}) + kXSin(\omega t - \phi) = F_0 Sin(\omega t) \tag{3.3}$$

Based on equation 3.3 the vector diagram of the forces can be drawn (Figure 3.3).

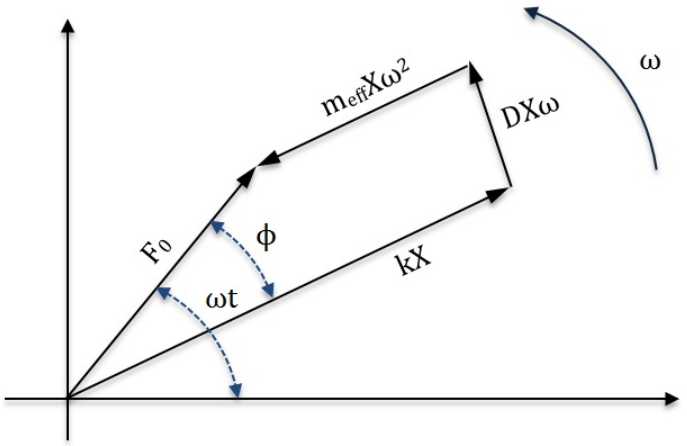


FIGURE 3.3: Force vector diagram (Adapted from [127]).

According to the diagram shown in Figure 3.3 the amplitude of the vibration can be therefore written as:

$$X = \frac{F}{\sqrt{(k - m_{eff}\omega^2)^2 + (D\omega)^2}} \tag{3.4}$$

Therefore, the steady state solution of the equation 3.1, will be:

$$x = \frac{F}{\sqrt{(k - m_{eff}\omega^2)^2 + (D\omega)^2}} sin(\omega t - \phi) \tag{3.5}$$

The eigenfrequency of the oscillator are obtained by equating $F_0$ to 0 in the Equation 3.1

$$f_n = \frac{1}{2\pi}\sqrt{\frac{k_n}{m_{effn}}} \tag{3.6}$$

Where $f_n$ is the resonant frequency of the *n*th mode. Thus, reduction of the effective mass results in an increase of the resonant frequency of the current mode. In addition, higher modes have less energy than fundamentals ones. In Equation 3.1 the term *D* determines the amount of damping in the system:

$$D = \frac{2\pi f_n m_{eff}}{Q} \tag{3.7}$$

where *Q* is the quality factor in a viscous medium like air or liquid, the Q factor mainly depends on friction, and it is an important design parameter for resonator applications. In terms of energy, *Q* factor can be expressed as:

$$Q = 2\pi \frac{\text{max. energy stored in one cycle}}{\text{energy dissipated per cycle}} \tag{3.8}$$

### 3.1.2 Damping

Since, there is still a challenge to clearly incorporate damping in dynamic systems with its detailed microscopic features, studies have been conducted in order to identify a general model of damping or to estimate the damping in a vibrating system [128]. One of the most

common approaches is the viscous damping or Rayleighs damping. In this prediction, it is assumed that the damping matrix is proportional to the mass and stiffness matrices.

$$[d] = \alpha[m] + \beta[k] \tag{3.9}$$

Where *d* is the Rayleigh damping term, $\alpha$ is the mass coefficient and $\beta$ is the stiffness coefficient. The coefficients of mass and stiffness, $\alpha$ and $\beta$, are not usually available in the literature. Instead, $\xi$, is regularly expressed as damping ratio. The relationship is defined in Equation 3.10

$$\xi = \frac{d}{d_0} \tag{3.10}$$

where $d_0$ is the critical damping.

In systems having a high quality factor, the damping ratio can be also expressed as:

$$\xi \cong \frac{1}{2Q} \tag{3.11}$$

The relationship between damping ratio and Rayleigh parameters, $\alpha$ and $\beta$, at a known frequency, *f*, is:

$$\xi = 0.5\left(\frac{\alpha}{2\pi f} + \beta(2\pi f)\right) \tag{3.12}$$

Therefore, by applying this relationship at two frequencies, $f_1$ and $f_2$, with different damping ratios, $\xi_1$ and $\xi_2$, the values of mass coefficient and stiffness coefficient can be obtained from:

$$\begin{bmatrix} \frac{1}{4\pi f_1} & \pi f_1 \\ \frac{1}{4\pi f_2} & \pi f_2 \end{bmatrix} \begin{bmatrix} \alpha \\ \beta \end{bmatrix} = \begin{bmatrix} \xi_1 \\ \xi_2 \end{bmatrix} \tag{3.13}$$

This method is used commonly in order to obtain results for numerically sensitive structural systems [128, 129].

Fundamentally, damping is due to the losses occurring within a dynamic system and it is important to consider its sources. The losses are produced by energy dissipation and a number of them are given below:

- Energy dissipation through the anchors that attach the resonator to the substrate
- Internal dissipation caused by vibrational structure
- Losses through thin layers (surface losses)
- Losses connected to the shape of the mechanical components, generated through phonon scattering
- Nyquist-Johnson noise produced by electronic circuitry microfabrication techniques
- Adsorption-desorption processes from residual gases
- Viscous damping

### 3.1.3 Sensitivity

In mass detecting systems, both the stiffness and the effective mass are influenced by the deposited mass ($\Delta$m) on the sensing element. If the added mass is small enough, in comparison to the paddle mass, change in the elastic properties and stiffness variation can be neglected. Having this assumption, the net effect of $\Delta$m associates with a decrease in the resonance frequency to a value defined by first-order approximation [130, 131]:

$$\frac{\Delta f}{f_n} = -\frac{1}{2}\frac{\Delta m}{m_{eff}} \tag{3.14}$$

where $\Delta f$ is the resonance frequency shifting. The optimisation of the paddle design helps to maximise the mass sensitivity $S_m$ of the device:

$$S_m = \frac{\Delta f}{\Delta m} \tag{3.15}$$

## 3.2 System-Level Model of The Device

As it is shown in the Figure 3.4, the overview of the system is depicted as a system-level model. The system design is composed of different stages, every stage requires modelling and calculations to better understand the performance of the device. As shown in this Figure, first the model is developed within a FEA COMSOL package with exact dimensions in order to calculated the resonant frequency of the device. This quantity is also calculated from the equation of motion, which is explained later in this chapter. Next is to carry out the force required to vibrate the device in order to get a measurable response. Since the driving method is designed to be electromagnetic, it requires a current carrying track and a constant magnetic field in the direction perpendicular to the track on the device. The strength of the magnetic field and the amount of current passing through the track play significant role in the amount of generated force. The produced force should be high enough to vibrate the micro paddle and provide detectable signal under the optical measurement system. In the miniaturised systems, current produces heat, and therefore, it is important to set the value, which does not exceed the melting temperature and maintains the stability of the device. Therefore, a

Joule heating simulation is carried out in order to find the limit of the current amount. In addition, it is important to consider detection condition for bio agents on the receptor layer. It is important to keep the temperature such that it won't damage the receptor layer and target species. The following sections give explain about the details of the modelling and calculations.

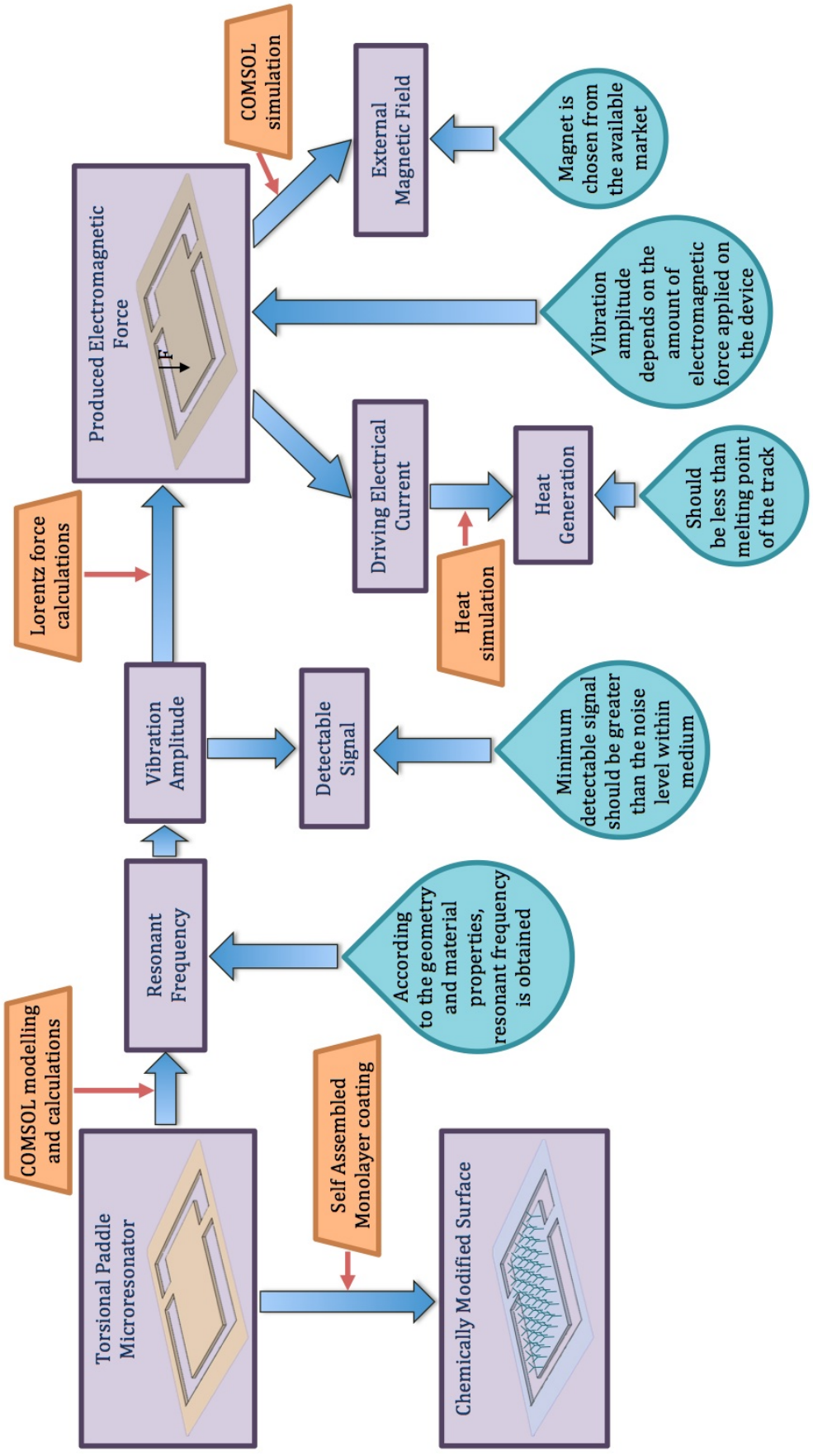


FIGURE 3.4: System-Level Model of the device design.

## 3.3 Concept and Design of Torsional Paddle Microresonator

This work has overcome the gap in the research in this field by developing a resonator, see Figure 3.5 which has the following advantages:

Micro paddle design provides an area for detection, which is independent of the mechanical design parameters such as spring constant and stiffness. In cantilever designs, the length of the micro cantilever sets the mechanical and vibrational behaviour of the device. So if the required vibration frequency and detection area do not match, the design becomes difficult. However, in the micro paddle design, the paddle area is where the detection takes place and shape and dimensions of the supports define the mechanical behaviour independent of the paddle size.

Another advantage is that, the surface of the paddle doesn't have any residual stress since the movement is torsional and stress occurs on the supporting anchors. Therefore, the surface of the paddle remains flat during the operation whereas in cantilever resonator design, the cantilever is constantly under bending and this causes stress and reduces the system's life due to fatigue.

Having established the advantages of the micro paddle resonator, the problem of its actuation has to be addressed. Since the support bridges will twist during the chosen torsional oscillation of the flat paddle, it is difficult to conceive of any thermal or PZT driven actuation. Thus, while PZT actuation is clearly applicable to drive small amplitude vertical displacement of a simple cantilever it cannot be used to drive a torsional system. Similarly, a simple biomorph will provide a tip oscillation but again it is impossible to envisage torsional drive using such a method. In conclusion, PZT or biomorph drive could be adapted to provide a simple vertical oscillation of the paddle but twisting or rotational motion cannot be achieved

in this way. The thought processes behind the novel Lorentz actuation, which does provide the twist drive, lie in electromagnetic motor theory. This is a classical effect in which a current carrying coil in a magnetic field provides an effective electric motor. The novelty in the current device was to recognise the usefulness of this drive method and to determine a way in which it could be adapted to a micro mechanical system. The key features are that the coil should be integral with the paddle with input and output conductors on each of the bridges one on the top surface and one on the bottom connected by a via. FIB technology provides one of the few ways in which this can be implemented. Combined with an in-plane magnetic field directed along the paddle surface this electric motor approach provides a torsional or twist drive mechanism with novelty in the concept, the design and the fabrication.

This Lorentz force drive system helps to keep the mass of the resonator low. This would increase the mass sensitivity, since the system mass is kept minimum whereas in other mostly presented works, an extra material such as PZT is integrated with the vibrating part of the device, which increases the system mass. In addition, Lorentz force produces push and pull force, which is bidirectional and gives a better control of the operation. This is a contact-less drive method, which requires an external magnetic field across the vibrating component; it is also a reversible drive method where the electrical current produces mechanical vibration and mechanical movement produces current. So this facilitates to have simple drive and detect system in one package.

### 3.3.1 Description of the TPM

The first stage of development of a chemically functionalised paddle microresonator system is the development of a the non-chemically specific mass sensitive element. The proposed

design is an asymmetric micropaddle resonator as shown in Figure 3.5. The paddle is made from a silicon nitride substrate. It has a thickness of 200 nm and has dimensions of 8 $\mu$m $\times$ 10 $\mu$m. Two support beams, each measuring 1 $\mu$m $\times$ 2.5 $\mu$m anchor the paddle to a fixed substrate. The asymmetrical disposition of the beams provides a larger edge displacement for measurement purposes which is demonstrated in section 3.5.

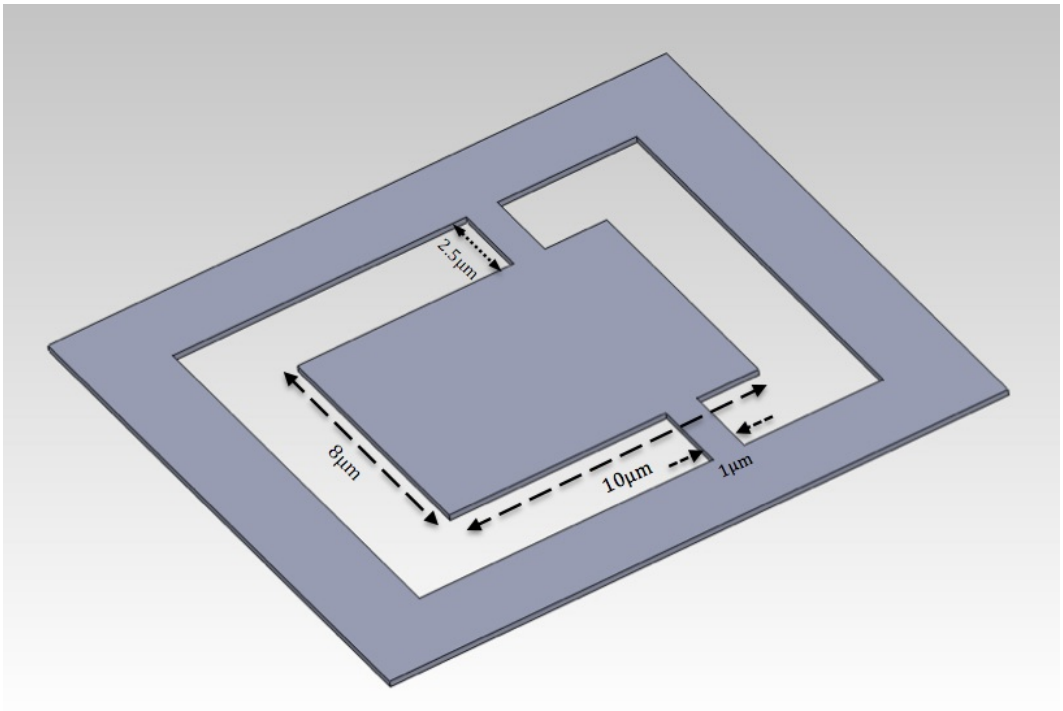


FIGURE 3.5: Plane micro paddle design.

In order to implement a Lorentz force electromagnetic driving system, a planar spiral coil of platinum (having a cross section of 100 nm by 100 nm) is deposited on both sides of the paddle and connected to each other through a via at the centre of the paddle. In the presence of a magnetic field an alternating current through the coil will produce a turning moment on the paddle, resulting in a torsional vibration, as shown in Figure 3.6. This dual coil design will provide twice the torque which would be achieved using a single spiral of conductive coil. In addition to this design which incorporates a spiral coil, two additional designs (one

with a dual loop and one with a single platinum track of cross section 300 nm by 300 nm) which have less complexity and are therefore easier to fabricate have been developed and shown in Figure 3.7.

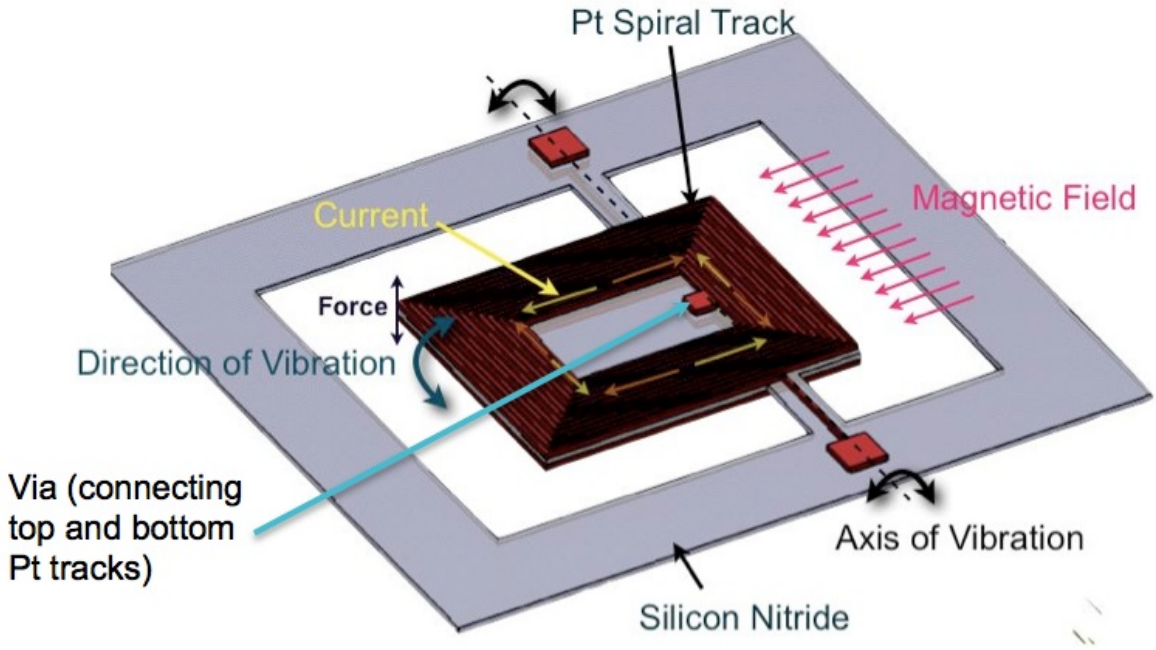


FIGURE 3.6: Torsional paddle microresonator scheme of operation.

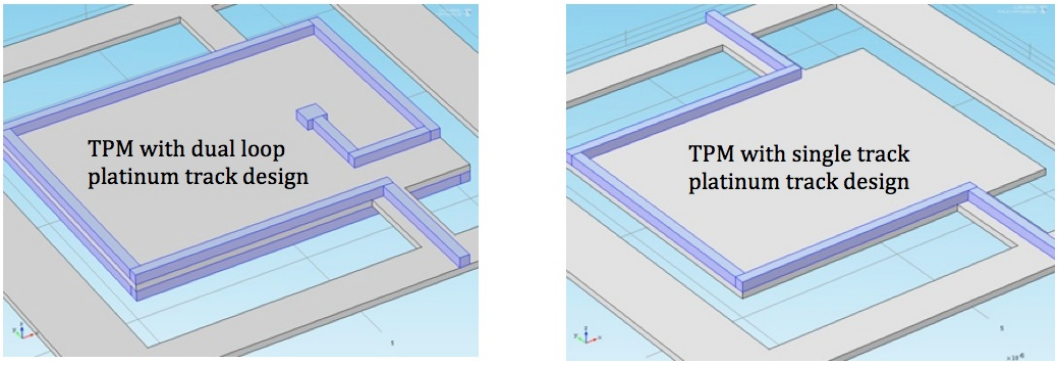


FIGURE 3.7: Two designs of TMP with dual loop platinum track and single platinum track.

The working principle used to resonate the TPM is based on a Lorentz force actuation mechanism. As shown in Figure 3.6, the two ends of the coil are connected to an electrical source and current flows through the platinum spiral coil. In presence of a planar magnetic

field, the part of the coil which is perpendicular to the magnetic field generates a force perpendicular to the paddle surface. The direction of the force can be reversed by changing the current flow direction. Since, the surface of the TPM is partially covered by the coil, the generated force causes a torsional effect about the neutral axis passing through the supporting legs (highlighted as axis of vibration in the Figure 3.6). Thus, there is a resonating effect when an alternating current (AC) passes through the coil. In order to vibrate the micro paddle to its high amplitude, the AC current can be tuned to match the natural frequency of the micro paddle.

The choice of substrate material for this purpose, is a square silicon nitride membrane with a frame size of 7.5 mm by 7.5 mm, a thickness of 0.2 mm and a window size of 0.5 mm by 0.5 mm as depicted in Figure 3.8.

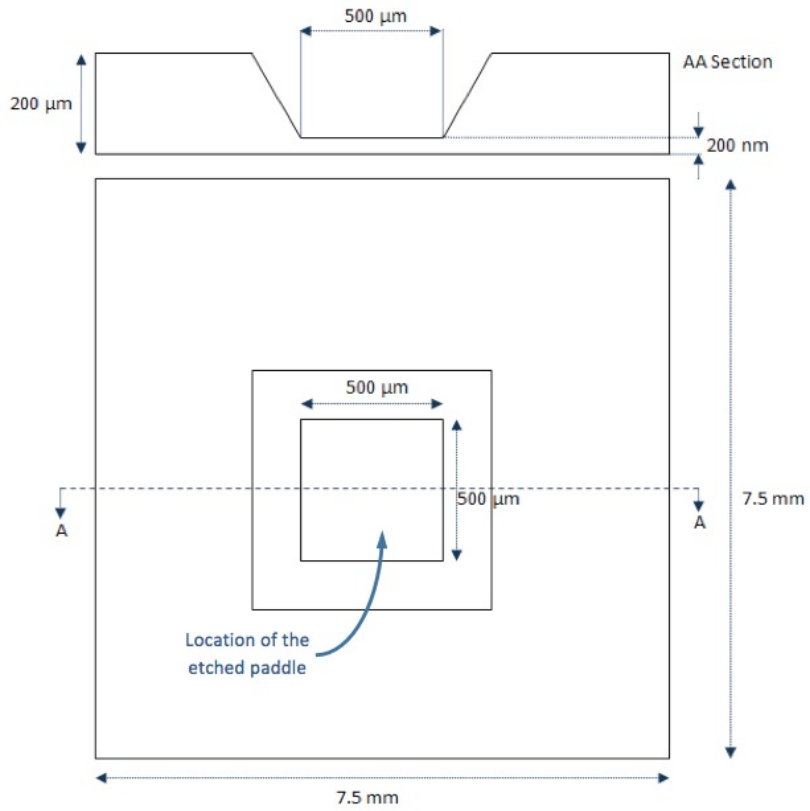


FIGURE 3.8: Schematic of the silicon nitride membrane.

### 3.3.2 TPM Operating Mechanism

As there is more than one motion involved in the operation of the paddle resonator, the system is considered a multiple degree of freedom (DOF) system. Figure 3.9 shows the torsional micro paddle resonator subjected to both bending and torsion thus requiring analysis as a 2 DOF system. In the following, the modes of operation influencing the designed TPM are described in detail.

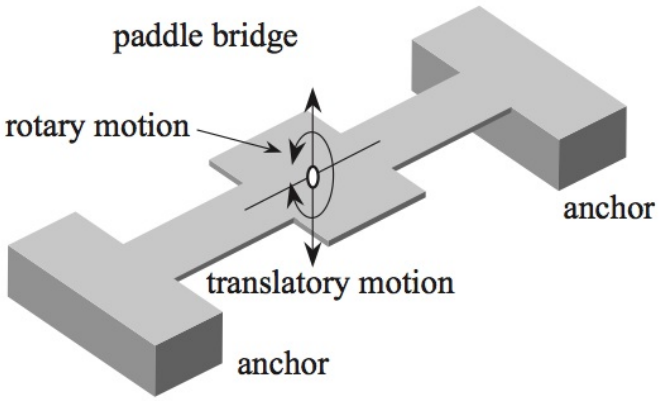


FIGURE 3.9: Microbridge as a 2-DOF system [132].

#### Torsional resonant frequency

As illustrated in Figure 3.10, the micro paddle consists of two equal length support legs or beams on either sides. When a force acts on the free end of the paddle, it generates a torsional moment or torque causing twisting of the beams by an angle that is proportional to the applied torque. The torsional stiffness of these beams or springs depend on the material properties and their geometry. In figure 3.10, the torsion acting on the beam is shown, where $\theta$ is the angle of twist, $\gamma$ is the shear strain, $\tau$ is the shear stress and $T$ is the applied torque.

Although in the proposed design rectangular torsional springs are used, in this section, circular torsional springs are first described because of the simplicity of the theory. Figure

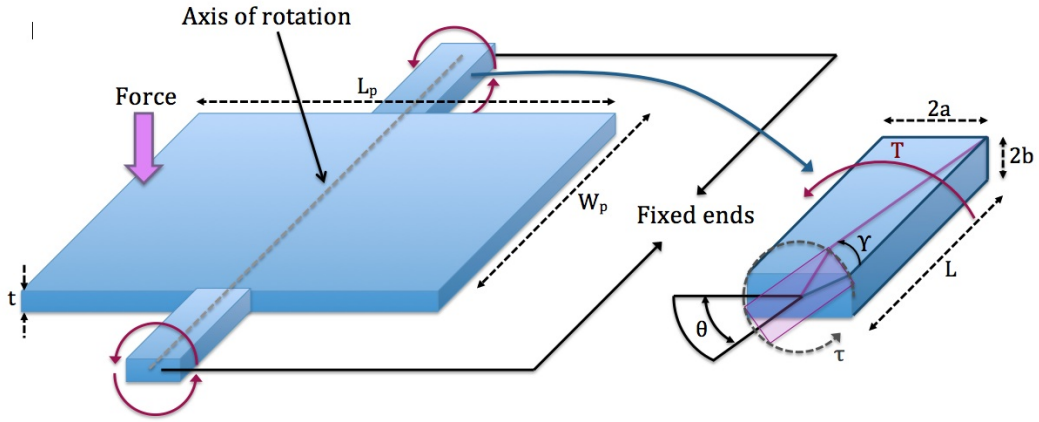


FIGURE 3.10: Schematic of a micro torsional paddle under torsional deformation

3.11 shows how the torque is applied on an element in a circular bar. Assuming a spring with circular cross section having a radius *r*, and length *l*, that is subjected to an applied torque *T* the shear strain $\gamma$ is given by:

$$\gamma = r\frac{\partial\theta}{\partial l} \tag{3.16}$$

Where $\theta$ is the angle of twist.

According to basic stress-strain theory, the relationship between $\gamma$ and $\tau$ is given by:

$$\tau = G\gamma = Gr\frac{d\theta}{dl} \tag{3.17}$$

Where *G* is the shear modulus. The shear force (*dF*) caused by stress is given by:

$$dF = \tau dA \tag{3.18}$$

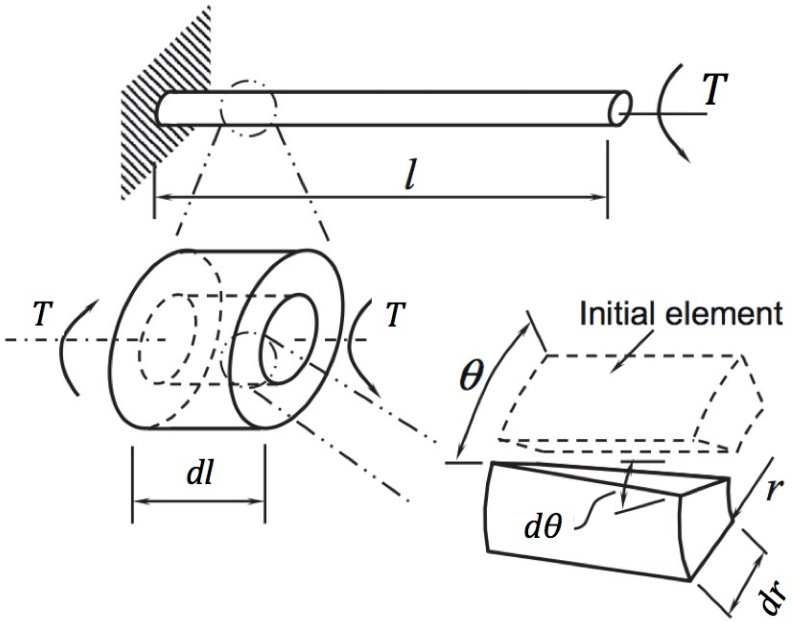


FIGURE 3.11: Circular torsional beam [133].

Thus the torque *dT* produced due to the force acting at radius *r* can be calculated as

$$dT = dF \cdot r = \tau dA \cdot r \tag{3.19}$$

The Figure 3.12 presents the torque produced based on the shear stress on the circular cross section.

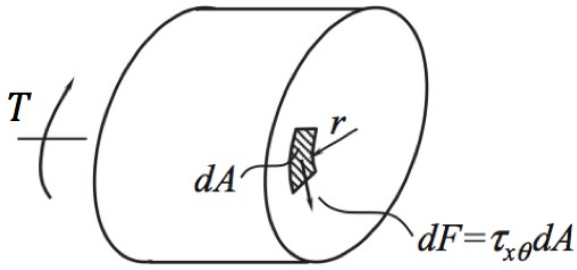


FIGURE 3.12: Torque produced due to shear stress on the cross section [133].

Thus the torque acting on the cross section perpendicular to the beam length is given by

the integration of the moment on the element:

$$T = \int_A \tau dA \cdot r = \frac{d\theta}{dl} G \int_A r^2 dA \tag{3.20}$$

This can be written as:

$$T = \frac{G d\theta}{dl} J \tag{3.21}$$

where *J* is the polar moment of inertia of the circular beam and for the infinitesimal area of $dA = r\, dr\, d\theta$, *J* can be calculated as:

$$J = \int_A r^2 dA = \int_{2\pi} \int_r r^2 \cdot r \cdot d\theta \cdot dr = \frac{\pi}{2} R^4 \tag{3.22}$$

Where *R* is the radius of the circular beam.

Integrating Equation 3.21 yields the angular displacement at the end of the beam:

$$\theta = \int_0^l \frac{T}{GJ} dl = \frac{Tl}{GJ} \tag{3.23}$$

Shear stress acts tangentially and uniformly in a small cross section of the support. When the angle of twist changes linearly across the length of the bar, the maximum shear stress can then be stated as follows:

$$\tau_{max} = GR\frac{\theta}{l} \tag{3.24}$$

The equations above describe the relationships between torque and angle of twist for circular shaft of radius *R*. However, in MEMS systems due to restrictions of MEMS fabrication

techniques, circular cross-sections are rarely encountered and instead rectangular or square cross-sections are more common. For such geometries, when a torsional load is applied, the cross-sections become warped with the greatest stress occurring at a point on the perimeter nearest the axis of twist and the corners of the rectangular and square cross sections having no stress [16, 134]. The analysis of torsion in such cases is more complex. Figure 3.13 shows the torque and shear stress in a rectangular bar.

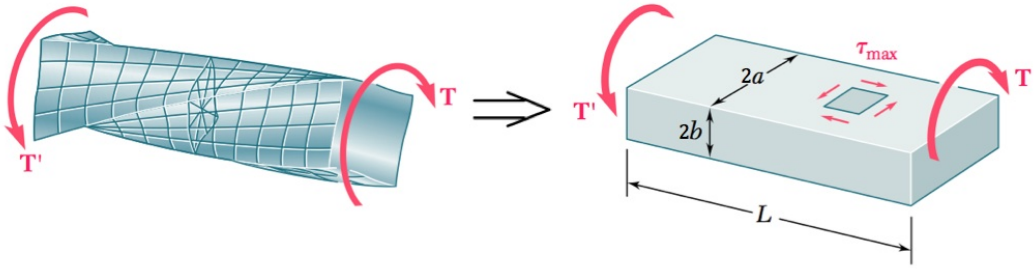


FIGURE 3.13: Torque and shear stress in a rectangular beam cross section [135].

In this case, the formula of the torque ($T$) and angle of deformation ($\theta$) is expressed as follows:

$$T = \frac{\theta}{L} KG \quad \text{or} \quad \theta = \frac{TL}{GK} \tag{3.25}$$

Where $K$ is a factor (torsional constant) that depends on the form and dimensions of the cross section. For a circular section, $K$ was shown to be the polar moment of inertia $J$. For rectangular cross section with length of $2a$ and width $2b$ where $a$ is greater than $b$ the torsional constant K is given by an infinite series as given in the following equation [136].

$$K = \frac{16}{3} b^3 a \left( 1 - \frac{192}{\pi^5} \frac{b}{a} \sum_{n=1,3,5,\ldots}^{\infty} \frac{1}{n^5} tanh \frac{n\pi a}{2b} \right) \tag{3.26}$$

The above equation can be given in a simplified form as given below by approximating the solution with a resulting error not greater than 4% [137]:

$$K = b^3 a \left( \frac{16}{3} - 3.36 \frac{b}{a} \left( 1 - \frac{b^4}{12a^4} \right) \right) \tag{3.27}$$

Using curve-fitting techniques, Equation polar moment of inertia above can be also be expressed as a closed-form equation as [133]

$$K = \frac{(2b)^3 (2a)}{3} \left[ 1 - 0.616 \left( \frac{b}{a} \right) - 0.087 \left( \frac{b}{a} \right)^2 + 0.125 \left( \frac{b}{a} \right)^3 \right] \tag{3.28}$$

The above equation is in excellent agreement with K in infinite series with an error of 0.08%.

The maximum shear stress $\tau_{max}$ is given by [136]:

$$\tau_{max} = \frac{16 G \theta b}{\pi^2} \sum_{n=1,3,5,\ldots}^{\infty} \frac{1}{n^2} \left( 1 - \frac{1}{cosh(n\pi a / 2b)} \right) \tag{3.29}$$

The above equation can be given in a simplified form by approximating the solution as given below [137].

$$\tau_{max} = \frac{3T}{8b^2 a} \left( 1 + 0.6095 \frac{b}{a} + 0.8865 \left( \frac{b}{a} \right)^2 - 1.8023 \left( \frac{b}{a} \right)^3 + 0.9100 \left( \frac{b}{a} \right)^4 \right) \tag{3.30}$$

Other approximate solutions for estimating the $\tau_{max}$ and angle of twist $\theta$ can be given by the following formulas:

$$\tau_{max} = \frac{T}{8\alpha_1 ab^2} \tag{3.31}$$

$$\theta = \frac{TL}{16\alpha_2 ab^3 G} \tag{3.32}$$

In the Equation 3.31, an appropriate $\alpha_1$ has to be extracted from the Table 3.1. This is also valid for the Equation 3.32 to substitute $\alpha_2$ [135].

TABLE 3.1: Coefficients of rectangular bars in torsion [135].

| **a/b** | $\alpha_1$ | $\alpha_2$ |
|---|---|---|
| 1.0 | 0.208 | 0.1406 |
| 1.2 | 0.219 | 0.1661 |
| 1.5 | 0.231 | 0.1958 |
| 2.0 | 0.246 | 0.229 |
| 2.5 | 0.258 | 0.249 |
| 3.0 | 0.267 | 0.263 |
| 4.0 | 0.282 | 0.281 |
| 5.0 | 0.291 | 0.291 |
| 10.0 | 0.312 | 0.312 |
| $\infty$ | 0.333 | 0.333 |

Now to incorporate the dynamics of a rotational system, an equation of motion for a torsional system has to be considered.

$$J_p\ddot{\theta} + b\dot{\theta} + K_t\theta = T_0 Sin(\omega t) \tag{3.33}$$

where $J_p$ is the polar mass moment of inertia, $b$ is the torsional damping factor, $K_t$ is the torsional stiffness, and $T$ is the torque applied to the system in a sinusoidal behaviour. For the free undamped oscilation where $b$ and $T$ are zero the equation of motion can be then expressed as:

$$J_p\ddot{\theta} = -K_t\theta \tag{3.34}$$

which can be simplified in following form,

$$\ddot{\theta} = \frac{-K_t\theta}{J_p} = -\omega^2\theta \tag{3.35}$$

by knowing $\omega = 2\pi f$ and having an assumption of a rigid structure with a vibrating plate about a weightless support of a perfect non-deformable shaft, natural frequency can be analytically obtained by:

$$f_n = \frac{1}{2\pi}\sqrt{\frac{K_t}{J_p}} \tag{3.36}$$

If the particular solution is assumed to be:

$$\theta = \Theta sin(\omega t - \phi) \tag{3.37}$$

The amplitude equivalent equation for a torsional system can be expressed in terms of angle of twist as follows:

$$\Theta = \frac{T}{\sqrt{(K_t - J_p\omega^2)^2 + (b\omega)^2}} \tag{3.38}$$

However as illustrated in figure 3.10, since there are two supports holding the middle plate, the above formula can be then modified to:

$$f_n = \frac{1}{2\pi}\sqrt{\frac{2K_t}{J_p}} \tag{3.39}$$

As it was mentioned earlier the damping of a system can be obtained by the Equation 3.7. This equation can be also expressed for a torsional system,

$$b = \frac{2\pi f_n J_p}{Q} \tag{3.40}$$

**Polar mass moment of inertia**

In the presented schematic of the Figure 3.10, the middle plate has a mass that is much greater than the supporting shafts which generates rotational resistance. This characteristic is also known as *Polar Mass Moment of Inertia ($J_p$)*, which has a unit of kg·m$^2$ and determines the amount of rotational deflection of the system. In the case of a symmetrical micro paddle as shown in Figure 3.10, the polar mass moment of inertia of an arbitrary rectangular cross-section with rotation about the y-axis through the centre of the cross-section is derived as follows:

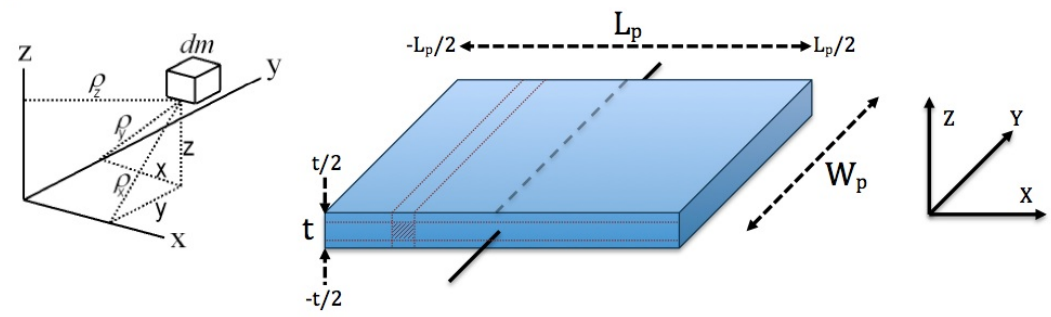


FIGURE 3.14: A schematic to support the calculation of mass moment of inertia $J_p$.

$$
\begin{aligned}
J_p &= \int \rho_y^2 dm \\
&= \int (z^2 + x^2) dm \\
&= \int_{-t/2}^{t/2} z^2 dm + \int_{-L_p/2}^{L_p/2} x^2 dm \\
&= \int_{-t/2}^{t/2} \rho L_p W_p z^2 dz + \int_{-L_p/2}^{L_p/2} \rho t W_p x^2 dx \\
&= \rho L_p W_p \left[\frac{z^3}{3}\right]_{-t/2}^{t/2} + \rho t W_p \left[\frac{x^3}{3}\right]_{-L_p/2}^{L_p/2} \\
&= \rho W_p \left[ t \left( \frac{L_p^3}{24} + \frac{L_p^3}{24} \right) + L_p \left( \frac{t^3}{24} + \frac{t^3}{24} \right) \right] \\
&= \rho W_p \left( \frac{L_p t^3}{12} + \frac{t L_p^3}{12} \right) = \frac{\rho W_p L_p t}{12} (L_p^2 + t^2) \\
&= \frac{m_p}{12} (L_p^2 + t^2)
\end{aligned}
\tag{3.41}
$$

In case of an asymmetrical configuration, where the support is located in a distance of a quarter of the length of paddle ($L_p$) from one end of the paddle the Mass Moment of Inertia can be derived from the same approach

$$
J_p' = \frac{m_p}{48} (7L_p^2 + 4t^2) \tag{3.42}
$$

This parameter is directly related to the design geometry and shows that, larger the *Mass Moment of Inertia*, smaller the angular acceleration about that axis for a given torque occurs. Calculating this parameter for different designs could be quite complex. For this purpose, Solidworks modelling package has been used to obtain more accurate results. Figure 3.15

shows the mass moment of inertia obtained for different designs. The result shown for every model is the moment of inertia taken at the centre of mass (shown in pink) and alighned with the output coordinate system (shown in blue).

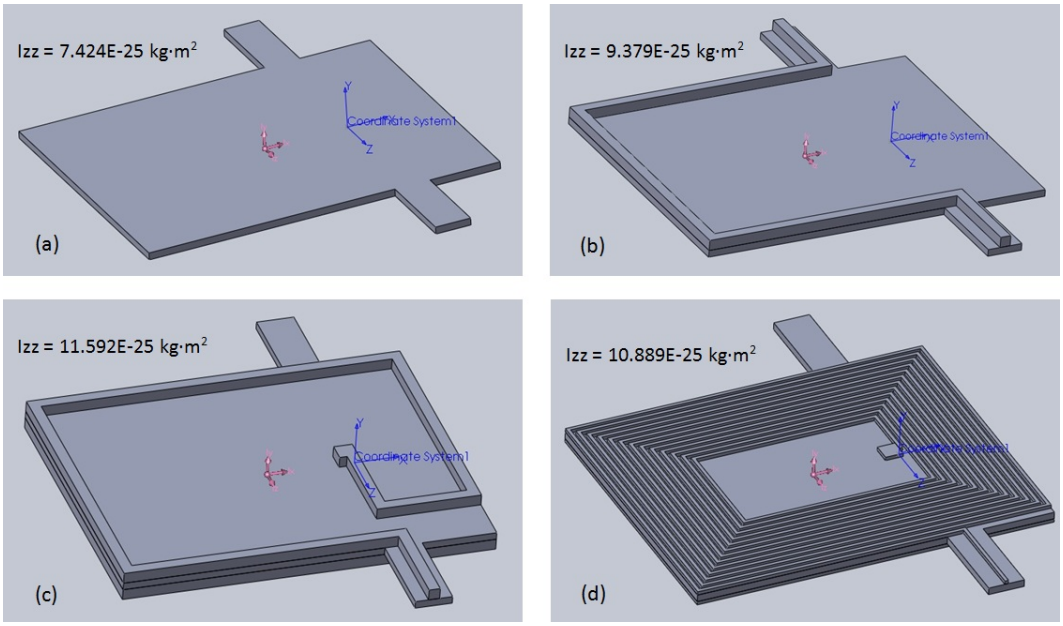


FIGURE 3.15: Mass moment of inertia obtained by Solidworks software package. (a) plain micro paddle, (b) micro paddle with a single track, (c) micro paddle with a dual loop track, (d) micro paddle with a dual spiral coil.

### Torsional stiffness

Consequently, torsional stiffness for a torsional system is a factor dependant on the applied torque and angular deformation. Having an assumption of uniform twist of a shaft segment of length ($L$) with overall angular deformation ($\theta$), a general formula of the torsional stiffness of a rectangular bar can be expressed by the equations [137]:

$$K_t = \frac{T}{\theta} = \frac{KG}{L} \tag{3.43}$$

where $K$ is the torsional constant as explained earlier, $L$ is the length of the supporting shaft, $G$ is the shear modulus and is dependant on the Poisson's Ratio ($\nu$) and Young's modulus ($E$) of the substrate material.

$$G = \frac{E}{2(1+\nu)} \tag{3.44}$$

The dimensions of the shaft determine the stiffness of the shaft. The stiffer the shaft, the higher the natural frequency of the device produced and the expected sensitivity to mass added. However, if the stiffness is too great, the resonant frequency will be too high to drive it with the available resources. From design and manufacturing aspects, the cross-sectional area of the shaft will be kept constant, i.e. the width of the shaft, since the thickness is defined by that of the silicon nitride membrane from where the micro paddle is milled. The length and the position of the support along the length of the paddle, therefore become the key design factors.

### 3.3.3 Electromagnetic Driving System

The initial experimental investigation of the interaction between coils carrying electric current was started by Ampere in years of 1820-5. His work was later continued by Oersted, Biot, and Savart. It was also found that if a coil carrying a current is placed close to a magnet, it will be effected by a force [138]. Thus, both magnet and a coil carrying a current are said to generate a magnetic induction $B$, which applies forces on other coils or magnets. $B$ is a vector quantity, which has magnitude and direction. This is equivalent to the lines of electric force that are in an electric field. The strength of $B$ is represented by making the number of lines per unit area normal to $B$ numerically equal to the magnitude of $B$. Electromagnetic

driving system provides the driving torque, which is denoted as $T_0$ in equation 3.33.

The force exerted on an element of a wire *ds* carrying a current *I* at a location where the magnetic induction is *B* can be expressed in a simple equation.

$$dF = I(\vec{ds} \times \vec{B}) \tag{3.45}$$

Figure 3.16, shows the direction of the force, *dF*, acting on section of a wire, *ds*, carrying a current in presence of the magnetic field, *B*.

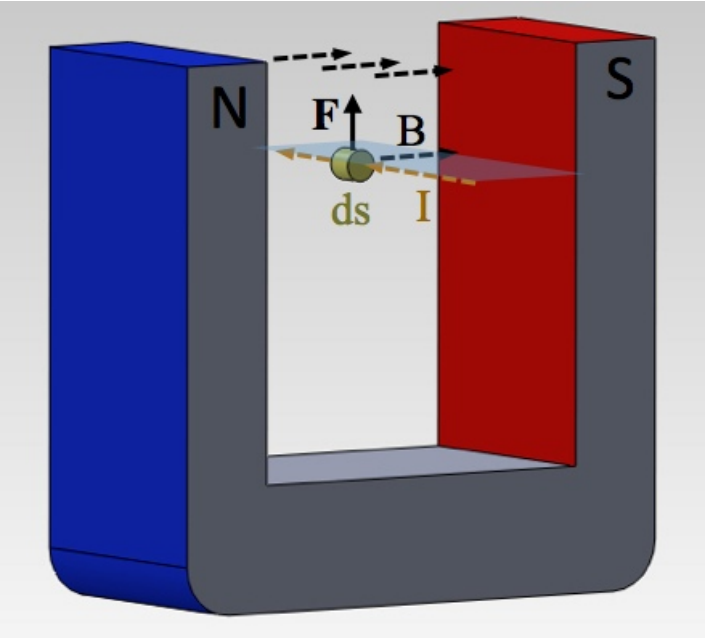


FIGURE 3.16: Electromagnetic force acting on a wire in presence of magnetic field.

Therefore, the unit of magnetic induction is the amount of induction, which exerts unit force on unit length of a wire carrying one unit of current (newtons (ampere metre)$^{-1}$). However, the most common unit used for magnetic induction is (weber/meter$^2$). It is also known that if a charge moves with velocity *v*, the term with *I*, and *ds* can be shown as:

$$I \cdot ds = \frac{dq}{dt} \cdot v(dt) = dq(v) \tag{3.46}$$

Therefore, the produced force can be expressed as:

$$dF = dq(\vec{v} \times \vec{B}) \tag{3.47}$$

This relationship is known as Lorentz force, which describes the force acting on a moving charge in presence of an electromagnetic field. The direction of the force generated is according to the right-hand rule. In Figure 3.16, the force generated pushes the wire upwards. So, when the direction of the current changes within the coil, the direction of the electromagnetic force shown in the Figure will be downward. Therefore, if the current passing through the wire will be an alternating current (AC) it can vibrate the wire in its place.

In the proposed design of the TPM, the same concept is implemented. A schematic of the design concept is presented in Figure 3.6. When the part of the coil, which is perpendicular to the direction of the magnetic field, carries a current, a force will be generated in the out of plane direction. Since, the coil is attached to the TPM, the paddle starts to move as the coil exerts force. In this design a connection is made from the hole in the middle of the paddle, which connects the top and button coil to each other. The symmetry of the coil pattern is in such that it will not change the current direction from the top to the bottom coil. Thus for this dual coil configuration, the force will be doubled for the same input condition.

## 3.4 Analytical Study of TPM Design

Analytical techniques were used to study the mechanical and electrical behaviours of the proposed TPM design. The effects of varying different design parameters on the performance of the TPM was evaluated. The calculations were based on the theories described in the previous section.

### 3.4.1 Natural Frequency

Equations of motion for the TPM were given in section 3.3.2 and a summary is given in Table 3.2.

TABLE 3.2: Summary of the equations used to obtain natural frequency of the designed TPM.

| Equation | Description |
|---|---|
| $f_n = \frac{1}{2\pi}\sqrt{\frac{2K_t}{J'_p}}$ | Free-Undamped Natural Frequency of TPM |
| $T = \int_A \tau dA \cdot r$ | Torque |
| $\tau = G\gamma = Gr\frac{d\theta}{dl}$ | Shear stress |
| $K_t = \frac{T}{\theta} = \frac{KG}{L}$ | Torsional spring stiffness |
| $K = \frac{b^3 a}{3}\left[\frac{16}{3} - 3.36\frac{b}{a}\left(1 - \frac{b^4}{12a^4}\right)\right]$ | Torsional parameter ($a$ and $b$ are half the width and thickness) |
| $J'_p = \frac{m_p}{48}(7L_p^2 + 4t^2)$ | Polar mass moment of inertia |

By substituting design parameters as given in section 3.3.1 into the relevant equations,

the natural frequency of the system was calculated to be 1.61 MHz for the paddle without a conductive track. The figure 3.15 illustrates three different designs of the conductive track integrated with micro paddle as well as plain micro paddle resonator. Equation 3.42 is representation of the mass moment of inertia associated with figure 3.15 (a). In figure 3.15 (b) and (c) conductive track has a 300 by 300 $nm^2$ cross section area. However, torque produced in figure 3.15 (c) is about twice the amount of the one in figure 3.15 (b). This is because there are two loops in figure 3.15 (c) and the length perpendicular to the magnetic field is about twice greater in the larger free end of the TPM. Therefore, when different mass moment of inertia is considered, the natural frequency will drop to 1.433, 1.289 and 1.33 MHz for figure 3.15 (b), (c) and (d) respectively. It is important to take into account that these values are based on pure theoretical approach and considering zero damping. Additionally, the material properties were used for this calculation is extracted from the literature and it is possible to have variations in every production batch.

### 3.4.2 Effect of Geometrical Parameters

As the key factors influencing the natural frequency of the TPM was mentioned in section 3.3.2. Here, variation of these factors are presented in different diagrams. Different geometrical features of the proposed TPM on its natural frequency are depicted in Figures 3.17, 3.18, 3.19.

Where the highlighted point on the curves show the value considered for the design of TPM. The effects of the locations of the paddle support beams, support beam length and support beam width on device performance in terms of its natural frequency of vibration are shown in Figures 3.17, 3.18, and 3.19 respectively. It is shown that the width of the

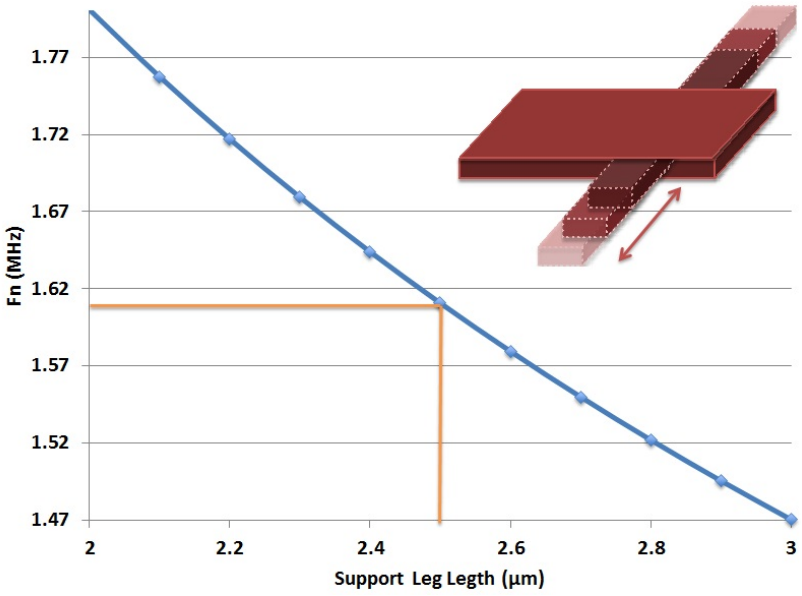


FIGURE 3.17: Natural frequency change due to variation in length of the supporting legs.

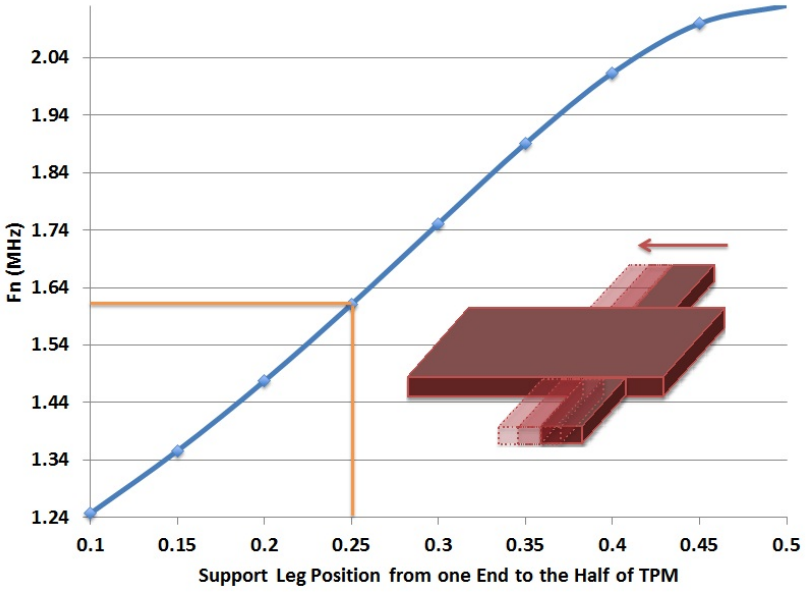


FIGURE 3.18: Natural frequency change due to variation in location of the supporting legs on the side of the paddle.

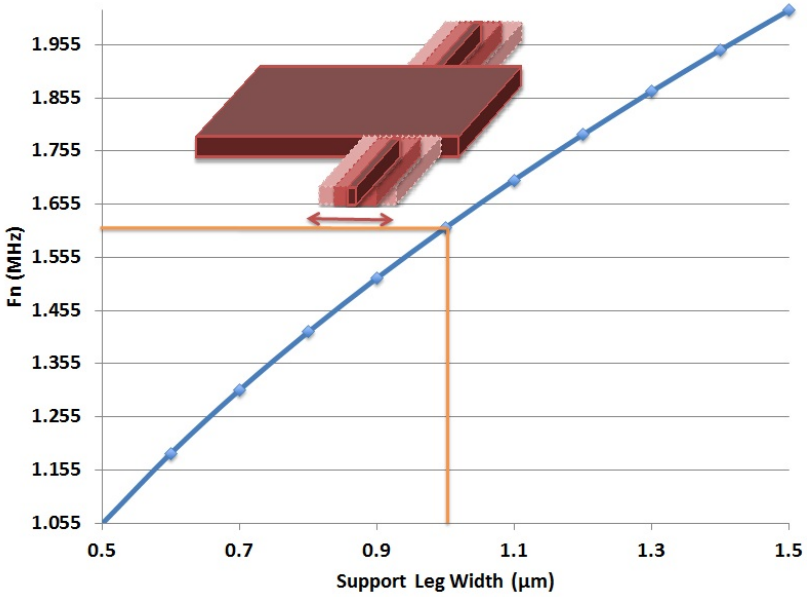


FIGURE 3.19: Natural frequency change due to variation in width of the supporting legs.

supporting legs have the maximum effect on the variation of the natural frequency. The least effect is due to the variation of the support length. Standard LPCVD silicon nitride (stochiometric) properties was used for this calculation[1].

In addition, as it was shown in section 3.4.1, the addition of conductive track can also influence the natural frequency of the TPM. The greater mass and dimension of the track results in lower natural frequency.

### 3.4.3 Self-inductance

In order to calculate self inductance, magnetic flux produced by the coil in presence of current has to be determined. In this design, rectangular spiral has been used and the formula for calculation of the total magnetic flux has been extracted from:

[1]http://www.mit.edu/ 6.777/matprops/lpcvd_sin2.htm

$$\phi_{zi} = \frac{\mu_0 I}{2\pi}\left[-\frac{b}{r+a} + \frac{b}{r-a} - \frac{a}{r+b} + \frac{a}{r-b}\right] \tag{3.48}$$

The formula was developed by M. Misakina [139]. The Equation 3.48 is a simplified form, in which the magnetic flux in the centre of the rectangular loop is calculated. For this study, there are 13 loops and this formula has been used separately for all 13 loops. The terms are described in the Table 3.3,

TABLE 3.3: Parameters used to calculate magnetic flux of a rectangular loop

| **Denoted sign** | **Description** |
|---|---|
| $\mu_0$ | Magnetic constant or magnetic permeability of vacuum |
| I | Current passing through the rectangular loop |
| a | Half width of the loop |
| b | Half length of the loop |
| r | Length of the hypotenuse that a and b make |

Figure 3.20 depicts the schematic of a rectangular loop with its dimensions.

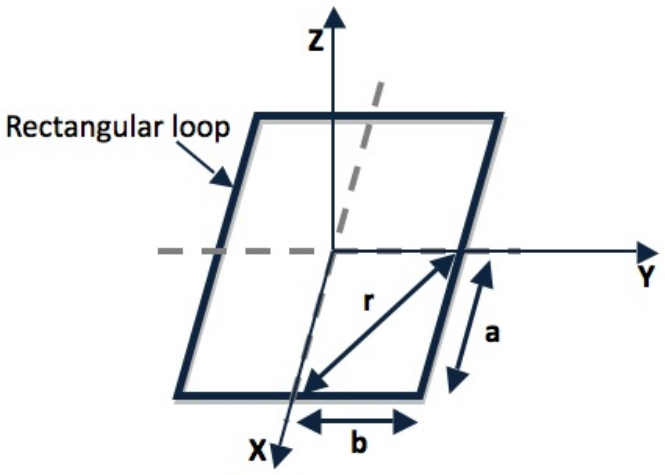


FIGURE 3.20: Geometry of a single rectangular loop of wire in X-Y plane.

The next step is to apply the formula for inductance and to substitute the magnetic flux in it as given below:

$$L = N\frac{d\varphi}{dI} = N\frac{\phi A}{I} \tag{3.49}$$

Where *N* is the number of loops, $\phi$ is the magnetic flux, *A* is the area of the loop and *I* is the current passing through the wire loop [140]. Every loop produces a certain amount of self induction (L). Since every loop is slightly different in size, to have a close precise answer each loop was considered separately and summation was made finally. The self inductance for this particular design was calculated to be $1.965^{-10}$ H. This value includes the inductance produced by both upper and lower coil.

### 3.4.4 Mechanical and Electrical Characteristics

In order to calculate the torque applied on the supporting legs, the force produced by the electromagnetic driving system needs to be calculated. Therefore, some electrical entities were calculated based on the formulas shown in Table 3.4 [138].

TABLE 3.4: Summary of the equations used to evaluate electromagnetic force acting the supports.

| Equation | Description |
|---|---|
| $\phi = \int B \cdot ds = Ba^2$ | Magnetic flux |
| $L = \frac{\phi}{I}$ | Induction |
| $F = I(l \times B)$ | Electromagnetic force |
| $T = F \cdot d$ | Torque |

In order to calculate the torque, it is assumed that a point load is acting on either sides of

the support legs on the micro paddle. The loads are considered to be applied on the centroid of two trapezoids. This is because the sections of the track which are perpendicular to the external in-plane magnetic field would exert the electromagnetic force on the paddle, form a trapezoid shape. Therefore, the centroid was calculated for these trapezoids. Figure 3.21 shows the location of the centroid of the trapezoid.

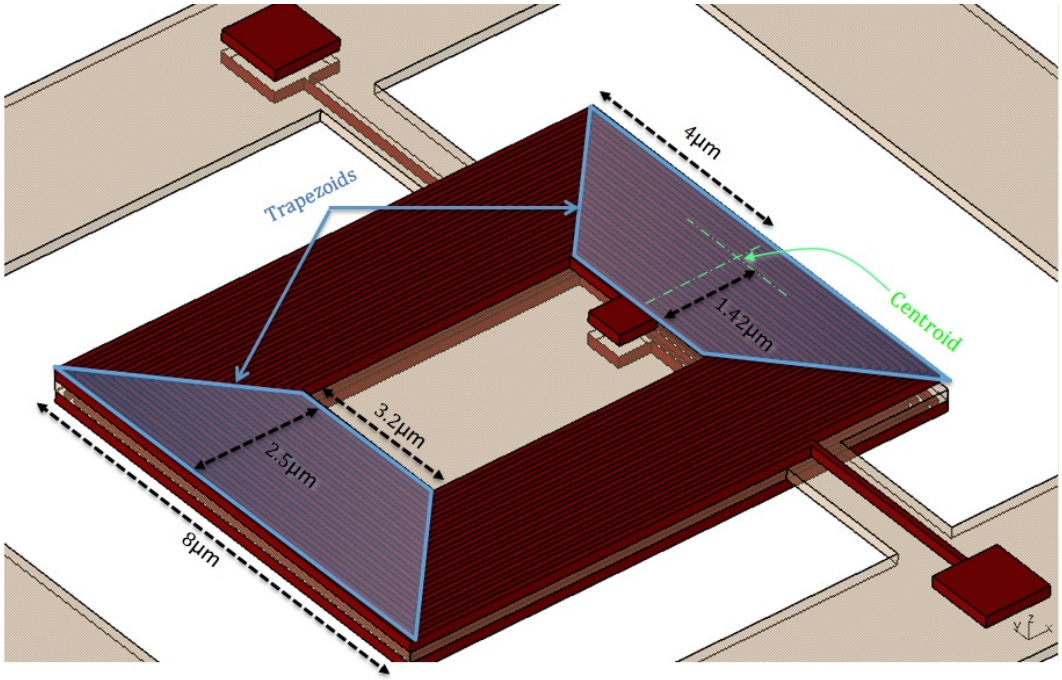


FIGURE 3.21: Location of the centroid in trapezoid.

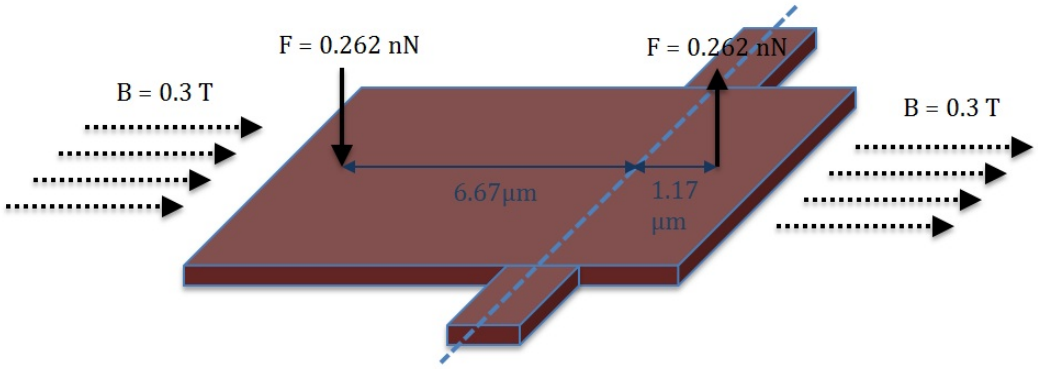


FIGURE 3.22: Point loads acting on the TPM integrated with dual planar spiral coil with the distance to the rotational axis.

Table 3.5 is the summary of the calculations. Here, the external in plane magnetic field was considered to be 0.3 Tesla. This is based on commercially available magnets specification in the market and the results collected from the simulation of the magnetic field explained later in section 3.5.4.

TABLE 3.5: Electrical and mechanical characteristics of the TPM.

| Sign | Description | Dual Coiled TPM | Dual Loop TPM | Single Track TPM | Unit |
|---|---|---|---|---|---|
| A | Cross section of the Pt track | 1E-14 | 9E-14 | 9E-14 | $m^2$ |
| f | Natural frequency | 1.33 | 1.28 | 1.43 | MHz |
| I | Current | 56 | 443 | 682 | $\mu$A |
| $\mu_0$ | Permeability of Vacuum | 12.5 | 12.5 | 12.5 | $\mu$ H/m |
| B | External magnetic field | 0.3 | 0.3 | 0.3 | Tesla |
| L | Induction | 1.965E-10 | 1.044E-10 | - | H |
| F | Force for each pair of trapezoids | 0.262 | 0.259 | 0.1296 | nN |
| T | Overall torque | 2.055E-15 | 2.592E-15 | 0.972E-15 | N.m |
| X | Maximum deformation | 8.906 | 11.235 | 4.213 | nm |

Here, platinum is used for the purpose of conductive track material based on available resources. In this case, the resistivity of the platinum track is 10-20 $\mu\Omega$ m. [2]

[2]FEI xP DualBeam Workstation, xPDB Manual Set: PN25421-A

The considered value for the current passing through the conductive track is based on the maximum current density that platinum track deposited by a focused ion beam system can tolerate. This value was experimentally obtained in different works and is shown to be maximum of 65 kA/cm$^2$ [141, 142].

Figure 3.22 shows how the point electromagnetic loads act on the paddle.

## 3.5 Finite Element Analysis

Finite Element (FE) Method is a numerical technique used to solve engineering problems. This method finds approximate solutions to partial differential equations (PDE) as well as integral equations. Recently, this technique has been used in many industrial fields, such as civil, mechanics, electronics, biomedical and aerospace [143–149].

The finite element method consists of three different stages; the pre-processing phase, analysis phase and post-processing phase. In the pre-processing phase, the user generates the geometry, specifies the material properties and boundary conditions. The analysis phase is where all the process of solving takes place and is purely done by a computer. This stage takes some time depending on the complexity of the model and the physics that has been added. In the post-processing phase usually a graphical output of results can be displayed and it is sometimes possible to get visually impressive figures and pictures. This part of the software is also very interactive and the influence of different parameters can also be shown separately. Figure 3.23 describes how the finite element method works in three steps of pre-processing, analysing, and post-processing.

In order to study the behaviour of the designed TPM, FE analysis was conducted following a preliminary analysis of the design. Various aspects of the TPM characteristics were

explored using COMSOL Multiphysics FEA package as explained in the following sections.

### 3.5.1 Analysis of the Natural Frequency Response

One of the essential characteristics of a resonator is its vibrational behaviour. Therefore, it is important to study this to enhance the stability of the TPM. Here, natural frequency of the TPM is predicted using COMSOL Multiphysics 4.2 package. By applying analysis of eigen frequency, the resonance frequency of the TPM was estimated and up to four resonance modes were analysed. The theoretical principles relating to this have already been covered in section 3.3.2 and analytical results are presented in section 3.4.1.

#### Pre-processing phase

To start this study, the linear elastic solid mechanics module was chosen and an eigen frequency solver implemented. Since the geometry of the plane paddle is quite simple, the modelling section of the FEA package was used to create a three dimensional model. The geometry was produced by subtracting 6 rectangular boxes from the main block as shown in the Figure 3.24.

After creating the geometry of the paddle, material properties were specified. Since the substrate material is LPCVD silicon nitride (stoichiometric) membrane, its material properties were specified as given in Table 3.6.

TABLE 3.6: Properties of LPCVD Silicon Nitride Membrane (stoichiometric)

| **Property** | **Name** | **Value** | **Unit** |
|---|---|---|---|
| Density | rho | 3180 | $kg/m^3$ |
| Young's modulus | E | 103.56 | GPa |
| Poisson's ratio | nu | 0.27 | 1 |

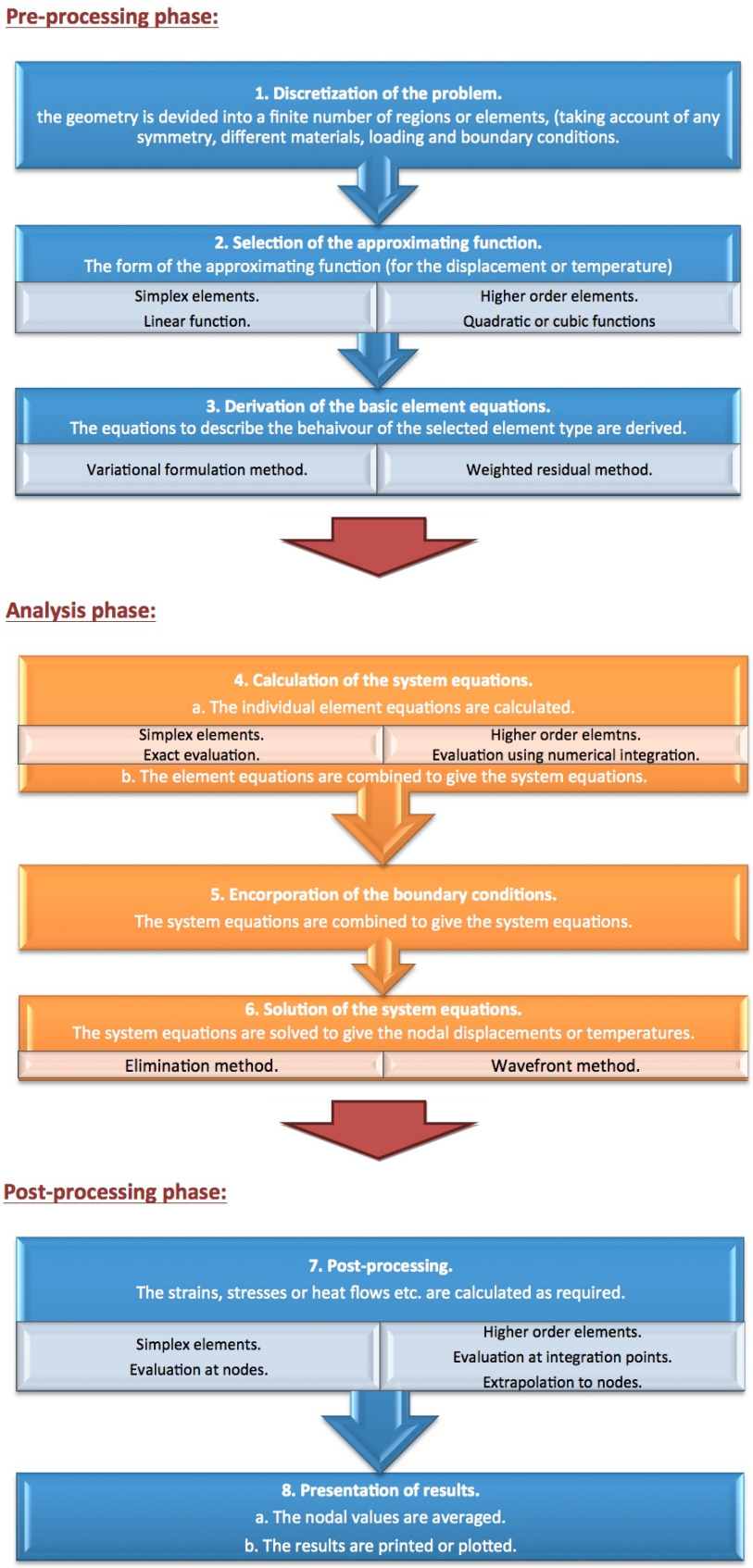


FIGURE 3.23: Structure of a Finite Element Analysis [150].

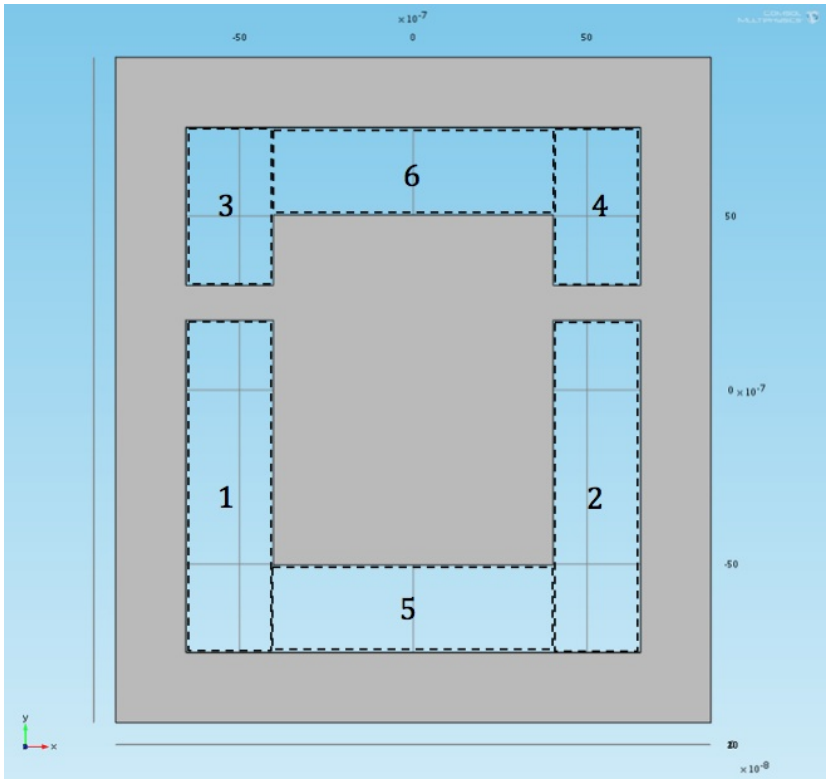


FIGURE 3.24: TPM model produced in COMSOL FEA package for frequency analysis.

In order to set boundary conditions for this model, fixed constraints were specified. This boundary condition was applied to all the exterior walls that are connected to the substrate. As shown in Figure 3.25, the blue area shows the fixed constraints.

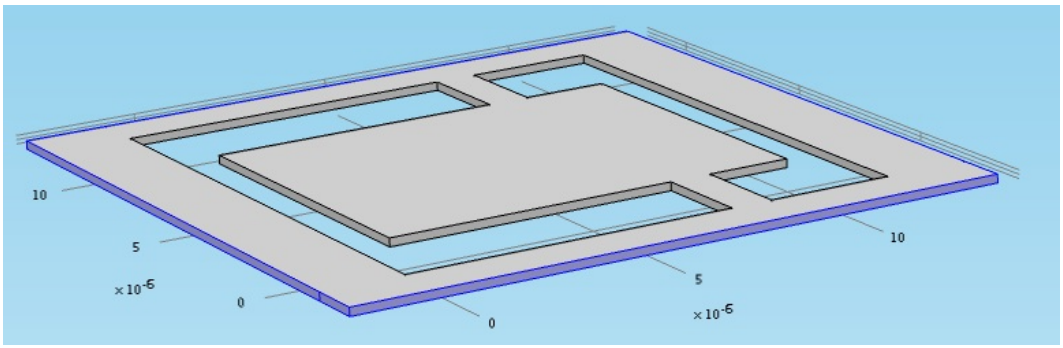

FIGURE 3.25: Selected exterior walls of the TPM to set for fixed constraint boundary condition in FEA package.

The model is divided into a number of elements or meshed. A free tetrahedral mesh was

selected from predefined drop down list for finer element size. After building the model, it was divided into 11142 elements. Figure 3.26 shows the meshed TPM.

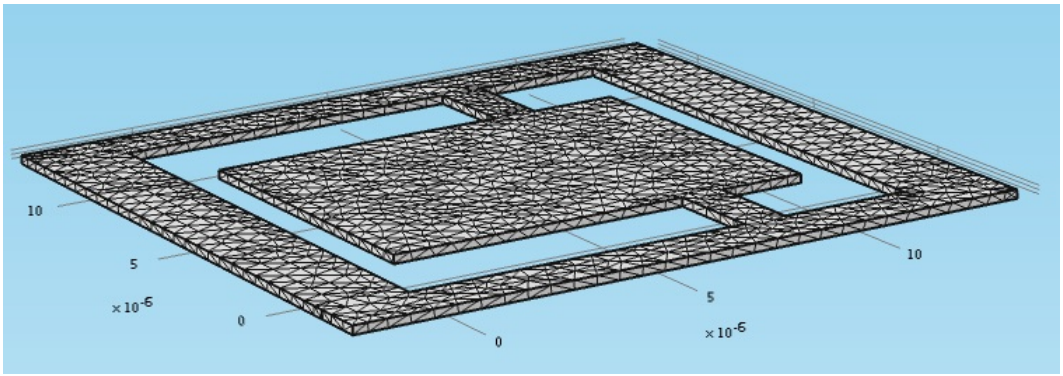


FIGURE 3.26: TPM after free tetrahedral meshing in COMSOL FEA package.

**Analysis phase**

In this stage the work is done by the computer. By selecting the solver which was previously defined in the start of the model, based on eigen frequency and vibrational analysis formulas the answer for all the mesh nodes can be calculated. The model is solved based on the defined physics. The results are then displayed in the post-processing section.

**Post-processing phase**

In COMSOL 4.2 FEA package, this section consists of 3D plots, 2D plots, 1D plots, and it is also possible to see the computed values such as average, maximum, minimum and integration of a line, surface or volume under derived values tree. According to the added physics, relevant answers can be seen in variety of formats in this section. In this Eingen frequency problem, the answers for first four resonant frequencies are shown in Table 3.7.

Figure 3.27 shows the mode shapes of the TPM in different resonant modes. The rainbow colour shows the maximum displacement in red and zero displacement in blue. Since no

TABLE 3.7: Eigen frequency results from COMSOL 4.2 FEA package for the designed TPM.

| Mode | Eigenfrequency (MHz) |
|---|---|
| 1 | 1.234314 |
| 2 | 3.764254 |
| 3 | 5.701995 |
| 4 | 12.2587 |

damping is considered for this model, maximum displacement is infinite.

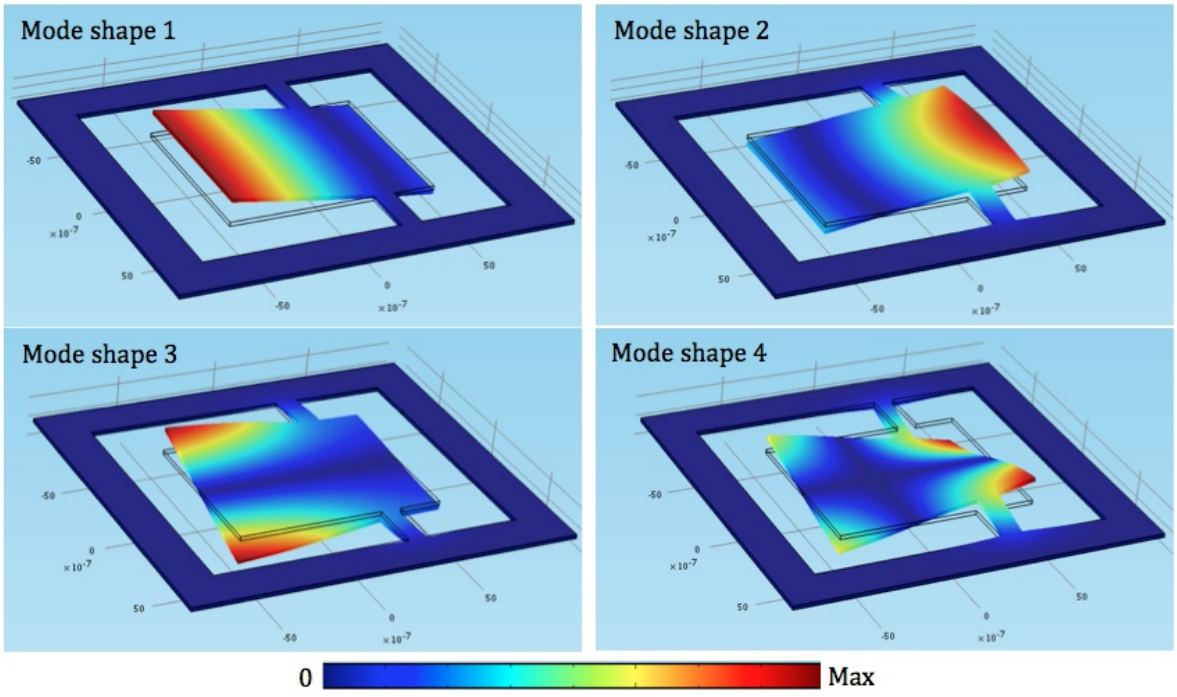


FIGURE 3.27: 3D deformation profiles in the first four resonant modes of the TPM.

Another parameter that has been looked at in this study is the Von Mises stress. As shown in Figure 3.28, Von Mises stress is maximum on the supporting anchors.

### 3.5.2 Analysis of the Inductance

Since one of the proposed driving systems consists of a two nano spiral coils, when current passes through the platinum track, it generates a self inductance. The purpose of this model

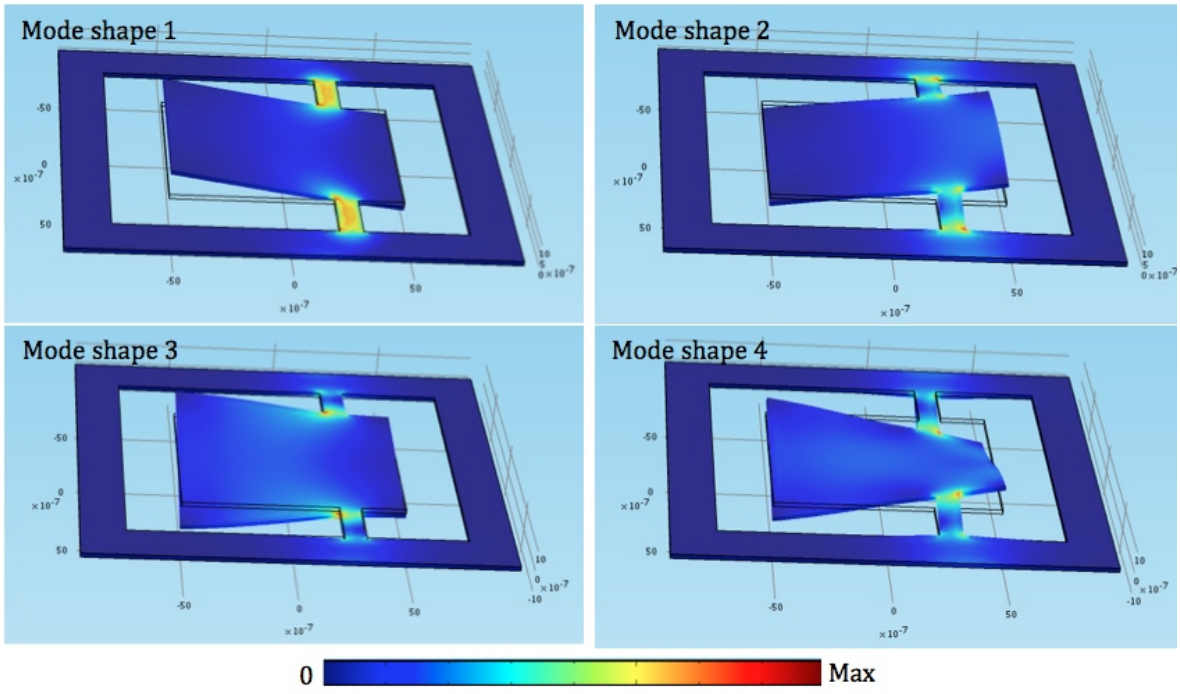


FIGURE 3.28: Von mises stress along the deformed TPM in the first four resonant modes of the TPM.

is to evaluate the self-inductance generated in TPM in this condition.

### Background knowledge

With a known magnetic field, it is possible to compute the self-inductance, $L$, from the relationship below:

$$L = \frac{2W_m}{I^2} \tag{3.50}$$

where $W_m$ is the magnetic energy and $I$ is the current. The input boundary condition is set to the current of 6 $\mu$A for the Terminal. In the analysis phase, the self-inductance $L$ becomes available as the $L_{11}$ component of the inductance matrix. The geometry of the model immersed in the air box is shown in Figure 3.29

The model uses the following equations:

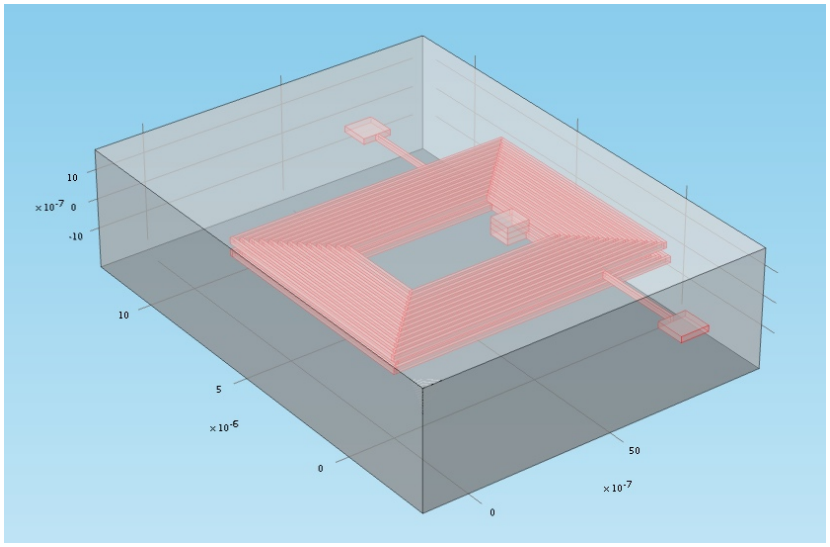


FIGURE 3.29: Geometry of the dual spiral coil model and the surrounding air box.

$$-\nabla \cdot (\sigma \nabla V - J^e) = 0 \tag{3.51}$$

$$\nabla \times (\frac{\nabla \times A}{\mu_0 \mu_1}) + \sigma \nabla V = J^e \tag{3.52}$$

where $\sigma$ is electrical conductivity, $A$ denotes the magnetic vector potential, $V$ is the electric scalar potential, $J^e$ indicates the externally generated current density vector, $\mu_0$ is the permittivity in vacuum, and $\mu_r$ is the relative permeability. The electrical conductivity in the coil is considered $10^6$ S/m and for air is set to 1 S/m. This small conductivity for air is required in order to avoid singularities in the computational process. The final relation is expressed as:

$$B = \mu_0 \mu_r H \tag{3.53}$$

where $H$ indicates the auxiliary magnetic field.

### Pre-processing phase

The model consists of the dual spiral-shape coil that is on either sides of the TPM and it is surrounded by the air box. However, in this model the paddle geometry is not included in order to avoid complications as shown in Figure 3.29. For this model three boundary conditions were considered. Every boundary condition corresponds to a different boundary group. Figure 3.30 shows the model and the type of boundary condition for all three groups.

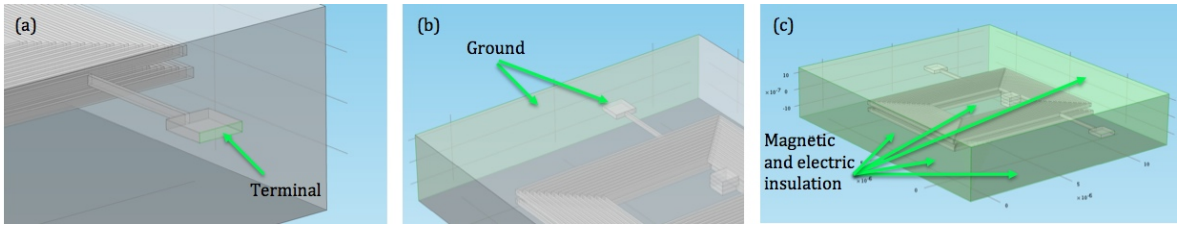


FIGURE 3.30: Boundaries of dual spiral coil model with the same type of boundary condition.

The boundary condition for the highlighted sections in Figure 3.30 (a) is the magnetic insulation bounadry with a terminal boundary condition. The boundaries in Figure 3.30 (b) are magnetically insulating but set to a constant 0 V potential. In Figure 3.30 (c) the remaining walls are magnetic and electric insulations.

### Analysis phase

Based on the Equations stated in section 3.5.2, stationary solver was used to evaluate the inductance matrix.

**Post-processing phase**

The simulated model is shown in Figure 3.31, in which, induced electrical potential and the magnetic flux lines are clearly displayed in the post processing section of the software. Difference in thickness of the stream line depicts the magnitude of the magnetic flux around the coil. As expected, the flux has been distributed symmetrically around the coil and largest flux is seen in the middle of the spiral coil. These signs indicate the successful simulation result since the number of elements also play an important role for convergence of the simulation process. In this particular model, the design is split to 141650 elements and minimum element quality is 0.2 which resulted in a process time of 6 hours. In the figure 3.31, the boundary of the wire shows the electric potential in the coil and how it changes from one end to the other. The stream line around the coil is the magnetic flux and the rainbow colour shows the potential of the magnetic flux. The thickness of the streamline illustrates the density of the flux. From this simulation, a self inductance of 1.5338E-10 H is determined, which is in a good agreement from the result obtained analytically.

### 3.5.3 Analysis of the Joule Heating Across the Conductive Track

**Background knowledge**

The effect of joule heating and temperature increase of the conductive track was investigated using COMSOL software package. This analysis allows an estimation of the limits that should be imposed to the input of the circuit, in order to prevent thermal damage to the device. As current passing through a conductor generates heat it is important to control the temperature increase. It has been reported that the melting point of an amorphous deposited platinum using a focused ion beam is around 580 - 650°C [151]. In addition, based on the

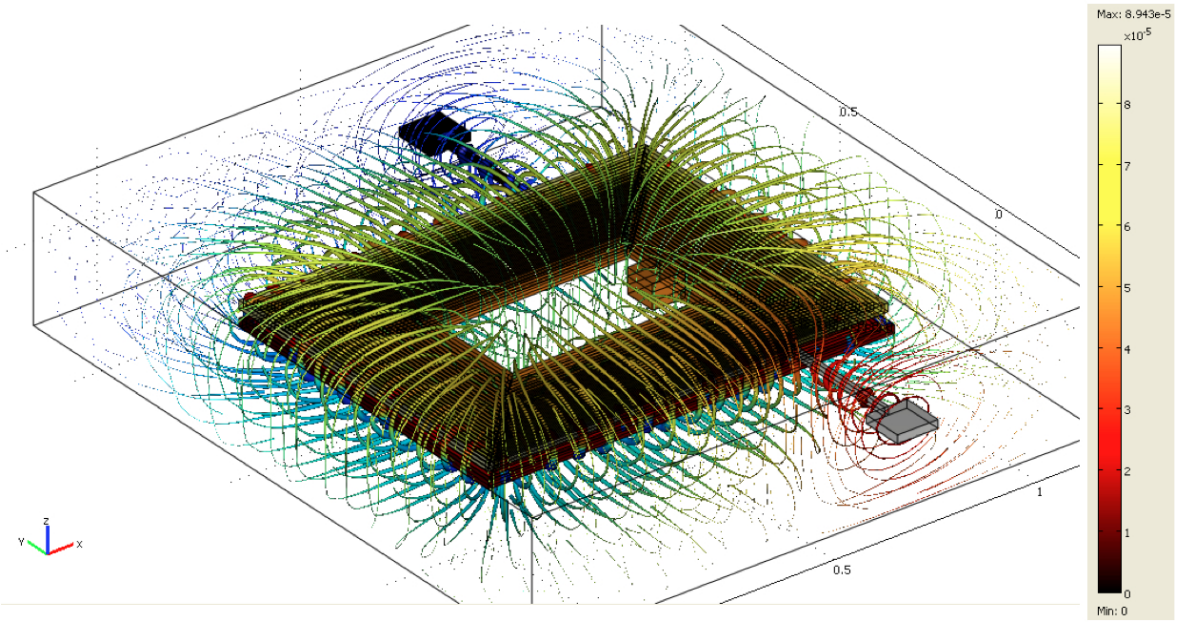


FIGURE 3.31: Electric potential in the wire and magnetic flux stream lines around the coil.

applied input current passing through the track, it is possible to obtain the voltage across the circuit.

**Pre-processing phase**

Here, the joule heating module from the electromagnetic heating physics settings was chosen. The model geometry was created within COMSOL. Next, material properties were assigned to the platinum track and silicon nitride substrate. The assigned properties of the Platinum in the simulation were chosen based on values presented in the literature for deposited platinum using focused ion beam technology [152–155]. As there is a wide variation in reported resistivity values, simulations were carried out using a range of properties in order to take into consideration these variations. This wide variation in reported values may be due to the presence of different elements and their ratios within the composition of such a conductor, which are key role in determining its properties.

Then the boundary conditions were applied as follows. One end of the track was chosen as an input terminal for the current and the other end was grounded. This generates a current distribution all over the platinum track. Since the device is within air, convective cooling was defined for the outer boundaries of the model. Here, a heat transfer coefficient of 5 ($W/m^2K$) was applied. Finally, the model was meshed.

### Analysis phase

In this section the solver associates all the inputs and boundary conditions and resolve the problem. In this analysis, stationary solver was selected.

### Post-processing phase

Based on the above mentioned input parameters and defined boundary conditions, the model was solved and the results are presented in the Figures 3.32, 3.33 and 3.34 representing the surface temperature, electric potential and current density plots of the three different designs respectively.

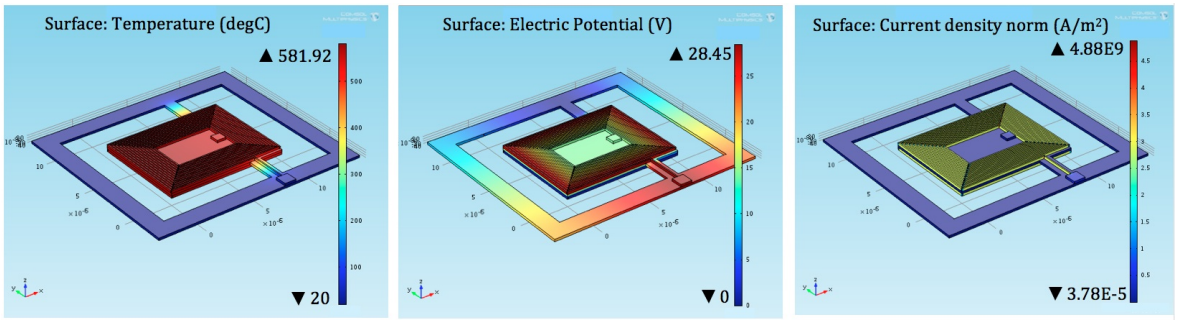


FIGURE 3.32: Joule Heating simulation diagrams of the TPM integrated with a Pt coil.

The value of applied current was chosen and set such that the predicted temperature increase did not exceed the melting point of the platinum track. In this analysis, based on

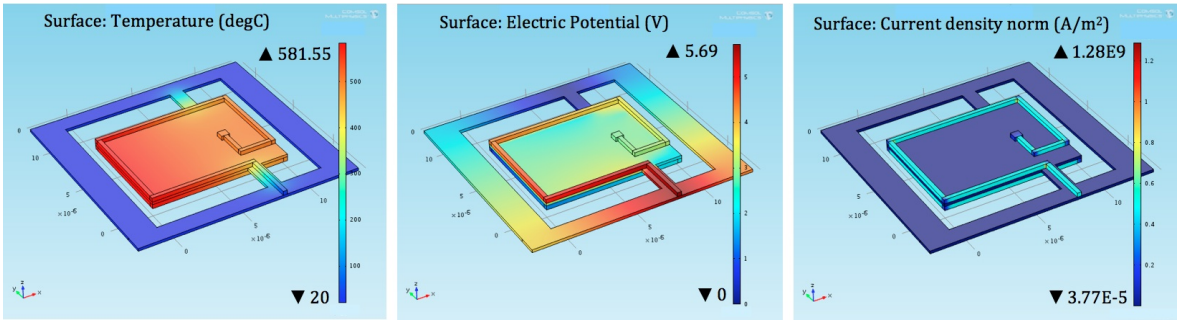


FIGURE 3.33: Joule Heating simulation diagrams of the TPM integrated with a Pt dual loop track.

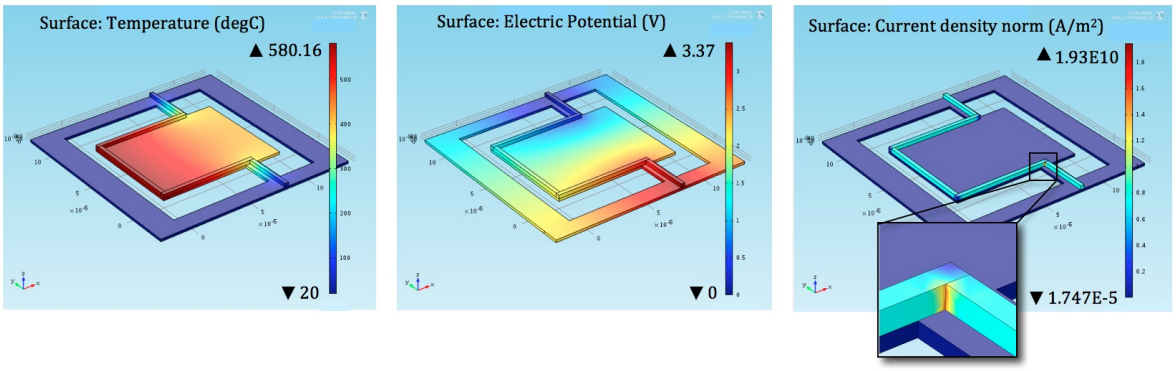


FIGURE 3.34: Joule Heating simulation diagrams of the TPM integrated with a Pt single track.

the literature, a temperature of 580°C was considered as the maximum critical temperature. Therefore, for the design shown in Figure 3.32, a current magnitude of 5.68E-5 (A) was applied as the terminal input. In designs presented in Figures 3.33 and 3.34, 4.43E-4 and 6.82E-4 (A) were applied as current inputs respectively. Thus, the force produced in each deign would vary according to the applied current. Designs presented in the Figures 3.32, 3.33, 3.34, produce forces of 2.48E-9 N, 2.13E-9 N, and 1.64E-9 N respectively.

As shown in Tables 3.8, 3.9 and 3.10 each of the presented designs was simulated using three different values of resistivity in order to assess the impact of variation in resistivity values.

TABLE 3.8: Collected results from simulating Joule Heat of the Platinum coil with three different resistivity.

| Resistivity | 5 | 15 | 20 | Ω $\mu$m |
|---|---|---|---|---|
| Max. Temp | 580.04 | 581.92 | 579.77 | °C |
| Voltage | 16.4 | 28.45 | 32.78 | V |
| Current | 9.85E-5 | 5.68E-5 | 4.91E-5 | A |
| Current Density | 5.00E9 | 2.75E9 | 2.50E9 | A/m$^2$ |

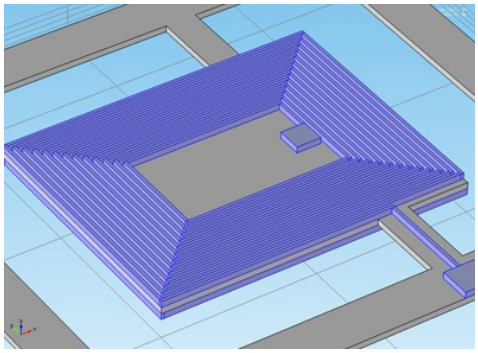

TABLE 3.9: Collected results from simulating Joule Heat of the Platinum dual track with three different resistivity.

| Resistivity | 5 | 15 | 20 | Ω $\mu$m |
|---|---|---|---|---|
| Max. Temp | 579.65 | 581.55 | 579.65 | °C |
| Voltage | 3.28 | 5.7 | 6.56 | V |
| Current | 7.66E-4 | 4.43E-4 | 3.83E-4 | A |
| Current Density | 2.21E10 | 1.28E10 | 1.10E10 | A/m$^2$ |

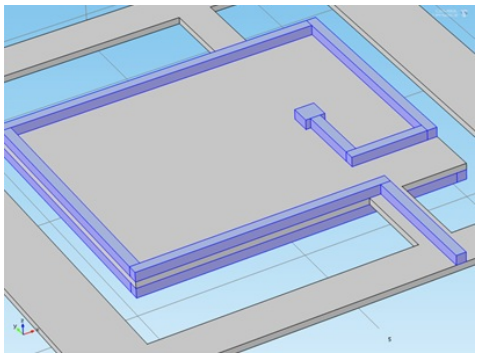

TABLE 3.10: Collected results from simulating Joule Heat of the Platinum single track with three different resistivity.

| Resistivity | 5 | 15 | 20 | Ω $\mu$m |
|---|---|---|---|---|
| Max. Temp | 577.07 | 580.16 | 580.86 | °C |
| Voltage | 1.94 | 3.3 | 3.9 | V |
| Current | 1.18E-3 | 6.82E-4 | 5.91E-4 | A |
| Current Density | 1.25E10 | 7.00E9 | 6.00E9 | A/m$^2$ |

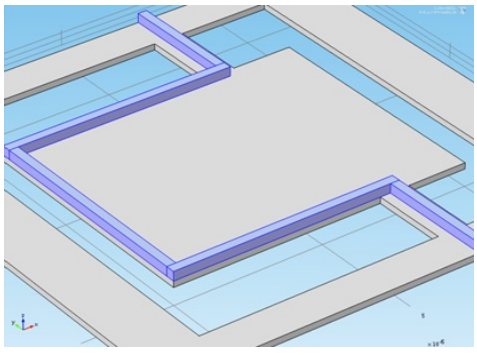

### 3.5.4 Analysis of the Magnetic Flux Around the Chip Carrier

#### Background knowledge

In this study it is important to know the magnetic flux within the plane of the membrane since the force produced to vibrate the micro paddle is dependant on the in plane magnetic flux passing across the membrane. The position of the magnets on the sides of the chip carrier, size and strength of the magnets are the parameters that have influence on the strength of magnetic flux. In addition, one of the concerns in the design assembly is the location of chip carrier legs. As it was described in section 3.3, the chip carrier is placed in between the magnets. Although, magnets are in minimum distance from the centre of the chip carrier in this configuration, the legs still might effect the magnetic flux across the chip carrier. Therefore, some models were designed to evaluate the magnetic flux across the chip carrier. This can help to measure the magnetic flux in the plane of the silicon nitride membrane along with the effect of the chip carrier legs on the strength of magnetic flux. As shown in Figure 3.35, due to the fact that the design is symmetrical, the model that was used for this analysis consists of half the original design. The same concept has been applied to the rest of the models.

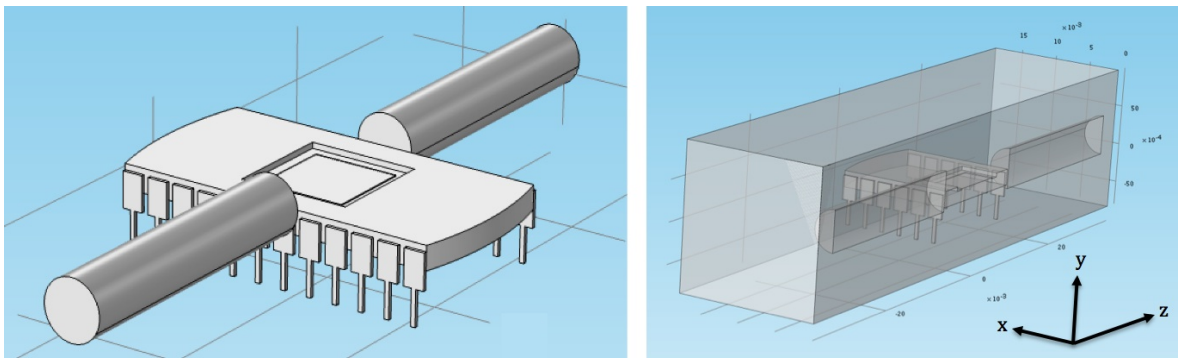


FIGURE 3.35: a) An actual 3D view of the geometry (consists of two cylindrical magnets and chip carrier). b) Modified geometry to be used by FEA package.

This imported geometry contains the chip carrier and two permanent magnets on its either sides. A rectangular box is the air volume around the geometry.

With assumption of a current free medium, where:

$$\nabla \times H = 0 \tag{3.54}$$

Scalar magnetic potential, $V_m$, can be then found from the relation:

$$H = -\nabla V_m \tag{3.55}$$

This is then equivalent to the electric potential for static electric fields. Now by applying relation between the magnetic flux density and magnetic field

$$B = \mu_0(H + M) \tag{3.56}$$

in combination with equation:

$$\nabla \cdot B = 0 \tag{3.57}$$

The equation for $V_m$ can be written as:

$$-\nabla \cdot (\mu_0 \nabla V_m - \mu_0 M_0) = 0 \tag{3.58}$$

Equation 3.58 is used in order to solve this model from AC/DC interface module.

According to the symmetry of the model, half of the whole model was considered for the simulation. The magnetic field is symmetric with respect to the *yz*-plane. This plane therefore serve as exterior boundaries to the geometry. In this plane the magnetic field is tangential to the boundary and can be defined by the Magnetic Insulation condition:

$$n \cdot (\mu_0 \nabla V_m - \mu_0 M_0) = n \cdot B = 0 \tag{3.59}$$

If the air box is large enough, the boundary condition applied on its remaining exterior boundaries has little influence on the field on the magnets surroundings. Despite the fact that an unlimited element domain would result in an ideal results, this model uses the magnetic

insulation condition for simplicity.

**Pre-processing phase**

In COMSOL 4.2, first a physics of "magnetic fields, no current" was chosen. As shown in the Figure 3.23, all the input data has to be given in the pre-processing phase. After importing the model geometry, different materials have to be assigned for each part in the geometry. Air properties was assigned for the surrounding rectangular box and ceramic properties was assigned for the centre of the chip carrier. Since, legs consist of a special nickel based alloy, *Alloy42*, a relative permeability, $\mu_r$, of 2500 assigned as a moderate value for this material. Cylindrical magnets are N42 NdFeB and their magnetic flux strength was measured by a Gaussmeter to be 0.5 Tesla. A relative permeability of 1.05 was found in the literature for this material [156]. Magnetic flux conservation was added to the physic of the simulation and magnet properties was set into the model in this section. A magnetization of 820 kA/m was set for the magnets in Z direction. This gives an average magnetic flux of 0.5 Tesla on each magnet pole. Next is to set a boundary condition for the symmetry wall as explained in section 3.5.4. In the final stage of this phase, a fine free tetrahedral mesh was used to split the geometry to 75663 small elements.

**Analysis phase**

A stationary solver was chosen for this analysis and calculations were done by the computer to solve for the equations described earlier.

### Post-processing phase

After solving the problem, results can be shown in this phase. Figures 3.36 and 3.37 show the magnetic flux on the plane of symmetry and on the the chip carrier plane. It is shown that the direction of the magnetic flux was changed around the legs and some irregularities were inspected.

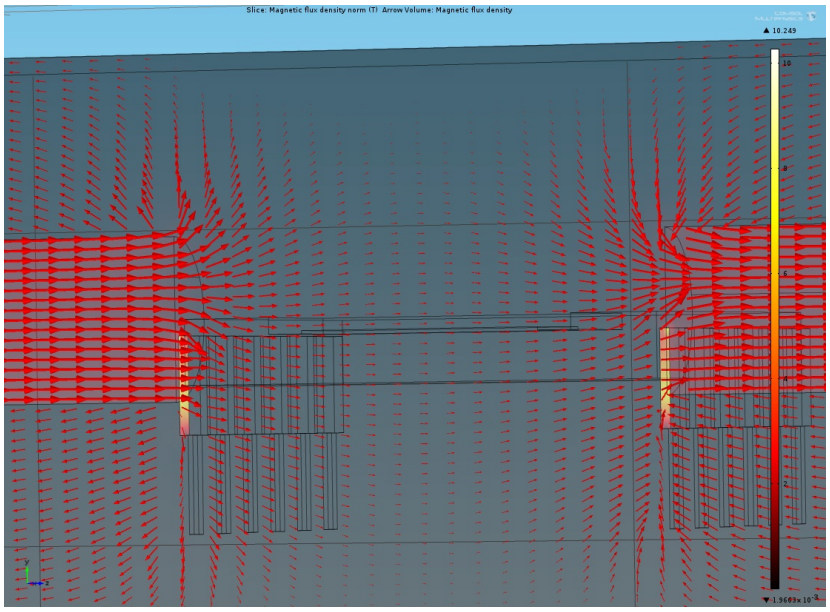


FIGURE 3.36: Magnetic flux density norm, T, in the symmetry plane (Arrow volume: Magnetic flux density)

Despite the fact that, the legs of the chip carrier consist of a ferromagnetic material, it was shown that the direction of the magnetic flux from the North pole of one magnet to the South pole of the other one is quite consistent and is in the expected direction. However, the strength of the flux has decreased to 0.026 Tesla in the middle of the chip carrier. However, without a ferromagnetic obstacle across the magnets, the magnetic flux would be 0.032 Tesla with 0.006 Tesla difference. Therefore, it was decided to remove some of the legs in order to reduce their effect on the magnetic flux strength. In addition to the considered configuration, some extra work was implemented to simulate the magnetic strength of the assembly with

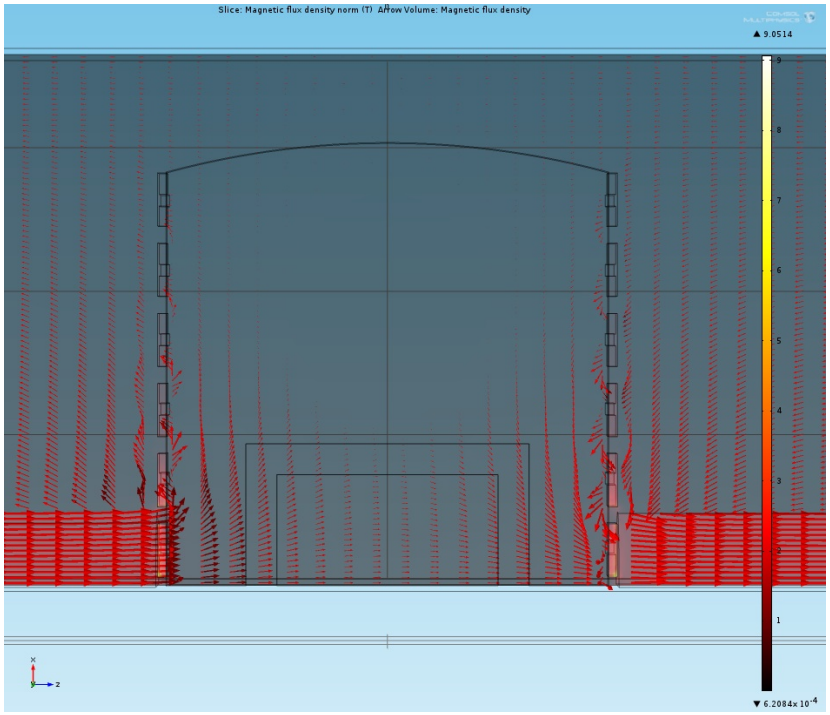


FIGURE 3.37: Magnetic flux density norm, T, in the chip carrier plane (Arrow volume: Magnetic flux density)

different magnets. The summary of the result is shown in Table 3.11

With reference to Table 3.11, it could be seen that the size and strength of the magnet could play a significant role on the magnetic flux across the two pole area. Among all 6 configurations, the maximum in plane magnetic flux was achieved by configuration 6, with 0.34 Tesla magnetic strength. However, the assembly of the configuration 6 would interfere with the mounting place of the chip carrier. Therefore, the side magnets were moved up slightly to provide a free space for the legs to be placed on the mounting switch. Again all the parameters were analysed for Configuration 7. This configuration still provides highest magnetic strength among all the other configurations. Additionally, to minimize the negative effect of chip carrier legs, in configuration 2-7, unnecessary legs were removed.

Furthermore, it is important to note that the magnetic strength is a quantity which is dependent on a variety of parameters such as mass and size of the magnet. In order to

TABLE 3.11: Summary of the simulations of magnetic flux density for different configurations on the assembly of the chip carrier, silicon nitride membrane and available choices of permanent magnets.

| No. | Assembly Configuration | Magnetic Flux Across Membrane | Magnet Strength | Magnet Dimension | Average Flux on the Magnet Pole Surface | In Plane Magnetic Flux (Centre of the Membrane) | Number of Mesh Elements |
|---|---|---|---|---|---|---|---|
| 1 | 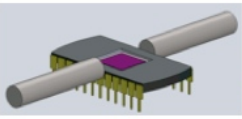 | 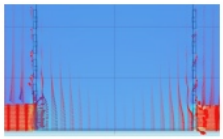 | 0.5 T | 5 mm Dia. x 25 mm | 0.05022 T | 0.0265 T | 75663 |
| 2 | 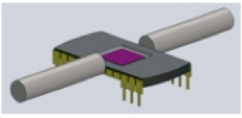 | 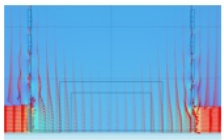 | 0.5 T | 5 mm Dia. x 25 mm | 0.506 T | 0.03175 T | 93956 |
| 3 | 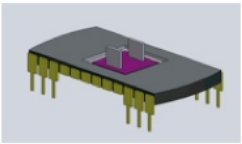 | 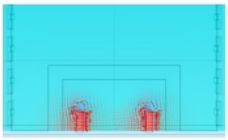 | 1.42 T | 3 x 3 x 0.5 $mm^3$ | 1.4106 T | 0.1975 T | 59832 |
| 4 | 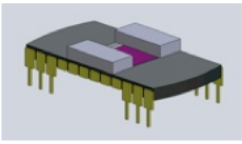 | 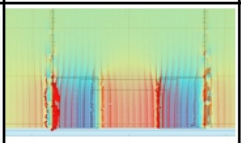 | 1.37 T | 10 x 4.5 x 2 $mm^3$ | 1.371 T | 0.25 T | 50639 |
| 5 | 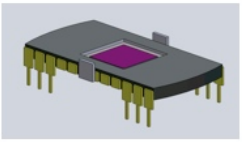 | 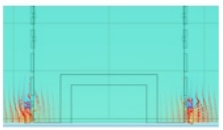 | 1.42 T | 3 x 3 x 0.5 $mm^3$ | 1.4213 T | 0.01177 T | 60790 |
| 6 | 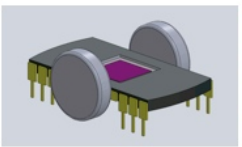 | 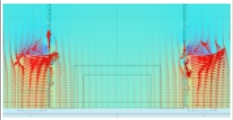 | 1.48 T | 12 mm Dia. x 3 mm | 1.473 T | 0.3487 T | 108621 |
| 7 | 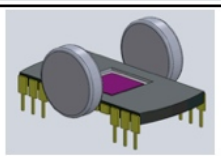 | 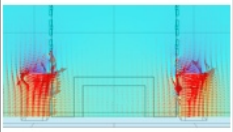 | 1.48 T | 12 mm Dia. x 3 mm | 1.4818 T | 0.3046 T | 103431 |

precisely evaluate a magnetic strength of a permanent magnet, magnetic induction, magnetic field strength, volume and the distance between the poles has to be taken into account. The largest magnetic strength will also change according to different materials, coatings and

surfaces. Based on the technical information provided by magnet producers [3] [4]. It has also been mentioned that the magnet strength is dependent on the object that is pulled towards the magnet. Therefore, based on the information provided for every magnet specification, for the simulation purpose, a magnetisation value was found based on a trial and error approach in order to have an average magnetic flux density equal to the stated magnet specification for the magnet poles.

### 3.5.5 Packaging of the device

In order to allow subsequent testing of the device, considerations to its assembly and packaging are made during the initial design stage. The membrane has to be placed on a chip carrier in the middle of an in-plane magnetic field. Based on available resources a cylindrical magnet with 5 mm diameter and 25 mm length was considered to provide an in plane magnetic field. Using such a permanent magnet, a proposed assembly of the device is shown in Figure 3.38.

In order to have maximum strength of the magnetic field around the membrane, the design is such that the location of the magnets is at the minimum possible distance from the membrane. However to hold the magnets in place, a lid was designed using the Solidworks package and fabricated using a 3D printer. As shown in Figure 3.39, the proposed final assembly of the chip carrier, silicon nitride membrane and lid are presented.

As shown in Figures 3.38 and 3.39, two identical magnets are proposed to be used on either sides of the chip carrier. This configuration assures a consistent in-plane magnetic field from one magnet to another across the silicon nitride membrane.

[3] www.neomagnete.com (Cited on 02/02/2012)
[4] www.first4magnets.com (Cited on 02/02/2012)

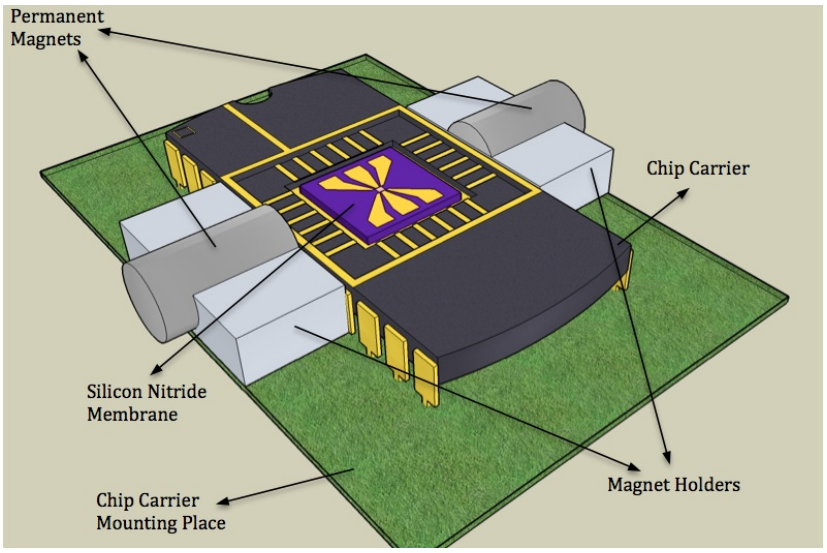


FIGURE 3.38: Position of the membrane on the chip carrier and location of magnets.

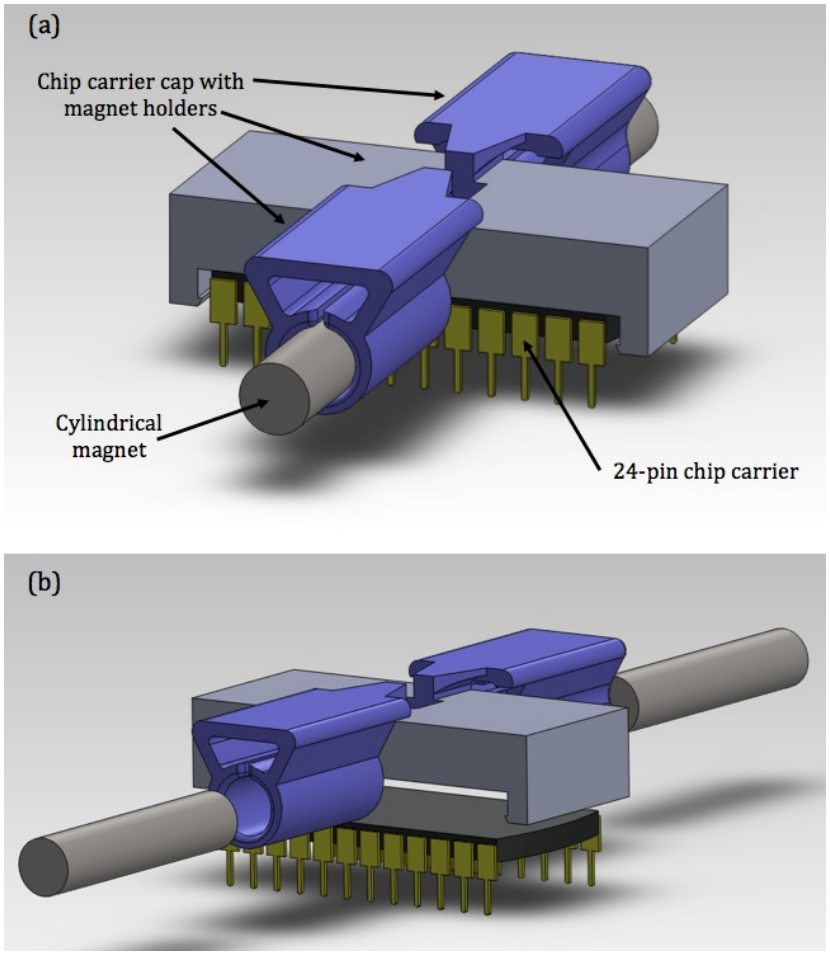


FIGURE 3.39: a) Assembly of the chip carrier, magnets and the cap, b) Exploded view of the assembly

### 3.5.6 Summary of The Design Parameters

Here the Table 3.12 presents a summary of the design parameters that have been considered in this chapter in order to develop the device according to these factors.

TABLE 3.12: Summary of the final design choices

| Parameter | Value | Reason |
|---|---|---|
| Length of Supports<br>Width of Supports | 2.5 $\mu$m<br>1 $\mu$m | Size of the supports are chosen based on the spring constant that is considered for the model to cause specific resonant frequency. In addition, it makes a balance between torsional resistance and the bend strength. So the deformation of the paddle would be proportional to the applied force. This prevents excessive load on the micro paddle and maintains the device from breakage. It also provides detectable amplitude of vibration. From machining point of view, it is in good machining tolerances, which helps machining repeatability. Figures 3.17, 3.18, and 3.19. show the effects of the sizes and widths of the supports. |
| Paddle plate length<br>Paddle plate width | 10 $\mu$m<br>8 $\mu$m | This is where the bonding between receptor layer and target molecules occurs. Therefore, it should be large enough to provide a good amount of detection so the mass of the molecules would amend the frequency. Long length causes the paddle to bend, which is undesirable and causes a different resonant mode shape. Short length would not provide enough space for the detection. Desirable size provides flat paddle to be moved in torsional direction from the axis of rotation. |
| Cross section of platinum track for dual coil design<br>Cross section of platinum track for single and dual loop design | 100 x 100 $nm^2$<br>300 x 300 $nm^2$ | Two different cross sections for current path was designed for three different configurations. One is to provide higher current path and another to provide maximum number of spiral turns. One produces maximum force in one line or two loops and the other provides a distribution of load within about 26 loops. 100 by 100 $nm^2$ cross section allows to have 13 loops on each side of the paddle, while still allowing reasonable amount of current passing through it. 300 by 300 $nm^2$ was chosen since this design was to have only two loop or track integrated with it. So it helps to have higher current density to put through the track. |
| Current | 56 $\mu$A<br>443 $\mu$A | To be in the safe side, two values were chosen. The lower value is considered for the wire with smaller cross section and the higher value is considered for large platinum cross section design. The values are chosen based on the heat generation simulation. It was shown that larger currents produce heat high enough to reach the melting point of the track. |
| Magnet (12 mm Dia. x 3 mm) | 1.48 Tesla | This magnet is chosen because of its superior magnetic field strength, which results in generating higher Lorentz force. In addition, other types of magnets with different sizes and strengths were simulated and details are gathered in Table 3.11. Here, the distance from the centre of the magnet pole to the location of the device on the membrane plays an important role in providing high magnetic field density. |

## 3.6 Complete System-Level Model

According to the models and calculations, the completed system-level model is shown in Figure 3.40. As it is shown, the obtained values are included in this Figure. It is shown that the expected resonant frequency is around 1.2 MHz, the vibration amplitude is between 4 to 11 nm, and the currents of 56 and 443 $\mu$A are set for the designed Lorentz force systems in order to be within the safe limit from the device melting point. In plane, horizontal magnetic field of 0.3 T is considered to be present across the device. These values, result in Lorentz force of around 0.2 nN and vibration amplitude about 4 - 11 nm.

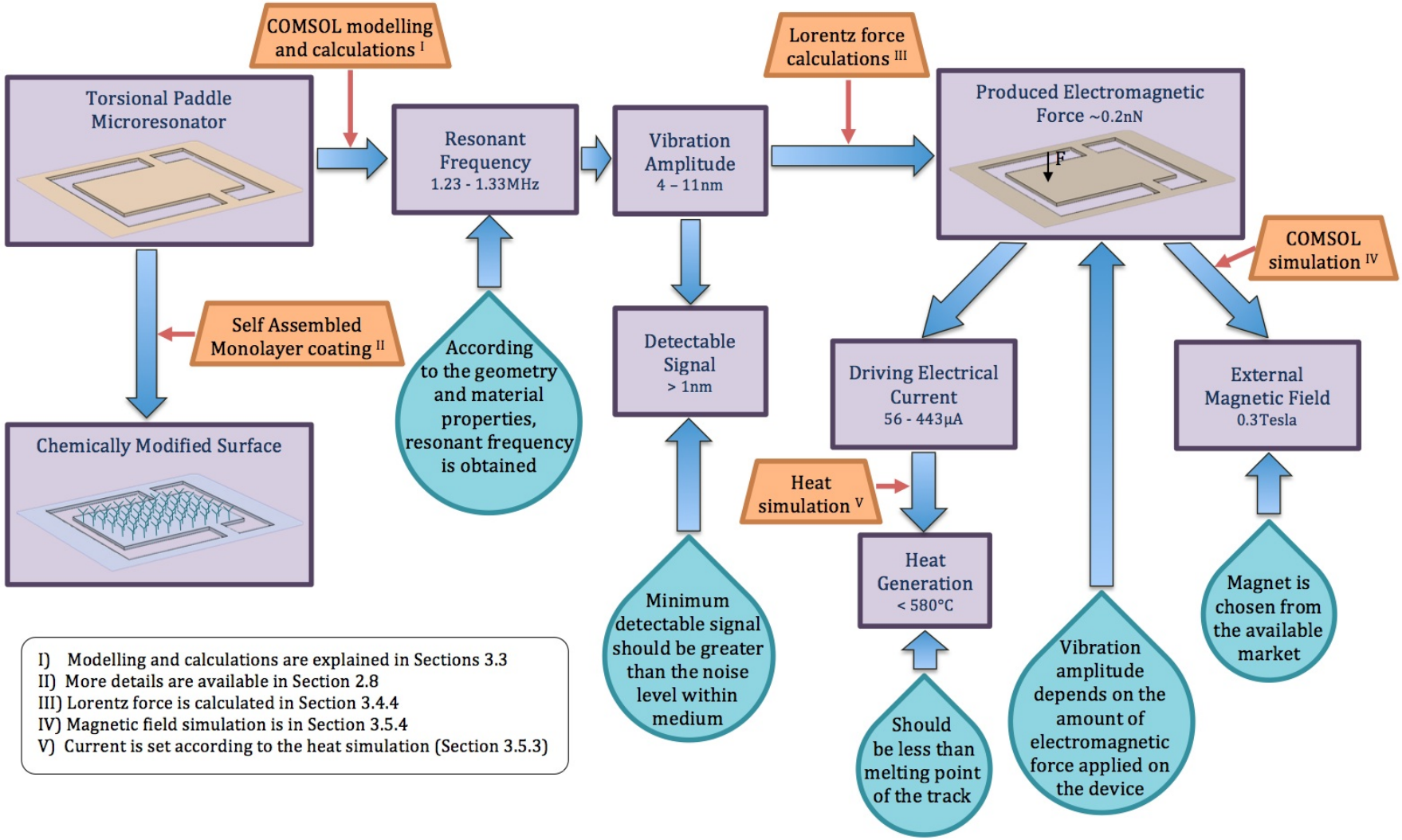


FIGURE 3.40: Complete System-Level Model of the designed tortional paddle microresonator device.

# 4

# Material and Fabrication

## Contents




**Summary** This chapter describes the substrate preparation and microfabrication processes used to fabricate the torsional paddle microresonator (TPM). An introduction to silicon nitride and silicon nitride membrane used in this study is given here. Mask fabrication, wire

pad deposition and focused ion beam (FIB) processing is explained in details in this chapter.

## 4.1 Material Properties

### 4.1.1 Silicon Nitride

Silicon nitride is a commonly used material in MEMS and microelectronics. Since, this material is electrically non-conductive, it is often used as an insulating layer. In addition, because of its good mechanical properties, the interest in its use as a structural material is growing in MEMS industry [157]. Reliability and performance of a micro device that is made from silicon nitride is very much dependant on its properties and this depends on how the silicon nitride is formed. Silicon nitride is usually made in a form of a thin film layer which is supported by a silicon substrate.

Thin films of silicon nitride are commonly deposited by the process of chemical vapour deposition (CVD). In this process, the reaction of gaseous species in the vicinity of a substrate material leads to deposition of a thin film on the surface of a substrate [158]. The three most common types of CVD process are low-pressure CVD (LPCVD), plasma enhanced CVD (PECVD) and atmospheric pressure CVD (APCVD).

The process of producing silicon nitride uses mainly two gases: Si-containing silane, (usually di-chlorosilane, $SiCl_2H_2$) and ammonia, $NH_3$ (Figure 4.1). The resulting film is formed in an amorphous phase [81]. For LPCVD silicon nitride, the processing temperature is about 570-900 °C [159, 160] and pressure below 1 Torr [161] . The chemical reaction of silane and ammonia gas to produce LPCVD silicon nitride results in an amorphous silicon nitride. In this reaction, hydrogen chloride and hydrogen gases are realised. This reaction is shown below [162]:

$$3SiCl_2H_2 + 4NH_3 \rightarrow Si_3N_4 + 6HCl + 6H_2 \tag{4.1}$$

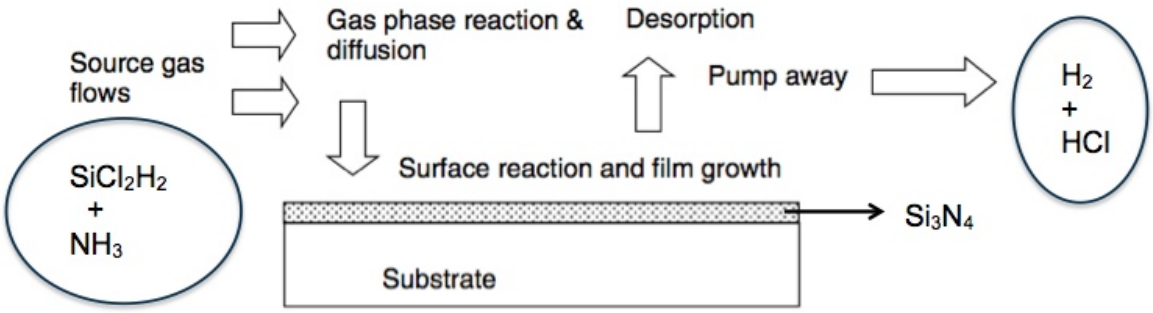


FIGURE 4.1: Chemical vapour deposition of silicon nitride (Adapted from [158]).

This reaction produces up to 8 atomic percentage hydrogen. The films usually have high tensile stress, ∼10 GPa, and therefore, films thicker than 200 nm may crack. The resistivity of silicon nitride at room temperature is about $10^{14}\Omega$m [162]. However, the properties of the reaction product is strongly dependant on deposition condition such as temperature, pressure and concentration of reactant gases. Thus, characteristics of every production batch varies.

Silicon nitride which is deposited by PECVD contains a higher quantity of hydrogen compared with LPCVD nitride and is nonstoichiometric [1]. The deposition temperatures used are between 250 °C and 350 °C [81].

Briefly, LPCVD is known as a technique commonly utilised at high temperature (>500 °) and PECVD is known as low temperature technique (<500 °). The film produced with these two techniques vary in several aspects such as thickness, uniformity, purity, density, electrical properties, and adhesion. Control of a PECVD process is rather more difficult and sensitive than LPCVD. In lower temperature process (PECVD) an extra energy source such as RF generator and light source is required to enhance the chemical reaction and the deposition rate is very low. Generally, LPCVD is known to have higher film quality compared with

[1] Change in the composition at the atomic scale where the products of a chemical reaction cannot be shown by a ratio of defined natural numbers.

PECVD [163].

The atomic structure of silicone nitride is shown in Figure 4.2. The figure shows how the organised arrangement of the atomic structure in melting condition turns into a random undesirable structure after quenching.

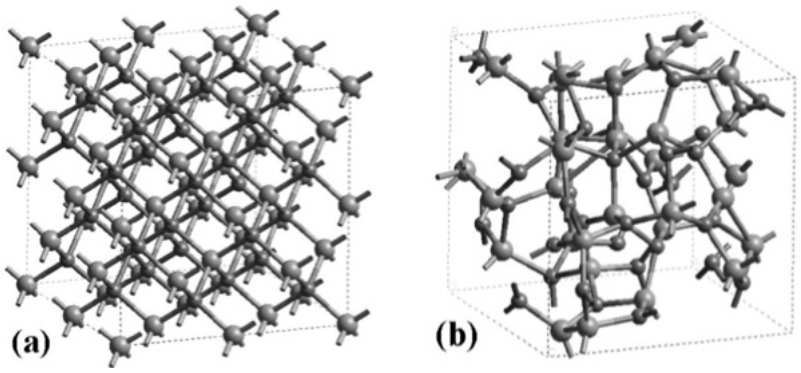


FIGURE 4.2: Atomic configuration of silicon nitride lattice. (a) Initial crystalline cell. (b) Final amorphous cell structure [164].

One of the requirements for fabrication of high performance microstructures and microdevices is substrates with low residual stress. Low pressure chemical vapour deposition (LPCVD) silicon nitride is known to be capable of meeting the required characteristics for MEMS devices.

The stress in thin films is very much dependent on deposited film structure and this is influenced by both, temperature and pressure. In different processing condition it is also possible to obtain films with compressive stress. Compressive stress would cause the micro machined pattern to buckle and tensile stress leaves cracks on the micro machined areas. However, a very low tensile stress is recommended.

One of the key properties is Young's modulus (E), this is a measure of material stiffness and is defined as a ratio of stress over strain. Different methods have been introduced in order to evaluate the Young's modulus of silicon nitride as shown in Table 4.1

TABLE 4.1: Formulas for determining Young's modulus, $E$, using different methods [157].

| **Method** | **Formula** |
|---|---|
| Static Beam | $\frac{PL^3}{\delta bh^3}$ |
| Resonant Beam | $\frac{ML^3\omega^2}{2bh^3}$ |
| Bulge Test | $\frac{p(1-\nu)a^4}{\delta^3 hc(\nu)}$ |
| Tensile Test | $\frac{P}{bh\varepsilon}$ |

where $h$, $b$ and $L$ are the thickness, width and the length of the sample; $P$ and $p$ are the applied force and pressure; $M$ is the effective mass; $\omega$ is the resonant frequency; $a$ is the dimension of the square membrane; $\delta$ and $\varepsilon$ are the measured deflection and strain, respectively. The function of the Poisson's ratio, $c(\nu)$, depends upon the geometry and is mostly approximated. Many researches have been conducted to evaluate properties of silicon nitride films. Some of the important material properties of silicon nitride are summarised from a variety of sources in Table 4.2.

TABLE 4.2: Summary of the Silicon Nitride Properties.

| Property | Value | Details | Reference |
|---|---|---|---|
| $\rho\ \left(\frac{kg}{m^3}\right)$ | 3100 | Sputtered film,thickness=0.29 $\mu$m | IEEE, Transactions on electron devices, (1978) [165] |
| | 3180 | LPCVD Silicon Nitride (stoichiometric) | H. O. Pierson, (1999) [166] |
| | 3000 | LPCVD Silicon Nitride (silicon-rich) | S. D. Senturia (2001) [16] |
| | 2900 - 3100 | stoichiometric LPCVD $Si_3N4$ film | S. M. Sze (2002) [162] |
| E (GPa) | 85 - 105 | Low stress LPCVD $Si_xN_y$ film | L. Kiesewetter et. al. (1992) [167] |
| | 104 - 156 | Sputtered film, thickness=0.29 $\mu$m | IEEE, Transactions on electron devices, (1978) [165] |
| | 130 - 146 | $\sim$0.3 $\mu$m thin film | Petersen and Guarnieri (1979) [168] |
| | 257 | Thin-film LPCVD silicon nitride | R. L. Edwards et. al. (2004) [169] |
| | 380 | Thin film, used in semiconductor fabrication | IEEE, MEMS Workshop (1990) [170] |
| | 230 - 265 | 0.2 - 0.3$\mu$m silicon nitride thin films | Schneider and Tucker (1996) [171] |
| | 270 | LPCVD Silicon Nitride (stoichiometric) | H. O. Pierson, (1999) [166] |
| | 210 | PECVD film grown on 0.2 $\mu$m LPCVD $Si_3N_4$ film | Sensors and actuators,20(1989), p.138 [172] |
| | 290 | LPCVD film, thickness = 0.2 $\mu$m (silicon-rich) | Sensors and actuators,20(1989), p.138 [172] |
| | 207 - 310 | bulk silicon nitride | W. Chuang et. al. (2004) [173] |
| | 290 | 0.5 $\mu$m LPCVD silicon nitride thin films | Tabata et. al. (1989) [174] |
| | 250 | - | M. Gad-el-Hak (2006) [157] |
| $\nu$ | 0.27 | LPCVD Silicon Nitride (stoichiometric) | H. O. Pierson, (1999) [166] |
| | 0.27 | LPCVD Silicon Nitride (silicon-rich) | S. D. Senturia (2001) [16] |
| | 0.23 | - | M. Gad-el-Hak (2006) [157] |

where $\rho$, $E$ and $\nu$ are density, Young's modulus and Poisson's ratio respectively.

## 4.2 Silicon Nitride Membrane

A variety of silicon nitride membrane windows are commercially available. As illustrated in Figure 4.3, they are usually square shaped and consist of a thin silicon nitride film within silicon supporting frames. These membrane windows are fabricated by LPCVD of silicon nitride onto a silicon substrate following which, a square shape section of silicon is etched using KOH [2] from the backside leaving a window of a thin silicon nitride film in the centre. A cross section of the silicon nitride membrane window is shown in Figure 4.4. The standard supporting frame sizes available are 5, 7.5 and 10 mm with thickness of 200 $\mu$m. The standard membrane sizes vary from 0.25 to 5.00 mm. The silicon nitride membrane can have different thickness ranging from 30 to 1000 nm.

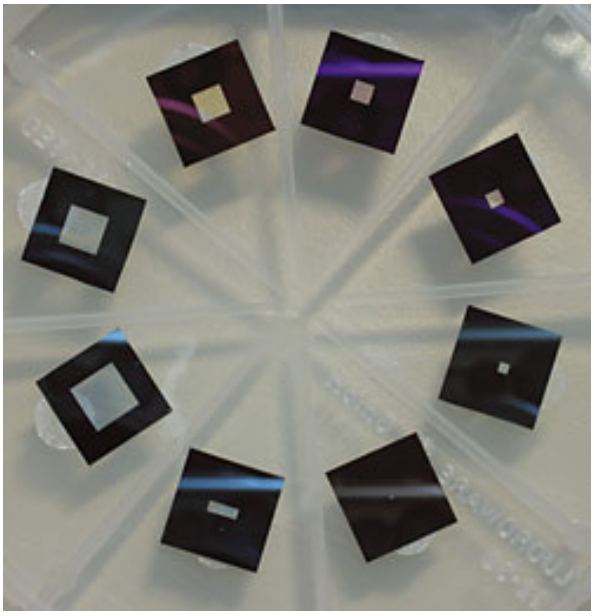

FIGURE 4.3: Standard silicon nitride membranes [1]

[2] Potassium hydroxide

[1] http://www.silson.com/index.html (Cited on 02/05/2012)

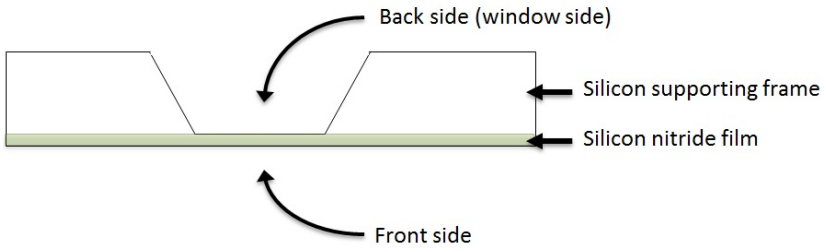


FIGURE 4.4: Cross sectional schematic of silicon nitride membrane window

For this project, membranes with frame size of 7.5 mm$^2$ and window size of 0.5 mm$^2$ are used. The silicon frame and film thickness are 200 $\mu$m and 200 nm respectively.

In order to use correct machining parameters during fabrication of a structure, knowledge of the sputtering yield is essential for accurate milling, as it determines the etch rate. Therefore, some experiments were carried out to determine the sputtering rate of silicon and silicon nitride membranes. As shown in Figure 4.5, a square area of 5 $\mu$m by 5 $\mu$m is etched using a focused ion beam milling system and acquired images were used to reconstruct a 3D image of the milled area. This technique is explained in detail in the Chapter 5.

Figure 4.5 (a) and (b) relate to a silicon substrate and removed volume has been calculated to be 7.26 $\mu$m$^3$. This is based on machining current of 50 pA with duration of 900 seconds. Using the sputter rate formula given in Equation 4.2 it has been shown the sputter rate is 0.16 $\mu$m$^3$/nC for this material.

$$R = \frac{\Delta V}{\Delta Q} = \frac{\Delta V}{It} \tag{4.2}$$

where, $V$ is the removed volume in $\mu$m$^3$ and $Q$ is the charge in nC. $Q$ is then equivalent to current ($I$) times time ($t$). The same method has been applied to a silicon nitride substrate with the same dimensions, machining parameter and duration (Figure 4.5 (c) and (d)) and led to 8.25 $\mu$m$^3$ material removal. Using the Equation 4.2 the sputter rate was found to be 0.183

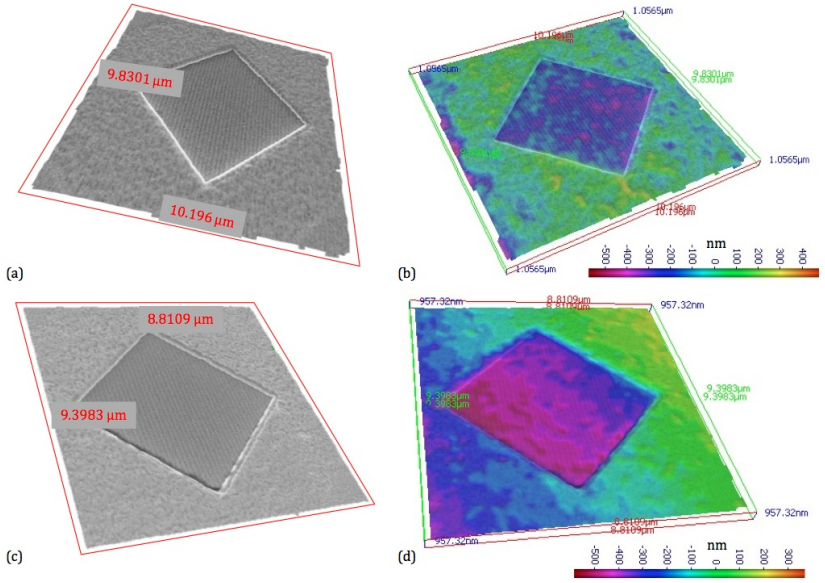


FIGURE 4.5: 3D reconstruction of the milled area for sputter rate analysis. (a) SEM 3D reconstructed image of milled silicon substrate, (b) colour coded image of the silicon milled area showing the depth of surface features, (c) SEM 3D reconstructed image of milled silicon nitride substrate, (d) colour coded image of the silicon nitride milled area showing the depth of surface features.

$\mu$m$^3$/nC. This value is in close agreement with the value of sputter rate of silicon nitride stated in the literature (0.2 $\mu$m$^3$/nC).

## 4.3 Sample Preparation

Prior to fabrication of the TPM, some considerations have to be taken into account based on the micromachining process and device packaging requirements. Due to the complexity of the TPM design and the required feature size, a very versatile micro machining equipment is required. Therefore, Focused Ion Beam (FIB) milling was used to fabricate the prototypes of the TPM. FIB gives flexibility to modify designs without writing new masks as well as having the capability to mill any material. The working principles and detailed descriptions of the FIB fabrication method are given in Section 4.4. The use of the FIB for fabrication necessitates a sample preparation step. The FIB micro machining process is designed based

on the bombardment of the substrate surface with positively charged Gallium ions. During the machining process, electrical charges accumulate over the localised machining area and if they cannot escape they will cause defects. As silicon nitride is an electrical insulator it is susceptible to localised accumulation of charges during the machining process. In order to avoid such defects due to charge accumulation or beam shifting (which is described in Section 4.4.4) the membrane has to be covered with a thin layer of conducting material and be grounded.

A second consideration is based on the principles of operation of the TPM device. As the driving system of the designed TPM is based on electromagnetic force, the sample requires an electrical input and output connection. Therefore two electrical connection pads are required for each TPM which can be patterned on the surface of silicon nitride frame through deposition of a conducting material via a stencil.

Based on the above mentioned requirements, in order to allow deposition of the conducting material on specific regions of the membrane, silicon based stencils were fabricated as described in the next section. The final sample after all the preparation steps is illustrated in the Figure 4.6.

FIGURE 4.6: Silicon Nitride sample after preparation steps mounted on sample holder.

### 4.3.1 Fabrication of Silicon Stencil

In order to deposit conducting material on selected regions of the membrane, two stencil designs were required:

1. Bond pad stencil: for creation of the electrical bond pads

2. Machining stencil: for coating the machining area with conducting material.

The stencils were fabricated using silicon wafer substrates. This section describes the design and fabrication of the silicon stencil masks.

#### Photolithographic Mask Design

Photomasks were designed as templates to optically transfer the desired stencil pattern to silicon substrate. The masks were designed using the computer aided design (CAD) software package, AutoCad, and were printed on polyester film sheets by a mask writer (JD Photo Tools). The mask layout is shown in Figure 4.7. As seen in the figure, a few designs were included on a single mask.

The white areas seen in the mask are optically transparent and allow light through them to expose photoresist. The columns C3, C6 and C9, provide the pattern for the connecting pads and C1, C4 and C7 deliver the pattern for a thin conductive layer required for machining process.

#### Photolithography

Photolithography is the process that uses optical techniques to transfer geometric patterns from a photomask into a photosensitive polymer (photoresist) layer. This pattern can subsequently be transferred into the substrate wafer by an etching process. For fabricating the

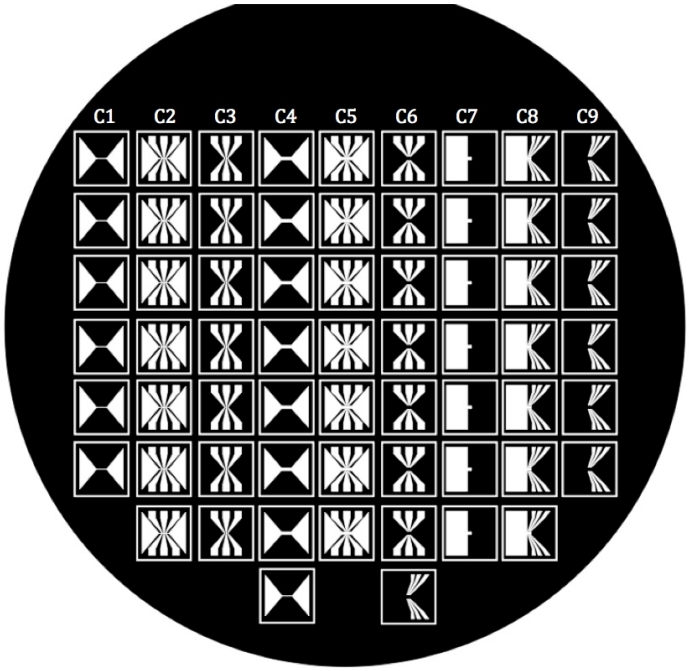


FIGURE 4.7: CAD design of the silicon mask for 100 mm diameter silicon wafer.

stencils, standard 525 $\mu$m thick 100 mm silicon wafer was used as a substrate. The main steps involved are given in the following sections and illustrated in Fig. 4.8 (steps 1 - 4).

A wafer cleaning process was carried out using organic solvents Acetone and Isopropyl Alcohol (IPA) to eliminate surface contaminants. The wafer was mounted in a spinner and sufficient Acetone was poured onto the surface. The spinning process was then initiated and IPA was dispensed onto the wafer. Spinning was continued until all the liquid evaporated from the surface. The wafer was then placed on a hotplate at a temperature of 110 °C for 50s to eliminate moisture that could adversely influence the adhesion of the resist to the wafer.

The cleaned wafer was then coated with a layer of positive photoresist, Shipley SPR-220 using a spin-coating process. This involved dispensing a small quantity of resist centrally on the wafer and carrying out a 3 step spin process (500 rpm, 10s; 2000 rpm, 30s; 500 rpm, 10s). This results in a photoresist thickness of approximately 7-8 $\mu$m [175]. The

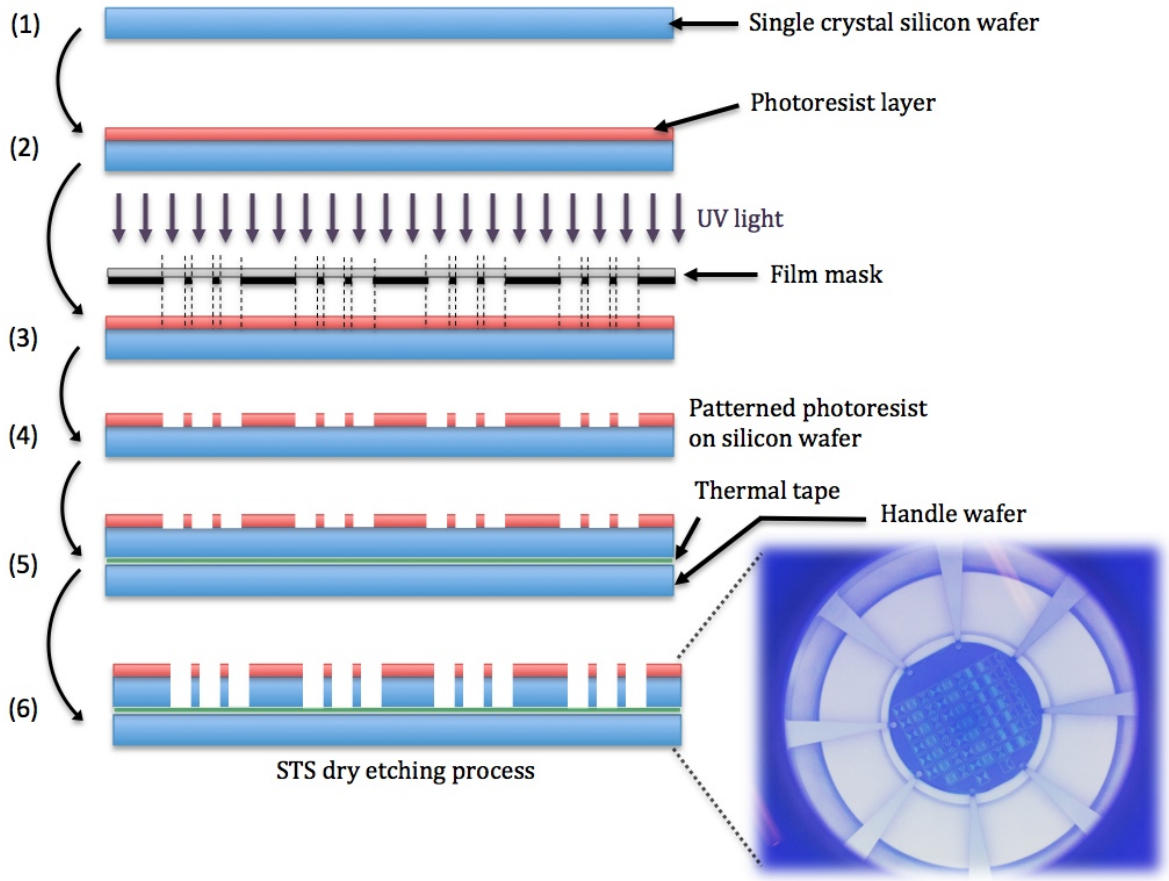


FIGURE 4.8: Process steps for fabrication of stencils

wafer was then soft baked on a hotplate at 115 °C for 90 s. Soft baking was carried out to decrease solvent levels in the photoresist and improve adhesion to the wafer. High solvent levels leave the photoresist tacky and susceptible to particulate contamination at subsequent handling stages [176]. The photoresist was exposed to UV light (260 mJ/cm$^2$) using a Canon Mask Aligner (PLA-501 FN) in hard contact mode for 40s. Following exposure to UV light, the wafer was then developed by immersing it in a solution of MF26A and agitating it for approximately 2 minutes. In this step, the regions of photoresist that were exposed to light (through transparent regions on the photomask) dissolved leaving the silicon wafer patterned with photoresist corresponding to the designed mask (Figure 4.9). Following this, the wafer was rinsed with distilled water.

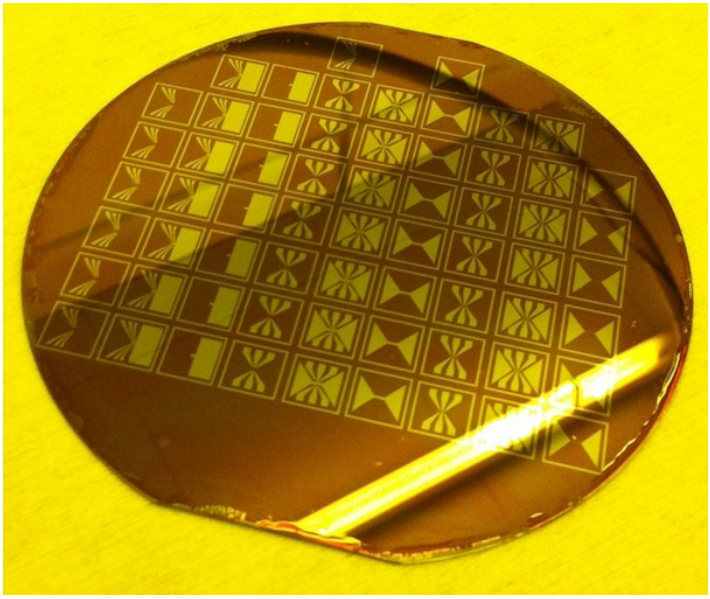

FIGURE 4.9: Silicon wafer coated with resist after exposing to the UV light through film mask

### Etching

Reactive Ion Etching is a dry etching technique where radio frequency (RF) power is used to drive chemical etching reactions under low pressures [158]. Here, stray electrons are accelerated towards the wafer. These electrons collide with molecules of a reactant gas (such as $SF_6$) to form excited and ionised species. Thus, a combination of chemical and physical processes are used to etch the silicon surface. Halogens such as fluorine and chlorine are used to etch silicon because the Si - halogen bond is much stronger than the Si - Si bond [158]. While excited molecules formed from dissociation of the reactant gas are involved in the chemical etching of silicon, the purpose of ion bombardment is to introduce directionality and enhance the physical removal of material. Thus high etch rates and anisotropy can be achieved.

Deep Reactive ion etching (DRIE), also known as the Bosch process or time multiplexed deep etching process (developed by Robert Bosch in 1992), is an anisotropic RIE etching

technique used to form very high aspect ratio structures in a silicon wafer [158, 177]. This process was used to cut through the silicon wafer to form the stencils.

A DRIE System manufactured by Surface Technology Systems (STS) was used to carry out the etching process. This is an inductively coupled plasma (ICP) etcher that generates high density etching species at low pressures and low DC bias.

As exposed regions of the silicon wafer have to be completely etched through to form the stencil, prior to placing the photoresist coated silicon wafer in the etcher, it was attached to a silicon handle wafer using thermal tape[3] Figure 4.8 (step 5). Next, an etching process was used to remove specific regions of the silicon wafer to form the stencil Figure 4.8 (step 6).

The process involves a cyclic mechanism with the use of alternating etch and sidewall passivation steps. During the etch phase, ions generated from sulphur hexafluoride ($SF_6$) plasma are accelerated towards the silicon substrate (which has a bias of - 5 to - 30 V). In the passivation phase, octafluorocyclobutane ($C_4F_8$) is used to deposit a teflon like polymer all over the substrate. Thus, in the subsequent etch step the directional ion bombardment allows the removal of material from the horizontal surfaces of the substrate, leaving the sidewalls protected by the chemically inert polymer layer. The parameters used for the etching process are given in Table 4.3

TABLE 4.3: The parameters used for the etching process with the STS ICP DRIE Etcher

| | Etch cycle | Passivate cycle |
|---|---|---|
| $SF_6$ Flow rate | 130 sccm | 0 sccm |
| $C_4F_8$ Flow rate | 0 sccm | 100 sccm |
| Duration | 12 s | 5 s |
| 13.56 MHz Platen power | 600 W | 600 W |

The DRIE process was carried out for 3 hours to etch through the whole silicon wafer

[3]REVALPHA thermal release tape

thickness. In order to strip off the photoresist layer and remove any contaminants, a cleaning step was implemented. A 30 minute long oxygen ($O_2$) plasma cleaning process was carried out using the STS etcher. This is a commonly used MEMS process where a plasma generated in sub-atmospheric pressures of oxygen creates highly reactive ions which bombard a surface and react with organics forming volatile species. The parameters used for the $O_2$ plasma cleaning process are given in Table 4.4.

TABLE 4.4: Parameters used for the $O_2$ plasma cleaning process with the STS Etcher

| | |
|---|---|
| $O_2$ Flow rate | 100 sccm |
| Duration | 30 minutes |
| 13.56 MHz Platen power | 800 W |

At the end of etching and cleaning process, the bonded wafers were removed from the STS etcher.

Since the silicon masks have to be released from the supporting silicon wafer, it is placed on a hot plate for 1 minute. The thermal tape loses its strength when it is heated up to 120 °C and all the structures can be released easily afterwards. After collecting all the silicon masks they were placed into a beaker of nitric acid. This also helps to clean the remainder of the resist mask such as silicon flakes on the realised silicon structures. In final stage, the individual stencil masks were cleansed, in the following order, with deionised water, acetone, isopropanol and deionised water again before being blown dry with nitrogen. The final produced stencil masks are shown in Figure 4.10.

### 4.3.2 Metal Deposition

The process of evaporation was used to deposit a layer of conducting metal (gold) onto the silicon nitride membranes via the fabricated stencils. In this process, molecules of a

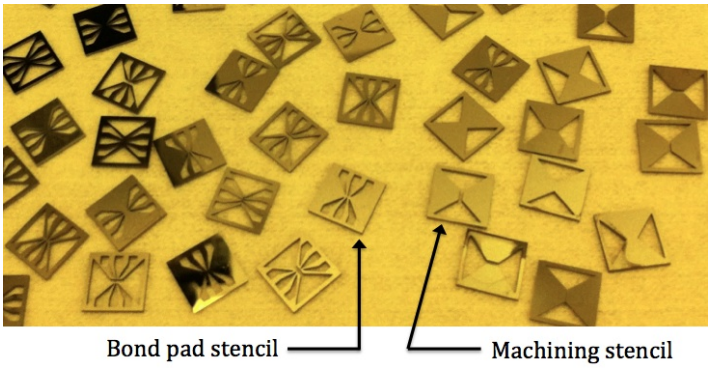


FIGURE 4.10: An optical image from the fabricated silicon stencil masks.

liquid metal gain sufficient energy to break their intermolecular bonds and leave the liquid surface in the form of gas molecules. The evaporation temperature is usually adjusted as the temperature at which the vapour pressure of a substrate reaches a value of more than 10 $\mu$m Hg [178]. It is recommended to set the vacuum level of $10^{-5}$ mbar for an effective evaporation.

The substrate is placed in a vacuum chamber, in which a source metal to be deposited is located. The source material is heated to the temperature that it starts to evaporate. The molecules evaporate in the vacuum chamber, and subsequently condense on the substrate surface. To heat the source metal two methods are used:

- The source metal is heated electrically using a high current (Thermal evaporation)
- An electron beam is directed at the source material causing local heating (E-beam evaporation)

The evaporation process was implemented using the Polaron E6100 machine as shown in Figure 4.11. This device is capable of providing the required level of vacuum.

The gold deposition process was carried out in three stages. In the first stage, the electrical connection pads were created. The silicon nitride membranes were attached to a substrate

FIGURE 4.11: The Polaron E6100 thermal evaporation system.

silicon wafer using thermal tape as shown in the Figure 4.12. The bond pad stencils were aligned over the silicon nitride membranes using an optical microscope and then secured using copper tape strips as shown in Figure 4.12.

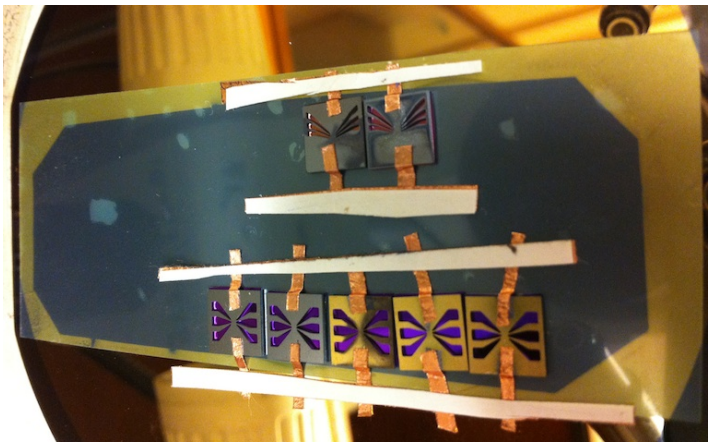

FIGURE 4.12: Silicon nitride membranes mounting place for thermal evaporation process.

The membrane and supporting silicon wafer were then mounted in the chamber of the

evaporator, such that the front side of the silicon nitride membranes faced the metal source.

The Polaron E6100 machine is capable of evaporating two separate source metals. As gold does not adhere to most materials, an adhesion layer was required to promote adhesion between the gold layer and silicon nitride membrane. Nickel (Ni) or Chromium (Cr) is usually used as an intermediate adhesion layer and a thickness of a few nm is sufficient. In this work, a layer of chromium was deposited to act as an adhesion layer prior to deposition of the gold layer.

After the metal deposition for defining the bond pads, the second stage of deposition was implemented. Here, the bond pad stencil mask was removed (Figure 4.13) and a second metal deposition step was implemented using the machining stencil. In this step, a layer of gold was deposited without any adhesion layer. Following this, the samples were removed from the evaporator chamber and released from the substrate wafer by heating on a hotplate at 120 °C until the samples detached from the thermal tape.

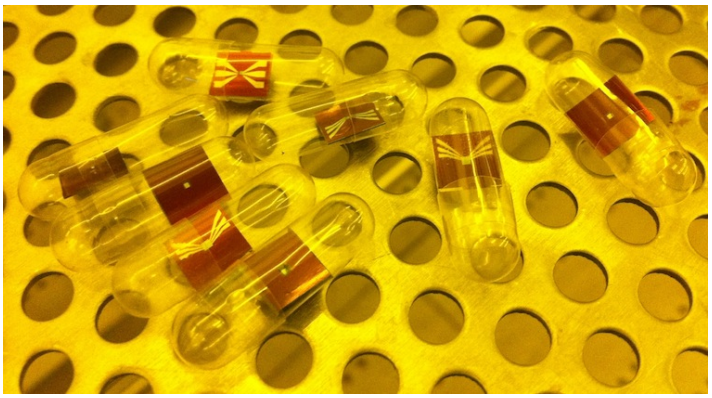

FIGURE 4.13: Silicon nitride membranes after bond pad deposition process.

As the FIB machining is implemented on both sides of the silicon nitride membrane, the window side of the samples also require gold coating. For this reason, the third or final stage of metal deposition was carried out. This time, the samples were attached to a silicon wafer

using thermal tape (front side bonded to the tape) and mounted in the chamber such that the window side of the membrane faced the metal source. Gold deposition was carried out as previously described directly on the sample without using a stencil. A gold layer of 20 - 30 nm was deposited in this way.

Before describing the FIB deposition method used to produce the drive coil, the rationale behind the decision to use the FIB for the coil fabrication will be discussed. Alternatives were considered, namely deposit and etch, and shadow mask patterning. Shadow mask patterning involves sputtering gold through a stencil mask aligned with the paddle. The Birmingham Group has some experience of this method, but the difficulties of the x, y, $\theta$ alignment with the accuracy required for the paddle coils were considered to be too demanding. Another method would be to use optical lithography after coating the paddle with a conductive layer such as gold, followed by wet or dry etch. The same alignment issues arise and in addition wet processing adds complexity; the group has no established dry etch process for gold. Both the shadow mask, and optical lithography methods require front to back alignment patterning to an accuracy which is not possible in our laboratory. Even if these methods had been judged viable, the via connecting the front and back coils would have to be formed using FIB. These arguments provide a clear indication that FIB is the best prototyping method for the torsional micropaddle resonator system. Details of the FIB method are discussed below. It should be noted that FIB has no serious limitations for fabricating this device in prototype quantities. Its usefulness as a prototyping tool is however balanced by the fact that it cannot easily be adapted to mass production. However, as discussed above, the prototype device could be manufactured effectively using standard production tools in a foundry environment.

## 4.4 Focused Ion Beam (FIB) Machining

### 4.4.1 Introduction to FIB Technology

The focused ion beam system was first developed by Krohn in 1961, as a result of research on liquid-metal ion sources (LMIS) for use in space [179]. Commercial focused ion beam systems have been manufactured since about two decades ago to meet demands of the growing semiconductor industry [180, 181].

FIB technology is widely used for processing environments, micro and nano technology researches and semiconductor industries. It is also a reliable tool for failure analysis and chip design applications [180]. This system enables localised machining such as subtraction (milling) and addition (metal and insulator deposition) processes. Usually, machining patterns can be produced within the user interface of FIB software as well as by writing a script in its available programming language environment. This capability turns this micro machining technique into a mask-less processing tool. Therefore, this system is a versatile tool for fabrication of three dimensional structures.

An image of a focused ion beam system is presented in Figure 4.14. The system components are mainly, the ion column, the work chamber, the vacuum system, the gas system and the control unit workstation.

Many FIB devices are equipped with an electron beam. This is beneficial for non-destructive inspection as the e-beam operates based on scanning electron microscope (SEM) principles. The substantial differences between ion and electron interactions with a sample surface are as follows:

1. **Ions are larger than electrons**

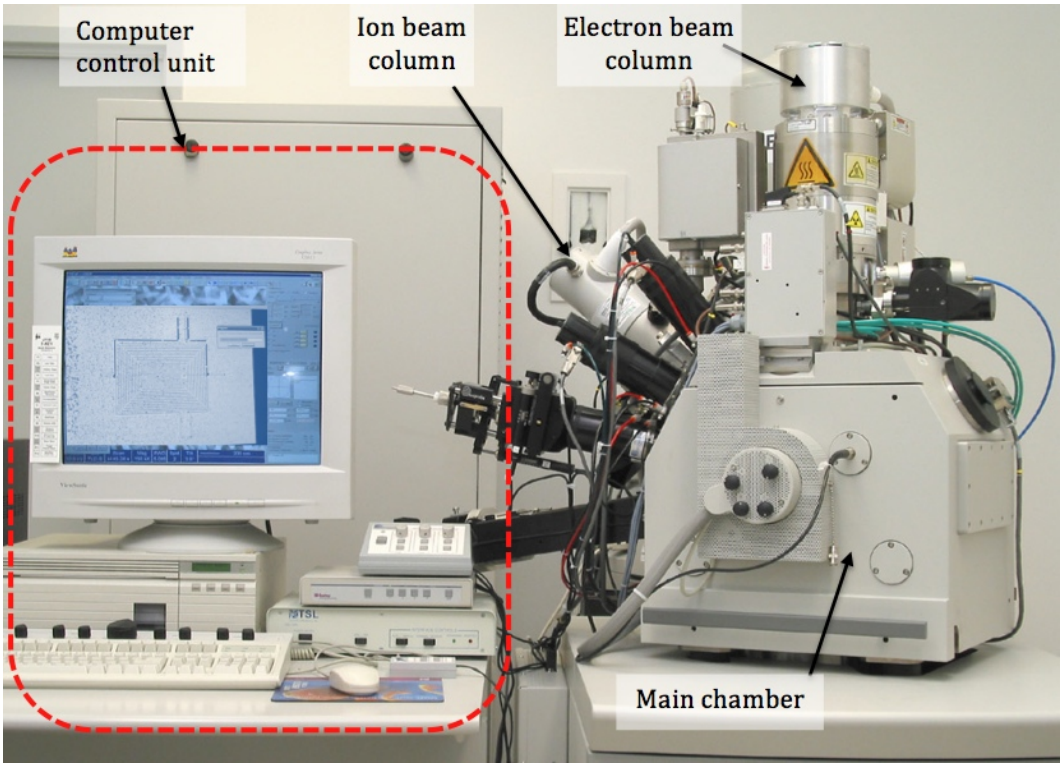


FIGURE 4.14: Dual beam SEM/FIB system setup.

- Therefore, ions collide with atoms at the surface of the substrate and interaction occurs between outer shell of the atoms on the substrate surface and ions resulting in atomic ionisation and breaking of chemical bonds of the substrate atoms.
- The penetration depth of the electrons are much higher than penetration of the ions of the same energy .
- when the ion is trapped within the substrate material, it is caught in the matrix of the material, a process known as ion implantation.

2. **Ions are heavier than electrons**

- Due to this fact, momentum produced by ions are higher than electrons. The momentum of a gallium ion is about 370 times greater for the same energy.
- The speed of the ion is much lower than that of an electron with same energy. This usually has no substantial consequences in the imaging mode; however it

might have an effect in high speed scanning.

- Efficiency of the magnetic lenses are low for the ions in compare to electrons. As a result in ion beam column electro-static lenses are used.

3. **Ions are positive and electrons are negative**
    - The difference in the charges mainly influences the control unit design. this effects polarity of the fields in terms of beam control and ion acceleration.

Basically, a focused ion beam system produces and directs high-energy ionised atoms of a relatively massive element which are focused onto a sample substrate in a form of a stream. This meets both, milling the surface as well as a method of imaging purposes. The ion's dense mass bombards the substrate surface and expel the surface atoms out of their positions and produces secondary electrons from the surface, allowing the secondary electron detector to detect these electrons and imaging the sample, before, during and after the machining process. However, imaging with raster of focused ion beam over the sample surface, sputters the surface atoms away and etches the sample imaging area.

As mentioned previously, ion beam is also capable of deposition of material available in a form of gaseous layer above the machining area. When energised atoms strike the molecules in the machining area, breaks down the gas and some leave the surface in a form of volatile gas and some remain on the surface, where intermolecular attractions fix them. In this process implantation of the ions into a surface also occurs.

### 4.4.2 FIB Operating Principle

A liquid metal ion source placed on the top of the ion column is used to produce ions (usually $Ga^{+}$). Ions are then accelerated towards the substrate. Electric field is used to focus ions into

a beam form then they subsequently pass through a apertures and are scanned over the surface of the sample. When ion strike the surface atom is either elastic or inelastic collision. Elastic collision leads to removal of atoms from the surface. This process is known as sputtering or milling. Whereas, inelastic collisions transfer some of the ions' energy to either surface atoms or electrons. This phenomenon results in emission of secondary electrons (the ones that are excited enough to leave their shell). Every FIB device operates with 4 independent functions, milling, deposition, implantation and imaging. In milling process, heavy ions from the beam strike and dig inside the substrate surface. Every time, small amount of material is removed, which leaves the surface as either secondary ions ($i^+$ or $i^-$) or neutral atoms as shown in Figure 4.15.

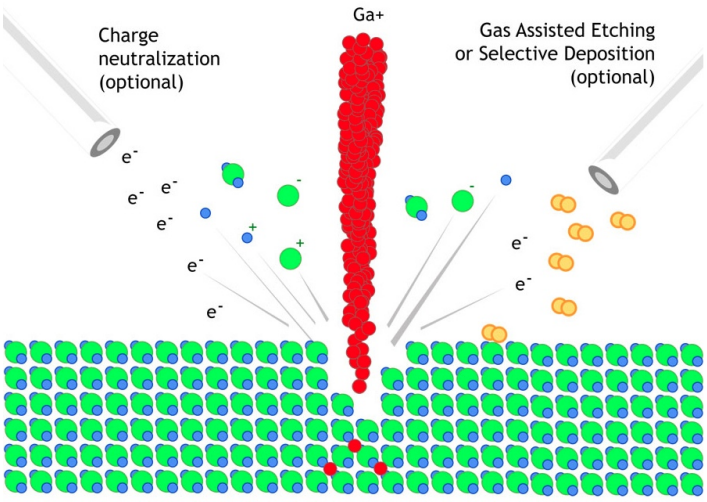


FIGURE 4.15: Bombardment of sample surface with heavy energised gallium ions in milling operation with FIB device[1].

This process can be turned into a deposition process by introducing gas delivery system, which allows the application of some materials such as platinum and tungsten to the surface of the substrate by decomposition of metal organic precursor gas where the ion beam is focused (Figure 4.16).

[1]http://www.fibics.com/fib/tutorials/introduction-focused-ion-beam-systems/4/ (Cited on 22/05/2012)

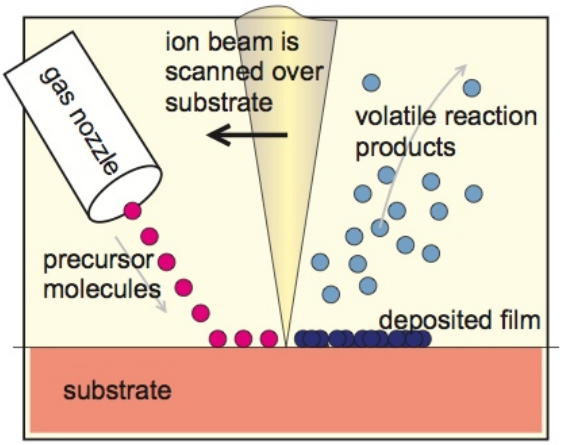


FIGURE 4.16: Principle of FIB deposition [180]

Effect of implantation is another important factor in modification of surface which occurs when the ion beam rasters over the sample. Implementation of ion beam has some disadvantages. For example it imposes some undesired damage on the sample. This has lead the FIB system to be merged with electron beam to consist a two-beam focused ion beam system. Integration of high resolution electron microscope with non-destructive imaging to machining abilities of FIB system sheds light to a priceless applications to emerge that were previously not possible [179].

### System Components of FIB

A focused ion beam system mainly consists of four subsystems, ion column, work chamber, vacuum system and gas delivery system and the control unit. The task and components of each subsystem is explored as follows:

1. **Ion Column**

   The working principle of an ion column is very much the same as electron column, the main difference is the use of Gallium ion ($Ga^{+}$) instead of electron in the beam.

Figure 4.17 shows the ion column and how the beam is generated and focused on the substrate.

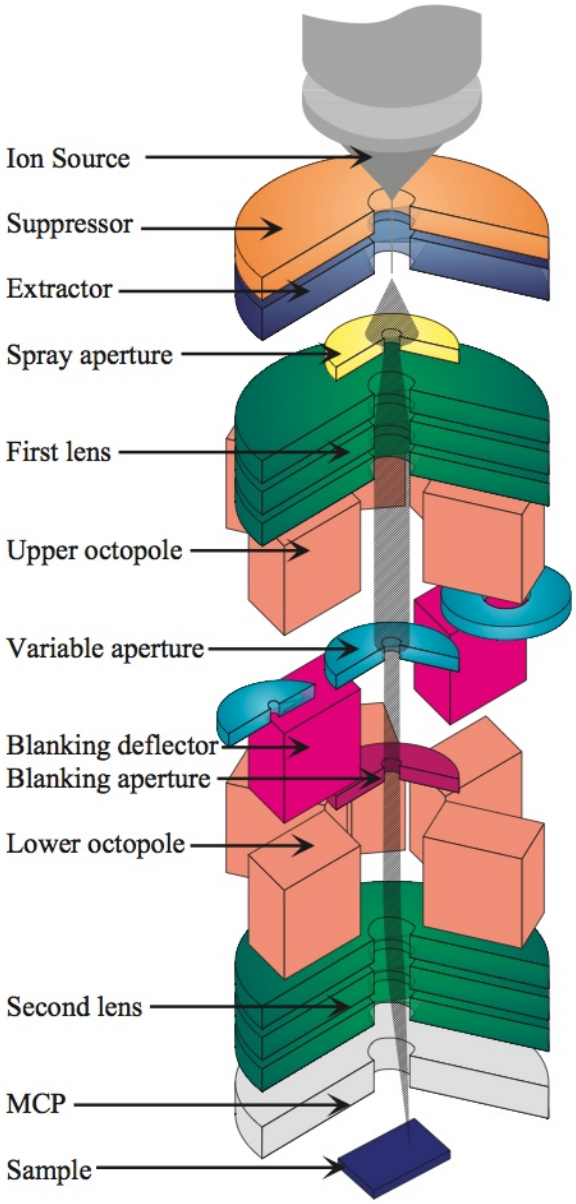


FIGURE 4.17: An schematic of FIB ion column [180].

Inside of the column has to be maintained in a vacuum level of $10^{-7}$ mbar. A powerful electric field inside the column produces the ion beam from the LMIS reservoir. Positively charged ions are transferred from the liquid gallium cone, that is located on a tip of tungsten needle by means of electric field. A typical extraction voltage is 7000

V. In normal working condition the extraction current is 2 $\mu$A. The ion beam is first refined by spray aperture and then condensed in the first electrostatic lens. The upper octopole then adjusts the beam stigmatism. The typical ion beam energy is between 10 to 50 keV (mostly 30keV is used). The beam currents can vary in the range of 1 pA to 10 nA. A variable aperture mechanism provides this four decade variation in the ion beam current allowing fine beam for high resolution imaging on sensitive samples and high beam current for fast and rough milling process. The beam can be blanked by a blanking deflector and aperture, while the lower octopole is used for raster scanning the beam over the sample in the user defined pattern as well as it corrects beam astigmatism. The second lens focuses the beam into a fine spot, providing ultimate resolution in the sub 10 nm range at a very low beam current. A multi channel plate (MCP) is utilised to collect the secondary particles to produce an image[180].

2. **Work Chamber**

   The samples were fed into a FIB working chamber through a loadlock (Figure 4.18). They were transferred onto a motorised five axis stage via conveyor rail.

   Usually stainless steel chamber is maintained at a vacuum level of $10^{-7}$ mbar. The loadlock system helps to keep the vacuum within the main chamber. For every load and unload process, the loadlock has be pumped down. Therefore, loading and unloading of the sample takes some time [180]. However this system is quicker than the one without a loadlock option. Prior to locating the samples onto the sample holder, they are usually mounted on a stub. Depending on the sample size and required configuration, different stubs might be used.

3. **Vacuum System and Gas Delivery**

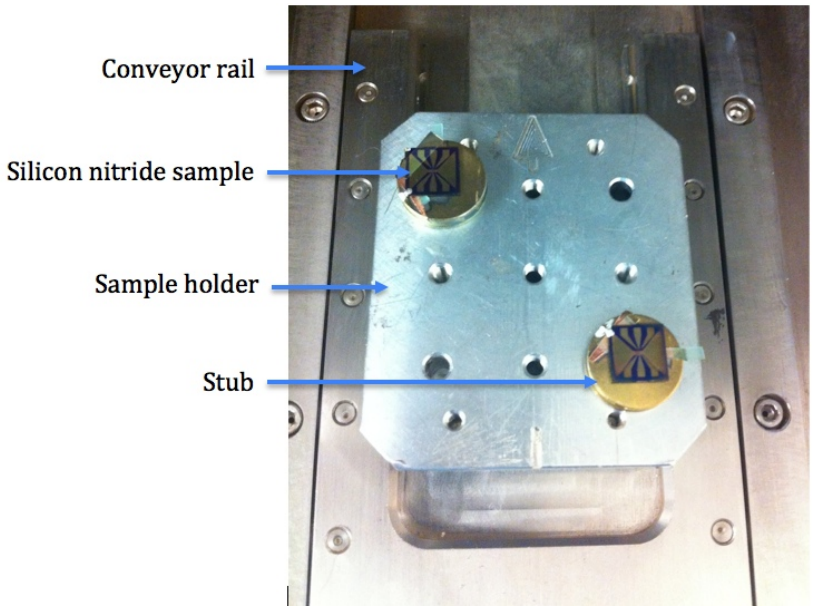


FIGURE 4.18: Samples on the sample holder in the FIB loadlock.

One of the main issues influencing the operational performance of the FIB device is the vacuum level inside the chamber. In order to meet this requirement, two vacuum pumps (forepump and turbo pump) are integrated for pumping the work chamber. In addition to this, the ion column is also equipped with one or two ion pumps [180]. To enhance the etching process and material deposition, a gas deliver system is combined with the FIB device. For this purpose, applicable gas containers are placed out side the main chamber and connected to a nozzle assembly inside the vacuum chamber through precise piping system.

4. **Control Unit**

   The control unit (user interface) is the most important subsystem of a FIB device. This allows the user to operate the device. All operations such as:

   - Loading and unloading of the samples
   - Manipulating the stage
   - Controlling gas delivery valves

- Patterning area
- Scanning area
- Controlling vacuum pumps
- Adjusting beam parameters

are carried out by the means of its computer software.

### 4.4.3 TPM Fabrication Steps

There are 3 designs produced for this project using a FIB device. First, a detailed explanation of the TPM integrated with dual spiral coil is presented followed by the fabrication process of the other two designs. Since the fabrication of the TPM with dual coil requires machining of the top and bottom surfaces of the TPM, the machining took place in two stages. In the first stage the sample was loaded with the window side facing up (as shown in Figure 4.4). For the second stage of the machining process, it was removed from the FIB device and flipped over into its front side.

Some main considerations that were taken into account during the fabrication process were residual stress, deflection of paddle, fracture, buckle, edge roughness, processing time, quality of the final pattern and precise geometrical dimensions.

In order to prevent any failure and obtain a high quality prototype device, the following steps were developed to fabricate the TPM. These steps were fine tuned based on preliminary fabrication experiments.

The following steps were implemented for the machining of the window side.

- **Step 1:** Deposition of platinum in the form of a rectangular plate with dimensions of 12 x 9 $\mu m^2$ and a thickness of 0.25 $\mu$m (Figure 4.19).

  Appropriate machining current is set based on the deposition area from the guidelines

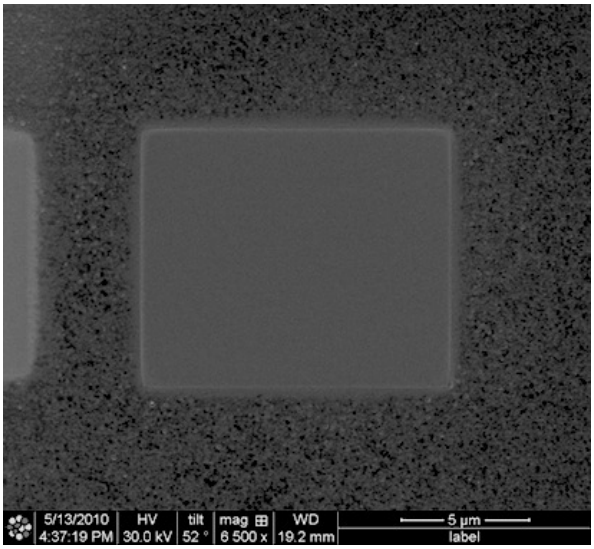


FIGURE 4.19: SEM image of deposited platinum block on the window side of the silicon nitride membrane.

provided in the FIB user manual, where the optimum current density for deposition is given as 2-6 pA/$\mu$m$^2$ (Figure 4.20). According to the dimension of the deposition area (11 $\mu$m by 10 $\mu$m), the appropriate ion current (220 to 660 pA) has to be selected from user interface to satisfy the efficient deposition growth section (the green area in the Figure 4.20).

Based on the guidelines provided by the FIB manufacturer, the longer the ion beam remains at the point on the sample surface, the less net deposition there is. The net deposition rate is the deposition rate minus the sputtering rate (material removal rate) [182]. It is crucial to set the ion current with required balance in metal deposition rate, otherwise the process will etch the sample surface or produce a rough deposition.

- **Step 2:** A rectangular spiral pattern was then loaded on the patterning area and milled as shown in Figure 4.21. The milling process continues until the beam hits the silicon nitride membrane.

  The spiral pattern was generated by using a programming script that is loaded via

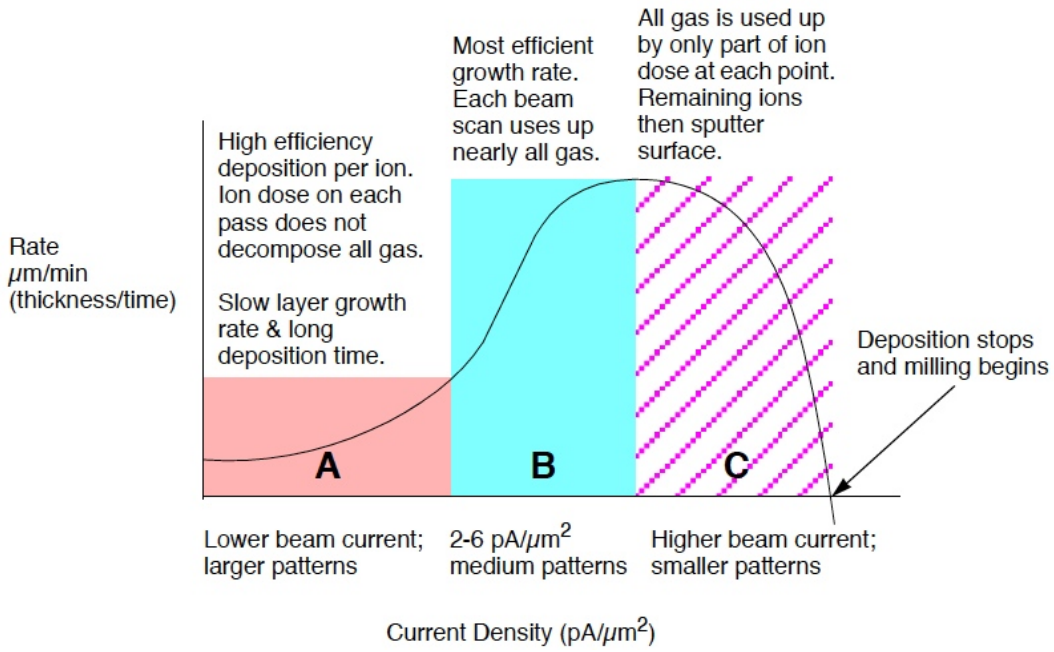


FIGURE 4.20: Gas assisted metal deposition efficiency in FIB system [1].

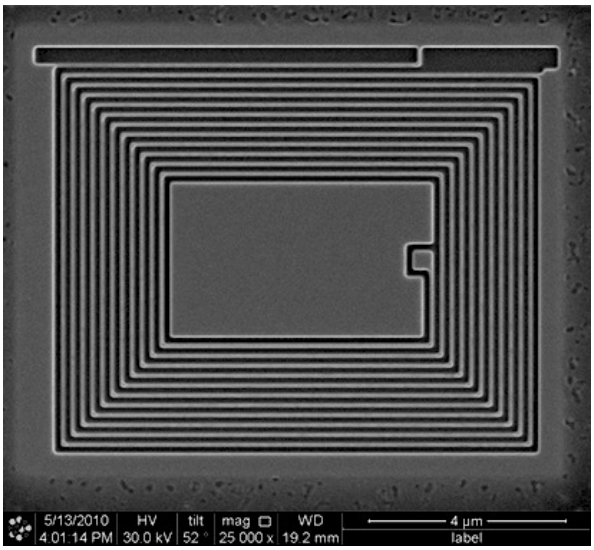


FIGURE 4.21: SEM image of milled platinum block by a rectangular spiral pattern.

pattern generating software within the interface of the FIB system. The milled pattern generates the nano coil of platinum with a cross sectional area of 100 $nm^2$ and a gap size of 100 nm. This approach has three advantages compared to direct deposition of the Pt coil. Firstly, there would not be an interconnection between the tracks. The deposited line of Pt produces a very thin film having a thickness of a few nanometres next to the deposited pattern and it continues to the half of the width of pattern (Figure 4.22 (a)). This is known as halo effect and can cause a short circuit in this design. Next, since the surface of the membrane is coated with a thin gold layer, possibility of interconnections caused by the gold layer can be avoided since it is milled away. This assures that there would not be any interconnection between the produced tracks. However, from a machining point of view, the gold layer is required to provide a path for the charges to leave the surface. This would avoid localised charges building upon each other causing the ion beam to shift in the middle of the machining process consequently ruining the pattern. The third advantage is that the milling produces a higher quality edge in the cross-section of the Pt track (Figure 4.22 (b)) compared to the cross-section produced by deposition of Pt in lines, which is attributed to the halo effect. A SEM image provided in Figure 4.23 shows the shadows around the deposition of Pt track deposited on a line. Mostly the halo effect occurs as the beam rasters over the machining area.

Deposited tracks do not have perfectly rectangular cross section in line deposition process, but it is more obvious to meet a better rectangular cross section in milling. The milling process also mills away the surface of the whole Pt block, which reduces the thickness of the deposited Pt block. This effect causes the Pt track to obtain a

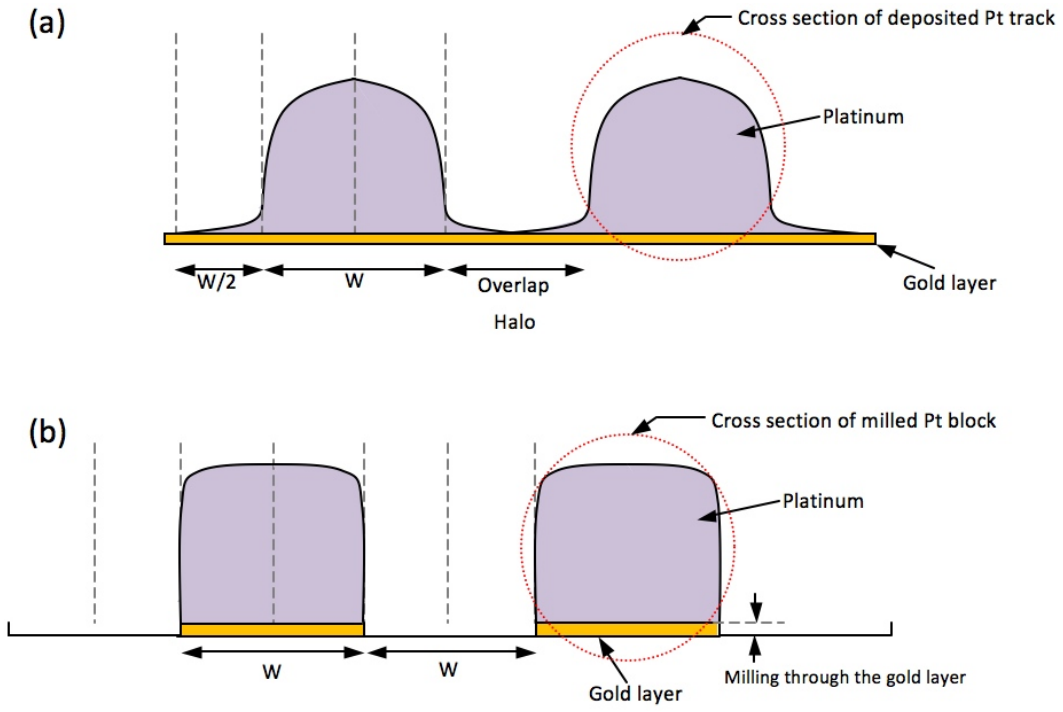


FIGURE 4.22: Platinum tracks produced by a) platinum deposition on a line in the FIB, b) milling through a block of deposited platinum.

thickness of about 100 nm as it was set in the design of the TPM.

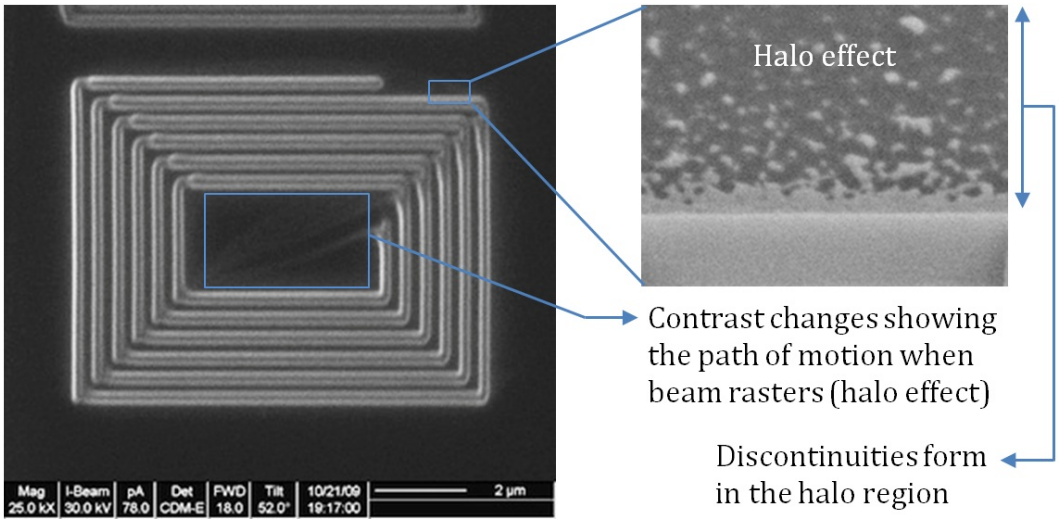


FIGURE 4.23: Deposition of the Pt track directly on the sample using the FIB.

- **Step 3:** In this step, undesired areas of the Pt block is etched away. This consists the central area of the coil as shown in Figure 4.21 and its outer boundary.

- **Step 4:** In the final stage of window side machining process, the edges are milled through the whole membrane to form the designed micro paddle (Figure 4.24).

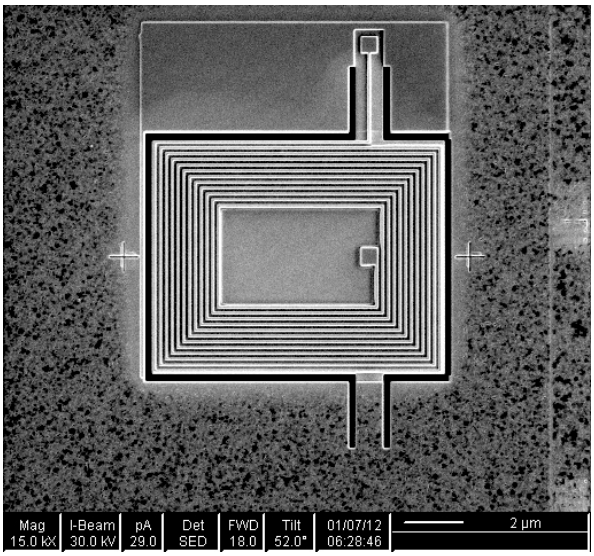


FIGURE 4.24: Forming the paddle by etching through the Pt and membrane around the Pt spiral coil.

- **Step 5:** After finishing first side machining, the membrane was removed from the main chamber, it was removed from the stub, flipped over to the front side and remounted onto the stub, then it was loaded again into the FIB working chamber.
- **Step 6:** Here, the first concern was to make the connections from back side to the front side of the membrane as a part of coil circuit. One via was required to connect the centre of the lower coil to the centre of the upper coil and another connection from the other end which is passed through the supporting leg. The milling for these two vias needed to etch through the silicon nitride membrane and stop where it hits the Pt material on the lower side. Therefore, very precise milling parameters were required to carry out the process. As shown in Figure 4.25.

  The test was carried out on the silicon nitride membrane to precisely cut through the membrane without over milling. Since the membrane is re-located back into the FIB,

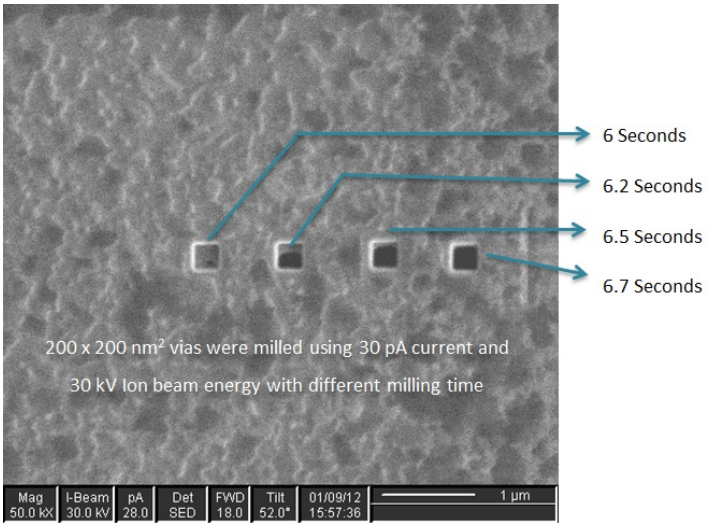


FIGURE 4.25: Milling parameters adjustment for connecting vias

it is crucial to make sure that the alignment is precise.

- **Step 7:** In this stage the same steps from 1 to 4 were repeated in order to accomplish the required surface machining of the front side membrane. Finally, more space was provided for the TPM where it is released from the membrane substrate (Figure 4.26).

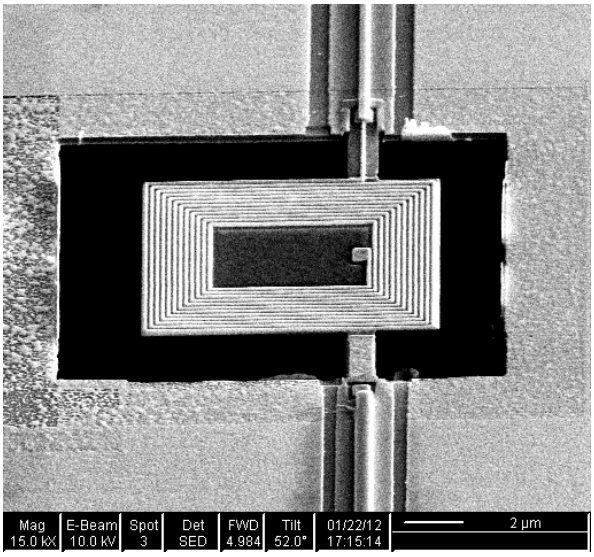


FIGURE 4.26: SEM image of the fabricated and finalised TPM fabrication, with more surrounding space

The etched area provides more free space when the TPM is vibrating. This helps the

performance of the TPM when it is operating in air.

- **Step 8:** The paddle is now ready and in this step all the connections to bond pads were made by deposition of Pt track from either ends of the coil locating at the end of each supporting leg. This stage required quite a long time processing time, since the pads are placed a rather long distance from the micro paddle (Figure 4.27).

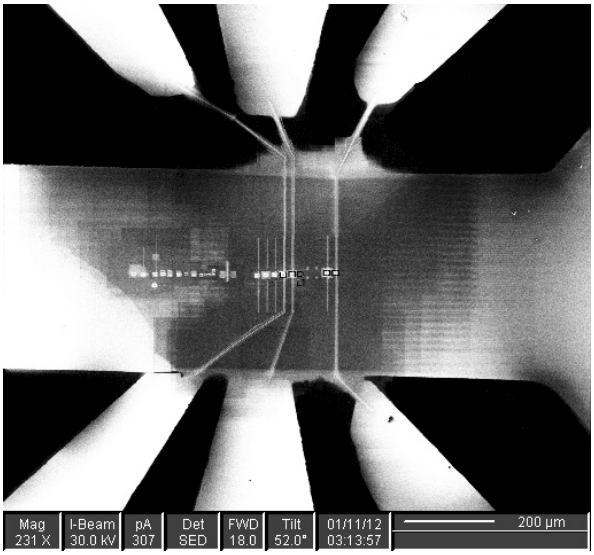


FIGURE 4.27: SEM image of the fabricated TPMs and connections to the bond pads.

In every membrane three TPMs were made to be connected to the bond pads. Each TPM is connected to two bond pads. In order to fabricate TPMs, in every membrane, usually more than three TPMs are made and after inspection the best three choice among them (in terms of cleanliness, geometrical accuracy) are considered to be connected to the bond pads. This prolongs the fabrication time, but assures high quality TPMs. The orientation of the pads were chosen to be perpendicular to the direction of the magnetic field. This allows to have organised and simple path for connecting tracks from one pad in one side to another pad in the opposite side of the sample. This

also helps to have neat wiring from the sample to the chip carrier. In addition, it allows connecting the outer most legs of the chip carrier from the centre, which doesn't interfere with the location of the magnets. The packaging is explained and shown in section 4.7.

- **Step 9:** Since a thin layer of gold is coated before FIB machining starts. To assure the isolation of the connecting wires, for all the 6 connections a milling process was carried out on either sides of every track (Figure 4.28).

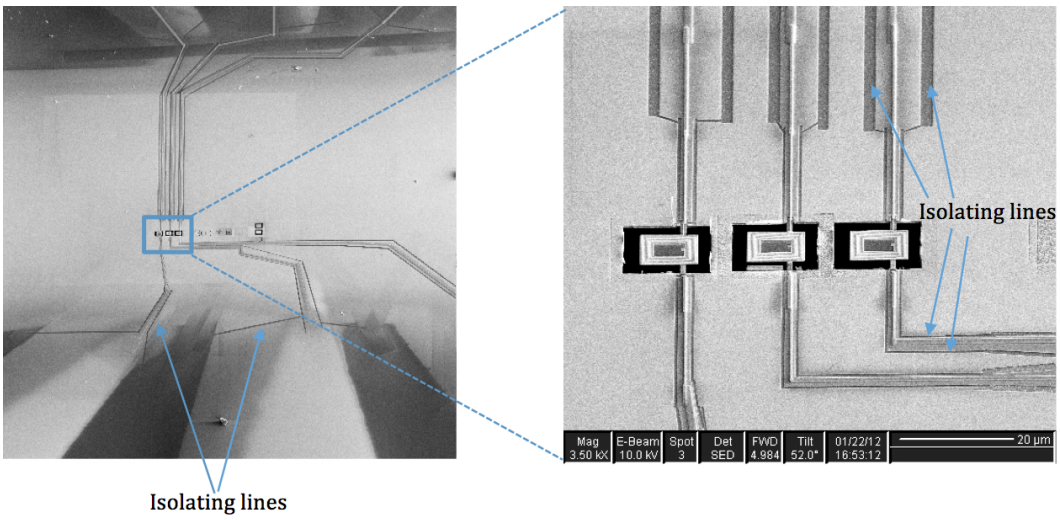


FIGURE 4.28: SEM image of isolated Pt wires for connection of TPM coil to bond pads.

Five samples, each consisting of three TPMs were produced for testing according to the above steps. During the process of milling 30, 50 and 100 pA currents were used with 30 KeV beam energy. Usually, higher currents are used for fast and rough milling and lower currents are used for polishing. The other two designs were produced with the same method apart from depositing a rectangular block of platinum and milling through it. these are shown in Figure 4.29 and 4.30. line deposition of the Pt track were used for these prototypes.

In the Figure 4.29 the opposite side of the TPM is the platinum track with same layout, which keeps the flow of the direction of the current the same as upper loop.

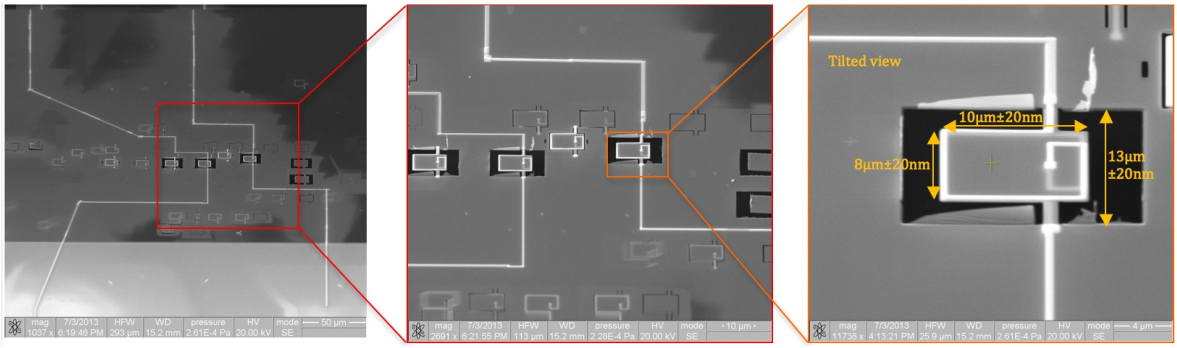


FIGURE 4.29: SEM image of the TPM integrated with dual loop platinum track.

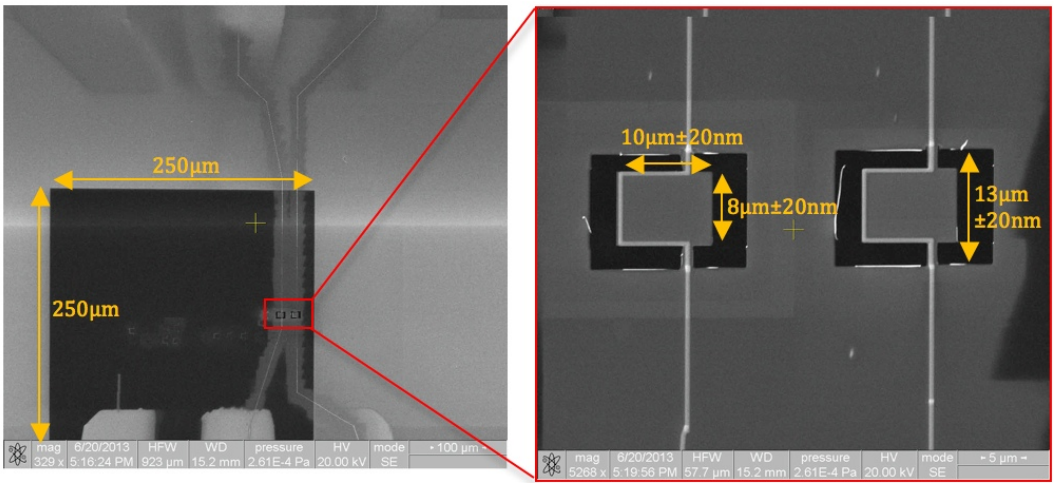


FIGURE 4.30: SEM image of the TPM integrated with a single platinum track.

### 4.4.4 TPM Machining Considerations

In the processing stage some precautions have to be taken into account and few has to be checked regularly to avoid any defect or failure during TPM fabrication process. One of the precautions in the fabrication of the TPM is to make sure the membrane is horizontally placed on the stub. This assures the machining avoids any inclined etches or deposition. It is very important to make the ground connection from the substrate to the stub. Accumulation of charges can shift the beam to a side during milling or deposition (Figure 4.31 (a))

Since, images taken by ion beam are destructive to the sample surface, usually continuous

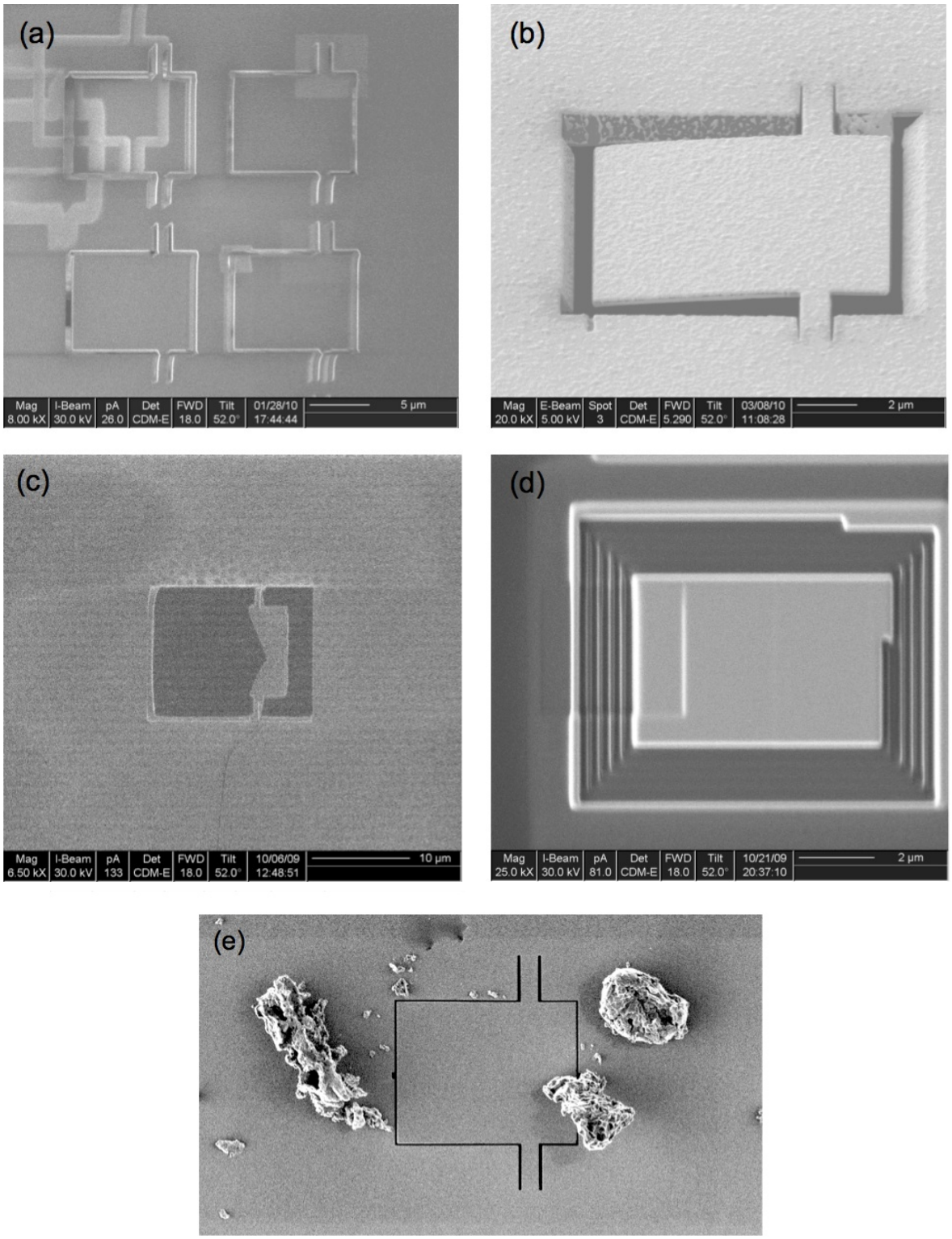


FIGURE 4.31: SEM images of number of failures during fabrication process of a TPM.

scanning is avoided in ion beam mode. Therefore, mostly one scan is captured. During pattern loading magnification might be amended. In order to avoid any dislocation of the pattern , before every process the magnification of the beam, has to be checked. Processing time also play an important role. Based on ion implantation surface characterisation might change and this will induce stress within the silicon nitride structure. Reyntjens and Robert (2001) [180], have shown there is a few tenth of nm implantation of the Ga ions in the sample surface during FIB milling. This effect can cause the micro paddle surface to bend (Figure 4.31(b)). Furthermore, some of the membranes have a high residual stress because of the production limitations. This can cause a fracture of the whole membrane during milling or the released structure shatters (Figure 4.31(c)). Therefore, it is recommended to always test every sample prior to the start of fabrication processes. FIB adjustments are ultimately affect the fabrication process along with the machine stability. Sometimes, because of the noise problem, defects can be produced. One of the important adjustments is the focus. This is a fundamental requirement for every step in fabrication process. Poor focus and stigmation can result in non uniform milling rates in x and y directions (Figure 4.31 (d)). In addition, since this machining requires both surface of the membrane to be machined, the grounding has to be accurately done by a liquid metallic paint. Last but not least, it is always recommended to keep the samples in a very clean environment free of dust particles. This becomes substantial when there is a need to relocate the samples from one laboratory to another. Dust particles can be easily attraced on the surface of the membrane and ruin the sample (Figure 4.31 (e)). It is important to acquire a vivid and clear image in order to accurately measure features and distances in an SEM image. This requires adjusting imaging parameters such as contrast and brightness. This procedure is explained in the following section.

## 4.5 SEM Image Acquisition Considerations

One of the Important aspects of sample inspection is to record an appropriate image illustrating all the aspects required for inspection. Electron beam spot size, its energy and image brightness and contrast play important role for this purpose. Small spot size give more accurate depiction of the feature being scanned. Thus, it is recommended to have a spot size smaller than the smallest feature size on the inspected sample. Brightness, is measured by beam current per unit area and solid angle. Increase in brightness is linearly associated with increase in accelerating voltage (beam energy). Beam current is directly related to the interactions with sample and requires to be sufficient to produce adequate signal to noise ratio. High level of vacuum is an inevitable factor to produce a high resolution image. High vacuum provides a long mean free path (MFP) [4]. Therefore, devices with high vacuum are known as top rated tools [5]

### 4.5.1 Brighness and Contrast Levelling

- Reduce contrast to about 10 percent.
- Increase brightness until image starts to become visible.
- Increase contrast until the image reaches the greatest dynamic range

[4] this is how far would one gas molecule have to travel before it hits another gas molecule (MFP at 1 atm is $10^{-7}$m, while at $10^{-10}$ Torr is 1000 km.

[5] Characterising and Testing of Nanotechnology Structures and Materials, Online Course of Advanced Field Emission Scanning Electron Microscopy, NACK Centre, The Pennsylvania State University (2010).

## 4.6 Geometrical Evaluation of Fabricated Paddles

In every fabrication step, the geometry of the milled sections were inspected to assure the produced feature is within the acceptable tolerances. Dimensions shown in Figure 4.32 indicated the geometrical tolerances of the TPM.

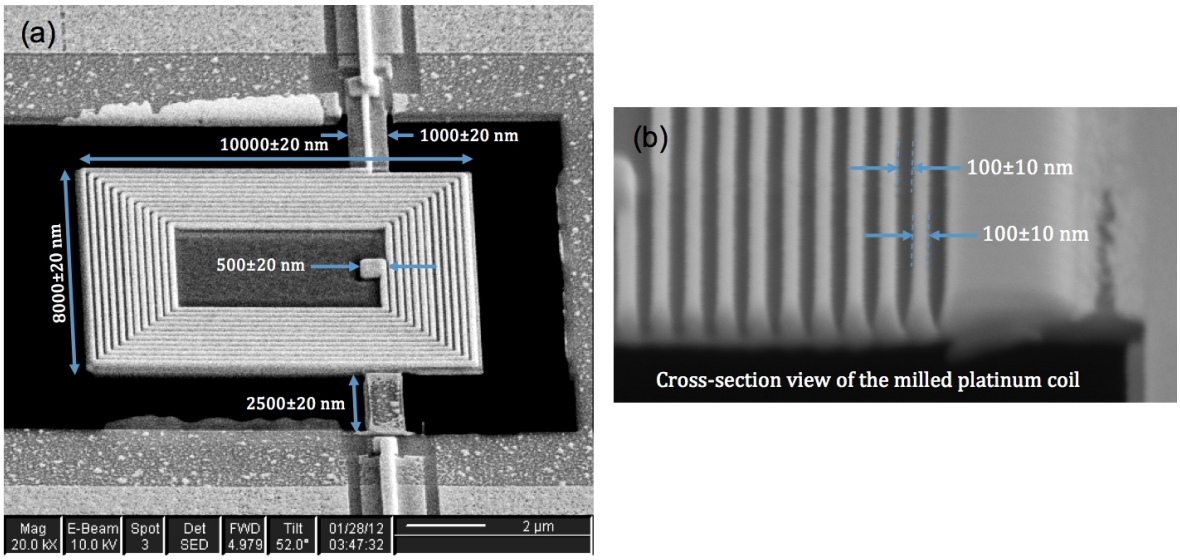


FIGURE 4.32: Dimensions of the fabricated TPM.

## 4.7 Packaging

It is required for the membranes to have an adequate packaging for the test and proof of performance. For this purpose, membranes had to be placed on a chip carrier. Design and schematic of the packaging was previously shown in the design chapter. According to the membrane size, an appropriate 24 lead side brazed chip carrier was used. The dimensions of the chip carrier chosen are shown in Figure 4.33

The silicon nitride membrane was then placed and fixed into the square area provided in

[1]Adopted from technical drawing sheet of 24 pin chip carrier (Part no: CSB02491) SPECTRUM semiconductor materials, INC.

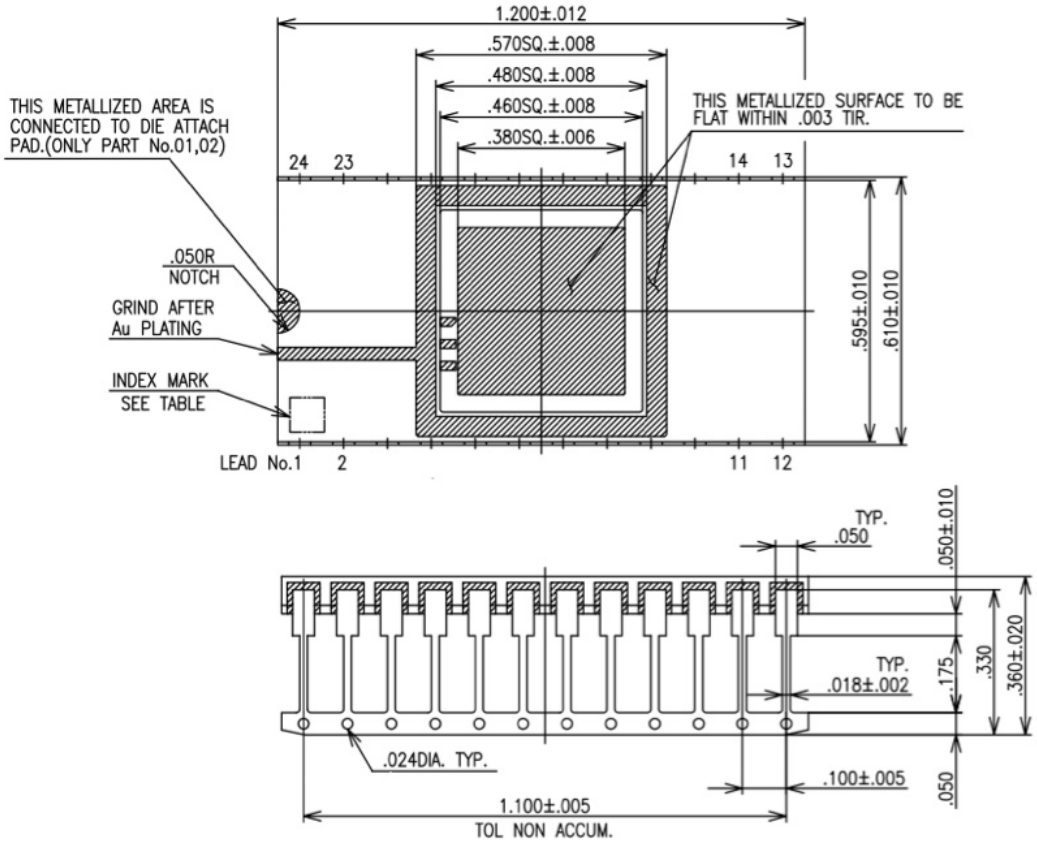


FIGURE 4.33: 24 pin lead side brazed ceramic chip carrier technical information [1].

the centre of the chip carrier. Next, the connections from the bond pads on the membrane and chip carrier carried out by wire bonding technique. In order to hold permanent magnets on the sides of the chip carrier three different designs were developed and fabricated using a 3D printer. Mr. Simon Rowan from technician team at school of Mechanical Engineering in Birmingham University helped to fabricate these holders. The choice of material used for 3D-prototyping is a bio-compatible material code-named MED610. It is rigid, transparent and its quality doesn't degrade in time. The design of the magnet holders also cover the top area of the chip carrier. This feature provides a compact packaging of the device. Figure 4.34 shows the physical assembly of the fabricated magnet holders, permanent magnets and chip carrier.

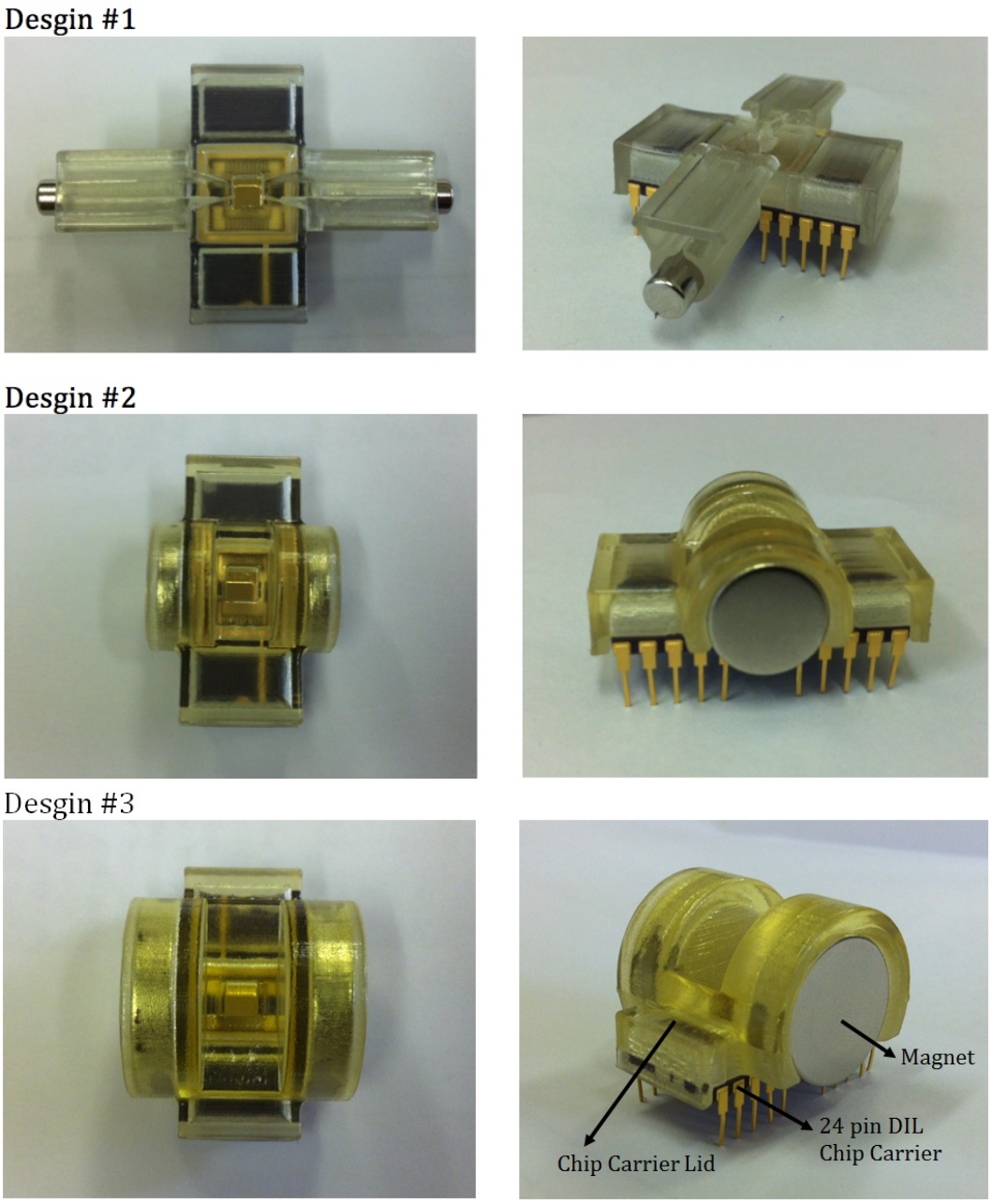


FIGURE 4.34: Three assemblies of the chip carrier, permanent magnets and chip carrier lid.

The 24 pin chip carrier is the same in the three assemblies shown in Figure 4.34. The main difference is the design of the magnet holders and the size of magnets. Three different magnet were used in these assemblies. In the first assembly, two cylindrical magnets with 5 mm diameter and 25 mm length were used. These magnets are N42 type with strength of 1.33 Tesla. In the second design assembly, the magnets dimensions are 12 mm in diameter and 3 mm in thickness. They are N52 type with strength of 1.48 Tesla. Finally in the last assembly, magnets with 18 mm diameter and 5 mm thickness were used. The strength of these magnets are 1.48 Tesla and they are N52 type. The magnets used in this project are all NdFeB. On the top of each holder a square hole was left. This allows the laser beam of the doppler laser vibrometer to scan through the package and measure membrane vibration for testing purposes. An optical image shown in Figure 4.35, is the picture taken from the membrane within the package using an optical microscope.

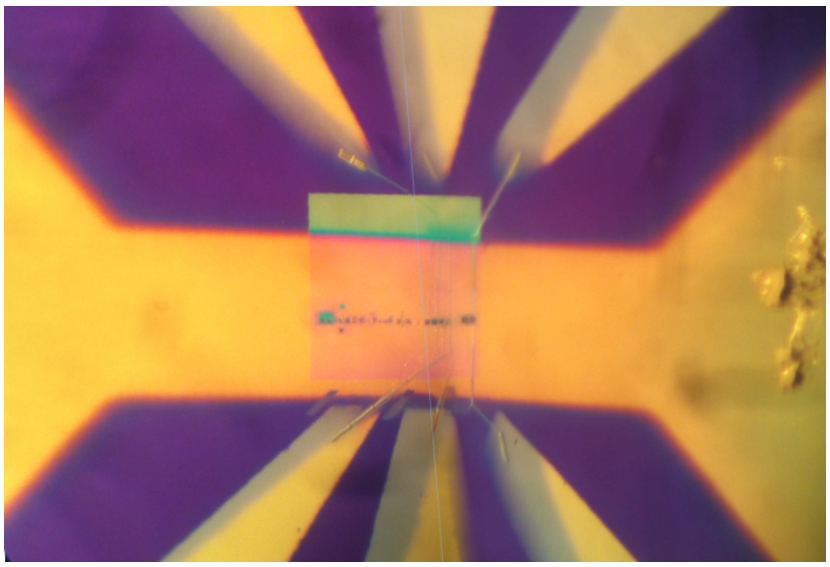

FIGURE 4.35: An image of the membrane window taken throw the packaging hole under optical microscope.

In this image a close view from the membrane window is given. It is shown how the gold masks were aligned. A central square in green colour is the membrane window, and is

covered by a thin layer of gold from left to right of the image. Chromium-gold deposition of the bond pads can be seen in six yellow areas on top and button of the image. The purple colour shows the silicon nitride film above the silicon supporting substrate. Narrow connecting tracks show how the micro coil deposited on either sides of the paddle is connected to the upper and lower bond pads.

## 4.8 Conclusion

In this chapter, an introduction to silicon nitride was given. Its structure was explained along with production method of LPCVD silicon nitride films. Its important material properties were introduced and shown from variety of sources. An introduction to silicon nitride membranes for micro and nano applications was appointed as well as their standard size and dimensions. Stencil mask fabrication method was described using photolithography and deep reactive ion etching methods. The thermal evaporation process was explained for thin metal deposition purpose using stencil masks. Focused ion beam machining was introduced along with its consisting components and operating principles. The advantages of FIB machining were outlined among other available micro machining techniques for this project. Fabrication of TPM was described in different steps along with some machining considerations. SEM image acquiring technique was introduced, along with description of influencing factors. Final TPM structure was evaluated in terms of dimensional accuracy. In final stage, device packaging was explained and images of the final packaged device illustrated.

# 5

# Test and Results

## Contents

**Summary** In this chapter, the characterisation of the fabricated TPM is described. The TPM was tested under a laser Doppler vibrometer and its vibrational behaviour was evaluated. The sensitivity of the TPM to added mass was measured experimentally. To study the surface characteristics of the device following fabrication, the surface roughness of the TPM was examined using a 3D reconstruction method. The wetability or hydrophilicity of the TPM was measured and enhanced.

## 5.1 Laser Doppler Vibrometery

In order to evaluate the vibrational behaviour of the TPMs, a laser Doppler vibrometer was used. A brief introduction to laser Doppler vibrometery followed by the methods used to characterise the fabricated TPM are given in the following sections.

### 5.1.1 Introduction

Object vibrations are typically evaluated using accelerometers or by implementing other mechanical methods. However, a drawback associated with the use of such techniques is that physical contact with the vibrating object is necessary. When the vibrating object has a small mass, mechanical contact can introduce considerable errors in the measured quantity. Additionally, it is not always possible to ensure the required contact between a transducer and the vibrating object under high temperatures and in locations that are difficult to access. In such conditions, a contactless measurement method such as the use of optical interferometric techniques can be implemented [183].

The Laser Doppler Vibrometer (LDV) is a velocity transducer, that allows direct measurement of specific mechanical parameters in a contactless manner. The instrument directs a laser beam at the surface of interest which scatters or reflects the light. The vibration amplitude and frequency are extracted from the Doppler shift of the laser beam frequency due to the motion of the surface. The output of an LDV is generally a continuous analogue voltage that is directly proportional to the target velocity component along the direction of the laser beam. Parameters such as mechanical resonance frequency, quality factor, displacement magnitude and settling time can be determined using such a device.

The use of the LDV as a tool for characterising MEMS devices is well established because of its high sensitivity and ability to provide high spatial resolution of vibration measurement [184]. Sub-nanometer displacements from near DC to several MHz can be measured. It can also be used to measure reliability of MEMS devices by enabling device parameters to be monitored for extended time periods [184].

The working principle of the LDV is based on the Doppler effect, which relies on sensing the frequency shift of backscattered light from a moving surface. When a laser beam is directed perpendicular to a sample surface, the Doppler frequency shift can be obtained from the equation below [184].

$$f_D = \frac{2V_z}{\lambda} \tag{5.1}$$

where $f_D$ is the Doppler frequency shift, $\lambda$ is the wavelength of the laser beam and $V_z$ is the velocity of the surface in the direction of the beam. In order to measure the velocity of an object the Doppler frequency shift has to be monitored at a known wavelength. A laser interferometer in the LDV is utilised in order to measure velocity and displacement of the vibrating body.

Basically, laser beam from the source is split into reference beam and test beam. The test beam is directed to the vibrating target and the scattered light from the target point is collected and interfered with the reference beam on a detector system. Commercial LDV systems add a known frequency shift to the test beam by means of a acousto-optic modulator. The test beam with summation of source ($f_0$) and modulator ($f_m$) frequencies hit target surface. Vibration of the target surface causes a Doppler shift ($f_D$) to the test beam. the reflected light now has a frequency of ($f_0$) + ($f_m$+$f_D$). This is then combined with reference light at the detector, which

is the beat frequency between the two beams ($f_m$+$f_D$). Detector gives a frequency modulated signal based on carrier frequency ($f_m$) and modulated frequency ($f_D$). This resultant signal is then demodulated to derive the velocity and displacement versus time of the vibrating target.

Fundamentally two coherent light beams with respective light intensities $l_1$ and $l_2$ are used, which allow optical interference. The resultant is not just the sum of the single intensities, but is in fact modulated according to the following formula‘[1]:

$$l_{tot}^2 = l_1^2 + l_2^2 + 2l_1 l_2 cos(2\pi\lambda + \Delta s) \tag{5.2}$$

where *s* is the detected displacement.

For more advanced applications a scanning LDV can be used. In this system the measurement beam can be positioned by a set of fast-moving micro vibrating parts. As a result, data can be collected from a set of points on the surface of the sample and deformation of the device can be depicted along the sample surface. Figure 5.1 shows a schematic of the LDV application in testing a micro mirror [184].

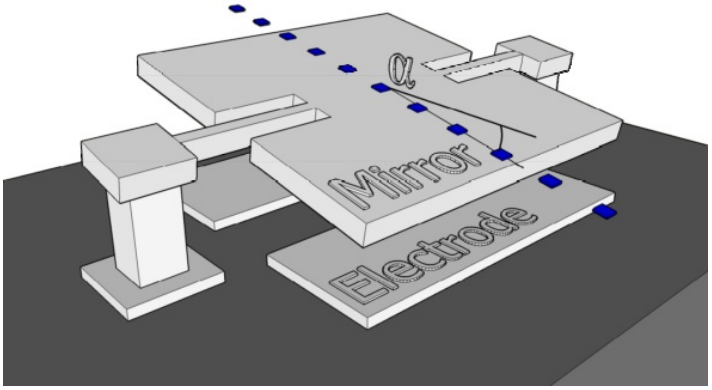


FIGURE 5.1: A schematic of a micro mirror MEMS device for LDV test [184].

[1]http://www.polytec-ltd.co.uk/uk/solutions/vibration-measurement/basic-principles-of-vibrometry (Cited on 14/09/12)

In the schematic shown in Figure 5.1 by monitoring several scan points, angle $\alpha$ can be calculated. The operating frequency and spot size of the LDV device are key factors for the choice of application. LDVs are capable of characterising out of plane vibrations at ultra high frequencies [184].

### 5.1.2 TPM Vibration Test

The resonance curve of the TPM was measured using a laser doppler vibrometer (Polytec UHF-120). An external piezoelectric actuator was used to apply a vibration to the silicon nitride chip. Figure 5.2 shows the experimental set up.

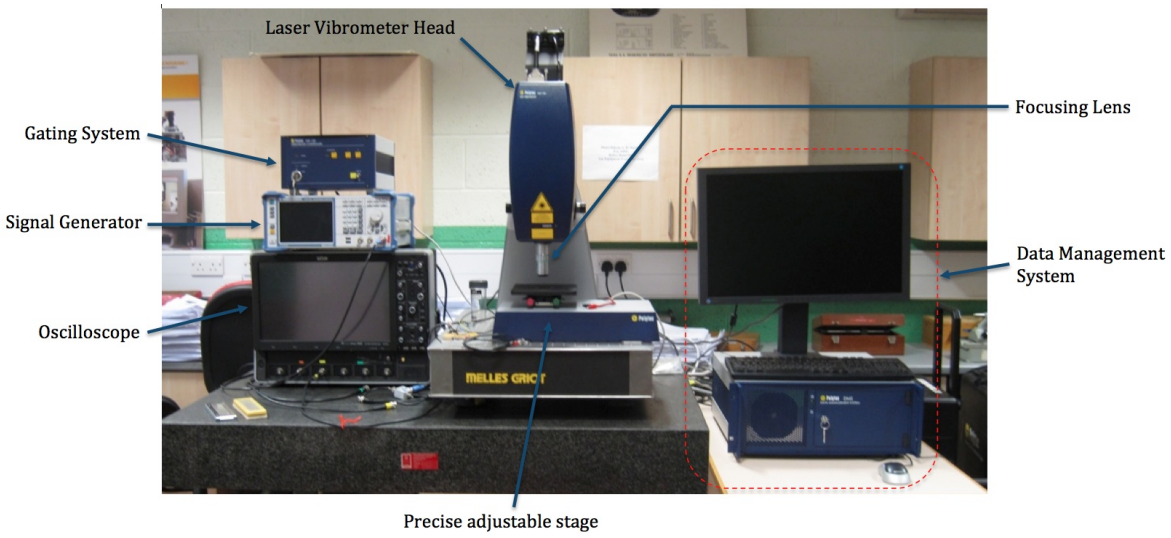


FIGURE 5.2: Set up illustration of the laser doppler vibrometer test.

In this system the laser head unit provided a detector signal that was obtained with a fast digital oscilloscope. The collected digital signal was then transferred to a data acquisition system (PC) where the carrier was extracted by a module in the software.

The system is integrated with a gate function to lower the power of the light and minimise the energy transfer from the measurement beam to the measurement spot. This helps easy

alignment of the beam on the sample to search and locate the point of interest. Additionally, this system is equipped with a camera and a bright field microscope illumination to monitor and control the measurement spot positioning. The minimum spot size is below 1 $\mu$m diameter [185], and can vary depending on the applied focusing lens. The device is capable of frequency measurements up to 1200 MHz. Since the measurement is performed by pointing the laser beam at predefined locations on the membrane, it is of paramount importance to prevent any movement of the membrane chip relative to the laser beam source [184]. In the initial test, the membrane was placed underneath the laser spot and was firmly fixed on the piezoelectric shaker disk using two strips of thermal tape. This is to make sure the window part of the membrane does not touch the tape. Then the shaker was glued on a fixed stand for the initial test (Figure 5.3).

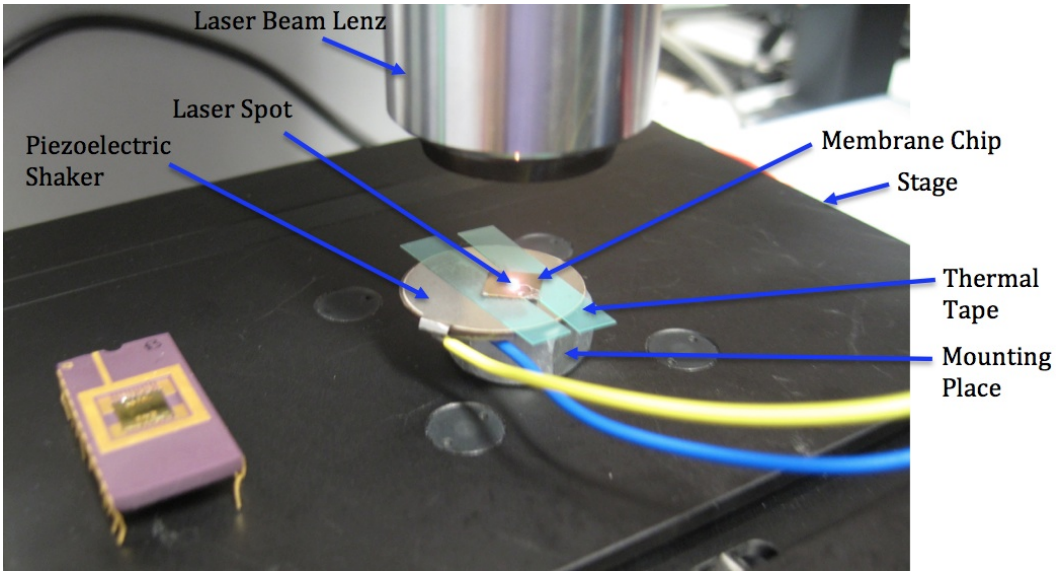


FIGURE 5.3: Silicon nitride chip mounting set up under the laser vibrometer beam.

A computer aided acquisition system was used in order to record the data generated from the vibrational behaviour of the TPM.

Experimental results were collected in a form of frequency response diagrams as shown

in Figure 5.4. These results were obtained for the TPM with deposited spiral coil.

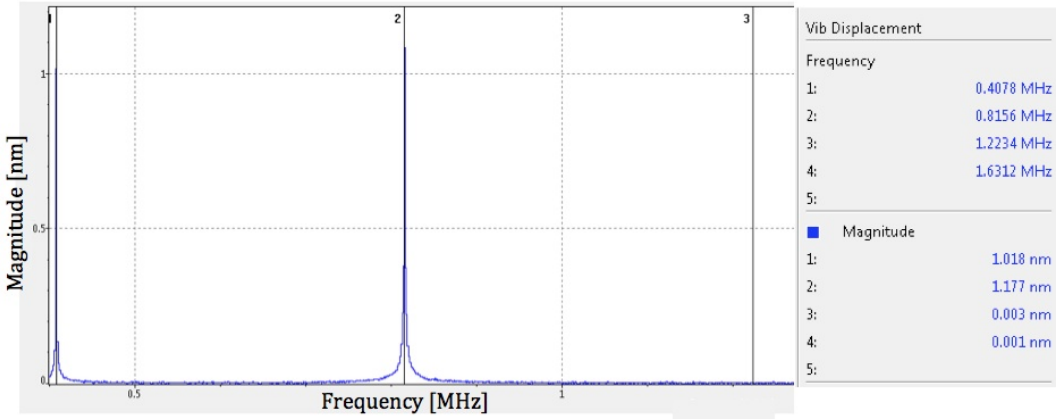


FIGURE 5.4: Frequency response of the coiled TPM using LDV.

The first peak on the left of the diagram shows the applied vibrating frequency to the membrane from a piezoelectric device. The second peak is the first resonance. It has been shown that the first resonance occurs at 0.8156 MHz which corresponds to the maximum vibrational amplitude of 1.177 nm. The same voltage and frequency drive point was used to measure amplitude of vibration of plain paddle. The frequency response of the plain paddle without deposited coil is shown in Figure 5.5. This figure shows that the maximum displacement has been reduced to 442.8 pm for the same driving vibrational frequency, which means that the resonance frequency was shifted and the plain paddle has a different resonance frequency. This is because the plain and coiled micro paddles have different masses. In this test the drive frequency was not changed to meet the vibration at resonance frequency of the plain micro paddle and its corresponding amplitude of vibration is therefore lower than what it is expected at resonance frequency.

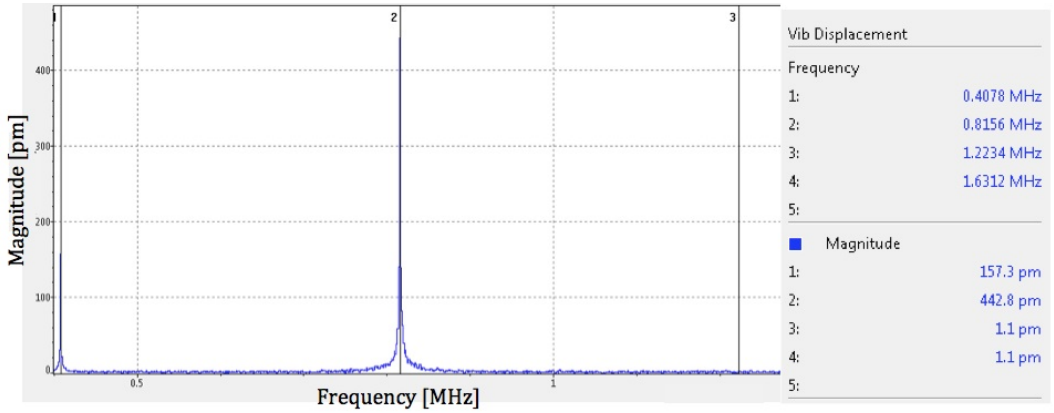


FIGURE 5.5: Frequency response of the plain micro paddle using LDV.

## 5.2 Frequency Response

The initial tests did not sweep through frequency, so the shape of the resonance could not be determined. Hence further tests was carried out using a configuration where the drive signal from the LDV, applied to the piezo shaker, was swept through the resonance peak. The chip was also now mounted in a 24 pin DIL chip carrier using thermo setting plastic to solidly fit the chip in place. In this configuration, the frequency response curve of the resonator was able to be recorded. The laser spot was positioned to give the maximum displacement signal amplitude, positioning was achieved using a grid mapping system as shown in Figures 5.7 and 5.8.

Next tests were implemented after mounting the membrane chip on a chip carrier. This configuration is shown in Figure 5.6

The frequency response in this configuration is depicted in Figure 5.7. This figure shows that the maximum peak at 0.818 MHz is 1.92 nm for the TPM integrated with spiral coil. While scanning over the plain paddle, over which there is no coil or platinum track present, the frequency spectrum depicted in Figure 5.8 is obtained.

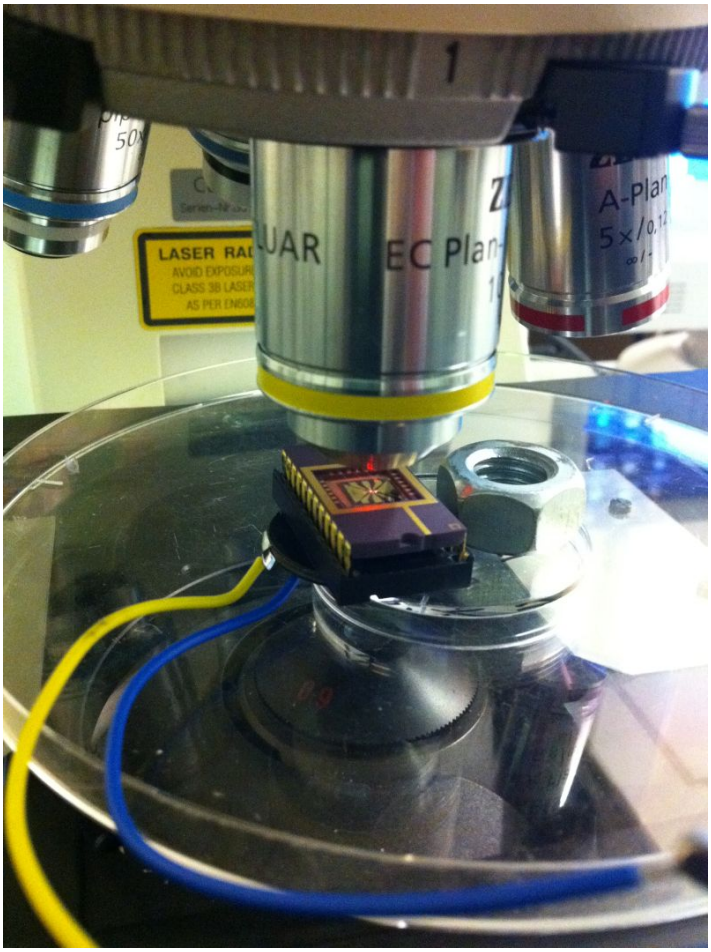


FIGURE 5.6: Test set up of the membrane mounted on the chip carrier under laser vibrometer system (at Aston University).

The frequency response shows the maximum peak of 3.67 nm at 0.841 MHz. This represents a difference of 23.750 kHz in comparison to the coiled TPM due to the reduced mass. This difference can be used to determine the mass sensitivity and will be discussed in Section 5.5.3.

## 5.3 Quality Factor Evaluation

As previously mentioned in Chapter 3, the rate of energy loss in a resonator can be characterised by evaluating its Q factor. A high Q factor is associated with a low rate of energy loss

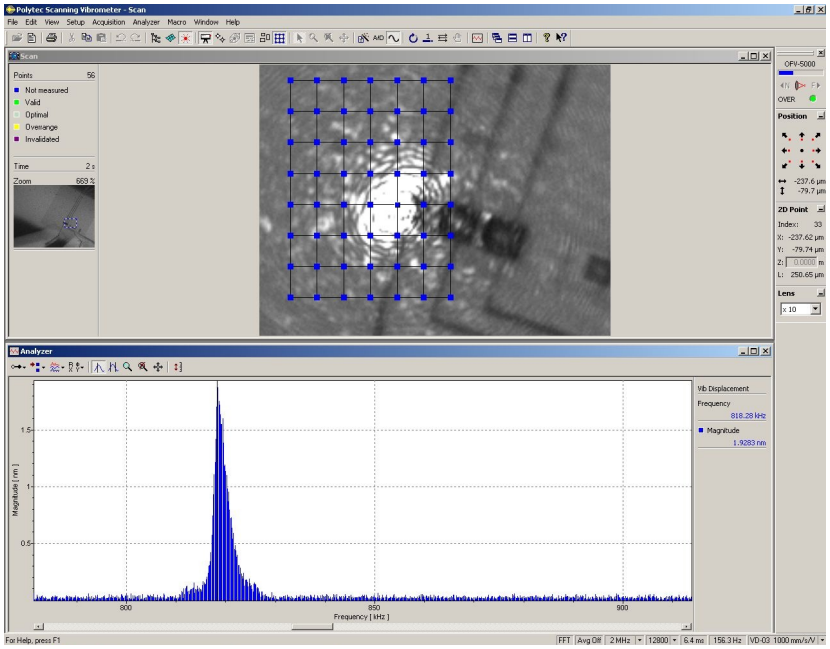


FIGURE 5.7: Frequency response of the coiled TPM mounted on chip carrier.

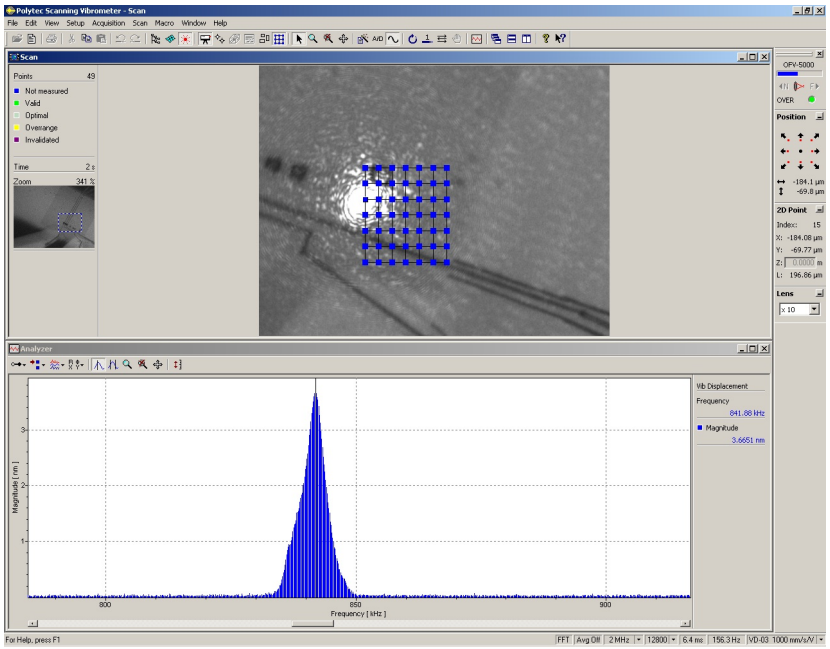


FIGURE 5.8: Frequency response of the plain TPM mounted on chip carrier.

from the system. First, the Q factor was determined from the Equation 5.3

$$Q = \frac{f_0}{\Delta f_{3dB}} \tag{5.3}$$

As shown in Figure 5.9, $f_0$ corresponds to the value associated with resonance frequency, and $\Delta f_{3dB}$ is the width of the frequency range where the energy is half its maximum value. The plotted data are related to the initial test (Figure 5.4), where single frequency drive was used to vibrate the TPM.

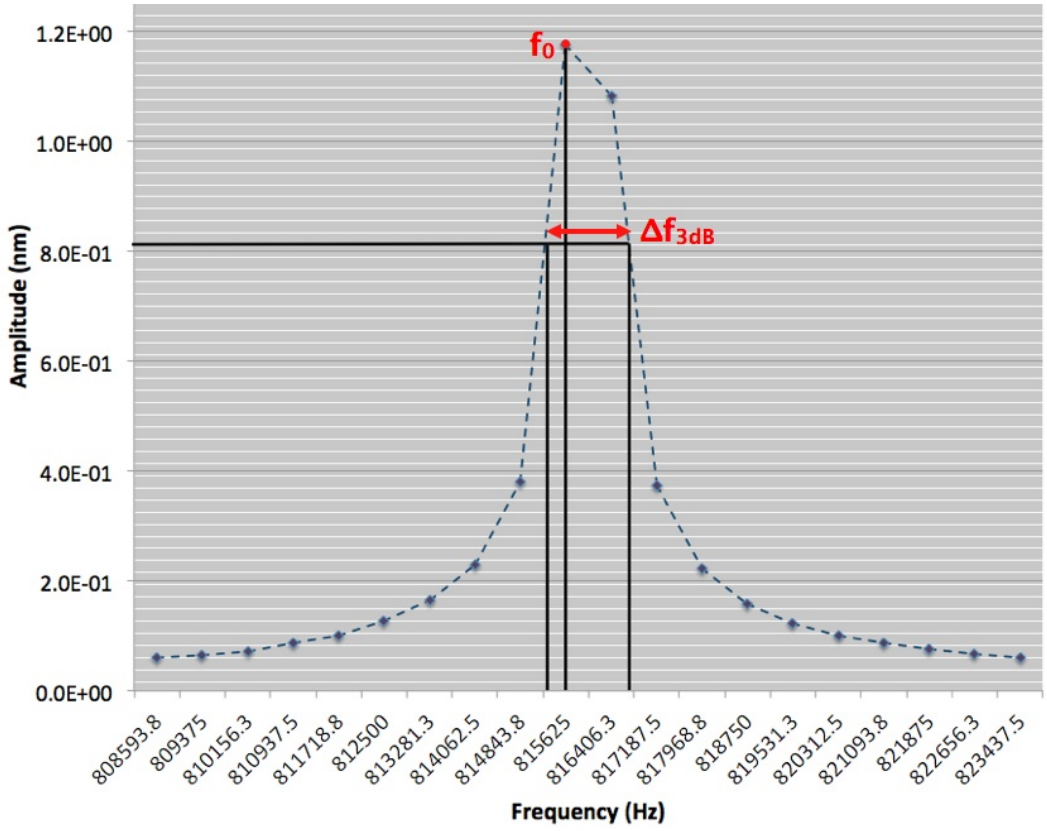


FIGURE 5.9: Frequency response of the TPM for quality factor evaluation.

From the experimental data collected, assuming the highest recorded amplitude occurs at the resonance frequency, the quality factor was determined to be 566 [23]. However, to obtain a more accurate value of the Q factor, a curve-fitting method was employed. This was

done in order to take into account the consideration that in reality the resonance occurs in between the two highest amplitudes. Previous works have shown that the most accurate fit for the resonance curve of MEMS resonators is the Lorentzian curve using nonlinear least-squares fit [186], applying frequency in the *x* axis and a variable proportional to the resonator deformation in the *y* axis. Equation 5.4 shows the formula of the Lorentzian curve.

$$y = \frac{y_{max}}{\sqrt{1 + 4Q^2(\frac{x}{x_r} - 1)}} \tag{5.4}$$

Where $x_r$ and $y_{max}$ correspond to each other and are constant for a set of data. $x$ and $y$ correspond to every point on the frequency-displacement diagram. The plot of deformation $y$ versus frequency forms a Lorentzian curve with the resonant frequency located at the position of the maximum magnitude.

Using this equation, the resulting Lorentzian curve is shown in Figure 5.10. The dotted points in the diagram show the collected experimental values from the measurement equipment and the continuous line represents the Lorentzian fit. Using this method the value of the quality factor was found to be 740 for the initial sample frequency spectrum diagram which was presented in Figure 5.4.

This data was collected without sweeping the frequency, so it is likely to be an over estimate fit where there are not enough data points within the measurement. It looks sharper than what it is in real case and it doesn't represent the resonant shape properly. Hence, curve fitting is also applied to the resonance peak obtained by sweeping the drive frequency. The Lorentzian curve fit to the frequency response previously obtained (Figures 5.7 and 5.8) are shown in Figure 5.11 and 5.12 respectively.

For these measurements, five results were collected for the coiled TPM and five results

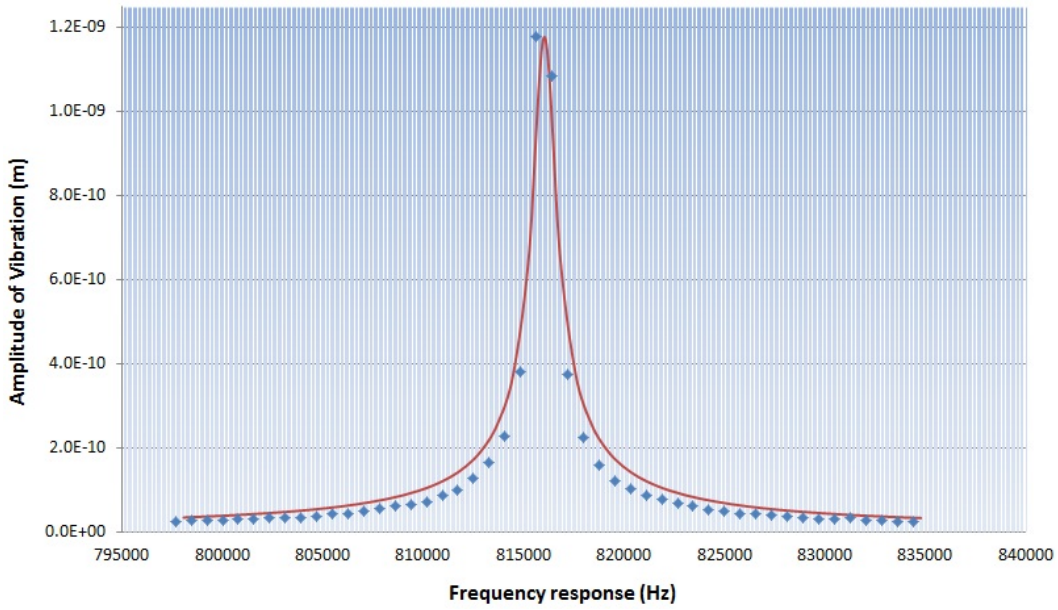


FIGURE 5.10: A Lorentzian curve fitting on the experimental measured data at the TPM frequency.

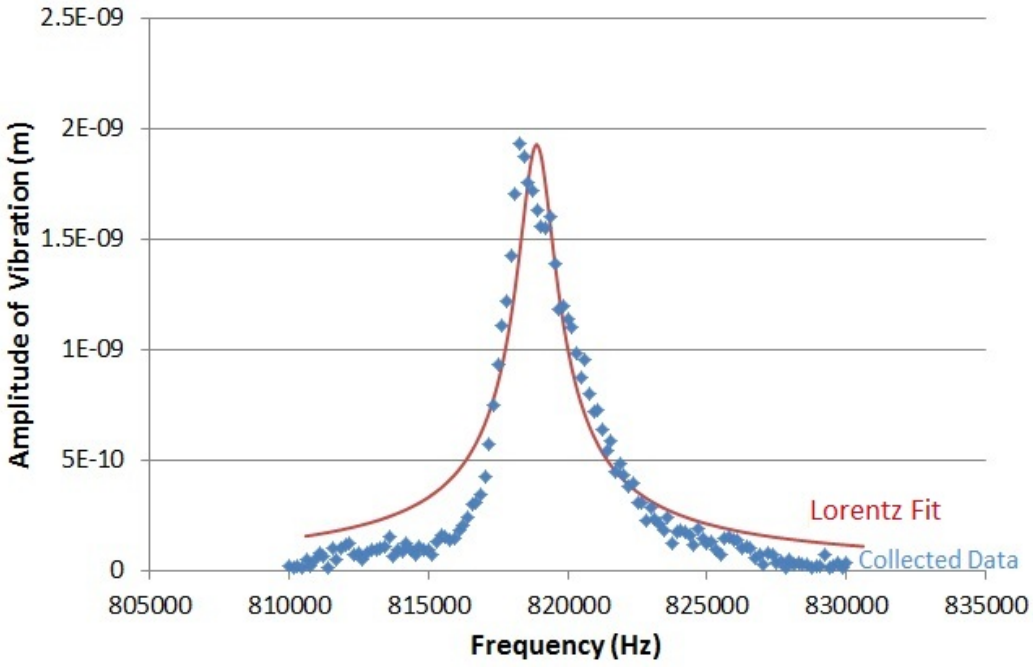


FIGURE 5.11: Lorentzian curve fit on the experimental measured data collected from the membrane mounted on the chip carrier. This result is collected from the TPM with integrated spiral coil.

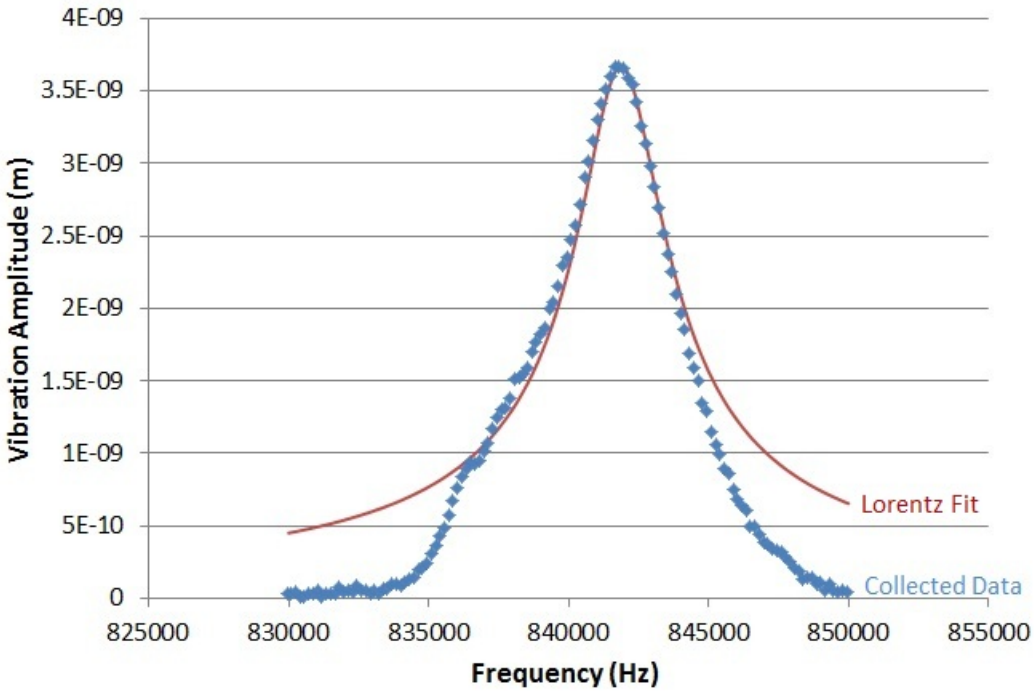


FIGURE 5.12: Lorentzian curve fit on the experimental measured data collected from the membrane mounted on the chip carrier. This result is collected from the TPM without platinum spiral coil.

were collected for the plain TPM. The coiled TPM was found to have a quality factor in the range of 360 - 500 and the plain TPM has a quality factor in the range of 270 - 310. The excessive discrepancy between the measured data and the predicted frequency in the small amplitudes of vibration can be caused by noise. The noise level in the amplitudes less than 50 nm is noticeable. Other sources of error can be related to energy dissipation, air damping, manufacturing accuracy and accuracy level of the measuring system. These parameters can amend the shape of the frequency diagram and its symmetry. The accuracy of the collected data is directly related to the measuring system. Smaller gaps between every two collected points would result in higher accuracy of the frequency response diagram.

## 5.4 Damping Factor

An introduction to the damping factor was provided in Section 3.3.2. Based on the described formula (Equation 3.40), the damping factor *b* would be 1.377E-20 (Hz·kg/m$^2$) for the coiled TPM and 9.33132E-21 (Hz·kg/m$^2$) for the plain TPM. However, this value is calculated by considering uniform and constant silicon nitride properties and the frequency obtained by laser vibrometer experiment.

## 5.5 Nanoindentation Test

As mentioned in section 4.1.1, the properties of silicon nitride such as stiffness, play a significant role in the behaviour of the TPM. In order to estimate the Young's modulus of the employed silicon nitride membrane, indentation testing was carried out using a table top nanoindentation tester (TTX-NHT, CSM Instruments) shown in Figure 5.13.

The test was carried out by POLYTEC representative in demonstration session at school of Mechanical Engineering in University of Birmingham.

### 5.5.1 Background

Indentation testing can be used to determine mechanical properties of thin layers such as thin films and coatings. Estimates of the hardness and elastic modulus of substrates can be obtained using indentation testing. It is carried out by pressing a sharp tip or indentor against a sample, normal to the sample surface and increasing the applied load up to a defined value. The load is then gradually removed. Applied loads are typically in the range of a few

FIGURE 5.13: Table Top Nanoindentation Tester (TTX-NHT) Device from CMS instruments.

hundreds of mN [2].

### 5.5.2 Indentation Test Results

The indentation test was carried out on a silicon nitride membrane. The load displacement curve obtained from the test is shown in Figure 5.14. Based on Figure 5.14 the elastic modulus of material is determined from the slope of the unloading curve. The modulus obtained in this manner is called indentation modulus. Five tests were carried out and a mean value of the Young's modulus was obtained to be 103.56 GPa. A similar value has also been reported by Kiesewetter et. al. as shown in Table 4.2.

The modulus obtained in this method is called "indendation modulus" of the sample

[2]CSM Instruments SA, Advanced Surface Mechanical Testing, CMS Indentation Testers brochure

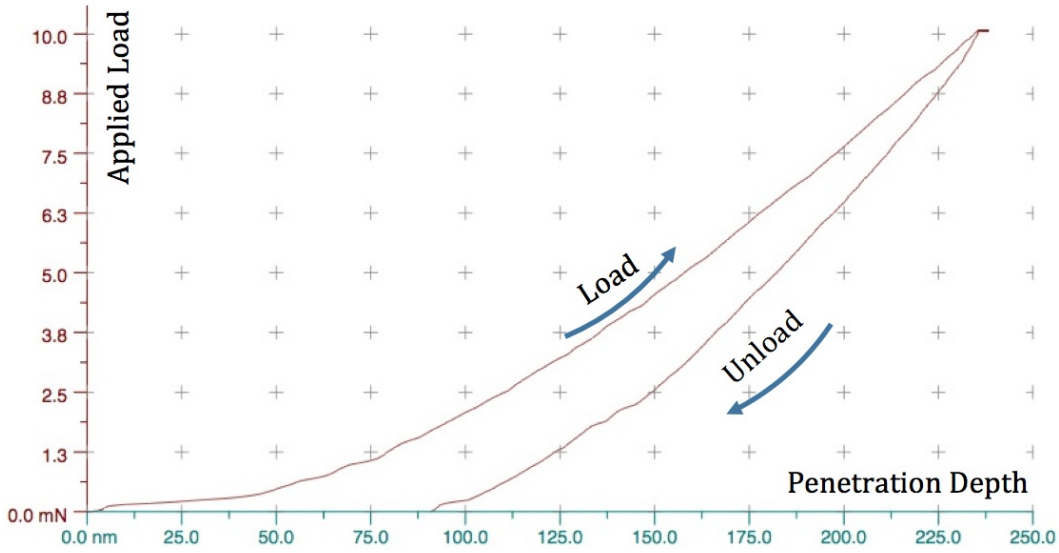


FIGURE 5.14: Load versus displacement diagram of the indentation test of silicon nitride membrane.

material, which is identical to the term "eastic modulus or "Young's modulus" [187]. Considering the measured value of the Young's modulus, the fundamental vibration frequency of the various designs of TPMs are given in Table 5.1.

TABLE 5.1: Resonance frequency of different designs.

| TPM Design | Resonance Frequency |
|---|---|
| Plain Paddle | 1.611 MHz |
| TPM with single Pt track | 1.433 MHz |
| TPM with dual loop track | 1.289 MHz |
| TPM with spiral coil | 1.331 MHz |

The discrepancy from the values measured in experiments are due to energy dissipation factors, increased mass loading from the air damping and dimensional accuracies due to the fabrication process of substrate and the device.

### 5.5.3 Added Mass and Sensitivity

Here the added mass is considered to be the mass of the deposited spiral platinum track. In order to determine the mass sensitivity of the sensor, the shift in frequency due to the added mass of the platinum track is used. For this purpose, first a plain micro paddle is used for the frequency measurement and then the same sample is integrated with dual platinum spiral coil and again the measurement was taken place. Density of the added FIB deposited platinum track is calculated theoretically according to the composition of the FIB deposited platinum. Previous work has shown using transmission electron microscopy that the deposited metal composition is 46% Pt, 24% C, 28% Ga, and 2% O [153]. By using the density of each element and multiplying it to its percentage and adding them up gives an average density of 12.06 g/cm$^3$ for the deposited platinum on the micro paddle. Table 5.2 represents the properties of the each element consisting the FIB deposited platinum.

TABLE 5.2: Properties of the elements consisting the FIB deposited platinum.

| Element | Percentage | Atomic weight (gr/mol) | Density (gr/cm$^3$) |
|---|---|---|---|
| Platinum | 46 | 195.084 | 21.45 |
| Carbon | 24 | 12.0107 | 2.26 |
| Gallium | 28 | 69.7230 | 5.904 |
| Oxygen | 2 | 15.9994 | 1.429 |

The Equations 5.5 shows how the density of the FIB deposited platinum is calculated.

$$D_{Pt} = \Sigma(D_{Ei} \times C_i) \tag{5.5}$$

where $D_{Pt}$ is the density of the FIB deposited platinum, $D_{Ei}$ is the density of the every existing element in the composition of the FIB platinum and $C_i$ is the percentage associated with every element. In order to calculate the volume of the deposited platinum, the overall

length of platinum track (400 $\mu$m) is multiplied by its cross section (100 nm$^2$) which is 4.0 , the added mass onto the micro paddle is 96.5 pico ($10^{-12}$) grams. This added mass of 96.5 pg corresponds to 23 kHz decrease in frequency between the plain paddle and paddle with pt spiral track, as was experimentally obtained (Section 5.1.2).

To verify the mass detection characteristics of the paddle, the added mass on the paddle was also calculated using Equation 2.5, by substituting the experimentally obtained values of 0.841 and 0.818 MHz in the formula.

This gives a calculated added mass of 54.06 pg which is in the same order of magnitude as the calculated value based on composition of deposited platinum. The sensitivity of the paddle to mass detection can be calculated from Equation 2.6 to be 2.35 fg/Hz.

## 5.6 Electrical Measurements

### 5.6.1 Resistivity Measurement

To ensure proper funcitoning of the TPM device, an electrical conductivity test was initially carried out using a parameter analyser and a probe station (showing in Figure 5.15)

The tested sample consists of two TPMs. According to the Figure 5.16 one is connected to the two middle bond pads (bond pads #3 and #4) and the other is connected to the two upper bond pads (bond pads #1 and #2). The lower two bond pads (bond pads #5 and #6) are not connected to any device on the membrane. The resistivity between the bond pads was measured using the parameter analyser as shown on the Figure. This test reveals that there are connections between the bond pads that are not supposed to be connected (connections

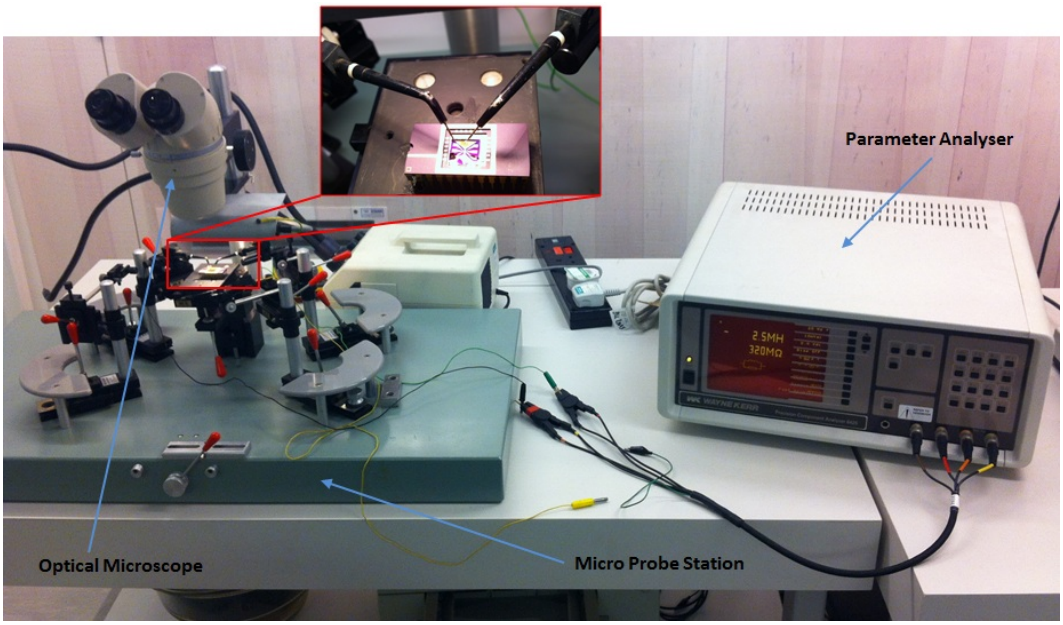


FIGURE 5.15: Parameter analyser and probe station set up for testing electrical properties of the fabricated platinum coil on the TPM.

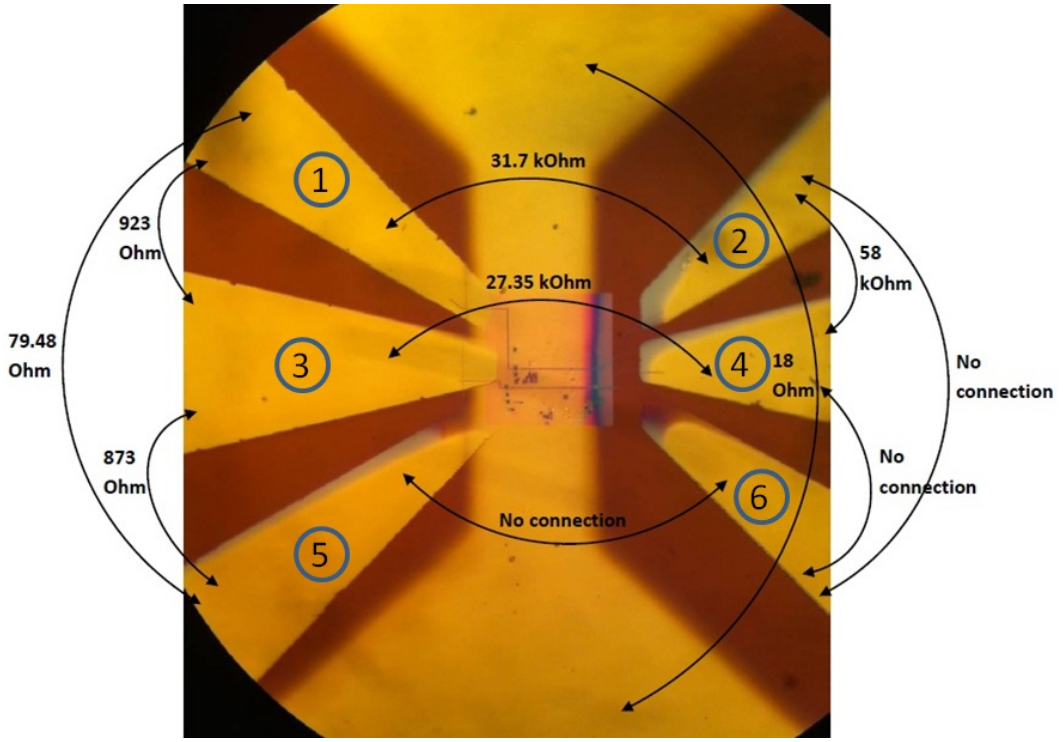


FIGURE 5.16: Resistivity measurements of two TPMs integrated with spiral dual Platinum coil mounted on chip carrier.

between #1, #3, #5 and #2, #4, #6). Although inspections were made during the fabrication to make sure the tracks were well isolated from the sputtered gold layer, the results of these tests indicate that the tracks were in fact not isolated from each other. In order to understand the reason for the presence of these connections, some experiments were designed and conducted as follows.

First, it was decided to measure resistivity of a raw sample and then use a normal FIB etch and an enhanced FIB etch method to isolate the bond pads from where they are in contact with middle gold layer. The result of this investigatory test is presented in Figure 5.17 (a). In this test three trenches were made under the top three bond pads. One with a normal etch method and the other two is with enhanced etch techniques. This test show the enhanced etch has isolated the bond pad from the middle gold layer (Figure 5.17 (b)).

Thus, isolation of the bond pads is possible using an enhanced etch FIB milling method.

Second, a fabricated sample was modified with enhanced etch method. For this purpose, the same etched patterns on either sides of the tracks were etched with 100 pA beam energy for another 20 nm depth and results are presented in Figure 5.18.

Since the connections were still existing between wrong bond pads, it was decided to modify the sample one more time but with different enhanced etch milling depths. Therefore, another 20, 30 and 40 nm depths were etched on the three TPMs fabricated on the membrane. The results are presented in Figure 5.19.

A comparison between Figure 5.18 and Figure 5.19 demonstrates that using a higher etching depth results in better isolation. According to these two figures, the resistance between the bond pads have increased after higher milling depth using the enhanced etch method. Therefore, enhanced etch was used to fabricate a new sample. However, due to the flow

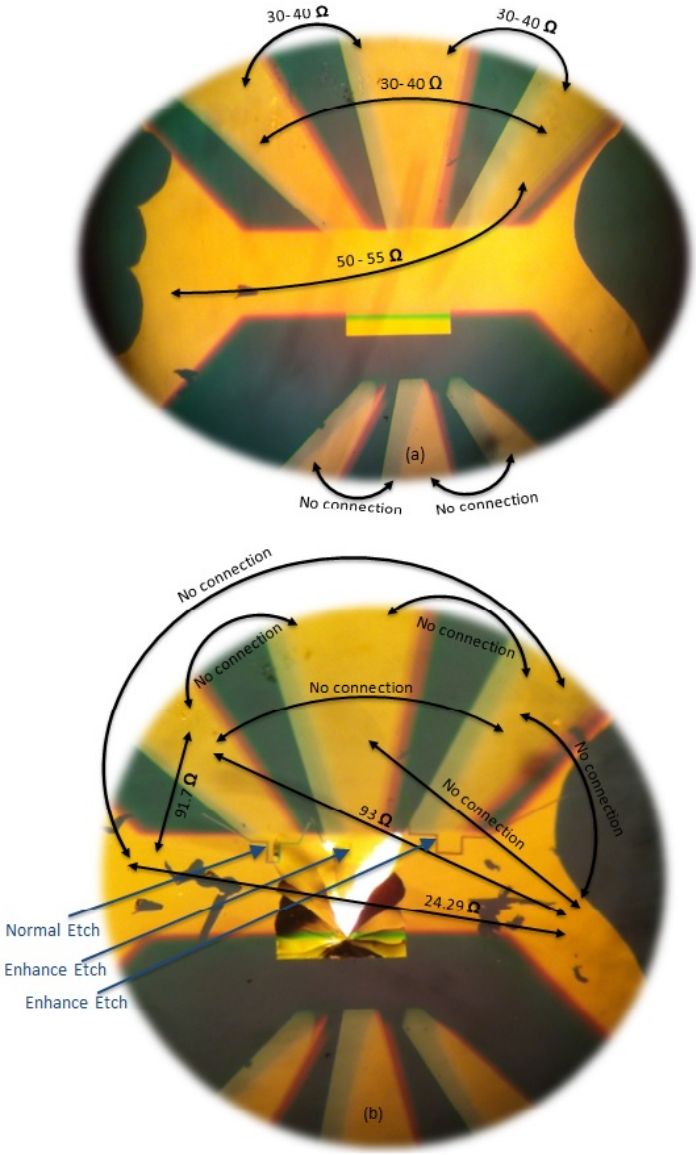


FIGURE 5.17: Connectivity test results. (a) using a common FIB milling, (b) using Enhanced Etch milling technique.

of gas during the enhanced etch it was noticed that thin pattern areas with widths in range of 100 nm does not meet the required dimensional accuracy, the gas results in widening of the etch area. This means when long thin patterns are used, for example 4 $\mu$m long by 100 nm width, the etched area will have a thicker width of 300$\pm$30 nm. But this method was successfully applied for fabricating paddles with dual loop platinum tracks and also a single line platinum track. Figure 5.20, illustrates an SEM image of the fabricated TPM with dual

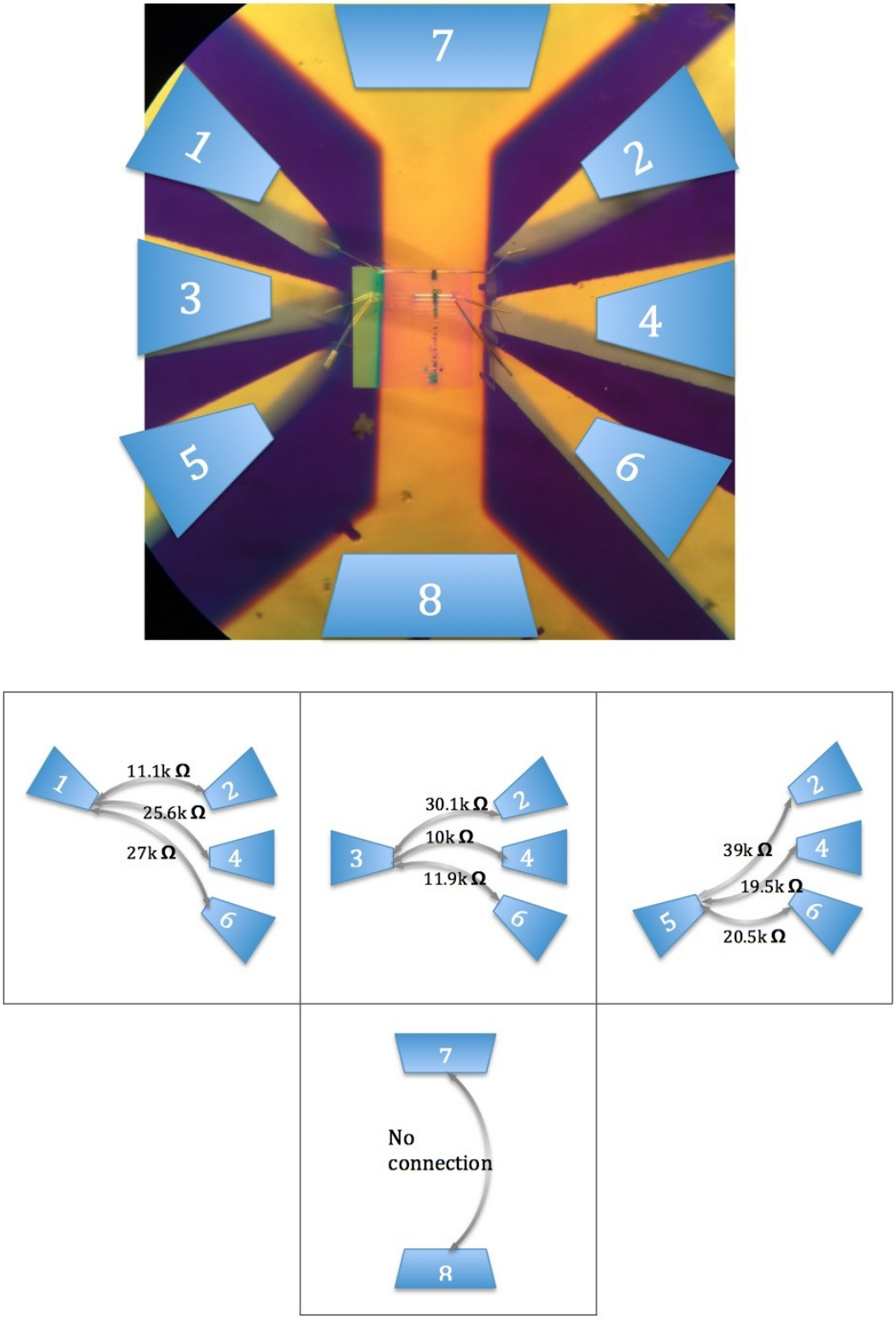


FIGURE 5.18: Resistivity measurements of three TPMs integrated with spiral dual Platinum coil mounted on chip carrier after 20 nm depth of Enhanced Etch on isolating sections.

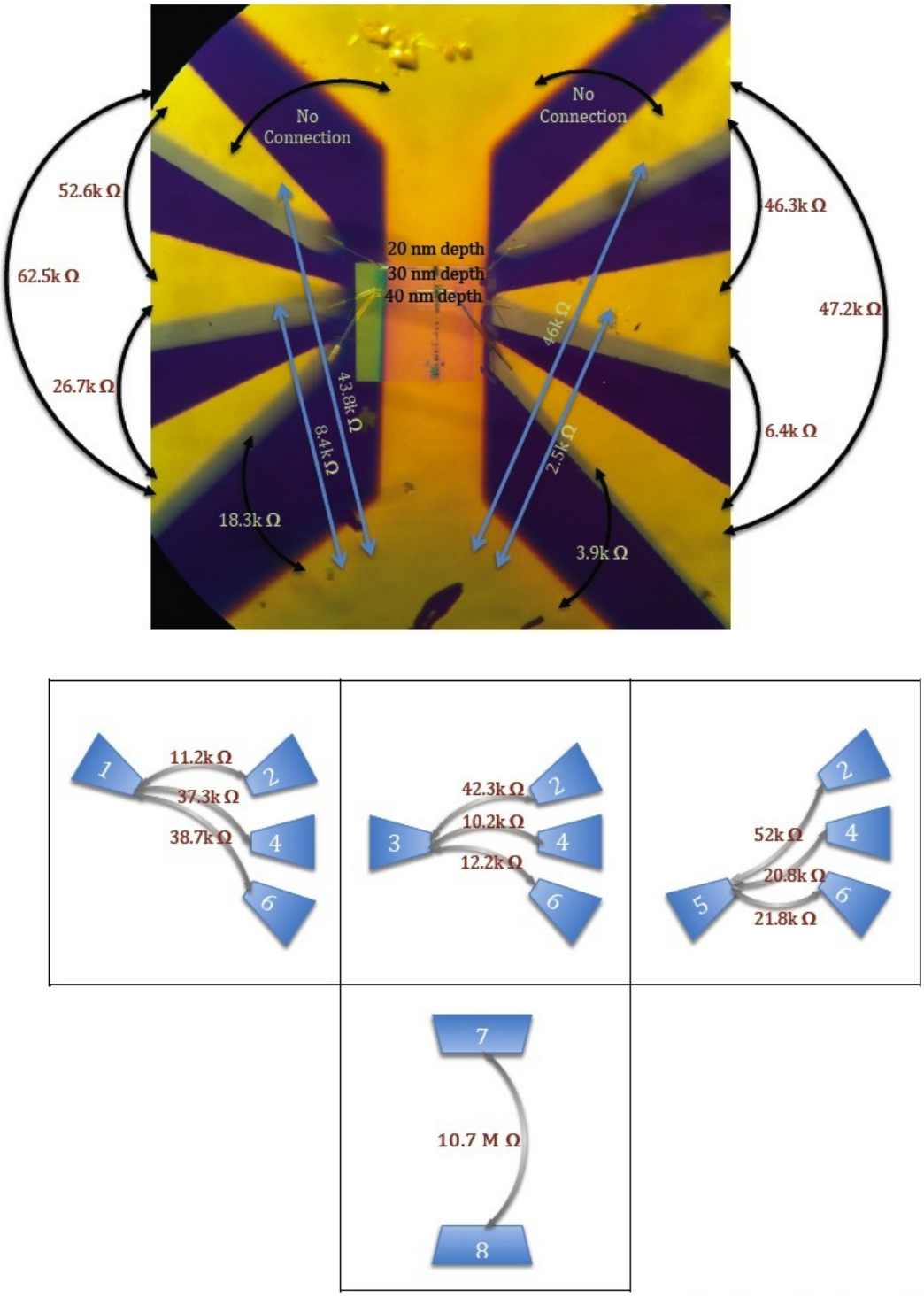


FIGURE 5.19: Resistivity measurements of three TPMs integrated with spiral dual Platinum coil mounted on chip carrier after extra 20, 30 and 40 nm depth of Enhanced Etch on isolating sections.

loop platinum track.

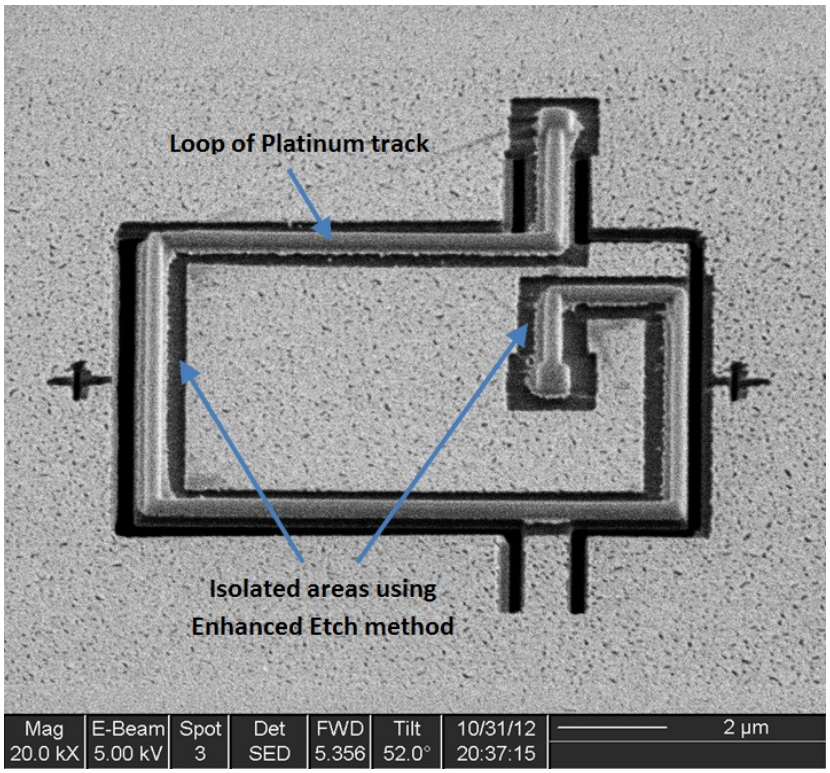


FIGURE 5.20: SEM image of the fabricated TPM integrated with dual loop platinum track.

The width of the enhanced etched area is 300±30 nm. This ensures that the track is isolated from the rest of the gold layer.

The results of the resistivity test for these two paddle designs are shown in Figures 5.21 and 5.22.

TPMs shown in Figure 5.21 (left) with a single platinum track has shown resistivity of 64.95 kΩ whereas the theoretical value is in the range of 92.7 - 185.5 kΩ. In the same figure, the other TPM (right) has shown a resistivity of 98.24 kΩ whereas theoretical value is in the range of 104.5 - 209.1 kΩ. TPMs depicted in Figure 5.22 are fabricated with dual loop platinum track. TPM with dual loop on the left has 125.2 kΩ resistivity whereas the value obtained theoretically is in the range of 68.5 - 137.1 kΩ. In the same figure, the other TPM

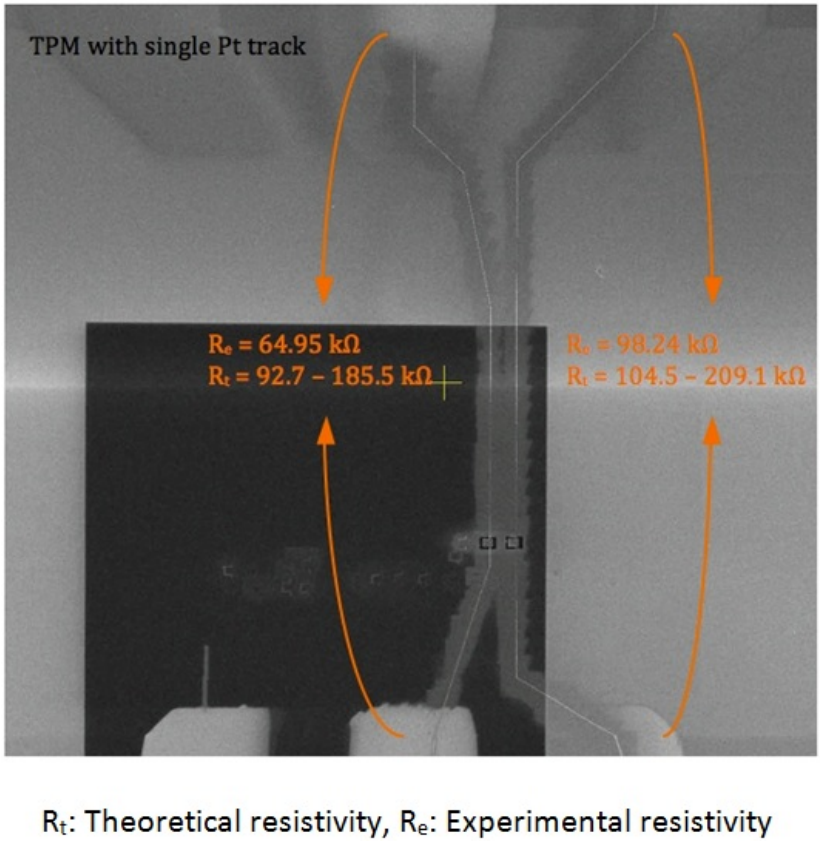


FIGURE 5.21: Experimental versus theoretical values of resistivity in fabricated single track TPMs.

(right) with the same dual loop track configuration has shown 26.11 kΩ resistivity and the theoretical value was in the range of 72 - 144 kΩ for this sample. Three of the fabricated samples show close resistivity to the theoretically approached values which indicates that there is no short circuit.

### 5.6.2 Wheatstone Bridge Test

In order to evaluate the response of the device by passing an alternative current through the platinum track, Wheatstone bridge test was carried out. As shown in Figure 5.23, there are four resistors arranged such that, there will be a zero current (*null*) passing through the middle connection. Here, by changing the AC current through the driver ($V$), the behaviour

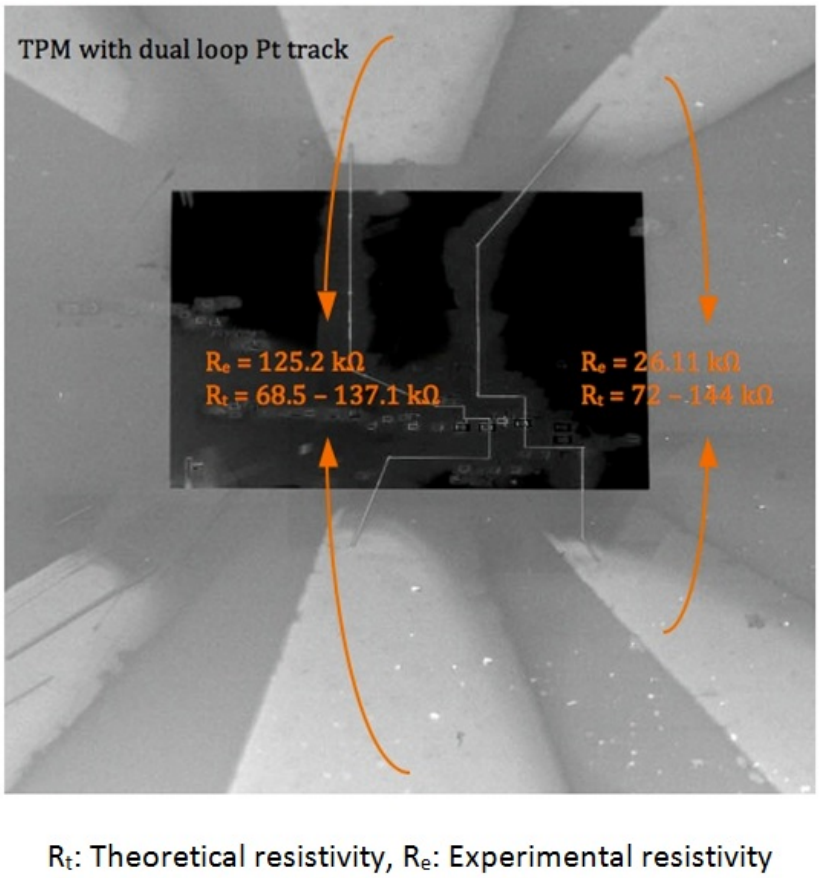


FIGURE 5.22: Experimental versus theoretical values of resistivity in fabricated dual loop track TPMs.

of the device ($R_p$) can be monitored.

In this test, the drive voltage was set to 5 volts. The test was started with low drive frequency and then gradually the frequency was increased up to the resonant frequency of the device. However, It was found that after 450 kHz the response shows a reduction in frequency spectrum, which indicates that stray capacitive effect ($C$) is taking place. This effect shows that the current is now passing through the substrate instead of device. Since the size of the bond pads are big, it is suspected that this is the reason why the current is now passing through the substrate and not the device. Therefore, in order to function the device a new design for bond pads needs to be fabricated that has smaller area.

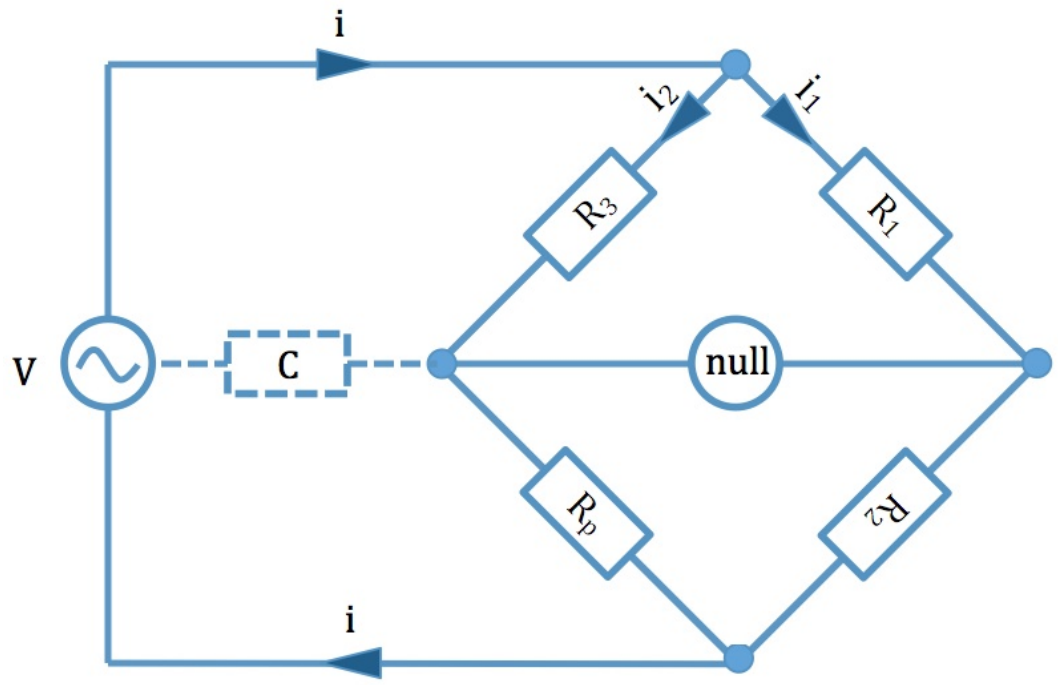


FIGURE 5.23: Schematic of a Wheatstone bridge system.

## 5.7 Surface Treatment

In addition to the mechanical and electrical properties of the TPM, the coil on the TPM also effects the surface characteristics. Since micro platinum coil brings surface roughness to the TPM surface, it increases the hydrophilicity of the TPM. Figure 5.24 is an SEM image showing a milled cross section of the TPM in 45° tilt angel.

Therefore, an $O_2$ plasma treatment was used to enhance the hydrophilicity characteristics of the TPM. For this purpose, silicon nitride membranes were inserted into a low-pressure radio frequency (RF) plasma chamber. The plasma treatment was performed at a working pressure of 40 mTorr and, an oxygen flow of 50 sccm in 40°C. The oxygen plasma power and exposure time were respectively 800 W inductively coupled power, 20 W platen power and 15 seconds. Increase in surface hydrophilicity was demonstrated by the decreased contact angle as shown in figure 5.25.

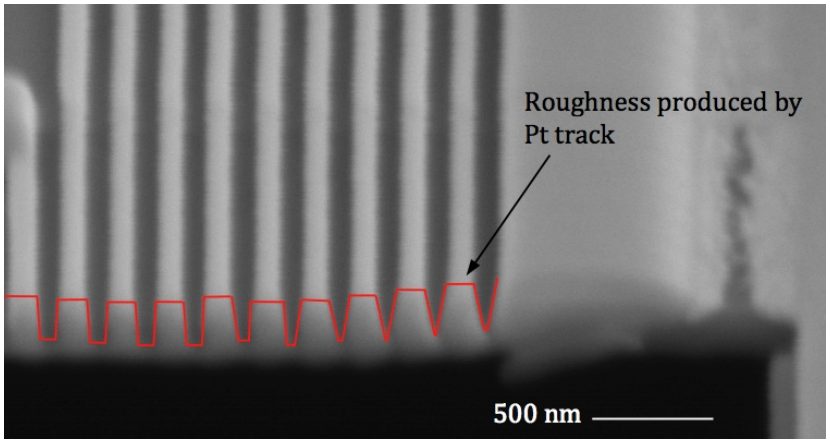


FIGURE 5.24: Surface roughness generated after deposition of platinum track.

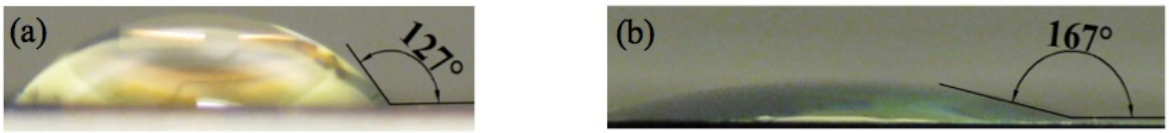


FIGURE 5.25: Contact angle is measured (a) before and (b) after surface treatment.

## 5.8 Discussions

This project involves design, manufacture, test and results. Measured results from the fabricated device was found to differ from the values predicted in the design stage. Figure 5.26 shows this relationship.

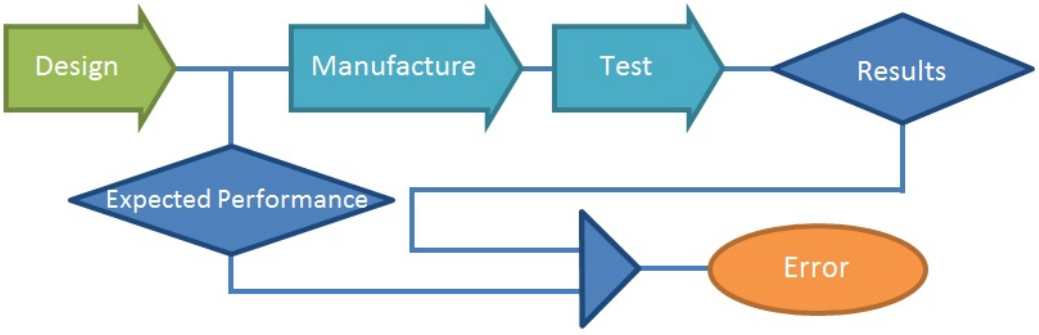


FIGURE 5.26: Diagram of the error produced in the system design.

Difference between the actual result and the predicted result can be due to variety of

parameters. Here it has been tried to explain some of the more likely reasons for these discrepancies. For this purpose, the predicted values and the actual test results are collected in Table 5.3 for easier comparison.

TABLE 5.3: Predicted and measured values.

| Parameter | Predicted values | Test result |
|---|---|---|
| Resonant frequency of the coiled micro paddle | 1.33 MHz | 0.818 MHz |
| Resonant frequency of the plain micro paddle | 1.23 MHz | 0.841 MHz |
| Amplitude of vibration | 4.21 - 11.23 nm | 1.92 - 3.67 nm |
| Resistivity of TPM with single track (Sample no.1) | 92.7 - 185.5 kΩ | 64.95 kΩ |
| Resistivity of TPM with single track (Sample no.2) | 104.5 - 209.1 kΩ | 98.24 kΩ |
| Resistivity of TPM with dual loop track (Sample no.1 ) | 68.5 - 137.1 kΩ | 125.2 kΩ |
| Resistivity of TPM with dual loop track (Sample no.2) | 72 - 144 kΩ | 26.11 kΩ |

From Table 5.3, it can be seen that the predicted results are greater for the resonant frequency and vibration amplitude. This can be due to the modelling conditions, which does not include damping effect. In addition, the drag force applied on a system has two components where one contributes to an additional mass applied on the cantilever and results in shift of the resonant frequency. According to the following formulas of the torsional stiffness and terms in torsional constant in compare to the polar mass moment of inertia, It was found that 10 percent change in width (*2a*) of the supports have the greatest effect in spring constant, then is the length of the supports and finally the mass have the least effect.

$$K_t = \frac{T}{\theta} = \frac{KG}{L} \tag{5.6}$$

$$K = b^3 a \left( \frac{16}{3} - 3.36 \frac{b}{a} \left( 1 - \frac{b^4}{12a^4} \right) \right) \tag{5.7}$$

$$J'_p = \frac{m_p}{48}(7L_p^2 + 4t^2) \tag{5.8}$$

One of the main factors is related to the model itself, the model is a simplified version of the real device, therefore, all the involving conditions are not considered in the modelled version. Material properties used in analysis might be different from the actual substrate material due to sensitive LPCVD silicon nitride production process which lead to slight difference in properties of the product of every produced batch. This also generates errors in the thickness of the silicon nitride membrane, which is difficult to control and also measure. Dimensional accuracies of the fabricated device such as thickness of the silicon nitride membrane, width and length of the FIB milled micro paddle, dimensions of the deposited platinum track have tolerances and might not be exact as the modelled device. The deposited platinum can have different growth rate at different machining times and this also increases the probability of having not an exact required depth. In addition, measurement facilities have a certain accuracy tolerances which might affect the recorded results. The amount of deformation according to the design is 8.9 nm for the dual coiled TPM. However, the measured vibration test shows 1.92 nm amplitude for this design. The predicted resonance was also obtained through COMSOL FEA package to be 1.23 MHz for the plain micro paddle but in the measurement 0.841 MHz was recorded. It is important to note that in the calculations, air damping is not included due to the complexity. The higher amplitude of vibration results in high Q factor when device is running in a vacuum, which is the case of the finite element analysis. Since Q factor is related to the energy dissipation, damping effects it and reduces the Q factor. Also sharp peak can increase the sensitivity and therefore it allows measuring small changes in resonant shift. As it was mentioned earlier about the differences in material

properties, the deposited platinum also can be effected. The consisting elements might have a different concentration and this can effect the electrical properties of the deposited track. To evaluate electrical performance, a resistivity test was carried out for four devices that were fabricated using enhanced etch method. Two devices with single platinum track has shown 64.95 and 98.24 kΩ whereas in the theory based on the track length the values are 92.7 - 185.5 kΩ and 104.5 - 209.1 kΩ respectively. The two dual loop track devices have shown 125.2 and 26.11 kΩ, whereas the theoretical values are 68.5 - 137.1 kΩ and 72 - 144 kΩ. The difference might be due to the different material properties used for the theoretical approach and the real material. Besides, the accuracy of the fabrication can effect this value. One of the difficulties in the deposition is that the control of the deposited depth is difficult and sometimes the growth rate changes based on the machine conditions. However, in these four tests, only one sample has shown a significant difference and the other three measurements are close to the predicted values. In general, the obtained test results are in a good agreement with the predicted values. According to the system-level model produced in chapter 3 it is clear that the device will be fully operational. In this chapter it was shown that the noise effects the frequency response diagram in the areas less than 1 nm, therefore, the designed parameters show that the Lorentz force will produce reasonable amount of force to vibrate the device well beyond this amount, which would be in good detecting limit. In order to operate the device, operating temperature of the receptor layer and target species should be considered. It is unlikely that the dipicolinic acid survives in few hundreds of degrees. However, based on the complexity of the Joule heating simulation, the obtained value is for one directional current but the device is designed to work with alternative current, which might lead to much lower temperature. Also, only a section of the membrane, where the device

is located, is simulated and therefore heat loss through the conduction will be much greater in a real device. In addition, if too much heat is generated while the device is operating in real case, a Peltier cooler can be added in order to control the temperature level and prevent critical heating. This issue is also included in future work tasks.

## 5.9 Conclusion

It has been shown that the fabrication of the TPM was successful and frequency response results indicate the required sensitivity was obtained. Electrical measurements shows the tracks were isolated and there is no short circuits. The surface treatment was implemented to increase hydrophilicity of the TPM surface which is a required properties for chemical compound coatings.

# 6

# Conclusion and Future Works

## Contents

**Summary** In this chapter the overall conclusion of the research project is given followed by the potential work for the further development of the fabricated mass sensor.

The aim of the work carried out in this thesis was to develop a mass sensor suitable for mass sensing in the range of fg. A literature survey has shown a great potential for the application of mass sensors in the health care, environment and security industries. A variety of approaches have been adopted to improve sensing capabilities, particularly in relation to bio sensing applications. MicroElectroMechanical Systems (MEMS) have shown to be a promising approach in developing sensors to fulfil the requirements in this sector. In Chapter 2, the various actuation and read out mechanisms that have been employed in MEMS based mass sensors were summarised. A review of the state of the art in mass sensing devices was carried out with a comparison of systems in terms of their novelty, strength and weaknesses.

In Chapter 3, the design and theory of operation of micro paddle resonators and their application for mass sensing were given. The proposed TPM relies upon an increase in the moment of inertia of the paddle about the torsional spring axis and a consequential reduction in the resonant frequency, upon mass adsorption [57]. This design allows for the independent optimisation of the paddle functionalisation surface and the torsional springs, which is not the case in cantilever based resonators. Three different paddle designs consisting of platinum track were designed and generated. The natural frequency of vibration of these devices was predicted analytically to be in the range of 1.2 to 1.5 MHz. The device is constructed to have no interacting surfaces at the characteristic length so drag force in a continuum dominates the damping [188].

Three designs of TPMs were proposed, TPM with single platinum track, TPM with dual loop platinum track and TPM with dual spiral platinum track. Analytical calculations were implemented to estimate the mechanical behaviour of the proposed paddle resonators in terms of their predicted fundamental frequencies and angular displacement. Finite element

simulations were also conducted to predict characteristics such as the device fundamental frequency, stress propagation pattern, generation of heat, inductance of the platinum spiral coil, and magnetic strength across the membrane within packaging. A complete system-level model is developed and explained in order to give a clear overview about all the predicted values and to ensure the functionality of the device.

The process for fabricating the TPMs was described in chapter 4. The paddles are fabricated from LPCVD silicon nitride membranes which have shown a great suitability for their use in micro resonating devices. In this research the use of state of the art fabrication approaches for realising micro torsional paddles was described. The focused ion beam milling technique was exploited and detailed fabrication steps were outlined in Chapter 4. The fabrication of a Lorentz force actuation system was also explored using focused ion beam induced deposition of an amorphous platinum track. Machining considerations were described along with methods for inspecting the fabricated prototypes. Fabrication technique show the reproducibility is not problematic since all the fabrication steps and patterning areas can be saved and loaded for subsequent fabrication of devices. A device for packaging the TPM was designed and produced using a 3D printer. This packaging system enabled magnets to be mounted across the chip carrier and protects the upper surface of the membrane.

In Chapter 5 the characterisation of the fabricated prototype TPM using a laser vibrometer device was presented. The Q factor of the resonator is key to achieve high mass resolution [27]. Device tests showed a good quality factor in the range of 270 to 500 in atmospheric pressure. In order to test the sensitivity of the device to added mass the resonant frequency of the plain paddle was compared with the resonant frequency of a paddle with a known calculated mass (spiral platinum track). The mass sensitivity of 2.35 fg/Hz was obtained.

The proposed plan for using the Lorentz force actuation mechanism was investigated. It was planned to measure resonance electrically using parameter testing equipments in Electrical Engineering department in this way it was hoped that resonance would be seen through variation of absorbed power. However, it proved impossible to measure the resistance of the coil in the resonance frequency of the TPM. It was concluded that this was due to stray capacitance effect around the contact pads. This meant that the contact pad capacitance acted as shunt impedance preventing current from flowing through the coil at higher frequencies. It is clear that in future work the chip layout will have to be redesigned to remove this effect or FIB should be used to isolate the contact pads then use a micro probe system.

Nanoindentation tests were conducted on the device membranes which enabled an estimation of the membrane stiffness (Young's modulus of 103.56 GPa). This parameter was then used for the analytical calculations and simulations. The tests conducted using the laser vibrometer showed that the natural frequency occurs at 0.8 MHz. The plain micro paddle and coiled micro paddle show a 23 kHz discrepancy, which is close to the predicted value using analytical approach, taking into account that in simulation and analytical calculations damping was not included.

Thus, to summarise a mico torsional paddle was realised with detection sensitivity of 2.35 fg/Hz. This was inspected based on shift in resonance frequency of 23.75 kHz after adding 54.06 pg of platinum mass. Additionally, the adoption of a MEMS based approach in itself offers a number of advantages such as:

- Small size which allows probing of areas that are difficult to access with current, more bulky systems. Additionally a compact design would allow a high density of sensors to be placed in a network of sensors, thus allowing simultaneous detection of bio-warfare

agents over a large area

- Ease of fabrication with consequent reduction in cost
- Capability for real time monitoring and detection

Potential future work associated with further development of this project can be indicated as follows:

- Actuation of the TPM by means of Lorentz force and integration with real time device measurement.
- Readout system utilisation.
- Investigation of mass detection with series of controlled test masses. Understanding of the effects of the position of the added mass on the TPM.
- Integration of chemical coatings onto the TPM and evaluation of its effects on absorption of target molecules and collaboration with chemical engineering department for this purpose.
- Accurate measurement of the heat generation while the device is operating. If the amount of heat is too high, the device needs to be integrated with a Peltier cooler in order to reduce and stabilise the temperature level.
- Collaborations are planned with Technical University of Wroclaw to operate the paddle in torsional mode using the Lorentz drive, later in 2014.

To summarise, the work presented in this thesis has shown a novel approach to produce single and dual side micro machined micro paddle resonators. The fabrication of the micropaddle and coils was undertaken with a focused ion beam system that facilitated the complicated fabrication process needed for the coils and micropaddle. Forming the micro paddle and deposition of a conductive track to develop the Lorentz force actuation method

was carried out in this system. Alternative conventional fabrication methods were considered but difficulties of alignment and other complexities together with the absence of key processes in our laboratory directed us toward the FIB method. This has several advantages, in particular speed and flexibility and is easy to align because of the intrinsic microscope capability. This makes it uniquely simple to align front and back coils with the connecting via and facilitates placement of the input, output connecting tracks on the narrow bridges. The spiral coil patterns were generated using a pattern programing software within the FIB system. The details of the developed processes are recorded in this thesis and can be used by researchers designing coils of similar dimensions or using focused ion beam to create other features of similar dimensions. Prototypes were produced and showed that the fabrication process was successful. The prototype micro paddle structure was formed on a thin silicon nitride film and two planar rectangular spiral coils deposited on either sides of it in order to provide a current passage. Detailed steps to produce such a structure are explained in the 4th chapter. In addition, another two designs, one with a single rectangular loop on either sides of the micro paddle, and one with a single track on only one side were developed and produced as prototypes. As well as prototype fabrication, analysis of the deformation versus applied force were obtained theoretically and were compared between the developed designs to find the best configuration to minimise the required magnetic field. Since Lorentz drive system is acted in existence of a magnetic field, the strength of the field plays an important role in the amount of force produced and the deflection caused. Vibration tests were carried out and have shown the mass sensitivity of the micro paddle prototypes. The work described in this thesis extends the state of the art in several specific ways. For the first time the concept of the Lorentz drive has been applied to a MEMS micropaddle resonator in the way described,

i.e. using an on board micro fabricated coil with a precisely located external field. There is an element of novelty in the 3D printed packaging unit. Packaging is a key, often overlooked aspect of MEMS and the way in which the button magnets and current connections are incorporated with the resonator in a single simple package is considered to be an advance. The Lorentz drive method is potentially a major advance, since it will enable the resonator to be driven with a single torsional mode. This is in contrast to the established shaker method, which is known to generate a mixture of in-plane and vertical modes in addition to the desired torsional vibration. The fabrication of the desired Lorentz coil aligned on both surfaces of the paddle with an aligned via would be very difficult to achieve in a typical university laboratory like ours using conventional micro fabrication technologies. The successful application of FIB to fabricate the coil and to connect it across the bridges to conventionally fabricated contact pads is a significant advance, as described above.

# References


[1] J. L. Arlett, E. B. Myers, and M. L. Roukes. *Comparative advantages of mechanical biosensors*. Nat Nano **6**(4), 203 (2011).

[2] R. Raiteri, M. Grattarola, H.-J. Butt, and P. Skladal. *Micromechanical cantilever-based biosensors*. Sensors and Actuators B: Chemical **79**(2-3), 115 (2001).

[3] B. Ilic, H. G. Craighead, S. Krylov, W. Senaratne, C. Ober, and P. Neuzil. *Attogram detection using nanoelectromechanical oscillators* **95**(7), 3694 (2004).

[4] J. Dazhong, L. Xinxin, Z. Zhixiang, B. Hanhan, W. Yuelin, L. Jian, and Y. Haitai. *Integrated resonant cantilever sensors with 2nd torsion-mode for fg-level resoluble biomedical detection*. In *Micro Electro Mechanical Systems, 2007. MEMS. IEEE 20th International Conference on*, pp. 107–110 (2007).

[5] B. Byrne, E. Stack, N. Gilmartin, and R. Okennedy. *Antibody-based sensors: Principles, problems and potential for detection of pathogens and associated toxins*. Sensors **9**(6), 4407 (2009).

[6] W.-K. Oh, Y. S. Jeong, J. Song, and J. Jang. *Fluorescent europium-modified polymer nanoparticles for rapid and sensitive anthrax sensors*. Biosensors and Bioelectronics **29**(1), 172 (2011).

[7] S. Mostafa, I. Lee, S. K. Islam, S. A. Eliza, G. Shekhawat, V. P. Dravid, and F. S. Tulip. *Integrated mosfet-embedded-cantilever-based biosensor characteristic for detection of anthrax simulant*. Electron Device Letters, IEEE **32**(3), 408 (2011).

[8] M. L. Cable, J. P. Kirby, D. J. Levine, M. J. Manary, H. B. Gray, and A. Ponce. *Detection of bacterial spores with lanthanide-macrocycle binary complexes*. Journal of the American Chemical Society **131**(27), 9562 (2009).

[9] T. B. Tims and D. V. Lim. *Rapid detection of bacillus anthracis spores directly from powders with an evanescent wave fiber-optic biosensor*. Journal of Microbiological Methods **59**(1), 127 (2004).

[10] B. Ilic, Y. Yang, and H. G. Craighead. *Virus detection using nanoelectromechanical devices* **85**(13), 2604 (2004).

[11] M. Su, S. Li, and V. P. Dravid. *Microcantilever resonance-based dna detection with nanoparticle probes*. Applied Physics Letters **82**(20), 3562 (2003).

[12] Y.-P. Ho and P. M. Reddy. *Identification of pathogens by mass spectrometry*. Clin Chem **56**(4), 525 (2010).

[13] L. Peng. *Application of the suspended microchannel resonator as a biosensing device to profiling signal transduction in receptor tyrosine kinases*. Tech. rep., MIT (2005).

[14] J. Lu, T. Ikehara, Y. Zhang, T. Mihara, T. Itoh, and R. Maeda. *High-q and cmos compatible single crystal silicon cantilever with separated on-chip piezoelectric actuator for ultra-sensitive mass detection*. In *Micro Electro Mechanical Systems, 2008. MEMS 2008. IEEE 21st International Conference on*, pp. 665–668 (2008).

[15] T. P. Burg, A. R. Mirza, N. Milovic, C. H. Tsau, G. A. Popescu, J. S. Foster, and S. R. Manalis. *Vacuum-packaged suspended microchannel resonant mass sensor for biomolecular detection*. Microelectromechanical Systems, Journal of **15**(6), 1466 (2006).

[16] S. D. Senturia. *Microsystem Design* (Springer Science Business Media, 2001).

[17] A. F. Pacheco. *Studies of Nanoconstrictions, Nanowires and Fe3O4 Thin Films*. Recognizing Outstanding Ph.D Research (Springer, London, 2011).

[18] S. Y. Yurish and M. T. Gomes. *Smart Sensors and MEMS*, vol. 181 of *Mathematics, Physics and Chemistry* (Kluwer Academic, London, 2004).

[19] L. G. Carrascosa, M. Moreno, M. Alvarez, and L. M. Lechuga. *Nanomechanical biosensors: a new sensing tool*. TrAC Trends in Analytical Chemistry **25**(3), 196 (2006).

[20] C. P. Wong, K. Moon, and Y. Li. *Nano-Bio-Electronic, Photonic and MEMS Packaging* (Springer, London, 2010).

[21] N. V. Lavrik, M. J. Sepaniak, and P. G. Datskos. *Cantilever transducers as a platform for chemical and biological sensors*, vol. 75 (AIP, 2004).

[22] M. Chaudhary and A. Gupta. *Microcantilever-based sensors*. Defence Science Journal **59**(6), 634 (2009).

[23] S. Chitsaz-Charandabi, P. D. Prewett, C. A. Hamlett, C. J. Anthony, and J. A. Preece. *Nano planar coil actuated micro paddle resonator for mass detection*. Microelectron. Eng. **88**(8), 2229 (2011).

[24] Z. Davis, W. Svendsen, and A. Boisen. *Design, fabrication and testing of a novel mems resonator for mass sensing applications*. Microelectronic Engineering **84**(5-8), 1601 (2007).

[25] H. Campanella. *Acoustic Wave and Electromechanical Resonators: Concept to Key Applications*. Integrated Microsystems (Artech House, 2010).

[26] X. Sun, J. Zheng, M. Poot, C. W. Wonf, and H. X. Tang. *Femtogram doubly clamped nanomechanical resonators embedded in a high-q two-dimensional photonic crystal nanocavity*. Nano Letters **12**(5), 2299 (1012).

[27] N. V. Lavrik and P. G. Datskos. *Femtogram mass detection using photothermally actuated nanomechanical resonators*. Applied Physics Letters **82**(16), 2697 (2003).

[28] E. T. Arakawa, N. V. Lavrik, and P. G. Datskos. *Detection of anthrax simulants with microcalorimetric spectroscopy: Bacillus subtilis and bacillus cereus spores*. Appl. Opt. **42**(10), 1757 (2003).

[29] X. Zhang, C. R. Yonzon, and R. P. V. Duyne. *An electrochemical surface-enhanced raman spectroscopy approach to anthrax detection*. Proceedings of SPIE **5221**, 82 (2003).

[30] *Biowarfare agent detection devices*. www.advnt.org (20/10/2011).

[31] *Biological agents detection*. http://www.smithsdetection.com (20/10/2011).

[32] C. J. Peters and D. M. Hartley. *Anthrax inhalation and lethal human infection*. The Lancet **359**(9307), 710 (2002).

[33] S. P. Mohanty and E. Kougianos. *Biosensors: a tutorial review*. Potentials, IEEE **25**(2), 35 (2006).

[34] S. P. J. Higson, S. M. Reddy, and P. M. Vadgama. *Enzyme and other biosensors: evolution of a technology*. Engineering Science and Education Journal **3**(1), 41 (1994).

[35] D. Barcelo, M. Lopez de Alda, M. P. Marco, and S. Rodriguez-Mozaz. *Biosensors for environmental applications: Future development trends*. Pure and Applied Chemistry **76**, 723 (2004).

[36] T. Vo-Dinh and B. Cullum. *Biosensors and biochips: advances in biological and medical diagnostics*. Fresenius' Journal of Analytical Chemistry **366**(6), 540 (2000).

[37] J. Fritz. *Cantilever biosensors*. Analyst **133**(7), 855 (2008).

[38] B. D. Malhotra and A. P. F. Turner. *Advances in Biosensors*, vol. 5 of *Prespectives in Biosensors* (Elsveir Science B.V., Amsterdam, 2003).

[39] J. J. Gooding. *Biosensor technology for detecting biological warfare agents: Recent progress and future trends*. Analytica Chimica Acta **559**(2), 137 (2006).

[40] D. W. Morrison, M. R.Dokmeci, U. Demirci, and A. Khademhosseini. *Clinical applications of micro and nanoscale biosensors*. In K. E. Gonsalves, C. L. Laurencin, C. R. Halberstadt, and L. S. Nair, eds., *BIOMEDICAL NANOSTRUCTURES*, pp. 433–454 (John Wiley and Sons, Inc., 2008).

[41] L. Wang, D. M. Sipe, Y. Xu, and Q. Lin. *A mems thermal biosensor for metabolic monitoring applications*. Microelectromechanical Systems, Journal of **17**(2), 318 (2008).

[42] G. Acharya, D. D. Doorneweerd, C.-L. Chang, W. A. Henne, P. S. Low, and C. A. Savran. *Label-free optical detection of anthrax-causing spores* **129**(4), 2 (2007).

[43] M. D. Yilmaz, S. Hsu, D. Reinhoudt, A. Velders, and J. Huskens. *Ratiometric fluorescent detection of an anthrax biomarker at molecular printboards*. Angewandte Chemie International Edition **49**(34), 5938 (2010).

[44] C. Ruan, L. Yang, and Y. Li. *Immunobiosensor chips for detection of escherichia coli o157:h7 using electrochemical impedance spectroscopy*. Analytical Chemistry **74**(18), 4814 (2002).

[45] A. A. Ansari, M. Alhoshan, M. S. Alsalhi, and A. S. Aldwayyan. *Prospects of nanotechnology in clinical immunodiagnostics*. Sensors **10**(7), 6535 (2010).

[46] D.-W. Lee, Y.-L. Lee, and J.-H. Kang. *Fabrication and evaluation of a novel protein sensor based on lorentz force*. Microelectronic Engineering **84**(5-8), 1719 (2007).

[47] O. Brand and H. Baltes. *Micromachined resonant sensors - an overview*. Sensors Update **4**(1), 3 (1998).

[48] B. Oliver. *Micromachined resonators for ultrasound based proximity sensing*. Ph.D. thesis (1994).

[49] W. P. Taylor and M. G. Allen. *Integrated magnetic microrelays: normally open, normally closed, and multi-pole devices*. In *Solid State Sensors and Actuators, 1997. TRANSDUCERS '97 Chicago., 1997 International Conference*, vol. 2, pp. 1149–1152 vol.2 (1997).

[50] R. S. Marks, D. C. Cullen, I. Karube, C. R. Lowe, and H. H. Weetall. *Handbook of BIOSENSORS AND BIOCHIPS* (John Wiley and Sons, Ltd., 2007).

[51] F. Ahmad, M. H. M. Khir, N. H. Hamid, and J. O. Dennis. *Analytical modeling of plus shape mems paddle bridge resonant sensor for weak magnetic fields*. In *Micro and Nanoelectronics (RSM), 2011 IEEE Regional Symposium on*, pp. 310–314 (2011).

[52] I. Birkby. *A review of microcantilevers for sensing applications*. MediLexicon, Intl. (2007).

[53] S. K. Vashist. *A review of microcantilevers for sensing applications*. AZojono, Journal of Nanotechnology Online **3**, 1 (2007).

[54] J. Lu, Y. Zhang, T. Itoh, and R. Maeda. *Micro disk resonator with on-disk piezoelectric thin film transducers for integrated mems ubiquitous applications*. In *Solid-State Sensors, Actuators and Microsystems Conference (TRANSDUCERS), 2011 16th International*, pp. 514–517 (2011).

[55] J. W. L. J. Y. Park, J. U. Bu. *Rf mems devices for wireless applications*. Journal of semiconductor technology and science **1**(1), 70 (2001).

[56] J. Yang, T. Ono, and M. Esashi. *Mechanical behavior of ultrathin microcantilever*. Sensors and Actuators A: Physical **82**(1-3), 102 (2000).

[57] B. Boonliang and et al. *A focused-ion-beam-fabricated micro-paddle resonator for mass detection*. Journal of Micromechanics and Microengineering **18**(1), 015021 (2008).

[58] V. A. Petrenko and V. J. Vodyanoy. *Phage display for detection of biological threat agents*. Journal of Microbiological Methods **53**(2), 253 (2003).

[59] S. S. Iqbal, M. W. Mayo, J. G. Bruno, B. V. Bronk, C. A. Batt, and J. P. Chambers. *A review of molecular recognition technologies for detection of biological threat agents*. Biosensors and Bioelectronics **15**(11-12), 549 (2000).

[60] L. A. Pinnaduwage, J. Hai-Feng, and T. Thundat. *Moore's law in homeland defense: an integrated sensor platform based on silicon microcantilevers*. Sensors Journal, IEEE **5**(4), 774 (2005).

[61] D. Jin, X. Li, J. Liu, G. Zuo, Y. Wang, M. Liu, and H. Yu. *High-mode resonant piezoresistive cantilever sensors for tens-femtogram resoluble mass sensing in air* **16**(5), 7 (2006).

[62] S. S. L. B. Freund. *Thin Film Materials: Stress, Defect Formation and Surface Evolution*. Materials Science and Engineering (Massachusette Institute of Technology, 2003).

[63] H. J. D. N. A. J. R. Xue Feng, Yonggang Huang. *The effect of thin film/substrate radii on the stoney formula for thin film/substrate subjected to nonuniform axisymmetric misfit strain and temperature*. Mechanics of Materials and Structures **1**(6), 1041 (2006).

[64] *Lpcvd silicon nitride (stoichiometric)*. http://www.mit.edu (16/11/2011).

[65] *Lpcvd silicon nitride (silicon-rich)*. http://www.mit.edu (16/11/2011).

[66] *Silicon nitride (si3n4), film*. http://www.memsnet.org (11/10/2011).

[67] T. T. Anja Boisen. *Design and fabrication of cantilever array biosensors*. Materials Today **12**(9), 32 (2009).

[68] G. Wu, H. Ji, K. Hansen, T. Thundat, R. Datar, R. Cote, M. F. Hagan, A. K. Chakraborty, and A. Majumdar. *Origin of nanomechanical cantilever motion generated from biomolecular interactions*. Proceedings of the National Academy of Sciences **98**(4), 1560 (2001).

[69] S. Schmid, S. Dohn, and A. Boisen. *Real-time particle mass spectrometry based on resonant micro strings*. Sensors **10**(9), 8092 (2010).

[70] J. P. Cleveland, S. Manne, D. Bocek, and P. K. Hansma. *A nondestructive method for determining the spring constant of cantilevers for scanning force microscopy*. Review of Scientific Instruments **64**(2), 403 (1993).

[71] C. Ziegler. *Cantilever-based biosensors*. Analytical and Bioanalytical Chemistry **379**(7), 946 (2004).

[72] A. Gupta, D. Akin, and R. Bashir. *Detection of bacterial cells and antibodies using surface micromachined thin silicon cantilever resonators*. Journal of Vacuum Science and Technology B: Microelectronics and Nanometer Structures **22**(6), 2785 (2004).

[73] P. I. Oden. *Gravimetric sensing of metallic deposits using an end-loaded microfabricated beam structure*. Sensors and Actuators B: Chemical **53**(3), 191 (1998).

[74] Y. T. Yang, C. Callegari, X. L. Feng, K. L. Ekinci, and M. L. Roukes. *Zeptogram-scale nanomechanical mass sensing*. Nano Letters **6**(4), 583 (2006).

[75] K. Jensen, K. Kim, and A. Zettl. *An atomic-resolution nanomechanical mass sensor*. Nat Nano **3**(9), 533 (2008).

[76] M. Li, H. X. Tang, and M. L. Roukes. *Ultra-sensitive nems-based cantilevers for sensing, scanned probe and very high-frequency applications*. Nat Nano **2**(2), 114 (2007).

[77] H. B. Peng, C. W. Chang, S. Aloni, T. D. Yuzvinsky, and A. Zettl. *Ultrahigh frequency nanotube resonators*. Physical Review Letters **97**(8), 087203 (2006).

[78] X. L. Feng, R. He, P. Yang, and M. L. Roukes. *Very high frequency silicon nanowire electromechanical resonators*. Nano Letters **7**(7), 1953 (2007).

[79] H. F. Ji, X. Yang, J. Zhang, and T. Thundat. *Molecular recognition of biowarfare agents using micromechanical sensors*. Expert Review of Molecular Diagnostics **4**(6), 859 (2004).

[80] K. L. Ekinci, X. M. H. Huang, and M. L. Roukes. *Ultrasensitive nanoelectromechanical mass detection*. Applied Physics Letters **84**(22), 4469 (2004).

[81] S. Beeby, g. Ensell, M. Kraft, and N. White. *MEMS Mechanical Sensors* (Artech House, Inc., 2004).

[82] B. Harrington, R. Abdolvand, A. Hajjam, J. Wilson, and S. Pourkamali. *Thin-film piezoelectric-on-silicon particle mass sensors*. pp. 238–241 (2010).

[83] K. Ikeda, H. Kuwayama, T. Kobayashi, T. Watanabe, T. Nishikawa, T. Yoshida, and K. Harada. *Silicon pressure sensor integrates resonant strain gauge on diaphragm*. Sensors and Actuators A: Physical **21**(1-3), 146 (1990).

[84] A. Meckes, J. Behrens, and W. Benecke. *Electromagnetically driven microvalve fabricated in silicon*. In *Solid State Sensors and Actuators, 1997. TRANSDUCERS '97 Chicago., 1997 International Conference on*, vol. 2, pp. 821–824 vol.2 (1997).

[85] J. S. Burdess, A. J. Harris, D. Wood, R. J. Pitcher, and D. Glennie. *A system for the dynamic characterization of microstructures*. Microelectromechanical Systems, Journal of **6**(4), 322 (1997).

[86] Y. Zhong, G. Zhang, C. Leng, and T. Zhang. *A differential laser doppler system for one-dimensional in-plane motion measurement of mems*. Measurement **40**(6), 623 (2007).

[87] D. R. Evans and V. S. J. Craig. *Sensing cantilever beam bending by the optical lever technique and its application to surface stress*. The Journal of Physical Chemistry B **110**(11), 5450 (2006).

[88] P. S. Waggoner, M. Varshney, and H. G. Craighead. *Detection of prostate specific antigen with nanomechanical resonators*. Lab on a Chip **9**(21), 3095 (2009).

[89] A. Herrera-May, L. Aguilera-Cortes, P. Garcia-Ramirez, and E. Manjarrez. *Resonant magnetic field sensors based on mems technology*. Sensors **9**(10), 7785 (2009).

[90] V. Ferrari, D. Marioli, A. Taroni, E. Ranucci, and P. Ferruti. *Development and application of mass sensors based on flexural resonances in alumina beams*. Ultrasonics, Ferroelectrics and Frequency Control, IEEE Transactions on **43**(4), 601 (1996).

[91] P. Srinivasan and S. M. Spearing. *Optimal materials selection for bimaterial piezoelectric microactuators*. Microelectromechanical Systems, Journal of **17**(2), 462 (2008).

[92] D. L. DeVoe and A. P. Pisano. *Modeling and optimal design of piezoelectric cantilever microactuators*. Microelectromechanical Systems, Journal of **6**(3), 266 (1997).

[93] P. G. Datskos, N. V. Lavrik, and M. J. Sepaniak. *Chemical and biological sensors based on microcantilevers smart sensors and mems*. vol. 181 of *NATO Science Series*, pp. 331–379 (Springer Netherlands, 2004).

[94] C. L. Britton Jr, R. L. Jones, P. I. Oden, Z. Hu, R. J. Warmack, S. F. Smith, W. L. Bryan, and J. M. Rochelle. *Multiple-input microcantilever sensors*. Ultramicroscopy **82**(1-4), 17 (2000).

[95] T. W. Kenny, W. J. Kaiser, J. A. Podosek, H. K. Rockstad, J. K. Reynolds, and E. C. Vote. *Micromachined tunneling displacement transducers for physical sensors*. Journal of Vacuum Science and Technology A Vacuum, Surfaces, and Films **11**(4), 797 (1993).

[96] G. Binnig and H. Rohrer. *Scanning tunneling microscopy from birth to adolescence*. Reviews of Modern Physics **59**(3), 615 (1987).

[97] A. P. Davila, J. Jang, A. K. Gupta, T. Walter, A. Aronson, and R. Bashir. *Microresonator mass sensors for detection of bacillus anthracis sterne spores in air and water*. Biosensors and Bioelectronics **22**(12), 3028 (2007).

[98] A. Gupta, D. Akin, and R. Bashir. *Single virus particle mass detection using microresonators with nanoscale thickness*. Applied Physics Letters **84**(11), 1976 (2004).

[99] B. Ilic, D. Czaplewski, M. Zalalutdinov, H. G. Craighead, P. Neuzil, C. Campagnolo, and C. Batt. *Single cell detection with micromechanical oscillators*. vol. 19, pp. 2825–2828 (AVS, 2001).

[100] K. L. Ekinci and M. L. Roukes. *Nanoelectromechanical systems*. Review of Scientific Instruments **76**(6), 061101 (2005).

[101] T. Thundat, E. A. Wachter, S. L. Sharp, and R. J. Warmack. *Detection of mercury vapor using resonating microcantilevers*. Applied Physics Letters **66**(13), 1695 (1995).

[102] M.-Y. Jung, D.-W. Kim, S. S. Choi, C. J. Kang, and Y. Kuk. *Characterization of bimetallic cantilever for chemical sensor application*. Japanese Journal of Applied Physics **38**(Part 1, No. 11), 6555 (1999).

[103] A. Boisen, J. Thaysen, H. Jensenius, and O. Hansen. *Environmental sensors based on micromachined cantilevers with integrated read-out*. Ultramicroscopy **82**(1-4), 11 (2000).

[104] B. Ilic, Y. Yang, K. Aubin, R. Reichenbach, S. Krylov, and H. G. Craighead. *Enumeration of dna molecules bound to a nanomechanical oscillator*. Nano Letters **5**(5), 925 (2005).

[105] E. Forsen, G. Abadal, S. Ghatnekar-Nilsson, J. Teva, J. Verd, R. Sandberg, W. Svendsen, F. Perez-Murano, J. Esteve, E. Figueras, F. Campabadal, L. Montelius, N. Barniol, and A. Boisen. *Ultrasensitive mass sensor fully integrated with complementary metal-oxide-semiconductor circuitry*. Applied Physics Letters **87**(4), 043507 (2005).

[106] C. Hagleitner, A. Hierlemann, D. Lange, A. Kummer, N. Kerness, O. Brand, and H. Baltes. *Smart single-chip gas sensor microsystem*. Nature **414**(6861) (2001).

[107] R. Goodacre, R. Shann, E. Gilbert, A. Timmins, B. McGovern, D. Alsberg, Kell, and N. Logan. *Detection of the dipicolinic acid biomarker in bacillusbacillus spores using curie-point pyrolysis mass spectrometry and fourier transform infrared spectroscopy*. Analytical Chemistry **72**(1), 119 (2000).

[108] K. M. Taylor and W. Lin. *Hybrid silica nanoparticles for luminescent spore detection*. Journal of Materials Chemistry **19**(1), 6418 (2009).

[109] H. Chassaigne and L. R. Taylor. *Characterization of horse kidney metallothionein isoforms by electrospray ms and reversed-phase hplc-electrospray ms*. The Analyst **123**(10), 2125 (1998).

[110] K. Ai, B. Zhang, and L. Lu. *Europium-based fluorescence nanoparticle sensor for rapid and ultrasensitive detection of an anthrax biomarker*. Angewandte Chemie International Edition **48**(2), 304 (2009).

[111] M. Shaw, S. Hill, and P. Jones. *Chelation ion chromatography of metal ions using high performance substrates dynamically modified with heterocyclic carboxylic acids*. Analytica Chimica Acta **401**(1-2), 65 (1999).

[112] A. Gultekin, S. E. Diltemiz, A. Ersoz, Y. Sariozlu, A. Denizli, and R. Say. *GoldâĂŞsilver nanoclusters having dipicolinic acid imprinted nanoshell for bacillus cereus spores recognition*. Talanta **78**(4-5), 1332 (2009).

[113] A. Gultekin, A. Ersoz, N. Y. Sariozlu, A. Denizli, and R. Say. *Nanosensors having dipicolinic acid imprinted nanoshell for bacillus cereus spores detection*. Journal of Nanoparticle Research **12**(6), 2069 (2010).

[114] Y. Zhou, B. Yu, and K. Levon. *Potentiometric sensor for dipicolinic acid*. Biosensors and bioelectronics **20**(9), 1851 (2005).

[115] H. Cheng, W. Luo, G. Wen, S. Huan, G. Shen, and R. Yu. *Surface-enhanced raman scattering based detection of bacterial biomarker and potential surface reaction species*. The Analyst **135**(11), 2993 (2010).

[116] A. Dhawan, Y. Du, F. Yan, M. Gerhold, V. Misra, and T. Vo-Dinh. *Methodologies for developing surface-enhanced raman scattering (sers) substrates for detection of chemical and biological molecules*. Sensors Journal, IEEE **10**(3), 608 (2010).

[117] S.-I. Makino, H. Cheun, M. Watarai, I. Uchida, and K. Takeshi. *Detection of anthrax spores from the air by real-time pcr*. Letters in Applied Microbiology **33**(3), 237 (2001).

[118] *www.advnt.org*. Advnt Biotechnologies, 04/08/2009 .

[119] *www.lifesafetysys.com*. Life Safety Systems, 04/08/2009 .

[120] *www.udetection.com*. Universal Detection Systems, 30/08/2011 .

[121] *www.smithsdetection.com*. Smiths Detection, 04/08/2009 .

[122] C. Davis, J. M. Kang, C. Dube, J. Borenstein, E. Nazarov, R. Miller, and ZapataAM. *Spore biomarker detection using a mems differential mobility spectrometer* **2**, 1233 (2003).

[123] A. Wig, E. Arakawa, A. Passian, T. Thundat, and T. Ferrell. *Photothermal spectroscopy of bacillus cereus and bacillus anthracis from 2.5 Âţm to 14.5 Âţm with microcantilevers*. Sensors and Actuators **114**(10), 206 (2006).

[124] M. Alvarez and L. M. Lechuga. *Microcantilever-based platforms as biosensing tools*. Analyst **135**(5), 827 (2010).

[125] N. K. Chaki and K. Vijayamohanan. *Self-assembled monolayers as a tunable platform for biosensor applications*. Biosensors and Bioelectronics **17**, 1 (2002).

[126] S. Charandabi, P. D. Prewett, C. A. Hamlett, C. J. Anthony, and J. A. Preece. *Nano planar coil actuated micro paddle resonator for mass detection*. Microelectron. Eng. **88**(8), 2229 (2011).

[127] C. Beards. *Structural Vibration: Analysis and Damping* (Arnold, 1996).

[128] S. Clarence de. *Vibration damping*. In *Vibration Damping, Control, and Design*, Mechanical Engineering Series, pp. 1–31 (CRC Press, 2007).

[129] S. K. Hara, Fumio. *Damping ad energy dissipation*. ASME PRESSURE VESSELS PIPING DIV PUBL PVP **256**(2), 55 (1993).

[130] M. Ghatkesar, V. Barwich, T. Braun, A. H. Bredekamp, U. Drechsler, M. Despont, H. P. Lang, M. Hegner, and C. Gerber. *Real-time mass sensing by nanomechanical resonators in fluid*. In *Sensors, 2004. Proceedings of IEEE*, vol. 2, pp. 1060–1063 (2004).

[131] O. Brand and H. Baltes. *Micromachined resonant sensors: an overview*. Sensors Update **4**(1), 3 (1998).

[132] N. Lobontiu. *Mechanical design of microresonators: modeling and applications*. nanoscience and technology (McGraw-Hill, 2006), illustrated ed.

[133] K. B. Lee. *Principles of Microelectromechanical Systems* (Wiley IEEE Press, 2011), 1 ed.

[134] J. J. Allen. Micro Electro Mechanical System Design (Taylor and Francis Group, 2005).

[135] F. Beer, E. Johnston, and J. DeWolf. *Mechanics of Materials* (McGraw-Hill, 1992), 6 ed.

[136] S. Timoshenko and J. N. Goodier. *Theory of Elasticity* (McGRAW-HILL, 1951).

[137] W. C. Young and R. G. Budynas. *Roark's Formulas for Stress and Strain* (McGroaw-Hill, 2002), 7 ed.

[138] B. I. Bleany and B. Bleany. *Electricity and Magnetism* (Oxford University Press, 1965), 2 ed.

[139] M. Misakian. *Equations for the magnetic field produced by one or more rectangular loops of wire in the same plane*. Journal of Research of the National Institute of Standards and Technology **105**(4), 557 (2000).

[140] D. F. John D. Kraus. *Electromagnetics*. Electrical and Computer Engineering (McGraw-Hill Higher Education, 1999), 5 ed.

[141] G. De Marzi, D. Iacopino, A. J. Quinn, and G. Redmond. *Probing intrinsic transport properties of single metal nanowires: Direct-write contact formation using a focused ion beam*. Journal of Applied Physics **96**(6), 3458 (2004).

[142] M. Chakravorty, K. Das, A. K. Raychaudhuri, J. P. Naik, and P. D. Prewett. *Temperature dependent resistivity of platinum-carbon composite nanowires grown by focused ion beam on sio2/si substrate*. Microelectronic Engineering **88**(11), 3360 (2011).

[143] M. Aurich, A. C. Filho, T. N. Bittencourt, and S. P. Shah. *Finite element modeling of concrete behavior at early age*. IBRACON Structures and Materials Journal **2**(1), 21 (2009).

[144] X. C. Zhang, E. B. Myers, J. E. Sader, and M. L. Roukes. *Nanomechanical torsional resonators for frequency-shift infrared thermal sensing*. Nano Letters **13**(4), 1528 (2013).

[145] Q. Li, L. Yiliang, and L. Liang. *Finite element analysis for stress and magnetic field of a 40 ka protection inductor*. Applied Superconductivity, IEEE Transactions on **20**(3), 1936 (2010).

[146] M. Mingkai, Z. Feng, L. Qiang, and F. C. Lee. *Finite element analysis of inductor core loss under dc bias condition*. In *Applied Power Electronics Conference and Exposition (APEC), 2012 Twenty-Seventh Annual IEEE*, pp. 405–410 (2012).

[147] M. Pustan, O. Belcin, and J. C. Golinval. *Dynamic investigations of paddle mems cantilevers used in mass sensing applications* (2011).

[148] B. Couteau, P. Mansat, A. Estivalezes, R. Darmana, M. Mansat, and J. Egan. *Finite element analysis of the mechanical behavior of a scapula implanted with a glenoid prosthesis*. Clinical biomechanics (Bristol, Avon) **16**(7), 566 (2001).

[149] M. Nurhaniza, M. K. A. Ariffin, A. Ali, F. Mustapha, and A. W. Noraini. *Finite element analysis of composites materials for aerospace applications*. Composites Manufacturing: Materials, Product and Engineering **11**, 7 (2010).

[150] M. Fagan. *Finite Element Analysis: Theory and Practice* (Prentice Hall, 1992), 1 ed.

[151] B. J. Inkson, G. Dehm, and T. Wagner. *Thermal stability of ti and pt nanowires manufactured by ga+ focused ion beam*. Journal of Microscopy **214**(Pt 3), 252 (2004).

[152] L. Penate-Quesada, J. Mitra, and P. Dawson. *Non-linear electronic transport in pt nanowires deposited by focused ion beam*. Nanotechnology **18**(21), 215203 (2007).

[153] T. Tao, J. Ro, J. Melngailis, Z. Xue, and H. D. Kaesz. *Focused ion beam induced deposition of platinum*. vol. 8, pp. 1826–1829 (AVS, 1990).

[154] T. Tao, W. Wilkinson, and J. Melngailis. *Focused ion beam induced deposition of platinum for repair processes*. Journal of Vacuum Science and Technology B: Microelectronics and Nanometer Structures **9**(1), 162 (1991).

[155] S. Smith, A. J. Walton, S. Bond, A. Ross, J. Stevenson, and A. M. Gundlach. *Electrical characterization of platinum deposited by focused ion beam*. Semiconductor Manufacturing, IEEE Transactions on **16**(2), 199 (2003).

[156] J. Pyrhonen, T. Jokinen, and V. Hrabovcova. *Design of Rotating Electrical Machines* (John Wiley and Sons, 2009).

[157] M. Gad-el Hak. *MEMS Introduction and Fundamentals*. Mechanical Engineering (Taylor and Francis, 2006), 2 ed.

[158] S. Franssila. *Introduction to Micro Fabrication* (John Wiley and Sons, 2004).

[159] T.-R. Hsu. *MEMS and Microsystems: Design and Manufacture* (McGraw-Hill, 2002).

[160] A. Benitez, J. Bausells, E. Cabruja, J. Esteve, and J. Samitier. *Stress in low pressure chemical vapour deposition polycrystalline silicon thin films deposited below 0.1 torr*. Sensors and Actuators A: Physical **37**(0), 723 (1993).

[161] J. G. E. Gardeniers, H. A. C. Tilmans, and C. C. G. Visser. *Lpcvd silicon-rich silicon nitride films for applications in micromechanics, studied with statistical experimental design*. Journal of Vacuum Science and Technology A: Vacuum, Surfaces, and Films **14**(5), 2879 (1996).

[162] S. M. Sze. *Semiconductor Devices: Physics and Technology* (John Wiley and Sons Inc., 2002), 2 ed.

[163] A. Stoffel, A. Kovacs, W. Kronast, and B. Muller. *Lpcvd against pecvd for micromechanical applications*. Journal of Micromechanics and Microengineering **6**(1), 1 (1996).

[164] F. Alvarez and A. A. Valladares. *The atomic and electronic structure of amorphous silicon nitride*. Revista Mexicana De Fisica **48**(6), 528 (2002).

[165] *Transduction on electron devices*. IEEE **ED25**(10) (1978).

[166] H. Pierson. *Handbook of Chemical Vapor Depostion [i.e. Deposition] (CVD): Principles, Technology, and Applications* (Noyes Publications/William Andrew Pub., 1999).

[167] L. Kiesewetter, J. M. Zhang, D. Houdeau, and A. Steckenborn. *Determination of young's moduli of micromechanical thin films using the resonance method*. Sensors and Actuators A: Physical **35**(2), 153 (1992).

[168] K. E. Petersen and C. R. Guarnieri. *Young's modulus measurements of thin films using micromechanics*. Journal of Applied Physics **50**(11), 6761 (1979).

[169] R. Edwards, G. Coles, and W. Sharpe. *Comparison of tensile and bulge tests for thin-film silicon nitride*. Experimental Mechanics **44**(1), 5 (2004).

[170] N. Vally. *Micro electro mechanical systems workshop*. IEEE (1990).

[171] D. Schneider and M. D. Tucker. *Non-destructive characterisation and evaluation of thin films by laser induced ultrasonic surface waves*. Thin Solid Films pp. 209–291 (1996).

[172] C. L. Muhlstein and S. B. Brown. *Mechanical Properties of Structural Films* (ASTM, USA, 2001).

[173] C. Wen-Hsien, T. Luger, R. K. Fettig, and R. Ghodssi. *Mechanical property characterization of lpcvd silicon nitride thin films at cryogenic temperatures*. Microelectromechanical Systems **13**(5), 870 (2004).

[174] O. Tabata, K. Kawahata, S. Sugiyama, and I. Igarashi. *Mechanical property measurements of thin films using load-deflection of composite rectangular membranes*, vol. 20 (1989).

[175] *Spr-220 series resist datasheet*. Shipley i-Line Photoresist (10/08/2011).

[176] K. Suzuki and B. W. Smith. *Microlithography: science and technology* (Taylor and Francis, 2007).

[177] G. T. A. Kovacs, N. I. Maluf, and K. E. Petersen. *Bulk micromachining of silicon*. Proceedings of the IEEE **86**(8), 1536 (1998).

[178] L. Holland. *Vacuum deposition of thin films* (Wiley, 1966).

[179] N. Yao. *Focused Ion Beam Systems: Basics and Applications* (Cmbridge University Press, 2007).

[180] R. Steve and P. Robert. *A review of focused ion beam applications in microsystem technology*. Journal of Micromechanics and Microengineering **11**(4), 287 (2001).

[181] J. Melngailis. *Focused ion beam technology and applications*. Journal of Vacuum Science and Technology B: Microelectronics and Nanometer Structures **5**(2), 469 (1987).

[182] *Fei (db 235) focused ion beam user manual, p. 5-13, 5-14*. FEI (FIB/SEM) Company (01/02/2001).

[183] P. R. Kaczmarek, T. Rogowski, A. J. Antonczak, and K. M. Abramski. *Laser doppler vibrometry with acoustooptic frequency shift*. AOptica Applicata **XXXIV**(3), 373 (2004).

[184] J. De Coster and S. Sangameswaran. *Applications of laser-doppler vibrometry during mems device qualification*. In J. Buytaert and J. Dirckx pp. 1–9 (2010).

[185] *Vibrometer operator's manual for polytec vibrometer series uhf-120*. Polytec GmbH (21/03/2012).

[186] M. J. Martin, B. H. Houston, J. W. Baldwin, and M. K. Zalalutdinov. *Damping models for microcantilevers, bridges, and torsional resonators in the free-molecular-flow regime*. Microelectromechanical Systems **17**(2), 503 (2008).

[187] A. C. Fischer-Cripps. *Nanoindentation*. Mechanical Engineering Series 1 (Springer Science+Business Media, 2011).

[188] L. D. Landau and E. Lifshitz. *Fluid Mechanics*, vol. 6 of *Course of Theoretical Physics* (1987).